PURDUE UNIVERSITY
LIBRARY

JOURNAL OF THE

AERO/SPACE SCIENCES

VOLUME 26 AUGUST, 1959 NUMBER 8

CONTENTS

Aerodynamics of Wings and Bodies at Transonic Speeds ..... JOHN R. SPREITER 465

An Experimental Study of the Flow Field About Swept and Delta Wings With Sharp Leading Edges ..... IVAN JASZLICS AND LEON TRILLING 487

Divergence of Plate Airfoils of Low Aspect Ratio at Supersonic Speeds ..... G. J. HANCOCK 495

Numerical Solution of the Boundary-Layer Equations Without Similarity Assumptions ..... R. F. KRAMER AND H. M. LIEBERSTEIN 508

A Cool Mercury Plasma Tunnel ..... HANS U. ECKERT 515

Analysis of a Simplified Model of Solid Propellant Resonant Burning ..... W. NACHBAR AND L. GREEN, JR. 518

Readers' Forum 527

MECHANICAL ENGINEERING
AUG 19 1959
LIBRARY

Published by
INSTITUTE OF THE AERONAUTICAL SCIENCES, INC.

JOURNAL OF THE AERO/SPACE SCIENCES

Editor: W. R. SEARS

Director, Graduate School of Aeronautical Engineering, Cornell University

Associate Editor: ROBERT R. DEXTER

Managing Editor: RITA J. TURINO

Editorial Assistant: CAROLINE TAYLOR

Editorial Committee

Aerodynamics and Fluid Mechanics

H. Julian Allen
Holt Ashley
Dean R. Chapman
Francis H. Clauser
Hugh L. Dryden
John C. Evvard
Antonio Ferri
Alexander Flax
Wallace D. Hayes
R. T. Jones
Carl Kaplan
H. W. Liepmann
C. C. Lin
H. F. Ludloff
Harold Luskin
Clark B. Millikan
Henry T. Nagamatsu
H. J. E. Reid
George S. Schairer
G. B. Schubauer
John Stack
Theodore Theodorsen
Arthur N. Tifford
Th. von Kármán

Flight Testing

R. R. Gilruth
Melvin N. Gough
W. L. Howland
W. F. Milliken, Jr.

Rotating Wing Aircraft

F. B. Gustafson
K. H. Hohenemser
Bartram Kelley
R. B. Maloy
Ralph McClarren
R. H. Miller
R. H. Prewitt
Igor I. Sikorsky

Structures

John E. Duberg
R. R. Heldenfels
N. J. Hoff
Samuel Levy
J. F. McBrearty
W. Ramberg
E. E. Sechler
F. R. Shanley
C. R. Strang
S. Timoshenko

Meteorology

C. F. Brooks
D. M. Little
F. W. Reichelderfer
K. C. Spengler

Vibration and Flutter

Lee Arnold
M. A. Biot
R. L. Bisplinghoff
Harold A. Cheilek
I. E. Garrick
Martin Goland

Aircraft Design

W. E. Beall
E. H. Heinemann
Hall L. Hibbard
Richard Hutton
C. L. Johnson
A. A. Kartveli
F. K. Teichmann

Electronics

K. C. Black
M. V. Kiebert, Jr.
David S. Little
Paul Rosenberg
Giles J. Strickroth

Physiologic Problems

H. G. Armstrong
Louis H. Bauer
Robert J. Benford
W. Randolph Lovelace, II
Ross A. MacFarland

Flight Propulsion

William Bollay
George W. Brady
R. P. Kroon
Frank E. Marble
Abe Silverstein
E. S. Taylor

Instruments

Alan G. Binnie
Charles H. Colvin
Frank R. Cook
C. S. Draper
S. G. Eskin
C. F. Savage
R. C. Sylvander

SUBSCRIPTION RATES

JOURNAL OF THE AERO/SPACE SCIENCES (formerly Journal of the Aeronautical Sciences), Published Monthly. United States and Possessions: 1 Year, $15.00; Single Copies, $1.50. Foreign Countries Including Canada (American Currency Rates): 1 Year, $16.00; Single Copies, $1.50.

AERO/SPACE ENGINEERING, Published Monthly. United States and Possessions: 1 Year, $5.00; Single Copies, $0.50. Foreign Countries Including Canada (American Currency Rates): 1 Year, $6.00; Single Copies, $0.50.

Notices of change of address should be sent to the Institute at least 30 days prior to actual change of address.

Manuscripts for publication, proofs, and all correspondence should be addressed to the Editorial Office of the JOURNAL.

Publication Office, 20th and Northampton Sts., Easton, Pa. Correspondence regarding subscriptions may be addressed to the Editorial Office of the JOURNAL OF THE AERO/SPACE SCIENCES, 2 East 64th Street, New York 21, N.Y.

© Copyright, 1959, by the Institute of the Aeronautical Sciences, Inc.

Second-Class Mail Privileges Authorized at Easton, Penna. Acceptance for mailing at a special rate of postage provided for in Section 1103, Act of October 3, 1917, authorized April 29, 1937.

JOURNAL OF THE AERO/SPACE SCIENCES

VOLUME 26 AUGUST, 1959 NUMBER 8

Aerodynamics of Wings and Bodies at Transonic Speeds

JOHN R. SPREITER*

Ames Research Center, NASA

SUMMARY

A summary is presented of basic concepts and principal results that have emerged from numerous experimental and theoretical investigations of transonic flow past thin wings and slender bodies. Emphasis is placed throughout on the correlation and evaluation of results provided by diverse methods for the approximate solution of the nonlinear equations of the small disturbance theory of transonic flow, and also on a critical examination of experimental results.

INTRODUCTION

ALTHOUGH the determination of the aerodynamic properties of wings and bodies at transonic speeds is a problem that is no harder to conceive than the corresponding problems for subsonic or supersonic speeds, nature has appeared reluctant to reveal its solution to either the experimental or theoretical worker. As a monument to this reluctance, there exists a great store of experimental data that terminate at some Mach Number short of unity, and a considerable body of theoretical results that do not agree with experimental observations in even the most general sense.

Two developments that started about a decade ago—namely, the transonic wind tunnel with partly open walls, and the small disturbance theory of transonic flow—are uniting, however, to bring an end to this state of affairs. Both developments have their difficulties, however, when the object is to obtain results of high accuracy for a wide class of bodies. The wind tunnel is, of course, versatile with regard to the shape of the body, but recent developments indicate that wall-interference effects are much larger than had been supposed—and are very hard to eliminate by simply testing smaller models. Transonic flow theory, on the other hand, appears to yield results of surprisingly good quality, but the versatility has been limited by the fact that the theory requires the solution of a nonlinear partial differential equation of mixed elliptic-hyperbolic type, for which the mathematical theory is in a rather primitive state. As a result of the latter difficulties, most of the solutions that had been obtained until recently with this theory were determined using the hodograph method, and were confined as a consequence to two-dimensional flows about wedge and flat-plate airfoils.

New methods for the approximate solution of the nonlinear equations of transonic flow theory have been discovered recently, however, which permit the calculation of theoretical results for a wide variety of two- and three-dimensional bodies having either flat or curved boundaries. These results are in good accordance with previous theoretical results obtained with the hodograph method, and with experimental results obtained in transonic wind tunnels using small models.

A closer examination of the comparisons between the theoretical and experimental results reveals, however, that the magnitude of wind-tunnel wall interference effects is much larger than had been anticipated, particularly at Mach Numbers very close to unity, and it is found that models of unusually small size must be used in certain cases to obtain data of acceptable quality. Although a complete understanding of these effects still remains to be developed, a preliminary analysis based on transonic flow theory provides insight into some of the essential features of these interference effects. One interesting conclusion of these studies concerns the emergence of the old-fashioned subsonic wind tunnel with solid walls as a useful and reliable instrument for obtaining data for flows with free-stream Mach Number 1.

It is the purpose of this paper to provide a résumé of the basic ideas of transonic flow theory together with

Received January 20, 1959

This paper was presented at the Eighth Japanese National Congress for Theoretical and Applied Mechanics, Tokyo, Japan, September 6–8, 1958, and is published here through the courtesy of the officers of the Japanese Congress.

* Aeronautical Research Scientist.

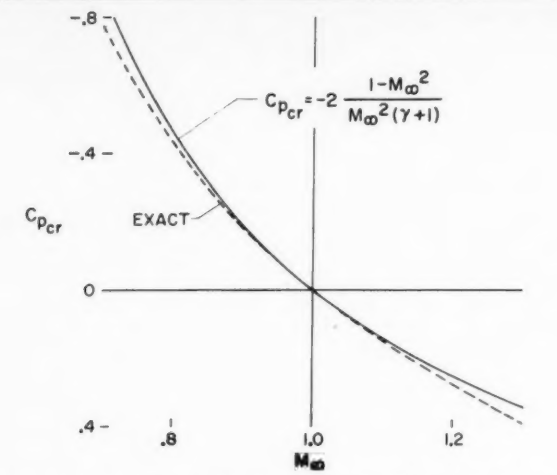

FIG. 1. Variation of critical pressure coefficient with Mach Number.

specific results for some of the more interesting applications. These results are compared, in most cases, with the corresponding results indicated either by experiment or by more exact theories.

FUNDAMENTAL EQUATIONS OF TRANSONIC FLOW THEORY

The small-disturbance theory of transonic flow has grown out of efforts of Oswatitsch and Wieghardt, Busemann and Guderley, von Kármán, and others (see references 1 to 6) directed originally toward providing a useful first approximation for flows with free-stream Mach Number very nearly equal to unity. It has evolved into a unified theory for subsonic, transonic, and supersonic flow, however, and is, moreover, the simplest theory proposed to date that is capable of yielding reliable results for thin wings and slender bodies throughout this entire range of speeds. The basic equations of this theory have been written in many slightly different forms.[7, 8] One form which has been found to have particular merit is outlined below.

Let the free-stream velocity and Mach Number be U_∞ and M_∞, introduce a Cartesian coordinate system with the x axis extending in the direction of the free stream, and denote the perturbation velocity components parallel to the x, y, and z axes by u, v, and w, respectively. They are the gradient of a perturbation potential φ that satisfies the following nonlinear partial equation:

$$(1 - M_\infty^2)\varphi_{xx} + \varphi_{yy} + \varphi_{zz} = M_\infty^2[(\gamma + 1)/U_\infty]\,\varphi_x\varphi_{xx} \equiv k\varphi_x\varphi_{xx} \quad (1)$$

It may be noted that this equation differs from the Prandtl-Glauert equation of linearized compressible flow theory by the retention of only one nonlinear term—namely, that written on the right-hand side.

Shock waves are a prominent feature of transonic and supersonic flows, and additional relations are needed for the transition through the shock. They are that φ is continuous across a shock wave, and that u, v, and w are discontinuous in such a manner that the values immediately ahead and behind the shock wave are related according to the following equation:

$$(1 - M_\infty^2)\,(u_a - u_b)^2 + (v_a - v_b)^2 + (w_a - w_b)^2 = M_\infty^2[(\gamma + 1)/U_\infty]\,[(u_a + u_b)/2]\,(u_a - u_b)^2 \quad (2)$$

The corresponding expression of linear theory differs only by omission of the term on the right-hand side.

The boundary conditions require that the gradient of φ vanish far ahead of the body, and that the flow be tangential to the body surface. The latter condition is approximated in transonic flow theory in exactly the same way as in linear theory. For example, the appropriate relation for a thin wing having ordinates $Z(x, y)$ is given by

$$(w)_{z=0} = U_\infty(\partial Z/\partial x) \quad (3a)$$

and that for axisymmetric flow past a slender body of revolution having an axial distribution of cross section $S(x)$ is given by

$$(r\varphi_r)_{r=0} = (U_\infty/2\pi)\,(dS/dx) \quad (3b)$$

where $$r = (y^2 + z^2)^{1/2}$$

The expression that relates the pressure coefficient C_p and the velocity is likewise approximated in the same way as in linear theory. Thus, the appropriate expression for use in the study of flow around thin wings is

$$C_p = -2(\varphi_x/U_\infty) \quad (4a)$$

and that for use in the study of axisymmetric flow around slender bodies is

$$C_p = -2(\varphi_x/U_\infty) - (\varphi_r^2/U_\infty^2) \quad (4b)$$

It is also presumed necessary to prescribe that the Kutta condition applies whenever the component of the velocity normal to a sharp trailing edge is subsonic and that the direct influence of a disturbance in the supersonic region proceeds only in the downstream direction.

Many investigations of transonic flows have been based on equations in which the coefficient $M_\infty^2(\gamma + 1)$ is replaced by $\gamma + 1$. The use of the latter expression is not recommended because considerable loss of accuracy results at Mach Numbers removed from unity (e.g., see references 7 and 8). It is a simple matter, however, to convert results derived through the use of

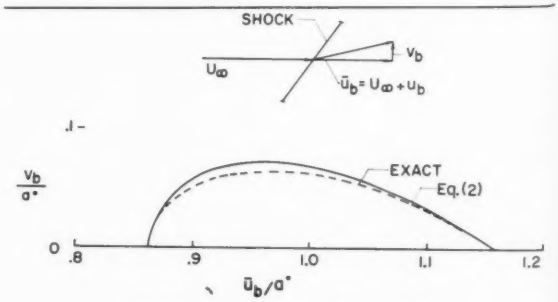

FIG. 2. Shock polar for $M_\infty = 1.2$.

this or any other expression for k so as to be consistent with the present formulation of transonic flow theory. Unless noted to the contrary, such a conversion has been applied whenever necessary to all of the theoretical results that are given in the following discussion.

Some Elementary Properties of the Equations of Transonic Flow Theory

Considerable insight into the nature of the approximation afforded by the small-disturbance theory of transonic flow can be gained by consideration of a number of elementary properties of the basic equations. Perhaps one of the most elementary properties of Eq. (1) is that the type is dependent on the sign of $1 - M_\infty^2 - ku$ as follows:

$$1 - M_\infty^2 - ku \begin{cases} > 0 & \text{elliptic (subsonic)} \\ < 0 & \text{hyperbolic (supersonic)} \end{cases} \tag{5}$$

The type is of significance in the theoretical study of compressible flow, because the governing equation should be of elliptic type wherever the velocity is subsonic and of hyperbolic type wherever the velocity is supersonic.

A second property of Eq. (1) is that the direction of the characteristic surfaces, or Mach conoids, varies from point to point in the flow field in such a manner that the surfaces makes an angle μ with the x axis that is given by the following relation:

$$\cot \mu = \sqrt{M_\infty^2 - 1 + ku} \tag{6}$$

The characteristic surfaces are real in regions where the quantity $M_\infty^2 - 1 + ku$ is greater than zero, but imaginary in regions where $M_\infty^2 - 1 + ku$ is less than zero.

A third elementary property of the equations of transonic flow theory is that they indicate that any infinitesimal stream tube has a throat at the point where $1 - M_\infty^2 - ku$ vanishes. This result can be readily seen by integration of Eq. (1) under the assumption of one-dimensional flow, in which case the following relation is found:

$$(1 - M_\infty^2 - ku)\,(du/U_\infty) = -(dA/A) \tag{7}$$

where A represents the cross-section area of the stream tube.

The significance of these three properties becomes clear upon recognition of the fact that the quantity $1 - M_\infty^2 - ku$ is equivalent to a first order to $1 - M^2$, where M is the local Mach Number. These results also illustrate how the quantity $1 - M_\infty^2 - ku$ constantly appears in the analysis and plays the same role in the small-disturbance theory of transonic flow as $1 - M^2$ in the more exact theories of compressible flow.

The properties of the nonlinear equations of transonic flow theory that are outlined above make an interesting contrast with the corresponding properties of the linearized equations of compressible flow. The results associated with the latter theory can be obtained immediately from Eqs. (5), (6), and (7) by replacing ku with zero. The relations that follow clearly illustrate the well-known properties of the linearized theory—that the type depends on the free-stream Mach Number rather than the local Mach Number, that the characteristic surfaces make the same angle with the x axis throughout the entire flow field, and that the equations contain no mechanism to indicate the possibility of a sonic throat in an infinitesimal stream tube.

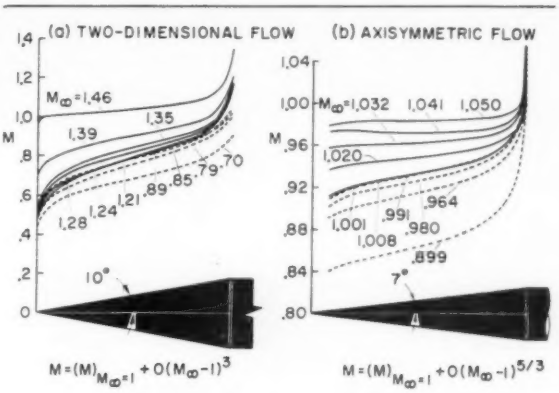

FIG. 3. Mach Number freeze, $(dM/dM_\infty)_{M_\infty=1} = 0$.

It follows from Eq. (5) that the critical value for u associated with the local occurrence of sonic velocity, and, therefore, also with the change in type of the differential equation, can be determined by equating $1 - M_\infty^2 - ku$ to zero. Combination of the resulting expression with Eq. (3a) for C_p leads to the following simple relation between the critical pressure coefficient and the free-stream Mach Number:

$$C_{p_{cr}} = -2[(1 - M_\infty^2)/M_\infty^2(\gamma + 1)] \tag{8}$$

It is essential that a theory for transonic flow provides a good approximation for the variation of the critical pressure coefficient with Mach Number. That the result given by Eq. (8) does indeed furnish a good approximation is illustrated graphically in Fig. 1. The solid line indicates the approximate results given by Eq. (8), and the dashed line indicates the corresponding result given by the exact relation for isentropic flow.

The degree of approximation afforded by the shock relation given by Eq. (2) is illustrated in Fig. 2 with the aid of the familiar shock polar diagram in which the lateral velocity component v_b behind a shock wave is plotted as a function of the longitudinal velocity component $\bar{u}_b$. The flow ahead of the shock is considered in this particular example to be uniform and parallel to the x axis and to be at a Mach Number of 1.2. The solid line indicates the approximate form of the shock polar calculated by use of Eq. (2). The corresponding exact result is indicated by the dashed line. It can be seen that the approximation furnished by the equations of transonic flow theory provides both the correct tangent at the right hand or weak shock end of the polar, and the correct jump in velocity at the left hand or normal shock end of the polar. This result may be contrasted with the approximation furnished by the linearized equations of compressible flow

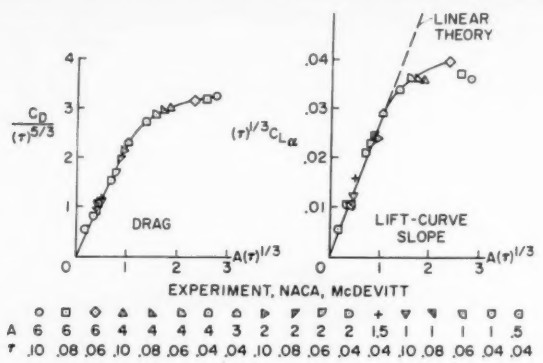
LINEAR THEORY
$\frac{C_D}{(\tau)^{5/3}}$
DRAG
$A(\tau)^{1/3}$
$(\tau)^{1/3}C_{L_\alpha}$
LIFT-CURVE SLOPE
EXPERIMENT, NACA, McDEVITT
A 6 6 6 4 4 4 4 3 2 2 2 2 1.5 1 1 1 1 1 .5
τ .10 .08 .06 .10 .08 .06 .04 .04 .10 .08 .06 .04 .04 .10 .08 .06 .04 .04

FIG. 4. Similarity rules, rectangular wings, NACA 63AOXX profiles, $\alpha = 0$, $M_\infty = 1$.

theory in which the shock polar is approximated by a straight line tangent to the weak shock end of the polar.

MACH NUMBER FREEZE AT $M_\infty = 1$

One of the most striking features of transonic flow is that the local Mach Number distribution on an airfoil section becomes independent of the free-stream Mach Number as the latter approaches unity (see reference 9, p. 274, ff., and reference 10, p. 293, ff.). This is illustrated in Fig. 3(a) by a series of local Mach Number distributions measured by Liepmann and Bryson[11, 12] on the surface of a single-wedge profile at several free-stream Mach Numbers. It can be seen that the local Mach Numbers remain virtually unchanged, or frozen, as the free-stream Mach Number varies from 0.85 to 1.24.

A corresponding series of plots for axisymmetric flow past a slender cone-cylinder has been prepared from data given by Page in reference 13 and is shown in Fig. 3(b). It can be seen that the range of free-stream Mach Numbers over which the local Mach Number distribution is frozen is very small, extending only from about 0.99 to 1.01. Attention is called to the fact that Page also shows that this effect may be completely masked by wind-tunnel wall interference unless the dimensions of the model are extremely small with respect to those of the test section. In the particular case shown in Fig. 3(b), the cone has a length of $5^1/_2$ inches and the test section has a square cross section 14 ft. on a side. Results of tests of the same cone in a test section 2 ft. square were affected by wall interference to such an extent that the Mach Number freeze could not be observed.

The great difference between the extent of the Mach Number range over which the local Mach Number freeze occurs in two-dimensional and axisymmetric flows is at least qualitatively consistent with the theoretical result given by Guderley[10] that indicates the leading term in the expansion of the deviation of M from its value for $M_\infty = 1$ is proportional to $(M_\infty - 1)^3$ for two-dimensional flows and to $(M_\infty - 1)^{5/3}$ for axisymmetric flows.

SIMILARITY RULES

One of the first results to be obtained from analysis of the equations of transonic flow theory was the similarity rule that relates the aerodynamic properties of families of airfoils of affinely related geometry in two-dimensional flow. This result, which is described in some detail by von Kármán in reference 6, was soon extended to three-dimensional flow and the corresponding rules for families of affinely related bodies of revolution and wings of finite span are given in references 14, 15, 16, and 7. The significance of these rules is that they indicate groupings of the pertinent dimensionless quantities that reduce the number of independent variables necessary to describe the solution for a family of related flows.

Wings of Finite Span

The information presented in Fig. 4 illustrates how the similarity rules can be used to organize experimental data and to reduce the amount of testing necessary to establish the aerodynamic properties of a family of wings of finite span. The similarity rules for drag and lift-curve slope, both at zero angle of attack, of an affinely related family of uncambered wings are

$$\bar{C}_D = \mathfrak{D}(\xi_\infty, \bar{A}), \quad \bar{C}_{L_\alpha} = \mathfrak{L}(\xi_\infty, \bar{A}) \tag{9}$$

where

$$\begin{aligned} \bar{C}_D &= \{[M_\infty{}^2(\gamma+1)]^{1/3}/\tau^{5/3}\} C_D \\ \xi_\infty &= (M_\infty{}^2 - 1)/[M_\infty{}^2(\gamma+1)\tau]^{2/3} \\ \bar{A} &= [M_\infty{}^2(\gamma+1)\tau]^{1/3} A \\ \bar{C}_{L_\alpha} &= [M_\infty{}^2(\gamma+1)\tau]^{1/3} C_{L_\alpha} \end{aligned}$$

They indicate that only two parameters, ξ_∞ and $\bar{A}$, are necessary to describe the results, rather than the four parameters—namely, aspect ratio A, thickness ratio τ, Mach Number M_∞, and possibly the ratio of specific heats γ if the tests are conducted in more than one gas—that are indicated by simple considerations of dimensional analysis. Greater simplicity is achieved by considering the situation at free-stream Mach Number 1, since the parameter ξ_∞ is then zero and the results depend on only a single parameter. This conclusion is confirmed by the experimental data from reference 17 presented in Fig. 4 for the lift and drag characteristics of a large family of wings of rectangular plan form having symmetrical airfoils of the NACA 63AOXX series.

It is interesting to observe that both curves have the same general form, and that they appear to display one trend for low aspect ratio wings and another for high aspect ratio wings. The curves approach straight lines through the origin for low aspect ratio wings and horizontal lines for high aspect ratio wings. The latter behavior indicates that the aspect ratio is dropping out as a parameter and that the lift and drag coefficients are approaching the values that they would have for two-dimensional flow. For wings having $A\tau^{1/3}$ less than about unity, the experimental values for the lift practically coincide with the predictions given by linear

theory that the lift-curve slope C_{L_α} is equal to $\pi/2$ times the aspect ratio. Linear theory does not provide a good approximation for the drag, however, since it predicts infinite values for all wings of finite thickness. Attention is called to the fact that these results indicate that the drag of the low aspect ratio members of this particular family of wings is proportional to the square of the frontal area, provided all of the wings have the same chord and are in flows having the same dynamic pressure.

Additional data of the type illustrated in Fig. 4 are given in reference 17 for the same family of wings and also for a related family of cambered wings of rectangular plan form. Similar results for wings of triangular plan form are given in reference 18.

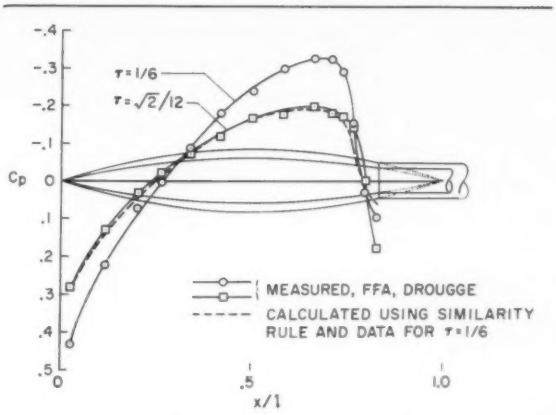

FIG. 5. Similarity rule, parabolic-arc bodies, $\alpha = 0$, $M_\infty = 1$.

Bodies of Revolution

The similarity rule for axisymmetric flow around slender pointed bodies of revolution states that the surface pressures on an affinely related family of bodies are related in accordance with the following expression:

$$C_p + (1/\pi)S''(x) \ln [\tau^2 M_\infty(\gamma + 1)^{1/2}] = \tau^2 \mathcal{P}[\bar{\xi}_\infty, (x/l)] \quad (10)$$

where $\bar{\xi}_\infty = (M_\infty{}^2 - 1)/M_\infty{}^2(\gamma + 1)\tau^2$

An application of this similarity rule to experimental pressure distributions on two parabolic-arc bodies of revolution at free-stream Mach Number 1 is shown in Fig. 5. The solid lines and data points represent the experimental results given by Drougge in reference 19 for bodies having thickness ratios of 1/6 and $\sqrt{2}/12$. The dashed line represents the results for the body of thickness ratio $\sqrt{2}/12$ calculated using Eq. (10) together with the experimental data for the body of thickness ratio 1/6. It can be seen that the results calculated with the aid of the similarity rule are in almost perfect agreement with the measured results.

The similarity rule for drag follows directly from Eq. (10) by integration. It is

$$(D/ql^2) + \{[S'(l)]^2/2\pi l^2\} \ln [\tau^2 M_\infty(\gamma + 1)^{1/2}] = \tau^4 \mathfrak{D}(\bar{\xi}_\infty) \quad (11)$$

where l indicates the length of the body and $S'(l)$ indicates the axial distribution of cross-section area at the stern of the body. This relation reduces to a particularly simple form if the body is either cylindrical or pointed at the stern, since then $S'(l)$ vanishes. It follows, for such bodies, that the drag at free-stream Mach Number 1 of various members of an affinely related family of bodies, all of the same length, is proportional to the square of the frontal area, just as was observed in Fig. 4 to be the case for various members of an affinely related family of low aspect ratio wings.

Comparisons similar to that shown in Fig. 5, but for Mach Numbers other than unity and for additional bodies, are given in references 19 and 20. These results show that the similarity rule for axisymmetric flow is useful for Mach Numbers in the neighborhood of unity, and also for Mach Numbers that are either sufficiently small or sufficiently large that the flow is either purely subsonic or purely supersonic. It is pointed out in reference 20, however, that a fundamental discrepancy arises near the bounds of the transonic range. This is evident from the fact that the expression for $\bar{\xi}_\infty$ given by Eq. (10) defining the Mach Number and thickness ratio of bodies in related flows indicates, in certain instances, that a transonic flow is to be related to a subsonic flow, or to a supersonic flow; whereas it is clear from elementary considerations of the differences between such flows, particularly with regard to the properties of the shock system and the associated drag, that the results indicated by the simple relations given by the similarity rules are unacceptable physically. It is conjectured that the source of this difficulty is associated with an insufficient attention in the derivation of the similarity rules for axisymmetric flow to the conditions of dependence and influence in regions of supersonic flow.

TRANSONIC EQUIVALENCE RULE

The transonic equivalence rule first stated by Oswatitsch (see reference 21 and 22 for a résumé) relates the flow around a slender body of arbitrary cross section to that around an "equivalent" nonlifting body of revolution having the same longitudinal distribution of cross-section area $S(x)$. This rule is closely related to one of the simplest results of transonic slender-body theory—namely, that the expression for φ in the vicinity of a slender body is approximately of the form

$$\varphi = \varphi_2(x; y, z) + g(x) \quad (12)$$

where φ_2 is the solution of Laplace's equation

$$\varphi_{yy} + \varphi_{zz} = 0 \quad (13)$$

for the given boundary conditions in the yz plane at each x station, and $g(x)$ is an additional contribution dependent upon M_∞ and $S(x)$. It is thus possible to determine $g(x)$ from the solution of the simpler problem of axisymmetric flow past the equivalent body. The equivalence rule, which is described in mathematical terms by

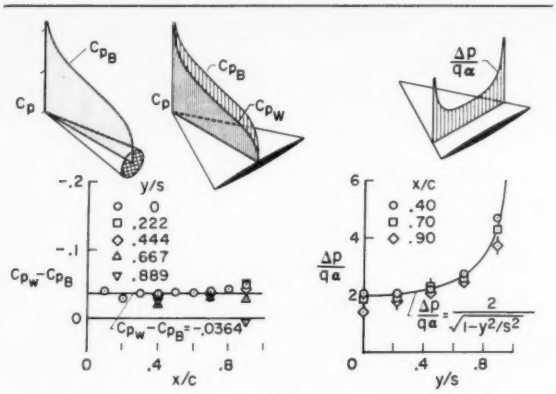

FIG. 6. Application of transonic equivalence rule to thin elliptic cone-cylinder, $A = 2$, $\tau = 0.06$, $\alpha = 0$, $M_\infty = 1$.

$$\varphi_W = \varphi_{2W} - \varphi_{2B} + \varphi_B \tag{14}$$

follows immediately by writing Eq. (12) once for a body of arbitrary cross section (subscript W), once for the equivalent body (subscript B), and subtracting one from the other.

The order of error in Eq. (14) has been established in reference 22 for the case where the quantities with subscript W refer to a thin wing of aspect ratio A, chord c, and thickness ratio τ. It is shown that the magnitude of the quantities $\varphi_W/U_\infty c$ retained in Eq. (14) is $0(A\tau \ln A)$, whereas that of the quantities discarded in the derivation for $M_\infty = 1$ is $0(A^4\tau^2 \ln A)$. Since the magnitude of the quantities discarded in the derivation of the same result in linearized theory is $0(A^3\tau \ln A)$, it follows that Eq. (14) can be applied to wings of greater aspect ratio at $M_\infty = 1$ than at other Mach Numbers.

A simple application of this theory for which experimental data are available for comparison is furnished by consideration of flow past a thin cone-cylinder of elliptic cross section. It is shown in reference 22 that the procedures described above lead to the following relation between the values for the pressure coefficient C_{p_W} on the surface of the conical part of such a body and C_{p_B} on the surface of the equivalent circular cone-cylinder:

$$C_{p_W} = C_{p_B} - (A\tau/8)\,[1 + \ln (A/8\tau)] \pm (\alpha A/2\sqrt{1 - y^2/s^2}) \tag{15}$$

The symbols A and τ refer to the aspect ratio and thickness ratio of the conical portion of the elliptic cone-cylinder, the plan form of which is described by $y = \pm s(x)$; α refers to the angle of attack; and the minus sign is to be used for the upper surface and the plus sign is to be used for the lower surface.

Consider, now, the application of Eq. (15) to a thin elliptic cone-cylinder having $A = 2$ and $\tau = 0.06$. Experimental results for the pressure distribution on such a cone-cylinder, and also on the equivalent body of revolution, have been given recently by Page in reference 13. The graph on the left in Fig. 6 shows a plot of the difference between the pressure coefficients at several related points on the nonlifting elliptic and circular cone-cylinders together with a line representing the theoretical prediction given by Eq. (15) for $C_{p_W} - C_{p_B}$. The graph on the right shows a comparison of the theoretical and experimental values for the aerodynamic loading $\Delta p_W/q$, or difference in C_{p_W} between the lower and upper surfaces, at a number of points on the elliptic cone-cylinder. It can be seen that the agreement between the theoretical and experimental results is satisfactory except in a small region near the base of the cone.

It is apparent from the above discussion that the aerodynamic loading, and thus the lift and other lateral forces and moments, on low aspect ratio wings and slender bodies arises entirely from φ_2. These quantities are thus independent of Mach Number and are the same as indicated by linearized slender-body theory for subsonic or supersonic flow. This result confirms statements made many years ago (e.g., see reference 23 or 24) that the aerodynamic loading on low aspect ratio wings at $M_\infty = 1$ is given correctly by linearized slender-wing theory.

TRANSONIC AREA RULE

Perhaps one of the best-known properties of transonic flows is the transonic area rule given by Whitcomb in reference 25, which states that, near the speed of sound, the zero-lift drag rise of thin low aspect ratio wing-body combinations is primarily dependent on the axial distribution of cross-sectional area normal to the air stream. This rule, which was proposed on the basis of certain elementary statements regarding the nature of transonic flow fields and was checked experimentally, is obviously closely related to the transonic equivalence rule, and indeed can be derived from it provided certain restrictions are accepted. The relation between these two rules has been explored in detail in reference 22, and it is shown that the following expression for the drag of an arbitrary body in terms of that of an equivalent body can be derived from the equivalence rule:

$$D_W = D_B - \frac{\rho_\infty}{2}\left(\int_{C_W} \varphi_{2W}\frac{\partial \varphi_{2W}}{\partial n}\,d\sigma_C - \int_{C_B} \varphi_{2B}\frac{\partial \varphi_{2B}}{\partial n}\,d\sigma_C\right) \tag{16}$$

Each of the integrals is a line integral along a curve C situated in a plane perpendicular to the x axis, that goes around the base of the body and also encloses any vortex wake that may be present. The difference $D_W - D_B$ is thus independent of Mach Number, and is the same as given by linearized slender-body theory. If the arbitrary body is inclined an angle α, the first integral provides a contribution to the drag that is proportional to α^2. This quantity is exactly the vortex drag. If attention is confined to nonlifting cases, there exist several classes of shapes for which the contribution of the two integrals cancel, and

$$D_W = D_B \tag{17}$$

One such class includes shapes that taper to a point at the rear, since then both integrals vanish. Another includes shapes that are cylindrical at the base, since then $\partial\varphi_{2W}/\partial n = \partial\varphi_{2B}/\partial n = 0$. Still another includes bodies that have the same shape and surface slopes at the base, since then both integrals are carried out over the same curve C, along which $\varphi_{2W} = \varphi_{2B}$ and $\partial\varphi_{2W}/\partial n = \partial\varphi_{2B}/\partial n$, and the integrals again cancel. These and many other cases for which the integrals cancel constitute the class of shapes for which the transonic area rule applies.

Some of the data which Whitcomb presented in reference 25 to support his statement of the transonic area rule are shown in Fig. 7. It can be seen from the plot on the left that the part of the drag that remains after the low-speed friction drag is subtracted is very nearly equal for this particular pair of bodies. Not all of the results presented by Whitcomb, particularly those for which the equivalent body is indented, are in as good agreement with the area rule as the results shown in this plot, but it is quite possible that some of these discrepancies may be associated with boundary-layer effects.

Whitcomb's main purpose, however, was not to investigate the accuracy of the area rule, but to find shapes for wing-body combinations having low drag through the transonic range. The area rule provides the key to the solution of this problem, however, because it suggests that the shape of a wing-body combination having low drag must be such that the equivalent body has the smooth form of a low-drag body of revolution. Thus, the cross-section area of the body must be reduced in the vicinity of the wing. Whitcomb's results, a sample of which is presented in the plot on the right in Fig. 7, show that such wing-body combinations have much lower drag than those without body indentation.

It is evident that neither the transonic equivalence rule nor the area rule can continue to apply as the lateral dimensions of the wings are extended indefinitely. Some insight into the range of applicability of these rules can be gained by examination of the experimental results for the drag of a pair of parallel parabolic-arc

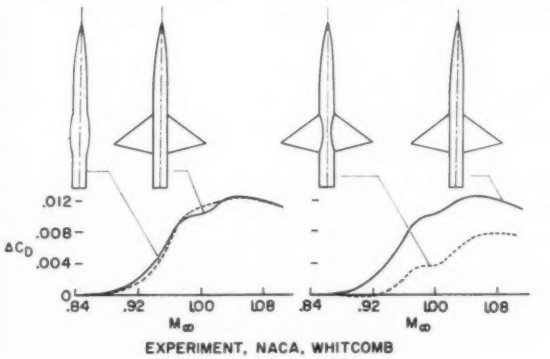

FIG. 7. Transonic area rule.

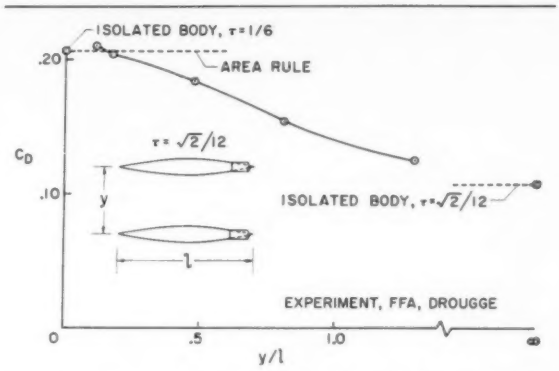

FIG. 8. Influence of lateral spacing on drag of a pair of truncated parabolic-arc bodies, $M_\infty = 1$.

bodies of revolution of thickness ratio τ of $\sqrt{2}/12$ in a flow with free-stream Mach Number 1, given by Drougge in reference 19 and shown here in Fig. 8. It can be seen that, if the distance between the bodies is sufficiently small, the drag coefficient based on maximum cross-section area, approaches that of a single body of thickness ratio 1/6 in accordance with the prediction of the area rule. The drag coefficient diminishes, however, as the two bodies are moved farther apart, and finally approaches a value equal to that of an isolated body of thickness ratio $\sqrt{2}/12$, as it obviously should.

Further insight into the range of applicability of the area rule can be gained by examination of the results for the drag of a family of rectangular wings presented in Fig. 4. The values for the drag of various of these wings are related to each other in accordance with the area rule over that part of the range of $A\tau^{1/3}$ for which the results can be represented by a straight line passing through the origin. It can be seen that the area rule is applicable to all of the wings of this particular family having a value for $A\tau^{1/3}$ less than about unity. It should be noted at this point that the equivalent bodies associated with this family of wings tend to be blunt and stubby, rather than pointed and slender. It would thus appear that the drag characteristics of the equivalent bodies of revolution might be considerably different from those of the related family of wings, even though the drag characteristics of the low aspect ratio members of this family of wings are related to one another in the manner predicted by the transonic area rule. Further discussion of the drag characteristics of this family of wings, as well as a related family of cambered wings, can be found in reference 26.

It is important to realize that the integrals in Eq. (16) do not always cancel, and that the area rule does not hold for all combinations of thin wings and slender equivalent bodies. The magnitude of the effects that may be encountered is illustrated in Fig. 9 for the particular case of a family of elliptic cone-cylinders for which the drag is given by the following equation:

$$C_{D_W} = C_{D_B} - \omega^2 \ln \left\{ (a/4b)\,[1 + (b/a)]^2 \right\} \tag{18}$$

The quantity C_{D_W} that appears in this relation repre-

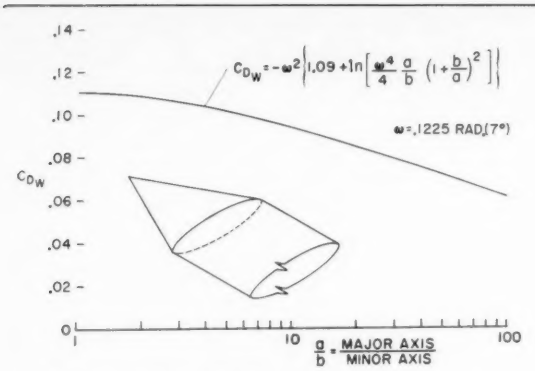

FIG. 9. Drag of elliptic cone-cylinders, $M_\infty = 1$.

sents the drag coefficient, based on maximum cross-section area, of the elliptic cone; C_{D_B} represents that of the equivalent body of revolution; the fraction a/b represents the ratio of the major to minor axis of the elliptic cross section; and ω represents the semiapex angle of the equivalent circular cone-cylinder. This relation, which is taken from reference 22, can be combined with the following theoretical expression for the drag of a circular cone-cylinder given in reference 20:

$$C_{D_B} = -\omega^2(1.09 + 4 \ln \omega) \tag{19}$$

to determine an expression for the drag of an elliptic cone-cylinder of arbitrary cross section. Numerical results for a family of elliptic cone-cylinders having the same axial distribution of cross-section area as a circular cone-cylinder with a semiapex angle ω of 0.1225 rad. (7°) are illustrated on the plot shown in Fig. 9. It can be seen that a marked decrease in drag occurs as the elliptic cross section is flattened. It should also be noted that the drag is a maximum when the cross section is circular. This latter result is in agreement with a more general conclusion found by Berndt[27, 28] in the course of a study of certain minimum and maximum properties of families of equivalent bodies at $M_\infty = 1$.

Hodograph Method

The initial step in many investigations of two-dimensional transonic flows is to linearize the governing differential equation for φ—that is, Eq. (1)—by use of the hodograph transformation in which the dependent and independent variables are interchanged. The process leads directly to the following pair of equations:

$$(1 - M_\infty{}^2)z_w + x_u = kuz_w, \quad x_w = z_u \tag{20}$$

provided the Jacobian of the transformation

$$J = u_z{}^2(M_\infty{}^2 - 1 + ku) - u_z{}^2 \tag{21}$$

does not vanish. The Jacobian cannot vanish in regions of subsonic flow, but can and frequently does vanish in regions of supersonic flow. As a result, application of the hodograph method to transonic flow is usually confined to the subsonic region and a limited part of the supersonic region. The remainder of the solution is then calculated by some other method, such as characteristics, that is more appropriate for supersonic flow.

Elimination of x, identification of z with the stream function ψ, and introduction of the new variables η and θ,

$$\eta = (M_\infty{}^2 - 1 + ku)/(U_\infty k)^{2/3}, \quad \theta = w/U_\infty \tag{22}$$

leads to

$$\psi_{\eta\eta} - \eta\psi_{\theta\theta} = 0 \tag{23}$$

which is recognized as Tricomi's equation, the simplest linear second-order partial differential equation of mixed type. Although it is not difficult to determine simple solutions of Tricomi's equation, and the principle of superposition is available because the equation is linear, the solution of boundary value problems associated with transonic flow around airfoils remains a very complex matter. The difficulties are diminished considerably when the airfoil is described by straight lines, and the hodograph method has been applied with considerable success in the study of transonic flow around wedge and flat-plate airfoils. Both analytical and numerical (relaxation) methods have been employed in these investigations.

The airfoil for which the most complete data is available is the single-wedge profile, for which an approximate solution for Mach Numbers less than 1 has been given by Cole[29] and improved recently by Yoshihara,[30] that for Mach Number 1 by Guderley and Yoshihara,[31] and that for Mach Numbers greater than 1 by Vincenti and Wagoner,[32] and experimental data for three different wedges have been given by Liepmann and Bryson.[11, 12] A graphical summary of the drag results from all of these sources (Cole's results are indicated by the dashed line) is shown in Fig. 10 in terms of the transonic similarity parameters $\bar{c}_d$ and ξ_∞ defined as indicated on the Figure. It can be seen that the data from the three wedges fall together to determine a single line in accordance with the prediction of the transonic similarity rule, and that this curve is in excellent agreement with the theoretical curve. Attention is called to the fact that all of the theoretical results shown on this graph have been modified from the form presented in the original papers, inasmuch as they were derived through consideration of a set of equa-

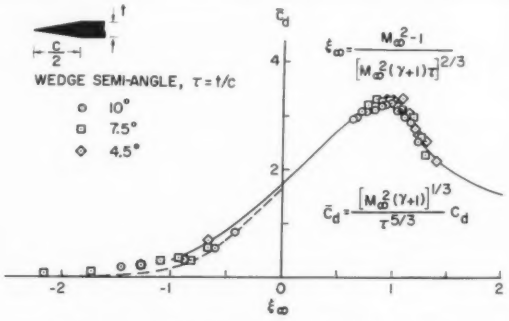

FIG. 10. Pressure drag, single-wedge sections.

tions for transonic flow theory that differ from those given in Eqs. (1) and (2) in that the quantity $M_\infty^2(\gamma + 1)$ is replaced by $\gamma + 1$. It is shown in references 7 and 8 that the agreement with the experimental results is not nearly so good when the theoretical results are retained in their original form. Theoretical results for a number of additional examples of hodograph solutions for transonic flow around wedge and flat-plate airfoils have been worked out by a number of authors over the last several years. Most of these are summarized in a recent book by Guderley.[10] Some additional comparisons of theoretical and experimental results similar to those shown in Fig. 10 are given in reference 33.

Attention was directed by Imai in reference 34 to the fact that it is much simpler to solve the problem of flow with free-stream Mach Number 1 past a finite wedge if the flow is considered to separate from the airfoil surface at the shoulder and follow a free-stream line along which the velocity is sonic, than if the flow is considered to perform a Prandtl-Meyer expansion around the corner. With this model, the flow is nowhere supersonic for all free-stream Mach Numbers up to and including unity, and the difficulties that are normally encountered as a result of the mixed type of the governing equations are averted. An exact solution of the equations of transonic flow theory for this problem was given recently by Helliwell and Mackie in reference 35, and an interesting approximate solution for the same problem was given almost simultaneously by Kusukawa in reference 36. The latter solution is determined in a very simple manner by use of an approximate relation between the pressure coefficient C_p in a compressible flow and the pressure coefficient C_{p_i} in a compressible flow, which reduces to the following form when the free-stream Mach Number is unity:

$$C_p = [(9/2)/(\gamma + 1)]^{1/3} C_{p_i}^{2/3} \qquad (24)$$

Kusukawa obtained this expression by application of the WKB method of approximation developed for the analysis of compressible flow by Imai (see reference 37, chapter VI). Combination of Eq. (24) with the approximate expression for the solution for incompressible flow leads to the following simple expression for the pressure distribution on the surface of a wedge of chord $c/2$ and semiapex angle τ in a flow with free-stream Mach Number 1:

$$\bar{C}_p = [(\gamma + 1)^{1/3}/\tau^{2/3}]C_p = 2[(3/\pi)\cosh^{-1}\sqrt{(c/2)/x}]^{2/3} \qquad (25)$$

A comparison of the exact and approximate pressure distributions is shown in Fig. 11. It can be seen that the two results are nearly identical numerically.

Additional results for free-stream line flow past an inclined flat plate and past a wedge in a choked channel have been given in references 38, 39, and 40. The latter two references also contain results for Mach Numbers less than unity.

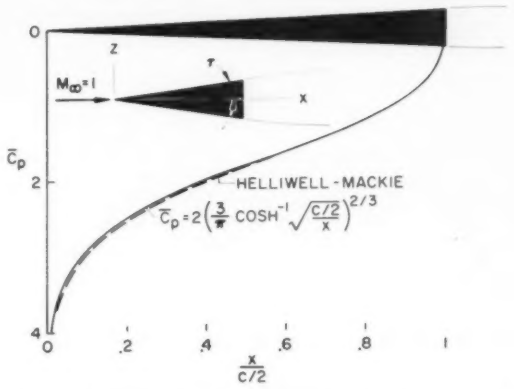

FIG. 11. Pressures, finite wedge, separated flow, $M_\infty = 1$.

METHOD OF SUCCESSIVE APPROXIMATION

There exists a large body of literature in which approximate solutions of both the complete equations for compressible flow and the simplified equations of transonic flow theory are sought by iteration. Of the considerable variety of methods of this type that are presently available for the analysis of flow around thin airfoils and slender bodies, perhaps the best known and simplest to describe is the method of successive approximation in which the solution is sought in the form of a power series in terms of the thickness ratio. In this method, the first approximation $\varphi^{(1)}$ is determined by solving the Prandtl-Glauert equation

$$(1 - M_\infty^2)\varphi_{xx}^{(1)} + \varphi_{yy}^{(1)} + \varphi_{zz}^{(1)} = 0 \qquad (26a)$$

which is obtained from Eq. (1) by replacing the right-hand side with zero. The result is precisely that of linear theory, to which the solutions of transonic flow theory converge as the Mach Number departs far from unity in either direction. The second approximation $\varphi^{(2)}$ is determined by solving the following equation, again linear:

$$(1 - M_\infty^2)\varphi_{xx}^{(2)} + \varphi_{yy}^{(2)} + \varphi_{zz}^{(2)} = k\varphi_x^{(1)}\varphi_{xx}^{(1)} \qquad (26b)$$

that is obtained by using the results of the first approximation to evaluate the right-hand side of Eq. (1). Higher approximations for either subsonic or supersonic flows follow in a similar manner.

Although a number of special techniques have been developed to aid in the analysis (see references 37, 41, 42, and 43 for a résumé), the difficulties of integration remain considerable and only a very small number of solutions have actually been obtained for approximations higher than the second. One of these is for subsonic flow past a symmetrical circular-arc airfoil for which Asaka has given the third approximation in reference 44. (The problem that Asaka treats explicitly is the determination of the third approximation to the solution of the complete equations of compressible flow theory, but it is a simple matter to extract the third approximation to the solution of the equations of the small-disturbance theory of transonic flow from his results.) The results for the variation with Mach Num-

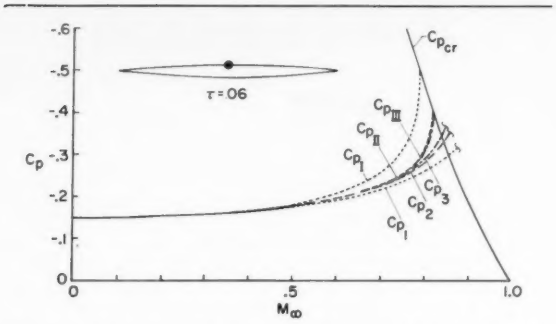

FIG. 12. Pressure, midpoint of circular-arc airfoil, $\tau = 0.06$.

ber of the pressure coefficient at the midpoint of such an airfoil having a thickness ratio τ are given by

$$C_p = -2.5465\,(\tau/\sqrt{1 - M_\infty^2}) - 0.5132[M_\infty^2(\gamma + 1)/(1 - M_\infty^2)^2]\tau^2 - 0.6339[M_\infty^4(\gamma + 1)^2/(1 - M_\infty^2)^{7/2}]\tau^3 + \ldots \quad (27)$$

A plot of the results indicated by the first three approximations, designated C_{p_I}, $C_{p_{II}}$, and $C_{p_{III}}$, is shown in Fig. 12 for the special case of $\tau = 0.06$. It can be seen that the addition of each term results in an increase in the value of the peak negative pressure coefficient, and that the curves representing the results pass through the line indicating the critical pressure coefficient without any noticeable effect. It is also a general property of the results obtained by the method of successive approximation that shock-free, dragless flow is indicated for all Mach Numbers up to unity. It is now generally believed that the series expression for the result fails to converge if the flow is transonic.

Before proceeding to the next topic, attention should be directed to an alternative method of successive approximation that has been applied to subsonic flows in references 8, 20, 45, and 46 to obtain results that overestimate, rather than underestimate, the variation of the peak negative pressure coefficient with Mach Number. This method is closely related to that described above, and can be described best by first noting that the general form for the series expansion of the result indicated by the method of successive approximation can be written in terms of reduced variables $\bar{u}$ and $\bar{\tau}$, as follows:

$$\bar{u}_n = \sum_{n=1}^{n} a_n \bar{\tau}^n \quad (28)$$

where

$$\bar{u} = [M_\infty^2(\gamma + 1)/(1 - M_\infty^2)]\,(u/U_\infty)$$
$$\bar{\tau} = [M_\infty^2(\gamma + 1)/(1 - M_\infty^2)^{3/2}]\tau$$
$$\bar{C}_p = \{[M_\infty^2(\gamma + 1)]^{1/3}/\tau^{2/3}\}C_p = -2(\bar{u}/\bar{\tau}^{2/3})$$

The Nth approximation of the alternative method can be determined directly from the nth approximation of the series expansion method by use of the following relation:

$$\bar{u}_N = 1 - \sqrt{1 - 2\bar{u}_n + \bar{u}_{n-1}^2} \quad (29)$$

It is shown in the appendix of the report version of reference 8 that the results obtained with Eq. (29) for flows that are subsonic everywhere converge, in the limit of an infinite number of iteration steps, to the same result that is ultimately obtained by use of Eq. (28). The result obtained by use of Eq. (29) clearly terminates with the occurrence of sonic velocity somewhere in the flow field, however, and no results are provided for mixed or transonic flows.

The first three approximations for the variation with Mach Number of the pressure coefficient at the midpoint of a symmetrical circular-arc airfoil have been calculated using Eq. (29) and the results, designated C_{p_I}, $C_{p_{II}}$, and $C_{p_{III}}$, are included in Fig. 12. It can be seen from this plot that all of the various approximations agree well at low Mach Numbers, but that substantial differences appear at Mach Numbers near the critical. The proper trend is defined within rather narrow limits at all Mach Numbers up to the critical, however, since the exact solution of the equations of transonic flow theory is presumed to indicate a variation of C_p with M_∞ that is somewhat greater than that indicated by the third approximation of the first method, but somewhat less than that indicated by the second method.

Integral Equation Method, $M_\infty < 1$

The basic equations of transonic flow theory can be recast into the form of a nonlinear integral equation by application of Green's theorem to appropriate regions surrounding the body, its wake, and the associated shock waves. There are many forms of Green's theorem, and it is possible to derive many different integral equations in this way. One integral equation that has been found useful in the analysis of two-dimensional transonic flow around an arbitrary nonlifting airfoil with free-stream Mach Number less than unity is

$$\bar{u} - \frac{\bar{u}^2}{2} = \bar{u}_L - \frac{1}{2\pi} \times \iint_{-\infty}^{+\infty} \frac{\bar{u}^2}{2} \frac{(\bar{x} - \bar{\xi})^2 - (\bar{z} - \bar{\zeta})^2}{[(\bar{x} - \bar{\xi})^2 + (\bar{z} - \bar{\zeta})^2]^2}\, d\bar{\xi}\, d\bar{\zeta} \quad (30)$$

where

$$\bar{u} = u/u_{cr} = [M_\infty^2(\gamma + 1)/(1 - M_\infty^2)]\,(u/U_\infty), \qquad \bar{x} = x, \quad \bar{z} = \sqrt{1 - M_\infty^2}\, z$$

The symbol $\bar{u}_L$ that appears in this equation represents the expression for $\bar{u}$ given by the solution of the linearized equations of compressible flow—that is, by Eq. (26a).

Discussion of the properties of Eq. (30) is facilitated by introduction of the abbreviation $I/2$ for the integral and rewriting in the form

$$\bar{u} = 1 \pm \sqrt{I - L} \quad (31)$$

where $L = 2\bar{u}_L - 1$. It follows immediately that $I \geq L$. The choice of plus or minus sign determines whether the flow is subsonic or supersonic. A change

of sign at a point where $I = L$ corresponds to a smooth transition through sonic velocity. A change in sign at a point where $I > L$ results in a discontinuous jump in velocity and corresponds physically to a shock wave. If I and L are continuous at such a point, the discontinuity corresponds to a normal shock wave. Such discontinuities are permissible when they proceed from greater to lesser velocities (compression shock), but are inadmissible when they proceed in the opposite direction.

It is necessary, at the present time, to introduce approximations to simplify Eq. (30) before results can be calculated for specific applications. One simplification that has proved useful in references 8, 46, 47, and 48 for the calculation of the pressure distribution on a number of convex airfoils is to approximate $\bar{u}(\bar{\xi}, \bar{\zeta})$ in the integral by

$$\left.\begin{aligned} \bar{u}(\bar{\xi}, \bar{\zeta}) &= \bar{u}(\bar{\xi}, 0)/[1 + (\bar{\zeta}/b)]^2 \\ b = -2[(1 - M_\infty{}^2)^{3/2}/M_\infty{}^2(\gamma + 1)] &\times [\bar{u}(\bar{\xi}, 0)/(d^2Z/dx^2)] \end{aligned}\right\} \quad (32)$$

thereby permitting integration with respect to $\bar{\zeta}$. The single integral equation that results can be solved by a procedure involving numerical and iteration techniques.

This method has been applied in reference 46 to determine the pressure distributions on five related families of airfoils having various locations for the point of maximum thickness ranging from 30 to 70 per cent chord. A résumé of the results for a 6 per cent-thick symmetrical circular arc airfoil is shown in Fig. 13. Part (a) shows that the pressure distributions for subcritical Mach Numbers are symmetrical and shock-free, and that the peak negative pressure coefficient increases slowly with increasing Mach Number, just as indicated by the higher order approximations in Fig. 12. Part (b) shows that the shock waves make their appearance as the Mach Number exceeds the critical, move rapidly rearward with increasing Mach Number, and reach the trailing edge at a Mach Number substantially less than unity. It may be noticed that the values for C_p remain nearly the same as at the critical Mach Number throughout the range of Mach Numbers in which the shock wave moves across the chord. When the Mach Number is increased sufficiently that the shock wave reaches the trailing edge, the entire pressure distribution resembles in form, but not in level, the pressure distribution at Mach 1. The latter result, which is indicated in Fig. 13 by a dashed line, is not calculated by using the integral equation method, but is determined by using the method described in the following section.

The results for supercritical Mach Numbers shown on part (b) of Fig. 13 indicate the existence of a small region immediately downstream of the shock wave in which the pressure gradient is negative. Although this detail of the flow is usually not apparent in experimental pressure distributions, and it is beyond the capabilities of the approximation afforded by use of Eq. (32) to provide a precise quantitative account of

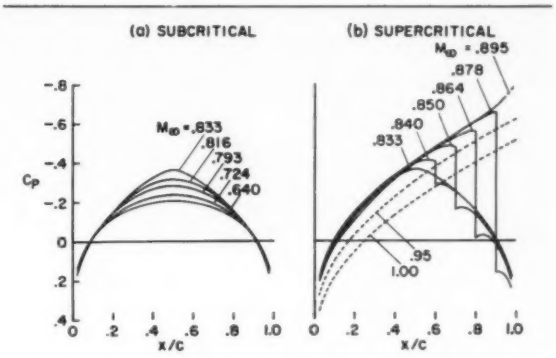

FIG. 13. Pressures, circular-arc airfoil, $\tau = 0.06$, $M_\infty = 1$.

this phenomenon, comparison with results of relaxation calculations published several years ago by Emmons[49] and with results of a recently published analysis by Zierep[50] of the conditions in the vicinity of the intersection of a shock wave and a convexly curved surface shows that this result is qualitatively correct for inviscid flow. It is shown in reference 50 that the pressure decreases immediately behind the shock wave as the two-thirds power of $\Delta x/R$, where Δx is the distance from the shock wave and R is the radius of curvature of the solid surface.† This phenomenon is nearly always masked by shock-wave boundary-layer interaction effects in experimental investigations, although it has been observed immediately outside the boundary-layer, by Ackeret, Feldman, and Rott,[51] and at the airfoil surface in recent tests conducted at Ames Research Center in which boundary-layer suction was employed.

In order to illustrate better the nature of the phenomenon that may arise from shock-wave boundary-layer interaction, two interferograms from reference 52 of the flow about 12 per cent-thick circular-arc airfoils are shown in Fig. 14. The conditions for the two flows differ only in that the boundary layer is laminar in part (a) and turbulent in part (b). The interferogram for the laminar case shows that the shock waves are of the λ type and that the flow separates near the mid-chord station. When the boundary layer is turbulent, however, it may be seen that the shock wave is of the single-wave type, and that the separation is delayed until about 70 per cent chord. Comparison of the theoretical and measured pressure distributions corresponding to these two flows (see reference 8) indicates substantial

† Note added in proof: The author has learned through correspondence with J. Zierep and D. G. Randall that this statement must be modified. Randall has shown in RAE TN Aero. 2592 that the analysis given in reference 50 leads, upon retention of the sign as well as the absolute magnitude of the curvature of the airfoil surface, to the rather startling conclusion that no shock can exist on a convex airfoil in inviscid transonic flow. P. R. Garabedian has pointed out, however, that a fundamental assumption employed in both of these studies—namely, that the curvature of the streamlines immediately behind the shock wave approaches that of the airfoil surface in a continuous manner—is in violation of the known asymptotic expansion of a subsonic flow at the point of intersection of a shock wave and a curved solid boundary. It appears, therefore, that the details of this particular facet of transonic flow remain an open question in need of further investigation.

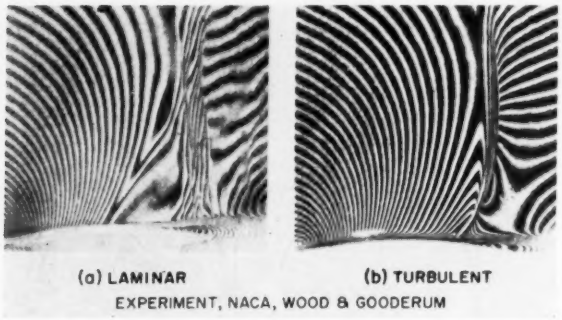

FIG. 14. Effect of boundary layer, circular-arc airfoil, $\tau = 0.12$, $M_\infty = 0.88$, $R_c = 600{,}000$.

agreement over the portion of the airfoil forward of the separation point, but quite different behavior over the remainder of the airfoil. This points to the fact that methods must be developed not only for determining the inviscid flow, but also for dealing with boundary-layer shock-wave interaction phenomena. Flight tests reported in reference 53 indicate, however, that this problem might be somewhat less difficult at larger Reynolds Numbers, inasmuch as the shock wave appears to be of the single-wave type for laminar, as well as turbulent, boundary layers.

METHOD OF LOCAL LINEARIZATION

A simple method for the approximate solution of the equations of transonic flow theory that has been applied in references 20, 45, and 54 is based on the idea of linearizing the equations in a small region by replacing part of the nonlinear term by a constant λ, and then introducing different values for different points in the field. Results obtained by such a procedure depend, of course, on the choice of λ and must be assembled in order to determine the final results. This step is accomplished by putting the results into such a form that a first-order nonlinear ordinary differential equation is obtained after replacing λ by the quantity it originally represented. In many cases, this equation is of sufficiently simple form that it can be integrated analytically and the solution expressed in closed analytic form. In other cases, the integration must be performed numerically, but the equation is of such a form that standard methods can be applied. Although the mathematical basis of the method is not established in all details, the utility of the method has been amply demonstrated by numerous comparisons with results indicated by other theoretical methods or by experiment. A simple account of the method follows.

Two-Dimensional Flow

Subsonic Flows—Consider, first, two-dimensional subsonic flow past a nonlifting airfoil, the upper surface of which has ordinates given by $Z(x)$. Introduce the symbol λ as an abbreviation for $1 - M_\infty^2 - ku$ and rewrite Eq. (1) in the form

$$\lambda\varphi_{xx} + \varphi_{zz} = 0; \quad \lambda = 1 - M_\infty^2 - ku > 0 \quad (33)$$

It is now assumed that λ varies sufficiently slowly that it can be considered as a constant in the initial stages of the analysis. The solution u_E at the airfoil surface is

$$u_E = (U_\infty/\pi\sqrt{\lambda}) \int_0^c [(dZ/d\xi)/(x - \xi)]d\xi = u_i/\sqrt{\lambda} \quad (34)$$

where the subscript i refers to the values for $M_\infty = 0$. Differentiation and subsequent replacement of λ by $1 - M_\infty^2 - ku$, so that the local value for λ is used at each point, lead to the following nonlinear ordinary differential equation for u:

$$du/dx = (1/\sqrt{1 - M_\infty^2 - ku})\,(du_i/dx) \quad (35)$$

This equation can be solved by separation of variables. The result, expressed in terms of C_p rather than u, is

$$C_p = -[2/M_\infty^2(\gamma + 1)]\left\{(1 - M_\infty^2) - [C + (3/4)M_\infty^2(\gamma + 1)C_{p_i}]^{2/3}\right\} \quad (36)$$

where $C_{p_i} = -2u_i/U_\infty$ and C is a constant of integration. If the flow is subsonic everywhere, C can be evaluated simply by use of the result suggested by Eq. (34) that $u = 0$ where $u_i = 0$. This procedure leads to the following relation between C_p and C_{p_i}:

$$C_p = -[2/M_\infty^2(\gamma + 1)]\left\{(1 - M_\infty^2) - [(1 - M_\infty^2)^{3/2} + (3/4)M_\infty^2(\gamma + 1)C_{p_i}]^{2/3}\right\} \quad (37)$$

Eq. (37) may be described as a pressure-correction formula that relates the pressure at a given point on an airfoil in compressible flow to the pressure at the same point on the same airfoil in an incompressible flow. A great number of pressure-correction formulas have been proposed in the past, and results indicated by Eq. (37) are compared with those indicated by several of these in reference 45. Since all of these expressions involve approximations that affect the final result in an unknown manner, it is more informative to compare results indicated by Eq. (37) with those provided by the method of successive approximations. Fig. 15 shows the results of such a comparison for the variation of C_p with M_∞ at the midpoint of a 6 per cent-thick circular-arc airfoil. It can be seen that the results indicated by Eq. (37) are quite similar to those provided by the third approximation with the alternative method of successive approximations based on use of Eq. (29). This finding illustrates that the quality

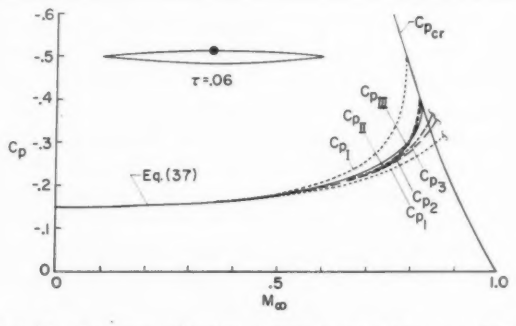

FIG. 15. Pressure, midpoint of circular-arc airfoil, $\tau = 0.06$.

of the results indicated by Eq. (37) is good, although the variation of the peak negative pressure with Mach Number is slightly too great.

It should be noted that Kusukawa[36] has also arrived at the relation indicated by Eq. (37) (except for a trivial replacement of $M_\infty^2(\gamma + 1)$ by $\gamma + 1$ due to a similar difference in the fundamental equations from which the result is derived) by application of the WKB method of approximation to the equations of transonic flow theory, as expressed in hodograph variables. It follows, therefore, that the approximate results given by Eq. (25) and shown in Fig. 11 for the pressure distribution on a finite wedge at free-stream Mach Number 1 can also be determined by application of the procedure described above.

Supersonic Flows—Application of the same procedures to supersonic flow, for which $\lambda < 0$, leads to the following results in place of Eqs. (36) and (37):

$$C_p = [2/M_\infty^2(\gamma + 1)]\left\{(M_\infty^2 - 1) - [C - (3/2)M_\infty^2(\gamma + 1)\,(dZ/dx)]^{2/3}\right\} \quad (38)$$

$$C_p = [2/M_\infty^2(\gamma + 1)]\left\{(M_\infty^2 - 1) - [(M_\infty^2 - 1)^{3/2} - (3/2)M_\infty^2(\gamma + 1)\,(dZ/dx)]^{2/3}\right\} \quad (39)$$

The latter relation is the exact equivalent, in transonic flow theory, of that given by simple wave theory for the surface pressure on an airfoil in supersonic flow. Simple wave theory is known (see reference 41), moreover, to be perfectly adequate for all practical purposes up to a Mach Number of 3, which is considerably in excess of the present range of interest. Within this Mach Number range, the results obtained by use of simple wave theory are almost identical with those obtained by use of shock-expansion theory.

Fig. 16 shows the pressure distribution on a 6 per cent-thick circular-arc airfoil at Mach Number 1.4 calculated by using Eq. (39) compared with that calculated by using simple wave theory. It can be seen that the two results are nearly identical. This result represents a considerable improvement over the corresponding result indicated by linear compressible flow theory, which would be represented in Fig. 16 by a straight line tangent to the simple wave curve at the midpoint of the airfoil.

Flows With $M_\infty = 1$—An essential feature of most flows with $M_\infty = 1$ is the transition from subsonic to supersonic flow somewhere along the chord. If the sonic point is situated at a point where the airfoil surface is smoothly curved, the transition is accomplished with a finite acceleration, and additional considerations are necessary because the foregoing results lead to infinite accelerations at the sonic point. The technique adopted is to apply the procedures described above to the relations that follow upon introduction of the symbol λ as an abbreviation for $k(\partial u/\partial x)$ in Eq. (1)—thus,

$$\varphi_{zz} = \lambda\varphi_x; \quad \lambda = k(\partial u/\partial x) > 0 \quad (40)$$

It is assumed, again, that λ varies sufficiently slowly that it can be considered as a constant in the initial

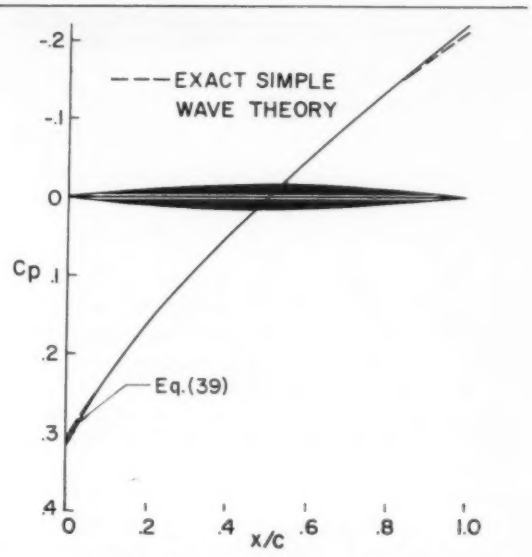

FIG. 16. Pressures, circular-arc airfoil, $\tau = 0.06$, $M_\infty = 1.4$.

stages of the analysis. The solution at the airfoil surface is

$$u_P = -(U_\infty/\sqrt{\pi\lambda})\,(d/dx) \times \int_0^x [(dZ/d\xi)/\sqrt{x - \xi}]d\xi \quad (41)$$

If $k(du/dx)$ is now restored in place of λ, a nonlinear ordinary differential equation is obtained that can be solved by separation of variables. The result, expressed in terms of C_p, is

$$C_p = -2\left[\frac{3}{\pi(\gamma + 1)} \times \int_{x^*}^x \left(\frac{d}{dx_1}\int_0^{x_1} \frac{dZ/d\xi}{\sqrt{x_1 - \xi}}\,d\xi\right)^2 dx_1\right]^{1/3} \quad (42)$$

where x^* is the value for x at which the local velocity is sonic.

Application to a single-wedge profile of chord $c/2$ and semiapex angle τ, for which the sonic point is known from *a priori* considerations to be situated at the shoulder, yields the following expression for the pressure distribution:

$$\bar{C}_p = [(\gamma + 1)^{1/3}/\tau^{2/3}]C_p = -2\left\{(3/\pi)\,\ln\,[x/(c/2)]\right\}^{1/3} \quad (43)$$

A plot of the results is shown in Fig. 17 together with the corresponding theoretical results given by Guderley and Yoshihara.[31] Although some approximations are introduced in the course of the latter analysis, the results are generally regarded as virtually an exact solution of the equations of the small-disturbance theory of transonic flow.

Application to smoothly curved airfoils requires the determination of the location of the sonic point. This can be readily accomplished, however, since the condition that du/dx be finite at the sonic point requires that $u = 0$ where $u_P = 0$. Thus x^* is the value of x for

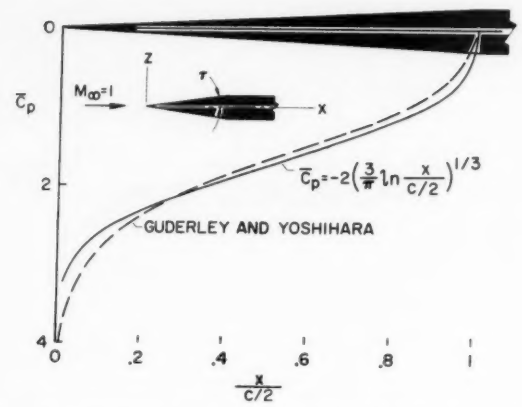

FIG. 17. Pressures, finite wedge, unseparated flow, $M_\infty = 1$.

which

$$(d/dx)\int_0^x [(dZ/d\xi)/\sqrt{x-\xi}]\,d\xi = 0 \qquad (44)$$

Application of Eqs. (42) and (44) to a circular-arc airfoil of maximum thickness t and chord c leads to the following expression for the pressure distribution at Mach 1:

$$\bar{C}_p = [(\gamma+1)^{1/3}/\tau^{2/3}]C_p = -2\{(12/\pi)\times \{\ln[4(x/c)] - 8(x/c) + 8(x/c)^2 + (3/2)\}\}^{1/3} \qquad (45)$$

where τ represents the thickness ratio t/c. A plot of this result is shown in Fig. 18 together with experimental pressure distributions from reference 55 for four such airfoils having thickness ratios of 6, 8, 10, and 12 per cent. These results are presented in terms of $\bar{C}_p$ rather than C_p because transonic flow theory indicates that the pressure distributions for all four airfoils should then define a single curve independent of the thickness ratio. It can be seen that the theoretical and experimental results are in substantial agreement. The most notable discrepancy is that found near the trailing edge, and can be attributed to flow separation induced by boundary-layer shock-wave interaction. Although part of the remaining discrepancy may possibly be the result of the experimental technique in which the airfoil is simulated by a bump on the tunnel wall and is hence imbedded in the wall boundary layer, results of a preliminary investigation reported in reference 46 reveal that it is plausible to attribute a substantial amount of the discrepancies apparent in this example, and also in a number of similar examples given in reference 45, to wind-tunnel wall interference.

Fig. 19 shows the results of a second application of Eqs. (42) and (44) to a special airfoil for which the theoretical pressure distribution has been given recently by Nocilla.[56] This comparison is of considerable theoretical interest because Nocilla's results are based on a numerical solution of the equations proposed for the study of compressible flow by Tomotika and Tamada.[57] The degree of approximation furnished by the latter set of equations should be much better than that of the equations of the small-disturbance theory of transonic flow enumerated at the start of this paper because (a) the fundamental equation for the stream function, as expressed in hodograph variables, approximates the exact equation to a much higher degree than does the corresponding equation—namely, Tricomi's equation given by Eq. (23)—of the small-disturbance theory of transonic flow from which Eqs. (42) and (44) are derived; (b) exact boundary conditions are imposed at the airfoil rather than the linearized boundary conditions given by Eq. (3a); and (c) the pressure is computed from the velocity using the exact relation for isentropic flow rather than the linearized relation given by Eq. (4a). Nocilla gives numerical results for the ordinates and velocity distribution at Mach 1 for two airfoils. The results for one of these is indicated in Fig. 19 by the dashed lines. The solid lines indicate the results calculated using Eqs. (42) and (44) together with a six-term series expansion for the shape of the airfoil. It can be seen that the airfoil shape is approximated very well by this series and that the agreement between the pressure distributions indicated by the two theories is probably sufficiently good for most practical purposes. The agreement is not quite so good over the rear part of the second airfoil for which Nocilla gives results in reference 56. It appears, however, that this discrepancy may not be due entirely to shortcomings of the approximation furnished by Eqs. (42) and (44), since the list of ordinates given in reference 56 contains some irregularities for points near the trailing edge.

Situations are frequently encountered, particularly in the analysis of flow past an airfoil having a cusped trailing edge, in which du/dx is positive over the front of the airfoil and negative over the rear. The expressions derived in this section are applicable to the front of such an airfoil, but not to the rear. It is possible to calculate the pressures on the rear by use of Eq. (38), however, if the constant of integration is selected so that the values for C_p match at the point where the two results are joined together. The results for such a case are shown in Fig. 20 together with experimental data from reference 58. The front half of this airfoil is the same as that of a circular-arc airfoil but the rear

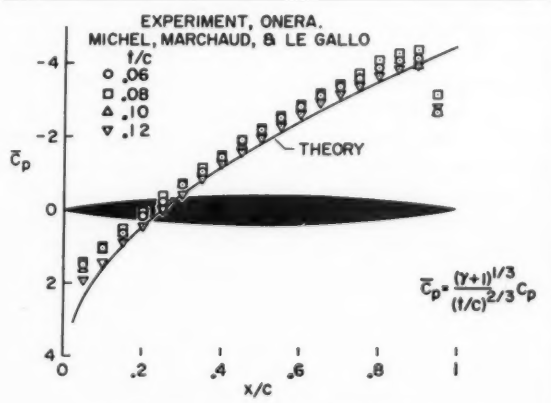

FIG. 18. Pressures, circular-arc airfoil, $M_\infty = 1$.

half is shaped in such a way that an inflection point is located at 75 per cent chord and the trailing-edge angle is zero. No analytic expression is given in reference 58 for the shape of the rear, but graphs of the ordinates and slopes can be found in references 58 and 45. The values for C_p for the front half are calculated by use of Eq. (45). Those for the rear half are calculated by use of the relation

$$\bar{C}_p = -2[\sqrt{(6/\pi)\,(-1 + \ln 4)} - (3/2\tau)\,(dZ/dx)]^{2/3} \quad (46)$$

that follows from Eq. (38) upon selection of such a value for C that C_p is equal, at the midpoint of the airfoil, to the value indicated by Eq. (45). It can be seen from Fig. 20 that the results join together in a satisfactory manner, and are in reasonable agreement with the experimental data. Although it was not practical in the example shown in Fig. 20, the selection of a point for joining the solutions can be made in many cases by requiring that dC_p/dx, as well as C_p, match.

Axisymmetric Flow

An analysis similar to that given for two-dimensional flows can likewise be given for axisymmetric flow. These procedures lead directly to the following nonlinear ordinary differential equation for u on the surface of a slender body of revolution:

$$\frac{d(u/U_\infty)}{dx} = \frac{S'''(x)}{4\pi} \ln (1 - M_\infty{}^2 - ku) + \frac{d}{dx}\left[\frac{S''(x)}{4\pi} \ln \frac{S}{4\pi x(l-x)} + \frac{1}{4\pi}\int_0^l \frac{S''(x) - S''(\xi)}{|x-\xi|}\,d\xi\right] \quad (47)$$

for subsonic flow, to

$$\frac{d(u/U_\infty)}{dx} = \frac{S'''(x)}{4\pi} \ln (M_\infty{}^2 - 1 + ku) + \frac{d}{dx}\left[\frac{S''(x)}{4\pi} \ln \frac{S}{4\pi x^2} + \frac{1}{2\pi}\int_0^x \frac{S''(x) - S''(\xi)}{x-\xi}\,d\xi\right] \quad (48)$$

for supersonic flow, and to

$$(u/U_\infty) = [S''(x)/4\pi] \ln \{[(d/dx)\,(u/U_\infty) - (S'S''/4\pi S)]\,(U_\infty k S e^{C_1}/4\pi x)\} + (1/4\pi)\int_0^x \{[S''(x) - S''(\xi)]/(x-\xi)\}\,d\xi \quad (49)$$

for flow with $M_\infty = 1$. The primes indicate differentiation with respect to x, the symbol C_1 represents Euler's constant ≈ 0.5772, and

$$(d/dx)\,(u/U_\infty) - (S'S''/4\pi S) = \partial u/\partial x$$

Application of Eqs. (47), (48), or (49) to the flow past smoothly curved bodies of revolution requires the evaluation of a constant of integration. A simple procedure that leads to satisfactory results in applications of Eq. (47) to purely subsonic flow, or of Eq. (48) to purely supersonic flow, is to specify that u be equal to the value indicated by the solution of the linearized equations of compressible flow theory at the point where $S''(x) = 0$. This procedure, which is analogous to that used in the analysis of two-dimensional flow, does not suffice in the case of Eq. (49). The reason is that this equation is singular at the point where $S''(x) = 0$, and infinitely many integral curves pass through this value for u at the point where $S''(x)$ vanishes. Of all these curves, only one is analytic (all derivatives finite) at this point, and selection of it suffices to determine a unique solution that is in good agreement with experimental data. This procedure assures that the solution for u can be expanded in a Taylor series in the neighborhood of the point where $S''(x)$ vanishes. The remainder of the solution can be determined by application of standard numerical methods. The particular method used to calculate the results presented in the following paragraphs is that of Milne.[59]

The procedures outlined above have been applied to calculate the pressure distribution at Mach 1 on the surface of the front part of a parabolic-arc body having a ratio τ of maximum diameter to length of 1/6. These procedures cannot be applied to calculate the pressures along the entire length of this body, however, because the velocity reaches a maximum at a point somewhat rearward of the middle, and then decreases continually along the remainder of the length of the body. The flow is, moreover, subsonic in the vicinity of the rear

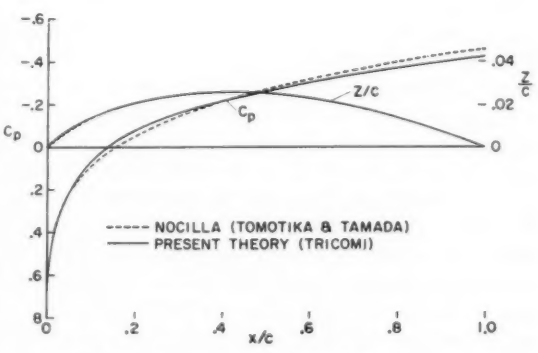

FIG. 19. Pressures, Nocilla airfoil, $M_\infty = 1$.

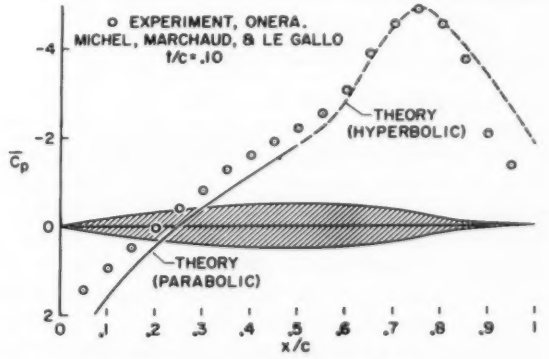

FIG. 20. Pressures, cusped airfoil, $M_\infty = 1$.

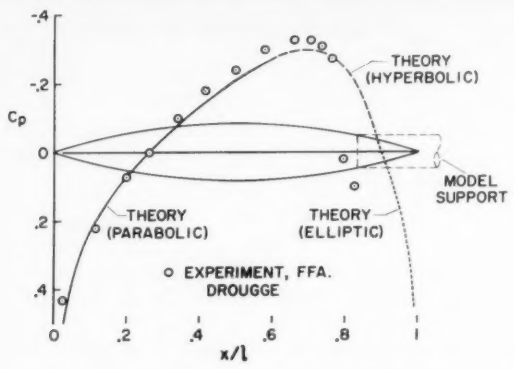

FIG. 21. Pressures, parabolic-arc body of revolution, $\tau = 1/6$, $M_\infty = 1$.

tip. It is thus necessary to consider the solution in sections and join the results together in the same manner as described in connection with two-dimensional flow past the cusped airfoil shown in Fig. 20. The results of such a calculation are shown in Fig. 21. The point at which the results calculated by use of Eqs. (49) and (48) are joined is at 61.1 per cent chord, and has been selected so that dC_p/dx, as well as C_p, match. The point at which the results calculated by use of Eqs. (48) and (47) are joined is at 87.9 per cent chord, and is fixed by the occurrence of sonic velocity. Both C_p and dC_p/dx match at the point where the two sets of results are joined together. The slight bend at this point is the consequence of a logarithmic infinity in dC_p/dx at the sonic point. Since this property of the equations prevents the application of Milne's method in the immediate vicinity of the sonic point, the solution has been determined in this region by application of the method of isoclines.

Experimental results obtained by Drougge[19] in tests of the forward 5/6 of a parabolic-arc body mounted on a cylinder extending downstream from the rear of the body are also included in Fig. 21. The theoretical and experimental results are in satisfactory agreement except over a small part of the body immediately forward of the point where the experimental body becomes cylindrical. This discrepancy is undoubtedly associated with the occurrence of a shock wave that must be detached from the corner because the local Mach Number is too small.

Approximate Application of Method

In the applications of the method of local linearization described in the preceding paragraphs of this section, certain approximations are introduced to determine an ordinary differential equation for u along the surface of an airfoil or a body of revolution, and then this equation is integrated with no further approximation. It may frequently occur, in application of the same procedures to more complicated cases, that the resulting ordinary differential equation may be very difficult, if not impossible, to integrate. The method may still be of value in such cases, however, because it may be possible to introduce further approximations of a related nature to simplify the equations to a more tractable form, while still retaining the essential nonlinear features of the solution. Two examples illustrating such techniques are presented below.

Consider, first, the problem of two-dimensional subsonic flow past an unstaggered cascade of thin nonlifting symmetrical airfoils having round noses. Although it is recognized that this particular case represents one of the simplest examples of flow through a cascade, knowledge of the solution for this and more complex cascade problems is of fundamental importance in two rather different practical applications—namely, the study of the flow in turbomachines and the study of wind-tunnel wall interference. Such flows have recently been the subject of extensive theoretical and experimental investigations by Schlichting and his colleagues, summaries of which are given in references 60, 61, and 62. Their theoretical analysis is based on the linearized theory of compressible flow, except for a modification of the boundary conditions at the airfoil surface to permit application to an airfoil with a round nose, and leads to the following expression for the longitudinal perturbation velocity component u at the airfoil surface.

$$u = (1/\sqrt{1 - M_\infty^2}) \int_0^c (U_\infty + u_i)\,(dZ/d\xi) \times \coth\left\{\pi[(x - \xi)/h\sqrt{1 - M_\infty^2}]\right\} \times (d\xi/h\sqrt{1 - M_\infty^2}) = u_i/\sqrt{1 - M_\infty^2} \quad (50)$$

where the airfoil chord and spacing are given by c and h, respectively, and the symbol u_i refers to the solution given by Eq. (50) for flow at Mach Number zero past an associated cascade of airfoils having the same shape, but smaller spacing h_i given by $h\sqrt{1 - M_\infty^2}$. Application of the procedure described in the preceding section on two-dimensional subsonic flow leads first of all to an expression similar to Eq. (50) except for replacement of $1 - M_\infty^2$ by λ. The subsequent differentiation with respect to x and substitution of $1 - M_\infty^2 - ku$ for λ leads to an equation for u that is extremely difficult to solve. Closer inspection of the equation suggests, however, that it may suffice to replace $\sqrt{\lambda}$ where it appears together with the airfoil spacing h with $\sqrt{1 - M_\infty^2}$ as in linear theory, and to introduce the variable quantity $\sqrt{1 - M_\infty^2 - ku}$ for only the $\sqrt{\lambda}$ that appears alone as a factor outside the integral sign. This procedure leads to an expression for du/dx on the airfoil surface that has the same form as Eq. (35). It follows directly that the pressure at a given point on an airfoil in compressible flow is related to that at the same point on an airfoil of the associated cascade in incompressible flow according to the relation given by Eq. (37). This result agrees [except for the slight difference noted previously in connection with Eq. (37)] with a similar statement given by Kusukawa[36] that is obtained by application of the WKB method of approximation. Results obtained for an application of the above procedure to the specific case of flow with

Mach Number 0.65 past an unstaggered cascade of nonlifting NACA 0010 airfoils having equal spacing and chord are shown in Fig. 22. The theoretical results indicated by the dashed line, which are computed using Eq. (37) and the experimental data points are taken from a recent paper by Feindt and Schlichting.[62] The solid line indicates the theoretical result calculated using the procedures described above together with the linearized solution given in reference 62. It can be seen that the present results represent a substantial improvement over those calculated by straightforward application of Eq. (50).

Consider next the problem of the calculation of the supersonic flow field associated with a smooth slender body of revolution. It is well known from the work of Whitham and Lighthill[63, 41] that the results indicated directly by linear theory, that is, by the following equations:

$$u = -\frac{U_\infty}{2\pi} \times \int_0^{x - \sqrt{M_\infty^2 - 1}\, r} \frac{S''(\xi)}{\sqrt{(x-\xi)^2 - (M_\infty^2 - 1)r^2}}\, d\xi \quad (51)$$

$$v_r = \varphi_r = \frac{U_\infty}{r} \times \int_0^{x - \sqrt{M_\infty^2 - 1}\, r} \frac{(x-\xi)S''(\xi)}{\sqrt{(x-\xi)^2 - (M_\infty^2 - 1)r^2}}\, d\xi \quad (52)$$

provide a good approximation for the conditions at the surface of the body, but not for the conditions in the flow at some distance from the body. It is possible to achieve a substantial improvement over the results indicated by linear theory by application of procedures similar to those employed above in the analysis of subsonic flow through a cascade. The first step in such a procedure is to replace $M_\infty^2 - 1$ by λ and to differentiate Eqs. (51) and (52) to determine differential equations for u and v_r. This differentiation can be carried out in various directions (note, e.g., that the differentiation is made in the direction of the x axis in the calculation of the surface pressures on thin airfoils, and in the direction of the body surface, which differs slightly from the x direction, in the calculation of the surface pressures on slender bodies of revolution). The form of Eqs. (51) and (52) with $M_\infty^2 - 1$ replaced by λ, together with certain well-known properties of supersonic flow, suggests that it is appropriate to perform the differentiation in the direction of the downstream characteristics, which are defined at this point in the analysis by the following differential equation:

$$dx/dr = \cot \sqrt{\lambda} \quad (53)$$

The subsequent replacement of λ by $M_\infty^2 - 1 + ku$ leads to an extremely complicated system of equations for u and v_r, and for the shape of the characteristic surfaces. Closer inspection of the equations suggests, however, that it may suffice to substitute $M_\infty^2 - 1$ for λ where it appears in the differential equations for the variation of u and v_r along the characteristics, and to introduce the variable quantity $M_\infty^2 - 1 + ku$ for only the λ that appears in Eq. (53) defining the location of the characteristics. This procedure leads to an expression for the shape of the characteristics that is exact within the framework of the equations of transonic flow theory, and to a pair of expressions for u and v_r along the characteristics that can be integrated easily. The result is precisely the counterpart in transonic flow theory of the result given previously by Whitman,[63] which states that linear theory gives a correct first approximation throughout the flow, provided that the value which it predicts for any physical quantity, at a given distance from the axis on the straight (approximate) Mach line $x - \sqrt{M_\infty^2 - 1}\, r =$ const., pointing downstream from a given point on the body surface, is interpreted as the value, at that distance from the axis, on the exact characteristic which points downstream from the said point.

Wind-Tunnel Wall Interference at Mach One

A source of uncertainty that is present in all wind-tunnel testing is associated with the finite dimensions of the test section. The study of wall interference and the determination of formulas for the calculation of corrections have consequently been the subject of numerous theoretical and experimental investigations. It is found, for bodies and test sections of typical proportions, that the influence of the walls is generally small at low Mach Numbers, but increases substantially as the Mach Number increases toward and into the transonic range. Although the effects of the walls are generally much less in the partly open test sections customarily employed in modern transonic wind tunnels than in the older type of tunnel with solid walls, recent theoretical and experimental investigations have disclosed the existence of wall-interference effects at Mach 1 that are much larger than had been previously supposed, and much harder to eliminate by testing smaller models than at subsonic Mach Numbers.

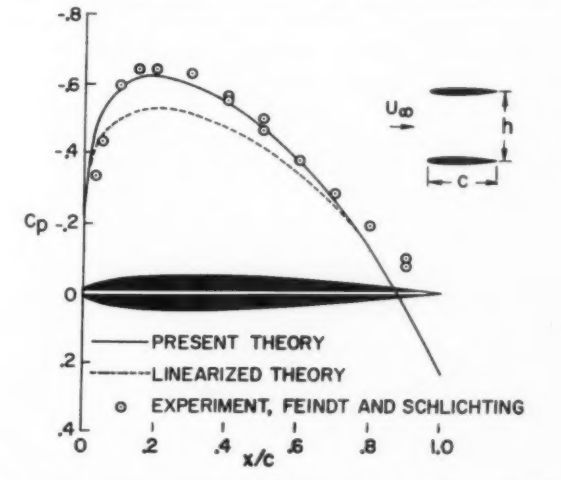

FIG. 22. Pressures, unstaggered cascade, $h/c = 1$, NACA 0010 airfoils, $\alpha = 0$, $M_\infty = 0.65$.

One of the most striking examples of large interference effects at Mach 1 is that described recently by Page in reference 13. He tested a slender cone-cylinder having a semiapex angle of 7° and length from apex to shoulder of 5.50 in. in two different transonic wind tunnels at Ames Research Center. The test section of one of the wind tunnels is 2 ft. square, that of the other wind tunnel is 14 ft. square. The pressure distribution along the conical part of the body as measured for Mach 1 in each of the wind tunnels is shown in Fig. 23. Also included in this Figure is a theoretical curve for unbounded flow past a 7° cone-cylinder calculated by use of the following expressions derived from Eqs. (46), (47), and (49):

$$\left.\begin{aligned} C_p = {} & -2\omega^2 \ln(\omega x/l) + \omega^2 \ln\left([16/(\gamma+1)\times \omega^2 e^{(1)}]\{(x/l)\,[1-(x/l)]\}\right) + \\ & (\omega^2/2)\left\{[1-(3x/l)]/[1-(x/l)]\right\} - \omega^2 \\ & \text{for } 0 \le x/l \le 1/3 \end{aligned}\right\} \quad (54)$$

$$\left.\begin{aligned} C_p = {} & -2\omega^2 \ln(\omega x/l) + \omega^2 \ln\left\{\omega^2 + [4(1-x^2/l^2)/(\gamma+1)\omega^2 e^{(1)}]\right\} - \omega^2 \\ & \text{for } 1/3 \le x/l \le 1 \end{aligned}\right\}$$

where the symbols l and ω represent the length and semiapex angle of the cone. It can be seen that substantial differences exist between the results measured in the two wind tunnels, and that even the results obtained in the larger wind tunnel are displaced from the theoretical results for an unbounded flow. It should be noted, however, that the theoretical results are of an approximate nature, and should not necessarily be taken as a standard for the pressure distribution on the cone in an infinite stream.

Considerable insight into the nature of wind-tunnel interference in a slotted test section at Mach 1 is provided by the theoretical investigation of Berndt described in reference 64. He found, though application of Guderley and Yoshihara's asymptotic solution for the conditions at large lateral distances from a slender body of revolution in a flow with free-stream Mach Number 1 (see reference 10, chapter XI), that the

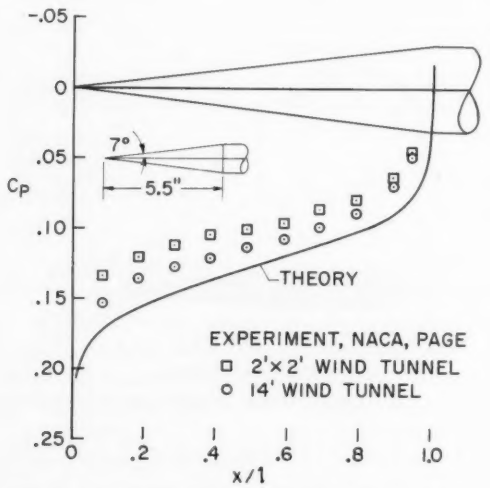

FIG. 23. Pressures, cone-cylinder, $\omega = 7°$, $M_\infty = 1$.

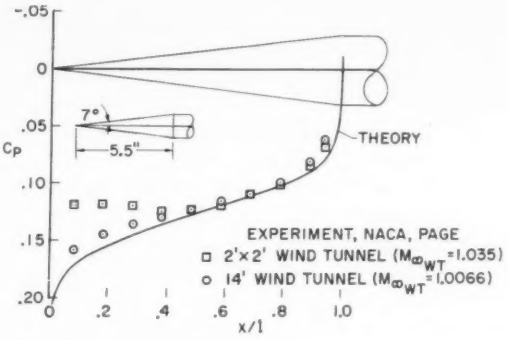

FIG. 24. Corrected pressures, cone-cylinder, $\omega = 7°$, $M_\infty = 1$.

adjustment of the slot width is not very critical, and that a Mach Number error due to wall interference at sonic speed is given approximately by

$$\left.\begin{aligned} \Delta M &= +0.26(r^*/R)^{6/7}\,(r^*/x^*)^{2/7} \\ M_{\infty_{WT}} &= 1 - \Delta M \end{aligned}\right\} \quad (55)$$

where $M_{\infty_{WT}}$ is the indicated Mach Number in the wind tunnel, R is the radius of the wind tunnel, and x^* and r^* are the coordinates of the sonic point on the body surface.

Examination of the experimental results given by Page in reference 13 reveals, however, that the correction indicated by Eq. (55) is too small and of the wrong sign to account for the differences between the various results displayed in Fig. 23. The experimental data shown in Fig. 23 were not obtained in wind tunnels with slotted walls, however, but in wind tunnels having walls that are thought to act more as though they are porous or perforated. Page consequently made a new analysis, similar to that given by Berndt, of wind-tunnel wall-interference effects in a porous test section at Mach 1, and found that the Mach Number error is given approximately by the following expression:

$$\Delta M = -0.82(r^*/R)^{6/7}\,(r^*/x^*)^{2/7} \quad (56)$$

in which the symbols have the same meaning as in Eq. (55). Application of this expression to the conditions of Page's experiments indicates that sonic free air conditions are simulated in the small wind tunnel when the measured Mach Number is 1.035 and in the large wind tunnel when the measured Mach Number is 1.0066. In this and the following examples, the location of the sonic point is taken to be at the station indicated by the theoretical result (that is, at the station where u vanishes) for flow in an unbounded stream.

Fig. 24 has been included to illustrate the effect of this Mach Number correction on the experimental data obtained from the two wind tunnels. The corrected data from both tunnels are now in very good agreement with each other over the rear half of the cone, and the agreement with the theoretical pressure distribution calculated by use of Eq. (54) is improved considerably. A notable discrepancy appears in the corrected data from the smaller tunnel for the pressures on the front half of the cone. It can be seen that the

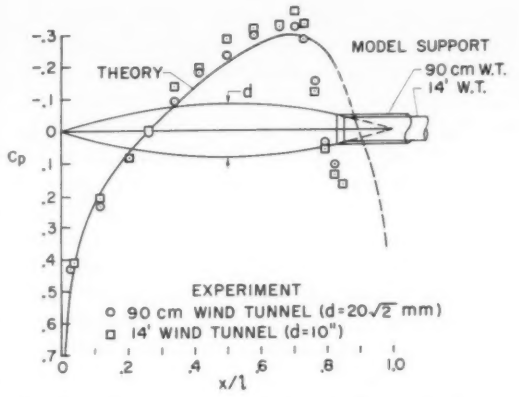

FIG. 25. Pressures, parabolic-arc body of revolution, $\tau = 1/6$, $M_\infty = 1$.

pressures stop climbing toward the large values associated with stagnation conditions at the apex, as should occur at Mach 1, but remain nearly constant at a level that is very nearly equal to the value for C_p of 0.12 that is indicated by conical flow theory to occur on the surface of an infinite 7° cone at a Mach Number of 1.035. It appears from this result that the correction formula given by Eq. (56) is not entirely satisfactory and that difficulties of a fundamental nature may arise in the correction of data for larger models that are more characteristic of normal wind-tunnel practice.

The results presented in Figs. 23 and 24 for the 7° cone-cylinder lead to very pessimistic conclusions regarding the maximum model size permissible for obtaining data of good quality, and also for successful application of correction formulas such as that given in Eq. (56). It appears, however, that wall-interference effects are particularly severe on this body, and that somewhat more optimistic conclusions follow upon similar inspection of results for other bodies. Consider, for example, the comparison of experimental and theoretical pressure distributions on the forward 5/6 of a parabolic-arc body of revolution having a ratio of maximum diameter to length of 1/6 shown in Fig. 25. Two sets of experimental results are included in this Figure. One is the same as that already presented in Fig. 21, and represents the measurements of Drougge on a body having a maximum diameter of $20\sqrt{2}$ mm. in a wind tunnel having a slotted test section 90 cm. square. The other represents the results of measurements on a geometrically similar body having a maximum diameter of 10 in. in a relatively smaller wind tunnel, the Ames 14-ft. wind tunnel. The theoretical results are for an unbounded flow and are the same as given previously in Fig. 21. It can be seen that all of the results agree reasonably well over the forward part of the body, but that noticeable differences develop over the middle and rear parts of the body. Attention is called to the fact that the results for both wind tunnels are on the same side of the theoretical curve, even though the theoretical results of Berndt and Page indicate that the corrections should be of opposite sign.

Further examination of the data from the slotted-wall wind tunnel discloses, however, that the necessary correction required to bring the results into alignment with the corrected results from the 14-ft. wind tunnel, and also with the theoretical results, is of the order of that indicated by Eq. (56) for the porous wind tunnel. Application of this expression to the conditions of the two experiments indicates that sonic free air conditions are simulated in the 90-cm. tunnel when the measured Mach Number is 1.021 and in the 14-ft. wind tunnel when the measured Mach Number is 1.037. A plot of the results corrected in this manner is presented in Fig. 26. It can be seen that the two sets of experimental results are brought into reasonably good agreement with each other and with the theoretical curve over the middle and rear parts of the body but that the corrected experimental results depart further from the theoretical curve over the forward part of the body than do the original uncorrected results.

A third set of experimental results are also included in Fig. 26. They are obtained from measurements using the same body as in the tests in the 14-ft. wind tunnel, but the tests were conducted in the Ames 12-ft. pressure wind tunnel. The test section of the latter wind tunnel has a circular cross section with solid walls, and cannot, therefore, be operated in the normal manner to obtain data for free-stream Mach Number 1. A number of theoretical papers by Guderley and others (see reference 10, chapter IX, for a résumé, and references 38, 39, and 40 for some more recent analyses) have shown, however, that the values for $C_p^* = (p - p^*)/q^*$ (where p^* and q^* represent the values for the static and dynamic pressures associated with sonic conditions) on the surface of wedge and flat-plate airfoils in a choked solid-wall wind tunnel are very nearly the same as the values for C_p in an unbounded flow with free-stream Mach Number 1. Although the validity of the corresponding statement for flow past airfoils of more arbitrary shape or past three-dimensional bodies has not been established theoretically, the data from the 12-ft. wind tunnel presented in Fig. 26 were obtained by operating the tunnel in the choked condition and identifying the resulting values for C_p^* with those for C_p for the body in an unbounded flow. It can be seen upon inspection of the various results

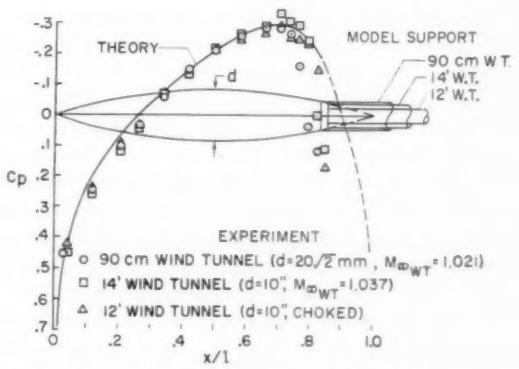

FIG. 26. Corrected pressures, parabolic-arc body of revolution $\tau = 1/6$, $M_\infty = 1$.

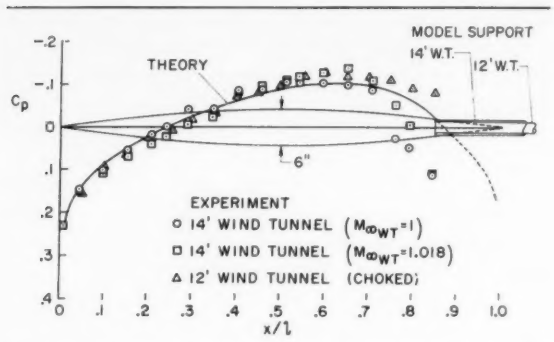

FIG. 27. Pressures, parabolic-arc body of revolution, $\tau = 1/12$, $M_\infty = 1$.

included in Fig. 26 that the data from the choked solid-wall wind tunnel are in good agreement with the theoretical curve along the entire length of the body, and tend toward values that, in many cases, are intermediate between the corrected and uncorrected values obtained in the transonic wind tunnels. This result provides a strong indication that the values for C_p^* on the surface of a three-dimensional body in a choked solid-wall wind tunnel are very nearly the same as those for C_p on the same body in an unbounded flow. It also provides additional evidence that the correction indicated by Eq. (56) may be too large.

Another interesting feature of wind-tunnel interference at Mach 1 is illustrated in Fig. 27, in which are presented theoretical and experimental pressure distributions for a parabolic-arc body having a ratio of maximum diameter to length of 1/12. The theoretical results are from reference 20 and have been computed using Eqs. (47), (48), and (49) in the same manner as described previously for the body of thickness ratio 1/6. Three sets of experimental results, all obtained using the same model having a maximum diameter of 6 in., are shown. The circular data points represent the experimental results measured in the Ames 14-ft. wind tunnel at an indicated Mach Number of 1, as reported in reference 65. Application of the correction formula given in Eq. (56) indicates, however, that sonic conditions in this particular test are simulated when the indicated Mach Number is 1.018 rather than 1. The square data points show the values for C_p measured at this Mach Number, and represent the corrected results for Mach 1. The triangular data points represent the results obtained from tests of the same body in the Ames 12-ft. tunnel operating in the choked condition. It can be seen that the relationship between the various experimental and theoretical results is substantially the same as for the body of thickness ratio 1/6 over the front part of the body, but that substantial discrepancies appear among the various results at stations rearward of about 60 per cent of the body length. The experimental data obtained in the choked solid-wall tunnel are, moreover, on the opposite side of the theoretical curve for an unbounded flow from the experimental data obtained in the transonic wind tunnel with partly open walls.

The source of these differences, and also the reason for the nonexistence of the differences in the results for the body of thickness ratio 1/6 given in Fig. 26, can be seen by examination of the diagrams shown in Fig. 28. The diagram on the left shows an abridged plot of the characteristic lines for an unbounded flow with free-stream Mach Number 1 about a parabolic-arc body of thickness ratio 1/6. This diagram is taken from reference 66 by Oswatitsch and has been calculated by use of the linearized theory of sonic flow described by Oswatitsch and Keune[67] to compute the conditions along the sonic line, and by use of a simplified method of characteristics based on the equations of the small-disturbance theory of transonic flow to compute the conditions in the supersonic region. The horizontal dashed line at some distance from the axis represents the position of the wall in the tests in the 12-ft. pressure wind tunnel. The nearest point of the wall in the 14-ft. transonic wind tunnel is 7/6 as far away from the axis of the body, and the nearest point of the wall in Drougge's tests in the 90-cm. wind tunnel is even farther from the body axis. It can be seen from this diagram that the wind-tunnel walls are sufficiently far away in all of the tests with the body of thickness ratio 1/6 that none of the characteristic lines that strike the wall can reflect back and influence the pressures on the rear of the body.

The diagram shown on the right in Fig. 28 presents the corresponding results for the body of thickness ratio 1/12. These results are obtained from those for the body of thickness ratio 1/6 by application of the transonic similarity rule for axisymmetric flow which states that the flow fields associated with sonic flow past an affinely related family of slender bodies of revolution can be brought into coincidence by stretching the lateral coordinates in inverse proportion to the thickness ratio. The position of the wall with respect to the model in the tests in the 12-ft. pressure wind tunnel is again indicated by the dashed line. This result shows that the walls in both the 12-ft. pressure wind tunnel and in the 14 ft. transonic wind tunnel are no longer sufficiently far away to prevent characteristics reflecting from the walls to impinge on the rear of the body. It can be seen, moreover, that the most forward reflected characteristic strikes the body at about 60 per cent of the body length in the test in the 12-ft. pressure wind tunnel. This position coincides very well with the station at which the experimental results shown in Fig. 27 begin to depart from the theoretical curve, and also from the experimental data obtained in the 14-ft. transonic wind tunnel. The effect of the reflected characteristics striking the body is to make the pressures more negative in the 12-ft. pressure wind tunnel, because the outgoing characteristics represent expansion waves that reflect from the solid wall of the tunnel as expansion waves. The sign of the corresponding effects in the 14-ft. transonic wind tunnel is not so simple to ascertain, since the reflections from the solid part of the wall are expansion waves and those from the open part of the wall are compression waves. It ap-

pears from the results presented in Fig. 27 that the influence of the reflections from the partly open wall of the 14-ft. wind tunnel is very nearly equal in magnitude but opposite in sign to that of the reflections from the solid wall of the 12-ft. pressure wind tunnel. This aspect of wind-tunnel wall interference imposes strong restrictions on the maximum length of bodies for which reliable results can be determined in either a transonic wind tunnel with partly open walls or a solid-wall wind tunnel operating in the choked condition. These restrictions become increasingly severe, moreover, as the thickness ratio is diminished, and it is necessary to use models that are not only smaller in diameter, but also smaller in length to prevent the reflected waves from impinging on the rear of the model.

It should be pointed out before closing this discussion that, although the preceding results for wind-tunnel interference effects at Mach 1 are all concerned explicitly with flow past slender bodies of revolution, the equations of transonic flow theory indicate that many of the same conclusions apply equally for slender bodies, such as wing-body combinations, of arbitrary cross section. This extension of the results for axisymmetric flow follows as a consequence of the transonic equivalence rule, which states that the distant flow field of a slender body of arbitrary cross section is the same as that of the equivalent body of revolution. An experimental confirmation of this result can be seen by consideration of the results already presented in this paper in Figs. 6, 23, and 24. The results presented in Fig. 6 show that the differences between the experimental pressure distributions on a thin elliptic cone-cylinder and an equivalent circular cone-cylinder are given satisfactorily by transonic flow theory. These tests were conducted in the Ames 2- by 2-ft. transonic wind tunnel, however, and it is evident from the results for the circular cone-cylinder, shown in Figs. 23 and 24, that the actual level of the pressures measured on both the elliptic and circular cone-cylinders are badly in error. These results, taken together with the fact that is apparent from all the comparisons presented in this paper that the theoretical results indicated by transonic flow theory are very reliable, provides a strong indication that the wall-interference effects on the thin elliptic cone-cylinder are very nearly the same as on the equivalent circular cone-cylinder.

Concluding Remarks

In summary, two principal conclusions emerge from the review of knowledge of the aerodynamic properties of wings and bodies at transonic speeds presented in the preceding pages. One is that substantial progress is being made in the development of methods for the approximate solution of the nonlinear differential equations that govern transonic flow. The other is that the results of calculations based on transonic flow theory are consistently of almost surprising accuracy considering both the small-perturbation approximation inherent in the fundamental equations of the theory

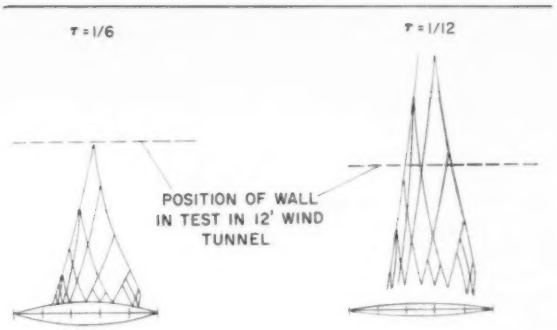

Fig. 28. Characteristic diagram, parabolic-arc body of revolution, $M_\infty = 1$.

and the novel nature of some of the procedures used to obtain approximate solutions of these equations. Much work remains to be done, however, in the application of these methods to an ever-increasing number of problems, and in the development of new methods for the analysis of important facets of the transonic flow problem, such as shock-wave boundary-layer interaction, that remain essentially unsolved at the present time.

While the development of a reliable theory for the prediction of the aerodynamic properties of wings and bodies at transonic speeds is a subject primarily of interest to aerodynamicists, it is hoped that the methods of approximation, as well as some of the results for specific applications, might also be of interest to mathematicians concerned with the solution of nonlinear partial differential equations. It should be clearly stated in this connection that the underlying reasons for the success of some of these methods remain only incompletely understood from a mathematical point of view. On the other hand, the demonstrated ability of these methods to reproduce closely the results of exact, but far more complicated, solutions and of experiments should be sufficient to warrant further mathematical study.

References

[1] Oswatitsch, K., and Wiegardt, K., *Theoretische Untersuchungen über stationäre Potentialströmungen und Grenzschichten bei hohen Geschwindigkeiten*, Lilienthal-Gesellschaft für Luftfahrtforschung, Ber. 13/1, pp. 7–24, 1942 (also available as NACA TM 1189).

[2] Busemann, A., and Guderley, K. Gottfried, *The Problem of Drag at High Subsonic Speeds*, Rep. and Trans. No. 184, British M.A.P., March, 1947.

[3] Guderley, K. Gottfried, *Considerations of Structure of Mixed Subsonic-Supersonic Flow Patterns*, Tech. Rep. F-TR-2168-ND, AAF, Air Materiel Command, Wright Field, October, 1947.

[4] Guderley, K. Gottfried, *On the Transition from a Transonic Potential Flow to a Flow with Shocks*, Tech. Rep. F-TR-2160-ND, AAF, Air Materiel Command, Wright Field, August, 1947.

[5] von Kármán, Theodore, *Supersonic Aerodynamics—Principles and Applications*, Journal of the Aeronautical Sciences, Vol. 14, No. 7, pp. 373–402; Discussion, pp. 403–409, July, 1947.

[6] von Kármán, Theodore, *The Similarity Law of Transonic Flow*, J. Math. & Phys., Vol. XXVI, No. 3, pp. 182–190, October, 1947.

[7] Spreiter, John R., *On the Application of Transonic Similarity Rules to Wings of Finite Span*, NACA Rep. 1153, 1953 (supersedes NACA TN 2726).

[8] Spreiter, John R., and Alksne, Alberta, *Theoretical Prediction of Pressure Distributions on Nonlifting Airfoils at High Subsonic Speeds*, NACA Rep. 1217, 1955 (supersedes NACA TN 3096).

[9] Liepmann, H. W., and Roshko, A., *Elements of Gasdynamics*, John Wiley and Sons, Inc., New York, 1957.

[10] Guderley, K. G., *Theorie schallnaher Strömungen*, Springer-Verlag, Berlin, Göttingen, Heidelberg, 1957.

[11] Liepmann, H. W., and Bryson, A. E., Jr., *Transonic Flow Past Wedge Sections*, Journal of the Aeronautical Sciences, Vol. 17, No. 12, pp. 745–755, December, 1950.

[12] Bryson, Arthur Earl, Jr., *An Experimental Investigation of Transonic Flow Past Two-Dimensional Wedge and Circular-Arc Sections Using a Mach-Zehnder Interferometer*, NACA Rep. 1094, 1952 (supersedes NACA TN 2560).

[13] Page, William A., *Experimental Study of the Equivalence of Transonic Flow About Slender Cone-Cylinders of Circular and Elliptic Cross Section*, NACA TN 4233, 1958.

[14] Oswatitsch, K., and Berndt, S. B., *Aerodynamic Similarity at Axisymmetric Transonic Flow Around Slender Bodies*, KTH Aero TN 15, Royal Inst. Tech., Stockholm, Sweden, 1950.

[15] Berndt, S. B., *Similarity Laws for Transonic Flow Around Wings of Finite Aspect Ratio*, KTH Aero TN 14, Royal Inst. Tech., Stockholm, Sweden, 1950.

[16] Spreiter, John R., *Similarity Laws for Transonic Flow About Wings of Finite Span*, NACA TN 2273, 1951.

[17] McDevitt, John B., *A Correlation by Means of Transonic Similarity Rules of Experimentally Determined Characteristics of a Series of Symmetrical and Cambered Wings of Rectangular Plan Form*, NACA Rep. 1253, 1955 (supersedes NACA RM A51L17b and A53G31).

[18] Page, William A., *Experimental Determination of the Range of Applicability of the Transonic Area Rule for Wings of Triangular Plan Form*, NACA TN 3872, 1956.

[19] Drougge, Georg, *Some Measurements on Bodies of Revolution at Transonic Speeds*, Actes, IX° Congrès International de Mecanique Appliquée, Tome II, pp. 70–77, 1957.

[20] Spreiter, John R., and Alksne, Alberta Y., *Slender Body Theory Based on Approximate Solution of the Transonic Flow Equation*, NASA Rept. 2, 1959.

[21] Oswatitsch, Klaus, *The Area Rule*, Appl. Mech. Rev., Vol. 10, No. 12, pp. 543–545, December, 1957.

[22] Heaslet, Max. A., and Spreiter, John R., *Three-Dimensional Transonic Flow Theory Applied to Slender Wings and Bodies*, NACA Rep. 1318, 1957 (supersedes NACA TN 3717).

[23] Spreiter, John R., *The Aerodynamic Forces on Slender Plane- and Cruciform-Wing and Body Combinations*, NACA Rep. 962, 1950 (supersedes NACA TN 1662 and 1897).

[24] Heaslet, Max. A., Lomax, Harvard, and Spreiter, John R., *Linearized Compressible-Flow Theory for Sonic Flight Speeds*, NACA Rep. 956, 1950 (supersedes NACA TN 1824).

[25] Whitcomb, Richard T., *A Study of the Zero-Lift Drag-Rise Characteristics of Wing-Body Combinations Near the Speed of Sound*, NACA Rep. 1273, 1956 (supersedes NACA RM L52H08).

[26] Spreiter, John R., *On the Range of Applicability of the Transonic Area Rule*, NACA TN 3673, 1956.

[27] Berndt, Sune B., *On the Drag of Slender Bodies at Mach Number One*, Zeitschrift für angewandte Mathematik und Mechanik, Bd. 35, Heft 9/10, p. 362, Sept./Oct., 1955.

[28] Berndt, Sune B., *On the Drag of Slender Bodies at Sonic Speed*, FFA Rep. 70, Aero. Res. Inst. of Sweden, 1956.

[29] Cole, Julian D., *Drag of Finite Wedge at High Subsonic Speeds*, J. Math. & Phys., Vol. 30, No. 2, pp. 79–93, July, 1951.

[30] Yoshihara, Hideo, *On the Flow Over a Finite Wedge in the Lower Transonic Region*, WADC Tech. Rep. 56-268, June, 1956.

[31] Guderley, Gottfried, and Yoshihara, Hideo, *The Flow Over a Wedge Profile at Mach Number 1*, Journal of the Aeronautical Sciences, Vol. 17, No. 11, pp. 723–735, November, 1950.

[32] Vincenti, Walter G., and Wagoner, Cleo B., *Transonic Flow Past a Wedge Profile With Detached Bow Wave*, NACA Rep. 1095, 1952 (supersedes NACA TN 2339 and 2588).

[33] Spreiter, John R., *Theoretical and Experimental Analysis of Transonic Flow Fields*, NACA—University Conference on Aerodynamics, Construction, and Propulsion, Vol. II, "Aerodynamics," a compilation of the papers presented, Lewis Flight Propulsion Laboratory, Cleveland, Ohio, October, 20–22, 1954.

[34] Imai, Isao, *Note on the Drag of a Finite Wedge at Mach Number 1*, Journal of the Aeronautical Sciences, Vol. 19, No. 7, pp. 496–497, July, 1952.

[35] Helliwell, J. B., and Mackie, A. G., *Two-Dimensional Subsonic and Sonic Flow Past Thin Bodies*, J. Fluid Mech., Vol. 3, Pt. 1, pp. 93–109, October, 1957.

[36] Kusukawa, Ken-Ichi, *On the Two-Dimensional Compressible Flow Over a Thin Symmetric Obstacle With Sharp Shoulders Placed in an Unbounded Fluid and in a Choked Wind Tunnel*, J. Phys. Soc. Japan, Vol. 12, No. 9, pp. 1031–1041, September, 1957.

[37] Imai, Isao, *Approximation Methods in Compressible Fluid Dynamics*, Technical Note BN-95 of the Institute for Fluid Dynamics and Applied Mathematics, University of Maryland, 1957.

[38] Sakurai, Takeo, *The Flow Past a Flat Plate Accompanied with an Unsymmetric Dead Air at Mach Number 1*, J. Phys. Soc. Japan, Vol. 11, No. 6, pp. 710–715, June, 1956.

[39] Helliwell, J. B., *Two-Dimensional Flow at High Subsonic Speeds Past Wedges in Channels with Parallel Walls*, J. Fluid Mech., Vol. 3, Pt. 4, pp. 385–403, January, 1958.

[40] Helliwell, J. B., *An Application of the Weber-Orr Transform to the Problem of Transonic Flow Past a Finite Wedge in a Channel*, Proc. Cambridge Phil. Soc., Vol. 54, Pt. 3, pp. 391–395, July, 1958.

[41] Sears, W. R., (Ed.), "High Speed Aerodynamics and Jet Propulsion," Vol. VI, Lighthill, M. J., *Higher Approximations*, (Section E of "General Theory of High Speed Aerodynamics"), Princeton Univ. Press, 1954.

[42] Van Dyke, Milton D., *Second-Order Subsonic Airfoil Theory Including Edge Effects*, NACA Rep. 1274, 1956.

[43] Van Dyke, Milton D., *Second-Order Slender-Body Theory—Axisymmetric Flow*, NACA TN 4281, 1958.

[44] Asaka, Saburô, *Application of the Thin-Wing-Expansion Method to the Flow of a Compressible Fluid Past a Symmetrical Circular-Arc Aerofoil*, J. Phys. Soc. Japan, Vol. 10, No. 6, June, 1955, pp. 482–492; Errata, *Ibid.*, Vol. 10, No. 7, p. 593, July, 1955, and Vol. 13, No. 1, p. 115, January, 1958.

[45] Spreiter, John R., and Alksne, Alberta Y., *Thin Airfoil Theory Based on Approximate Solution of the Transonic Flow Equation*, NACA Rep. 1359, 1958 (supersedes NACA TN 3970).

[46] Spreiter, John R., Alksne, Alberta Y., and Hyett, B. Jeanne, *Theoretical Pressure Distributions for Several Related Nonlifting Airfoils at High Subsonic Speeds*, NACA TN 4148, 1958.

[47] Oswatitsch, K., *Die Geschwindigkeitsverteilung bei lokalen Überschallgebieten an flachen Profilen*, ZAMM, Bd. 30, Nr. 1/2, pp. 17–24, Jan./Feb., 1950.

[48] Oswatitsch, K., *Die Geschwindigkeitsverteilung an symmetrischen Profilen beim Auftreten lokaler Überschallgebiete*, Acta Physica Austriaca, Bd. 4, Nr. 2/3, pp. 228–271, December, 1950.

[49] Emmons, Howard W., *Flow of a Compressible Fluid Past a Symmetrical Airfoil in a Wind Tunnel and in Free Air*, NACA TN 1746, 1948.

[50] Zierep, Jürgen, *Der senkrechte Verdichtungsstoss am gekrümmten Profil*, ZAMP, vol. IXb, Fasc. 5/6 Sonderband, pp. 764–776, 1958.

[51] Ackeret, J., Feldmann, F., and Rott, N., *Untersuchungen an Verdichtungsstossen und Grenzschichten in schnell bewegten Gasen*, Mitteilungen aus dem Institut für Aerodynamik, Zurich, Nr. 10, 1946 (also available as NACA TM 1113, 1947).

[52] Wood, George P., and Gooderum, Paul B., *Investigation With an Interferometer of the Flow Around a Circular-Arc Airfoil at Mach Numbers Between 0.6 and 0.9*, NACA TN 2801, 1952.

[53] Harrin, Eziaslav N., *A Flight Investigation of the Effect of Shape and Thickness of the Boundary Layer on the Pressure Distribution in the Presence of Shock*, NACA TN 2765, 1952.

[54] Spreiter, John R., and Alksne, Alberta Y., *Aerodynamics of Wings and Bodies at Mach Number One*, Proceedings of the ASME Third U. S. National Congress of Applied Mechanics, 1958.

(*Continued on page 517*)

An Experimental Study of the Flow Field About Swept and Delta Wings With Sharp Leading Edges†

IVAN JASZLICS* AND LEON TRILLING**

Massachusetts Institute of Technology

SUMMARY

A series of experiments was performed to define the flow field on the upper surface of high aspect ratio swept wings and narrow delta wings at high angles of attack.

It was found that near the root section of either type of wing the flow is conical. The edge of the vortex sheet which originates at the leading edge is a straight line whose position relative to the leading edge depends only on incidence. On swept wings, the vortex edge turns downstream as soon as the vortex sheet covers the front half of the wing chord, and the flow under the vortex sheet outboard of that turning point is uniform and parallel to the leading edge of the wing. On narrow delta wings, the conical symmetry persists almost to the trailing edge.

SYMBOLS

V_∞	=	free-stream velocity—i.e., nominal wind velocity in wind-tunnel test section
V	=	local velocity
α	=	angle of attack
Λ	=	sweep angle
x, y, z	=	Cartesian coordinates in chord lengths (see Fig. 5)
ξ	=	chordwise coordinate, fraction of local chord (see Fig. 6)
ζ	=	distance from wing surface, measured parallel to the z axis (see Fig. 7)
ψ	=	deviation of local flow direction from x axis, in xy plane (see Fig. 7)
p_∞	=	free-stream static pressure
p	=	local static pressure
ρ	=	density of air
C_p	=	$C_p = p - p_\infty/(1/2)\rho V_\infty^2$ static pressure coefficient
Γ	=	circulation, vortex strength

(1) INTRODUCTION—FLOW PAST STALLED SWEPT AND DELTA WINGS

DURING the middle 1940's, it became generally recognized that transonic drag rise on aircraft wings is appreciably delayed if the leading edge of the wing is swept back so that the velocity component normal to it is below the critical value. Likewise, in the lower supersonic regime, if the lifting surface is kept inside the Mach cone through its foremost point, leading-edge shocks are avoided and wave drag is reduced. Since the drag of high-speed airfoils is proportional to the square of thickness, there is also a premium on thin airfoils, often with very small leading edge radius of curvature. In fact, thin swept wings or thin delta wings are characteristic of most high-performance aircraft designed after 1947 in the United States and abroad.

But while this class of lifting surfaces has excellent high-speed performance, its low-speed behavior poses serious problems. In order to carry its load at low speed, the modern wing must be flown at high incidence, and its stall characteristics are poor for two reasons.

A thin sharp-nosed airfoil has a strong suction peak at the leading edge, and the boundary layer is prone to separate there and to form a bubble; sometimes the flow reattaches so that only a minor problem is caused, but, in most cases, the leading edge separation denotes the onset of stall for the entire section.

The problem is complicated by the effects of sweepback which, in the presence of a spanwise pressure gradient, appears to suck the slow air in the inner core of the boundary layer toward the wing root near the leading edge and toward the tip further downstream. There is, consequently, a flow pattern with a strong vortex forming near the apex of the wing (the intersection of leading edge with the root chord); this vortex separates and is eventually swept downstream where it may seriously interfere with the flow over the control surfaces. At the same time, slow air accumulates near the wing tips, and they lose their effectiveness as lifting and control surfaces.

Since the problem appears to lie in the cross flow in the core of the boundary layer, designers have attempted to solve it by preventing this cross flow, or, at least, controlling it by means of fences, vortex generators, indentations of the leading edge, conical camber sections, and other devices which inhibit the development of extended backflow or cause the vortices to be shed at controlled fixed points along the span.

But these "fixes" do not remove the problem, and since transonic aircraft are likely to live with it, it is useful to seek a better understanding of separated flows on the upper surface of swept wings and delta wings. The first analytical study of this problem was due to Legendre[1] who calculated the performance of a delta wing with separated conical vortex fields. Other calculations which refine Legendre's original work are due to Brown and Michael,[2] Edwards,[3] Mangler and Smith,[4] Nikolski,[5] and others. Most of these theories are worked out for delta wings where conical symmetry

Received May 14, 1958. Revised and received May 2, 1959.

† This research was supported by the USAF, through the Office of Scientific Research of the Air Research and Development Command, Contract No. AF18(600)-1306, and their sponsorship is gratefully acknowledged.

* Student, now employed by the Boeing Airplane Company, Seattle, Wash.

** Associate Professor, Department of Aeronautics and Astronautics.

greatly simplifies the analytical formulation of the problem. Pappas and Kunen[6] have attempted to construct a model for a swept wing whose properties vary slowly in the spanwise direction.

At the same time, a number of experimental studies of this phenomenon have been performed. On the one hand, by means of lampblack or china clay coatings on the surface of a wing, one obtains the direction of the flow within the inner core of the boundary layer, as Emslie, Hosking, and Marshall,[7] Ornberg,[8] Black,[9] and Drougge[10] have done; another approach is to find the vortex by tuft grid, vortometer, or vapor screen visualization techniques; it was followed by Brown and Michael,[2] Drougge,[10] Ornberg,[8] Kuethe,[11] Fink,[12, 13] Hopkins and Sorensen,[14] Küchemann,[15, 16] and others. When the vortex path is located, its behavior is analyzed by detailed local pressure surveys by Ornberg[8] and Drougge.[10]

It turns out that the agreement between measured and computed vortex paths is not close. Observation of lampblack traces and vapor screen photographs suggests that this may be due to the fact that the analytical model of a single vortex connected to the leading edge by a vortex sheet is too simple; there appear to be several interacting vortices whose rate of growth is not easily evaluated.

The investigations reported here have two main objectives. First, it was desired to obtain systematic, complete data on the stalled flow past a swept wing at low speed; while measurements on delta wings are numerous and generally quite consistent, no extensive data on swept wings appear to be available. Detailed pressure and velocity surveys were therefore taken at several sweep angles and angles of attack on a very high aspect ratio wing with sharp leading and trailing edges. In this manner, leading edge curvature and aspect ratio effects are minimized, and attention is focused on angles of sweep and attack and Reynolds Number as the basic parameters.

The data were then correlated with other available data, and a simple model of the flow was constructed which may be helpful in understanding the behavior of swept wings. It was not found possible to explain analytically all the features of the model or to construct a satisfactory theory for the flow.

The main findings were that the flow is conveniently divided into two main zones. Near the root chord, the flow behaves essentially as it does on a delta wing; the vortex lies along a ray presumably because the main mechanism at work is the generation of vorticity at the leading edge, which proceeds at a uniform rate. As the vortex approaches the trailing edge, the effect of the Kutta condition there makes itself felt and the vortex veers downstream in a direction parallel to the main flow. The position of the turn of the vortex is a function of angle of attack. The flow outboard of the main vortex consists of a uniform vortex sheet through the leading edge with nearly undisturbed flow above it and uniform flow parallel to the leading edge under it. As long as the boundary layer is turbulent, there appears to be no important Reynolds Number effect.

(2) Description of the Experimental Equipment

The Wind Tunnel

The measurements presented here were carried out in the 4.5 ft. by 6 ft. low-speed wind tunnel of the Massachusetts Institute of Technology. The tests were run at several different wind velocities to determine a possible effect of the Reynolds Number.

The Experimental Wings

Two experimental sweptback wings (designated as Wing No. 1 and Wing No. 2) and a sharp-edged delta wind (Wing No. 3) were used in the tests. The swept wings were made of 1/4-in. steel plate with sharp leading and trailing edges. The chord of Wing No. 1 was 8 in. perpendicular to the trailing and leading edges, with a span of 70 in. at 0° angle of sweep. Wing No. 2 had the same span, with a chord of 4 in. The delta wing had an aspect ratio of 0.93 (77° leading edge sweep), with a root chord of 22 in. (see Fig. 1.)

Probes

Two modified "three-dimensional" cobra head probes were used to obtain the speed and direction of the flow at numerous points above the wings. One had five degrees of freedom, the other had four degrees of freedom (see Figs. 2 and 3).

The total pressures at the four openings of the probes were measured on four separate manometers, and the direction of the velocity vector was obtained from an experimental calibration curve. The local static pressures were determined by a static pressure head mounted with five degrees of freedom.

To determine the vortex paths over Wing No. 1 at two different sweep angles and two angles of attack, a vortometer similar to the one recently described by Hopkins and Sorensen[14] was used (see Fig. 2). The vortometer was constructed almost entirely of brass for ease in working. The mounting and probe arms were both 1/4 in. diameter stock and the latter was tapered for purposes of streamlining. The cylindrical propeller was 1/2 in. long by 1/16 in. diameter. Ordinary beads were used as thrust bearings.

Probe Mounting

The probe mounting consisted of two carriages free to move in the stream direction and normal to it; the upper one was clamped to two rails on the roof of the tunnel and the lower one carried a rotating head which also permitted vertical motion (see Fig. 3). The cobra head with five degrees of freedom had a variable pitch angle.

Limitations

The probable error in the location of points of measurement was about ± 0.01 chord length along the longitudinal and lateral axes, about ± 0.0025 chord length along the vertical axis. The maximum pitch angles of the cobra head with five degrees of freedom

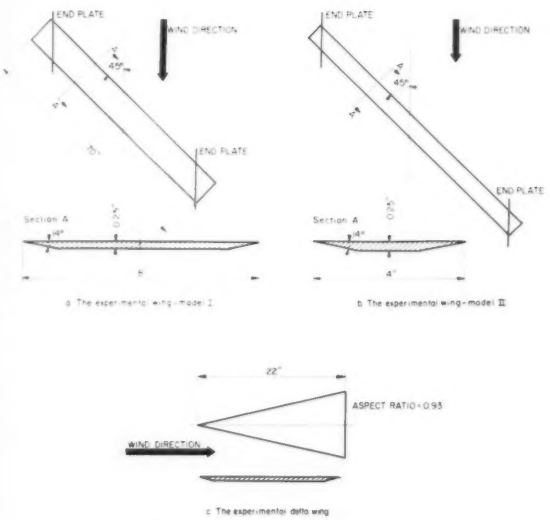

FIG. 1. Sketch of models.

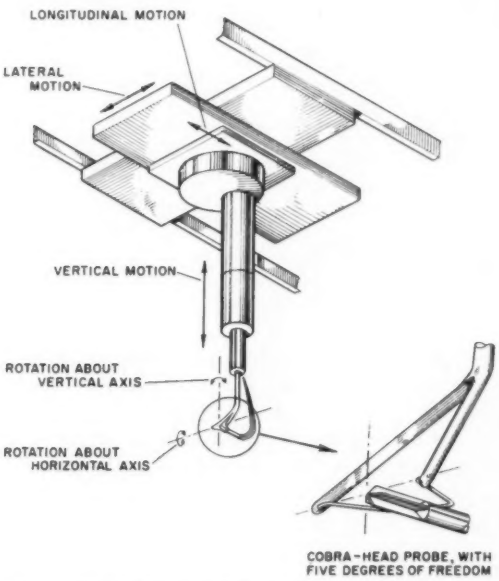

FIG. 3. Probe mounting with five degrees of freedom.

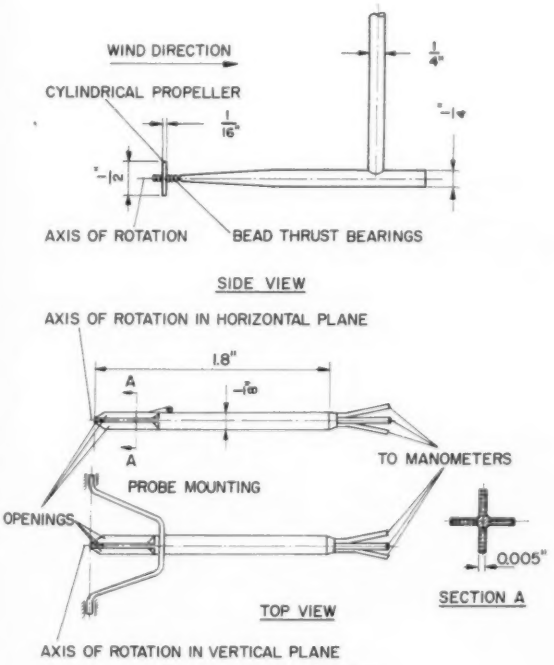

FIG. 2. Sketch of probes.

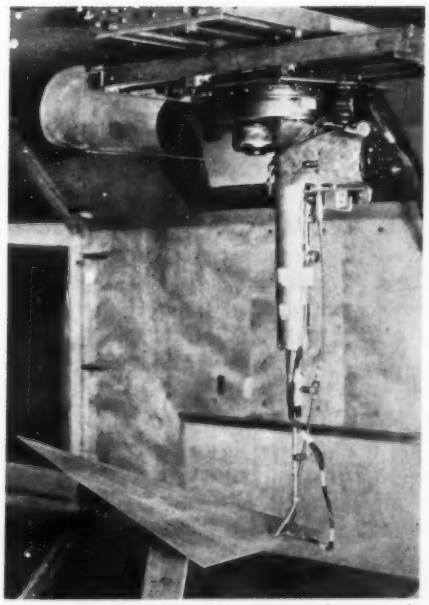

FIG. 4. View of the delta wing and probe mounting.

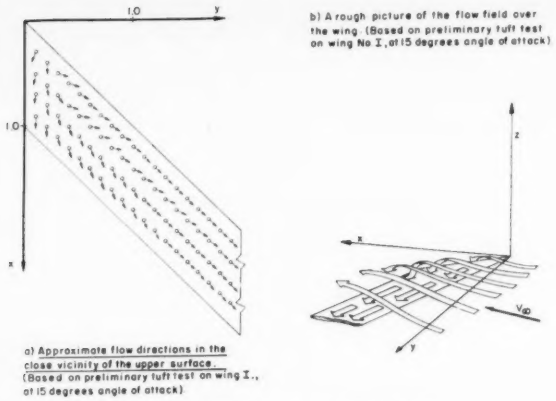
1.0
y
1.0
x
b) A rough picture of the flow field over the wing. (Based on preliminary tuft test on wing No. I, at 15 degrees angle of attack)
z
x
y
V_∞
a) Approximate flow directions in the close vicinity of the upper surface. (Based on preliminary tuft test on wing I., at 15 degrees angle of attack)

FIG. 5. Flow pattern on swept wing.

were $+20°$ and $-32°$ from the horizontal, because of the geometry of the probe mounting. The maximum measurable yaw angle was $\pm 85°$ from the wind direction—actually, well over the measured values.

In certain regions, where very turbulent stream conditions existed, no velocity measurements could be obtained. In these regions, the vortex path was determined only by pressure and vortometer measurements.

Installation

The wings were rigidly mounted on the turntable of the wind tunnel at different angles of attack and sweep. The swept wings were provided with end plates. Originally, their purpose was to seek more nearly two-dimensional flow past a high aspect ratio swept wing. Such a flow could not be obtained but the end plates were retained to simulate the presence of a fuselage near the root chord.

Fig. 4 shows the delta wing, with the cobra head probe with five degrees of freedom.

(3) Measurements on the Swept Wings

Preliminary Survey at 15° Angle of Attack and 45° Sweep Angle

A preliminary test was made to investigate the local directions of flow in the region over Wing No. 1. Cotton tufts were glued to the upper surface of the wing, and a rough picture of flow directions was obtained near the surface. Also, a tuft-sonde was used for a first investigation of the flow direction above the surface up to the region of undisturbed flow. This test showed the existence of a vortex sheet separated from the leading edge and a spanwise flow under this vortex sheet.

Going downstream, the vortex sheet seemed to spread out rapidly. The inboard part of the vortex sheet was bound by a free vortex. Between the wing root chord and the vortex the flow direction did not differ much from V_∞ (Fig. 5).

Velocity Measurements at 15° Angle of Attack and 45° Sweep Angle

Velocity measurements were made at different spanwise stations of Wing No. 1, at an air speed of 130 ft./sec. ($Re = 7.6 \times 10^6$).

Since the preliminary survey had shown that the vortex path was on the upstream part of the wing, most of the measurements were concentrated there, between $y = 0.09$ and $y = 1.46$. Few measurements were made outboard of the vortex path—there was no need of them because of the negligibly small chordwise and spanwise velocity gradients.

The distribution of points of measurement may be seen in top view on Fig. 6. At every point, the measurements were made at several different values of z (distance above the wing surface). The velocities were determined by their directions and by their absolute magnitude.

Velocity profiles are plotted on Fig. 7. Near the vortex, the flow under the vortex sheet is turned more than $45°$ from V_∞. As one travels outward under the vortex sheet, the effect of the vortex core becomes smaller, and far enough from the vortex line the flow is approximately uniform and has a spanwise direction.

To determine the vortex path, two velocity components (v and w) and the absolute value of the dimensionless velocity (V/V_∞) were plotted along various chords. It was assumed and later verified by detailed measurements that the vortex core is parallel to the xy plane. Then the w component of velocity must have a local zero along the vortex line; the other two components and the absolute value of the velocity must have a local maximum (or minimum) along that line. No velocity measurements were made between $y = 1.16$ and 1.46 because of the strong turbulence there.

The vertical position of the vortex was determined by plotting the absolute values of velocity components parallel to the xz plane (q_{xz}) at different chordwise positions. The point of maximum velocity determined the vortex center at each chordwise section. Fig. 8 shows

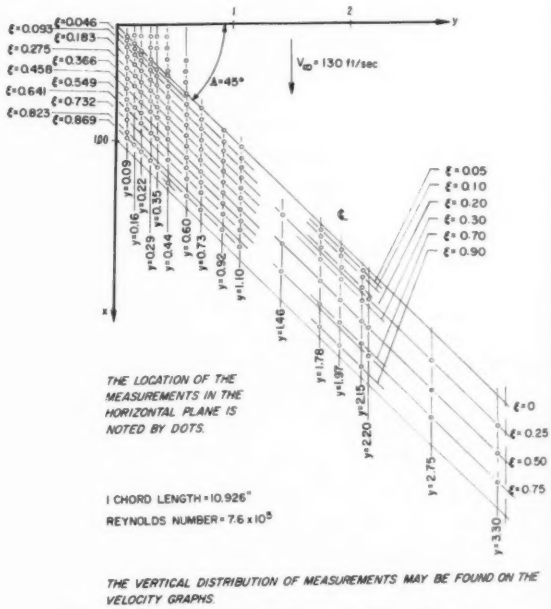

FIG. 6. Locations of velocity over Wing No. 1 at $V_\infty = 130$ ft./sec. $\alpha = 15°$.

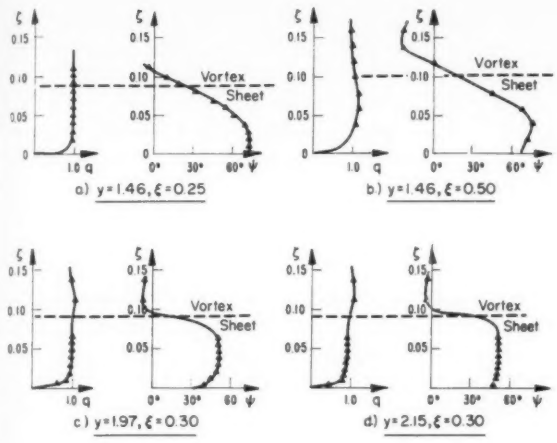

FIG. 7. Dimensionless velocity profiles across vortex sheet Wing No. 1, $\alpha = 15°$, $\Lambda = 45°$, $Re = 7.6 \times 10^6$.

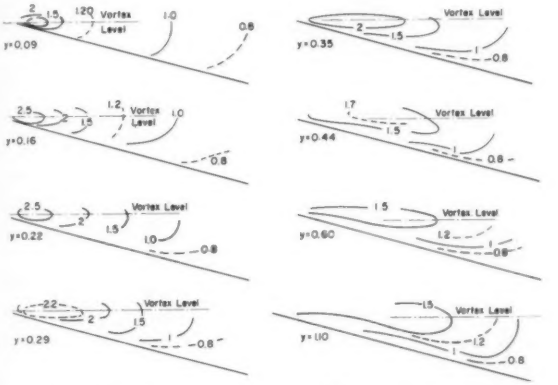

FIG. 8(a). Velocity components parallel to xz plane at different chordwise sections Wing No. 1, $\alpha = 15°$, $\Lambda = 45°$, $Re = 7.6 \times 10^6$.

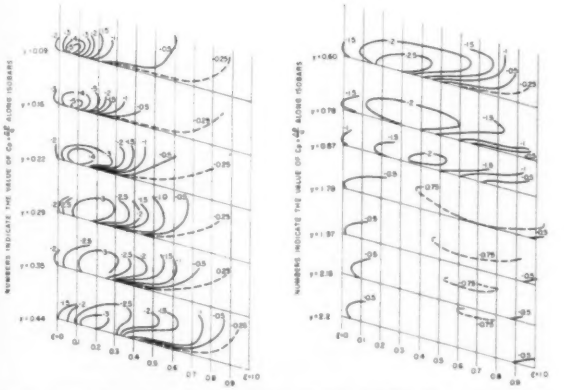

FIG. 8(b). Pressure distribution above Wing No. 1 at 15° angle of attack.

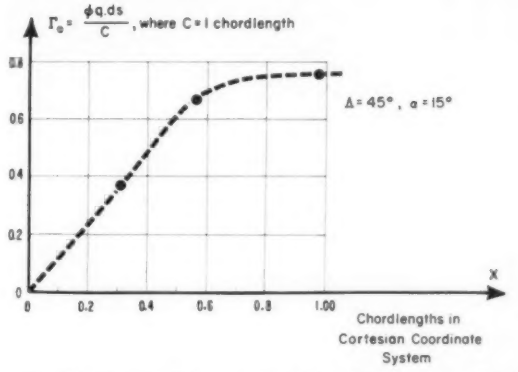

FIG. 9. Vortex strength as a function of the x coordinate.

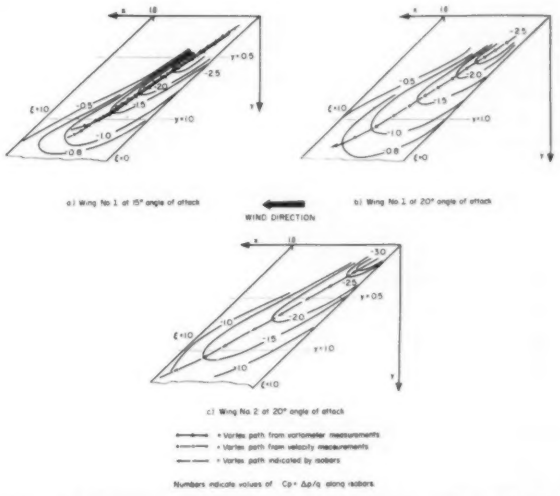
WIND DIRECTION
Vortex path from vortometer measurements
Vortex path from velocity measurements
Vortex path indicated by isobars

FIG. 10. Pressure distribution on the upper surface of the swept wing.

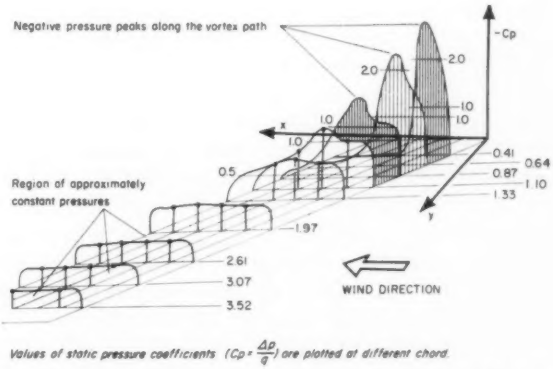
Negative pressure peaks along the vortex path
-Cp
Region of approximately constant pressures
WIND DIRECTION
Values of static pressure coefficients (Cp = Δp/q) are plotted at different chord.

FIG. 11. Static pressure distribution on the upper surface of Wing No. 1 at 15° angle of attack.

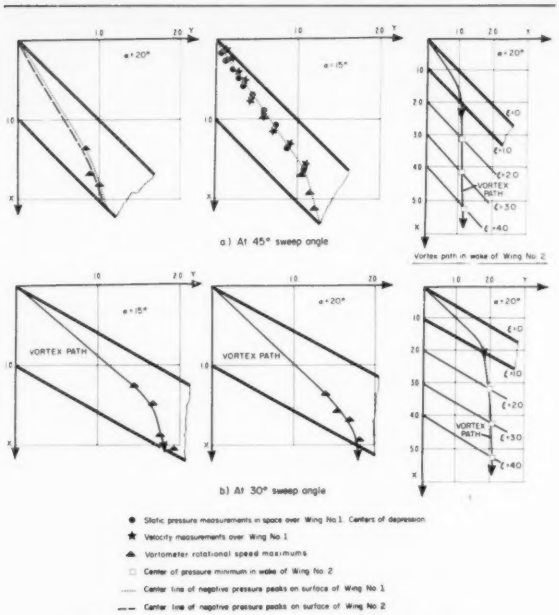
a) At 45° sweep angle
Vortex path in wake of Wing No. 2
VORTEX PATH
b) At 30° sweep angle
Static pressure measurements in space over Wing No.1. Centers of depression
Velocity measurements over Wing No.1
Vortometer rotational speed maximums
Center of pressure minimum in wake of Wing No. 2
Center line of negative pressure peaks on surface of Wing No.1
Center line of negative pressure peaks on surface of Wing No.2

FIG. 12. Vortex path over experimental wing.

the curves of q_{xz} = constant at eight different chordwise sections.

The vortex strength and the circulation $\Gamma/V_\infty c$ was determined by contour integration of the velocities in three different chordwise planes. The path of integration was a triangle, determined in each chordwise plane by the points ($\xi = 0$, $z = +0.029$); ($\xi = 0.87$; $z = +0.029$); and ($\xi = 0.87$; $z = -2.1$). The vortex strength as the function of coordinate x is plotted on Fig. 9.

Static Pressure Measurement on Wing No. 1 and Wing No. 2

The static pressure distribution was measured on the upper surfaces of Wing No. 1 and Wing No. 2, at 15° and 20° angle of attack and 45° of sweep. Wing velocities were 59 ft./sec., 95 ft./sec., and 130 ft./sec. Thus, the value of Reynolds Number varied between $Re = 1.7 \times 10^5$ and $Re = 7.6 \times 10^5$. Practically no effect of Reynolds Number was found on the pressure distributions, except for points very close to the trailing edge. Even there the effect was small.

Fig. 10 shows the distribution of pressure coefficients on the surfaces of Wing No. 1 and No. 2, and Fig. 11 gives a picture of the C_p distribution on Wing No. 1 at 15° angle of attack.

Comparison of the isobar graphs with the vortex lines determined by velocity or vortometer measurements shows that the line of minimum pressures coincides with the vortex path, and the vortex path can be determined simply by pressure measurements (Fig. 12).

Static Pressure Measurements in Space Over Wing No. 1

The static pressure field was measured over Wing No. 1 at 15° angle of attack, 45° sweep angle, and 130 ft./sec. wind velocity ($Re = 7.6 \times 10^5$).

The isobars are plotted at various chordwise sections on Fig. 8(b). It is seen that the line of minimum pressures coincides with the vortex path.

The field of static pressures is almost uniform outboard of the vortex path, except near the vortex sheet where the pressures are lower than in the surrounding space. Wake pressure distributions and vortometer measurements are also reported in reference 17.

Determination of Vortex Path

The vortex path determined from the measurements described above is plotted on Fig. 12. The experimental results from different methods coincide quite well, indicating that each of the methods is adequate to determine the vortex path. It is proposed to use static pressure measurements on the surface as the simplest method, unless velocity measurements are needed.

The whole surface may be divided into three regions of different properties:

(a) The section between the vortex line and the root chord, where there is only a slight difference between the local and free-stream pressures (characteristic C_p values: $C_p \sim -0.05$; $C_p \sim -0.15$).

(b) The domain along the vortex, having high negative C_p values.

(c) Region of approximately uniform spanwise flow under the vortex sheet having a nearly constant low negative pressure coefficient, slightly varying with the angle of attack (characteristic C_p values: $C_p \sim -0.3$; $C_p \sim -0.6$).

(4) TESTS ON THE DELTA WING

Velocity surveys were made in the cross planes $x = 0.36$, $x = 0.73$, and $x = 0.91$ at angles of attack of 6° and 12°. A yaw-sensitive cobra head of four degrees of freedom was used to obtain the flow directions and dynamic pressures in the vicinity of the surface. Far from the surface where the flow direction is not parallel to the plane of the surface, a "three-dimensional" cobra head was used with five degrees of freedom (see Fig. 6).

The velocity profiles obtained from these measurements and resulting contours are given in reference 17. The position of the vortex core was determined by the

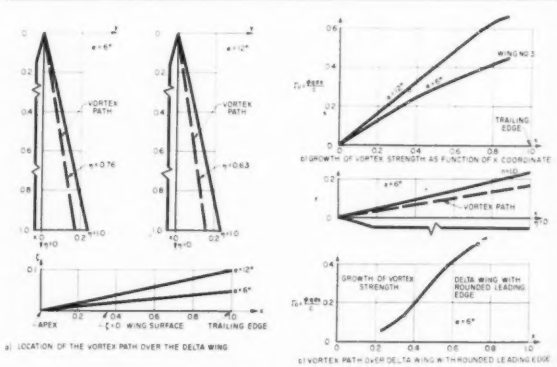

FIG. 13 Cross flow over the delta wing.

intersection of zero downwash and zero sidewash lines. The vortex path over the wing is shown on Fig. 13.

Growth of vorticity downstream of the wing apex was estimated by integrating velocities around the vortex center in various cross planes. The path of integration consisted of:

(1) A line segment through the (upper) inflow peak parallel to the y axis.

(2) A line segment through the (lower) outflow peak parallel to the y axis.

(3) A line segment in the plane of symmetry, intersecting (1) and (2).

(4) A line segment parallel to (3), intercepted by lines (1) and (2).

The velocities along lines (1) and (2) were known from reference 17 and those on lines (3) and (4), comparatively small, of similar magnitude and of such direction as to cancel one another during the integration, were neglected. Fig. 13 also shows the circulation measured around the vortex path, as a function of the x coordinate.

Some additional measurements were made on another delta wing with rounded leading edges and same size and planform. The airfoil section of that wing was an NACA 16-003 profile. For comparison, Fig. 13 also shows the vortex path and growth of vorticity over that wing.

(5) Location of Vortex Path Over Swept and Delta Wings With Leading Edge Separation

The preceding sections have described detailed measurements of the flow on the upper surface of swept and delta wings at high incidence. The results of these measurements and of similar measurements by other investigators (Ornberg, Drougge, Michael and Brown, Fink, etc.) suggest certain generalizations about this class of flows.

The first important question which arises with both delta wings and swept wings is to determine the location and strength of the vortex sheet in the neighborhood of the root chord region and its effect on the local pressure distribution.

The second question, which is especially important in the case of long swept wings, is to define the conditions under which the edge of the vortex sheet turns from a

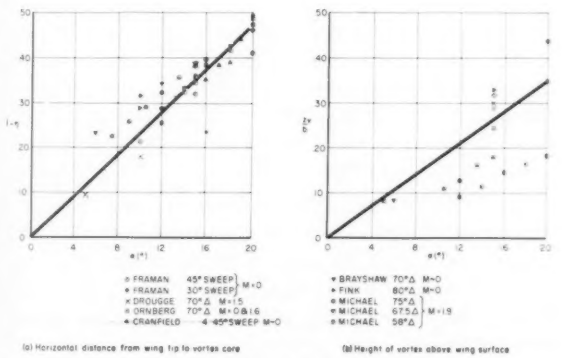

Fig. 14. Location of vortex core.

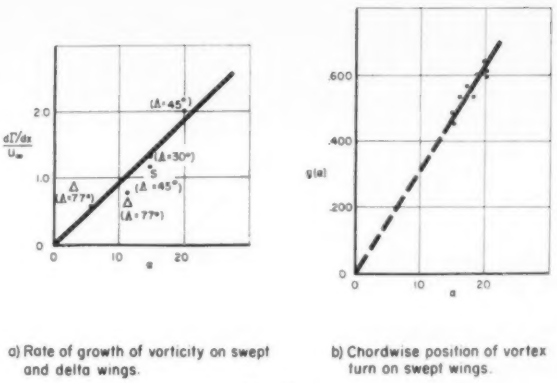

a) Rate of growth of vorticity on swept and delta wings.

b) Chordwise position of vortex turn on swept wings.

Fig. 15.

ray through the wing apex to a line parallel to the mean flow.

As long as the flow is essentially conical, one observes that vorticity is generated at a constant rate so that the strength of the edge vortex increases linearly with distance from the apex (see Fig. 9 for the swept wing and Fig. 13 for the delta wing), and the rate of vorticity production $d\Gamma/dx$ is apparently a linear function of angle of attack [(a) in Fig. 15]; it is independent of Reynolds Number as long as the leading edge is sharp (in this respect, conditions are similar to the Kutta condition generally obtained at a trailing edge); it is independent of Mach Number as long as the leading edge is well behind the Mach cone—it is apparently independent of trailing edge geometry.

The horizontal projection of the position of the vortex edge appears to be a function only of angle of attack. Fig. 14 shows the percentage of span which measures the distance from wing edge to vortex edge for a number of wings, both delta and swept, whose sweep angle varies from 30° to 80°; the measurements were taken by a variety of methods in a number of wind tunnels at Mach Numbers from zero to 1.9. All the data fit fairly well on a straight line of equation $1 - \eta = 1.3\alpha$.

The vertical position of the vortex edge is more difficult to measure accurately. It is apparent from Fig. 8 that the vortex edge very nearly trails off in a straight line level with the wing apex; this appears confirmed (except in Michael's supersonic experiments with very thin deltas) by the visual reports of other observers [(b) in Fig. 14].

The effect of the vortex on the chordwise pressure distribution is shown on Fig. 11. As the vortex strength increases—and this effect is obtained either by increasing the angle of attack at a fixed spanwise position, or, as was done here, by moving outboard at a constant angle of attack—the leading edge suction peak disappears, the lift contribution of the upper wing surface decreases, and its center of pressure moves back.

In general, the examination of the flow field in the conical flow region indicates that the general features of the models suggested by Legendre, Brown and Michael, Mangler and Smith, et al., are qualitatively correct but do not predict the vortex path with suffi-

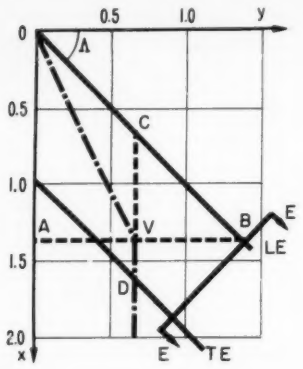

Swept Wings

FIG. 16.

cient accuracy. Some empirical correlations were obtained from experiments in this report which should be analyzed in terms of a more precise discussion of the mechanism of flow separation near the leading edge; in particular, some observers find a group of several vortices and the structure of the sheet is not yet clearly understood.

While an examination of the data gives a good picture of the conical portion of the flow field, another important parameter in defining the flow past swept wings is the spanwise position at which the vortex sheet edge turns downstream. The data show that it is independent of Reynolds Number, and depends primarily on the sweep angle and the angle of attack.

A simple model of the geometry of the situation is shown on Fig. 16. From the apex 0 to V, the vortex trace follows a line whose equation is of the form

$$1 - \eta = BV/BA = f(\alpha)$$

where $f(\alpha)$ is given on Fig. 14. In addition, it is likely that the vortex edge turns downstream when it has reached a certain chordwise position which depends on the angle of attack

$$CV/CD = (CV/c)\cos\Lambda = g(\alpha)$$

where c is the chord-length measured normal to the leading edge. A simple consideration of the geometry of Fig. 16 then gives

$$AV = c(1 - f)g/f \sin\Lambda$$

This result separates the effect of sweep from the effect of incidence in analyzing the location of the turnoff point.

To verify the above speculation and to estimate the function $g(\alpha)$, all the available data on swept wings (nine measurements at sweeps of 30° and 45°, and incidences of 15° to 20°) were used to compute $g(\alpha)$, under the assumption that $f(\alpha)$ is given by Fig. 14. While the range and volume of the data are not sufficient to draw reliable conclusions, (b) in Fig. 15 shows that the data are at least consistent, and $g(\alpha)$ seems to be a nearly linear function. Now, it is plausible that $g(\alpha)$ should increase with angle of attack; at low incidence, one observes a small bubble near the leading edge, and $g(\alpha)$ is close to zero. As α grows, the bubble grows and $g(\alpha)$ increases. A detailed calculation of the velocities induced at the leading edge by the sheet OV and the vortex OV is quite difficult and has not been attempted.

The flow in the separating region outboard of the swept-off vortex, in the case of very high aspect ratio wings of the type considered here, becomes essentially a two-dimensional Kirchoff-Helmholtz wake; the edges of the wake are the separated vortex sheet and a vortex sheet shed at the wing trailing edge. The energy of the cross flow determines the pressure in the cavity. This model accounts for the uniform pressure measured on the upper wing surface (in the wake) (see Fig. 11, for example). If, as the measurements suggest (see Fig. 7, for example), the velocity in the wake is parallel to the leading edge and equal to the free-stream velocity, the flow normal to the leading edge (in the vertical plane through EE on Fig. 16) is a Helmholtz flow past a flat plate of incidence $\alpha/\cos\Lambda$ at a velocity $V_\infty \cos\Lambda$ where the pressure in the cavity is equal to the free-stream pressure. This problem has been solved by Lord Rayleigh (see, for example, Lamb, *Hydrodynamics*, Chapter 4, p. 103.) The shape of the resulting wake may then be estimated. Actually, turbulent mixing will modify the flow in the wake so that a few chord lengths behind the trailing edge its detailed structure can no longer be recognized.

(6) Concluding Remarks

The present report describes a detailed investigation of the low-speed flow past swept wings and delta wings with sharp leading edges at high incidence. While a theoretical solution of this complex problem was not carried out, a number of useful results were deduced from the measurements.

(1) Vorticity is generated at the leading edge at a rate independent of position along the span, presumably as a result of local flow separation. The amount of vorticity generated per unit length measured in the streamwise direction is a function of angle of attack only, and a nearly linear function; this result holds for both delta and swept wings.

(2) The edge of the resulting vortex sheet forms a ray through the wing apex, which remains in a horizontal plane through the apex. The ratio of the horizontal distance from root chord to vortex edge to the distance from root chord to leading edge is a unique linear function of angle of attack for a wide range of sweep angles and angles of attack.

(3) This conical flow pattern remains valid for narrow delta wings up to the close neighborhood of the trailing edge. In the case of swept wings, when the vortex reaches a chordwise position which is a fixed linear function of angle of attack, the vortex sweeps downstream.

(*Continued on page 544*)

Divergence of Plate Airfoils of Low Aspect Ratio at Supersonic Speeds

G. J. HANCOCK*
University of London

SUMMARY

In Part (I), as a first approach to a theoretical investigation of low aspect ratio rectangular plate wings of constant thickness, the two assumptions are made that: (a) the spanwise form of the structural distortion is known, leaving the chordwise distortion arbitrary; and (b) the aerodynamic forces are approximations of the supersonic linearized theory. The form of the chordwise distortion is then deduced from the differential equation representing the state of neutral equilibrium for small displacements at the critical divergence speed.

Secondly, this problem is investigated using measured structural flexibility coefficients together with theoretical aerodynamic coefficients.

Thirdly, the usual series solution based on the Rayleigh-Ritz approach is discussed, using the same assumptions as in the first method.

All the results of these methods are consistent and indicate that the transonic regime at $M = 1$ is the most critical for divergence.

In Part (II), it is established that sweeping the leading edge of a plate airfoil of constant thickness increases its stability. For angles of sweep less than 30°, the critical conditions occur when the leading edge is sonic, but for angles greater than 30° the critical conditions occur when $M = 1$.

SYMBOLS

a	= speed of sound in the free stream
A_n	= undetermined constants
A_j	= surface area of area j
$b(\xi)$	= integrated loading function
b_n	= undetermined constants
$\{B_{ij}\}$	= general matrix combining aerodynamic and structural influence matrices
c	= chord
D	= $Et^3/12(1 - \nu^2)$
E	= Young's modulus
$f(\xi, \eta)$	= nondimensional distortion of plate
$f_n(\bar{K})$	= functions in the asymptotic solution
$G(\eta)$	= spanwise distortion mode = $(1/26)[45\eta^2 - 20\eta^3 + \eta^6]$
K, K_1, $\bar{K}$	= divergence parameters
l	= semispan
l_j	= loading on area j
M	= Mach Number
$P.E.$	= potential energy
$P(x, y)$	= aerodynamic loading
$p(x, y)$	= defined by $P(x, y) = p(x, y)\ \alpha(x, y)$
$S.E.$	= strain energy
t	= wing thickness
V	= free-stream velocity
(u, v)	= oblique coordinates
$w(x, y)$	= distortion of plate; $w(x, y) = cf(\xi, \eta) = W(\xi) \times G(\eta)$
$W(\xi)$	= chordwise distortion
(x, y, z)	= Cartesian coordinates
(ξ, η)	= $[(x/c), (y/l)]$
α	= incidence
α_i	= incidence of area i
β	= $(M^2 - 1)^{1/2}$
$\{\delta_{ij}\}$, $\{\bar{\delta}_{ij}\}$	= measured structural influence coefficients
γ_1, γ_2, Γ	= divergence parameters
ν	= Poisson's ratio, assumed 0.3
φ	= angle of sweep

Received July 7, 1958. Revised and received October 1, 1958.

* Lecturer, Department of Aeronautical Engineering, Queen Mary College, University of London.

PART (I) RECTANGULAR WINGS

(1) INTRODUCTION

IN THE CONTEMPORARY DESIGN of small high-speed missiles, rocket models and wind tunnel models, it is convenient to use metal plate airfoils of low aspect ratio. Since the structural characteristics of these types of wings are quite different from the conventional built-up aircraft wings, in the respect that chordwise deformation is of fundamental concern for the plate airfoils but only of secondary importance for aircraft wings, it is expected that our ideas of aeroelastic behavior may be considerably modified. In this paper, the simplest form of aeroelastic instability—i.e., divergence—is investigated for plate airfoils of constant thickness at supersonic speeds. This type of instability has been experienced on certain rectangular wings (on missiles) which failed structurally by the rolling up of the leading edge of the wing. Consequently, it has become standard design procedure to sweep the leading edge of such wings in order to eliminate the possibility of this divergence instability.

A concentrated attack on the problem of divergence of general wings at supersonic speeds has been made by Biot in a series of papers, which have been summarized recently.[1] This approach is concerned with the exact solution of some particular cases of divergence—e.g., a two-dimensional wedge in a supersonic stream—together with approximate evaluations of the more difficult practical cases. However, the main assumption is the aerodynamic one that the flow may be regarded as two-dimensional over the whole wing—i.e., that tip effects are negligible—and is only valid for wings of reasonable aspect ratio at reasonable supersonic speeds. This assumption breaks down for the type of problem investigated in this note where the aspect ratio is small and where, as it will be seen, the Mach Number varia-

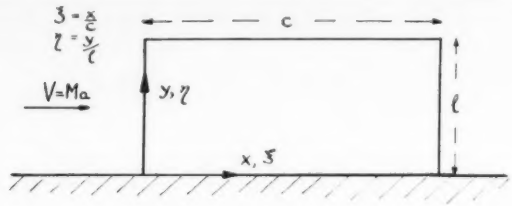

FIG. 1. Coordinate system.

tion is of fundamental importance in the problem of divergence.†

The divergence problem is developed in two main methods. In the first, which is a purely theoretical one, the form of the spanwise distortion is assumed, and the form of the chordwise distortion is calculated from a differential equation, established in the usual manner of minimizing the total energy—i.e., the strain energy of the distorted plate plus the potential energy of the applied aerodynamic forces—in the equilibrium of neutral stability at the critical divergence speed. The second method is semiexperimental in which structural flexibility influence coefficients were measured over a number of areas on a particular rectangular plate and are used together with some theoretical aerodynamic influence coefficients to evaluate its divergence characteristics. This latter method is used as a check on the former theoretical approach. Since neither of the above methods offers any direct extension to problems involving change of thickness distribution over the rectangular plan form, a third method, using the standard Rayleigh-Ritz technique, is briefly discussed.

In all these methods, the aerodynamic forces are based on the linearized equations of supersonic flow but are approximations of the exact linearized solutions for cambered airfoils in order to make any divergence calculations possible. However, with the application of the linearized theory, finite forces are predicted for Mach 1, as suggested by the slender wing theory, so that divergence conditions may be calculated even for $M = 1$. It is known that the assumptions on which the derivations of the linearized equations are based are not valid in the transonic region but are valid at speeds below and above this region. Hence, it may be argued that any results obtained for Mach 1 from this theory may at least indicate the qualitative behavior of the fundamental parameters. This point is relevant to the present paper since it is shown that for rectangular plates divergence is most likely to take place at Mach 1. Stability then increases with Mach Number until, at a certain supersonic speed, the possibility of divergence apparently disappears (see Fig. 6.) The reason for this is that the mode of divergence at Mach 1 is the rolling up of the leading edge, but, as the Mach Number increases, the effective aerodynamic center moves rearward from the leading edge until a Mach Number is reached at which this mode cannot be sustained. Apparently, no other mode of deformation can then produce divergence. Therefore, from a design point of view, conditions at Mach 1 are the critical ones.

The theoretical approach is given in Sections (2–5), the method of measured influence coefficients is discussed in Section (6), and the Rayleigh-Ritz method in Section (7).

(2) Mathematical Approach

This investigation is concerned with the possibility of the structural instability of a thin solid low aspect ratio rectangular wing of constant thickness in a supersonic stream. It is assumed that the wing is rigidly attached at its root to an infinite wall which is parallel to the direction of flow.

Cartesian coordinates of reference are taken with the origin at the root of the leading edge, the x-axis in the direction of flow, the y-axis in the spanwise direction, and the z-axis forming a right-handed set. If the chord is denoted by c, the semispan by l, then nondimensional coordinates are defined as

$$\xi = (x/c),\ \eta = (y/l) \tag{1}$$

The velocity of the main stream is denoted by V, corresponding to a supersonic Mach Number M. This model is shown in Fig. 1.

The plate is set at zero incidence to the air stream. Initial incidence only affects the finite aeroelastic distortion at speeds below the critical divergence speed, the distortion tending mathematically to infinity as the air speed approaches the divergence speed. Divergence is, therefore, regarded as the condition in which the static effects of structural stiffness and aerodynamic loading retain the plate in equilibrium in a certain mode of distortion.

It is assumed that the plate deflection at the critical divergence speed is given by

$$z = w(x, y) = cf(\xi, \eta) \tag{2}$$

The strain energy $S.E.$ of the plate is given by the standard thin plate formula[2]

$$\begin{aligned} S.E. &= (1/2) \iint_{\text{wing}} D(x, y)\{(w_{xx} + w_{yy})^2 + \\ &\qquad 2(1 - \nu)\,(w_{xy}{}^2 - w_{xx}w_{yy})\}\,dx\,dy \\ &= (1/2)D(l/c) \int_0^1 \int_0^1 \{[f_{\xi\xi} + (c^2/l^2)f_{\eta\eta}]^2 + \\ &\qquad 2\,(1 - \nu)(c^2/l^2)(f_{\xi\eta}{}^2 - f_{\xi\xi}f_{\eta\eta})\}\,d\xi d\eta \end{aligned} \tag{3}$$

where $D(x, y) \equiv D = Et^2/12(1 - \nu^2)$,
t = constant plate thickness,
E = Young's modulus, and
ν = Poisson's ratio.

The potential energy $P.E.$ of the applied aerodynamic

† Since this paper was completed, reference 6 has been published. Here divergence of low aspect ratio rectangular plate wings is discussed, using aerodynamic slender wing theory. Mach Number effects are therefore neglected. Comparison of these results with the present paper are included in Section (4) of Part (I).

loading $P(x, y)$ is given

$$P.E. = -\int\int_{\text{wing}} P(x, y)w(x, y)dx\,dy \qquad (4)$$

It is now assumed that the local aerodynamic loading depends only on the local angle of incidence—that is,

$$P(x, y) = -f_\xi p(\xi, \eta) \qquad (5)$$

where the function $p(\xi, \eta)$ is a function of the plate plan form and Mach Number, and is given by the linearized supersonic flow theory for the rigid rectangular wing at a constant incidence. This assumption is most accurate for the region unaffected by the wing tips—that is, the so-called two-dimensional region. However, for the wing tip regions it is not true, but at least it represents qualitatively the effects in this region, since the pressure loading tends to zero at the wing tips and introduces no pressure discontinuities between the two-dimensional and wing tip regions. This is discussed further in Section (3). Hence, Eq. (4) reduces to

$$P.E. = c^2 l \int_0^1 \int_0^1 f f_\xi p(\xi, \eta)d\xi\,d\eta \qquad (6)$$

The final assumption, in order to reduce the problem to an amenable form, is that

$$f(\xi, \eta) = W(\xi)G(\eta) \qquad (7)$$

$$G(\eta) = (1/26)(45\eta^2 - 20\eta^3 + \eta^6) \qquad (8)$$

This assumption may be justified because (a) the chordwise deflection is fundamental in the determination of the aerodynamic loading and the divergence mode, while the spanwise variation is of secondary importance, and (b) experience of divergence indicates that the mode of failure appears as a rolling up of the leading edge, so that $G(\eta)$ should be assumed as accurately as possible for this neighborhood. Therefore, $G(\eta)$ is calculated on the assumption of a parabolic loading on a uniform cantilevered beam, ensuring that it satisfies the correct edge conditions for a reasonable loading distribution. On substitution of Eqs. (7) and (8) in Eq. (3), the strain energy becomes

$$S.E. = (1/2)D(l/c) \times \int_0^1 \{a_0 W''^2 + a_1 WW'' + a_2 W^2 + a_3 W'^2\}d\xi \qquad (9)$$

where
$$a_0 = \int_0^1 G^2(\eta)d\eta = 0.249$$

$$a_1 = 2\nu(c/l)^2 \int_0^1 G(\eta)G''(\eta)d\eta = (c/l)^2\, 0.132$$

$$a_2 = (c/l)^4 \int_0^1 [G''(\eta)]^2 d\eta = (c/l)^4\, 3.077$$

$$a_3 = 2(1-\nu)(c/l)^2 \int_0^1 [G'(\eta)]^2 d\eta = (c/l)^2\, 1.631$$

assuming that $\nu = 0.30$, and where the dashes denote differentiation with respect to ξ. Similarly, on substitution of Eqs. (7) and (8) in Eq. (6), the potential energy becomes

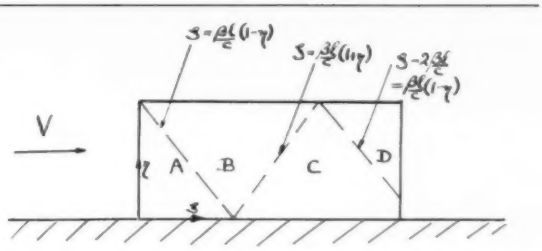

FIG. 2. Areas of pressure loadings.

$$P.E. = \int_0^1 WW'b(\xi)d\xi \qquad (10)$$

where
$$b(\xi) = c^2 l \int_0^1 p(\xi, \eta)[G(\eta)]^2 d\eta \qquad (11)$$

It is now necessary to evaluate the aerodynamic function $b(\xi)$, and this is presented in the following section.

(3) Determination of Aerodynamic Characteristics

The function $p(\xi, \eta)$ is defined in Eq. (5) and is now written down by reference to Fig. 2.

Hence,

(a) over area A, $p(\xi, \eta) = (2\rho a^2 M^2/\beta)$ where $\beta^2 = M^2 - 1$ and a = speed of sound,

(b) over area B, $p(\xi, \eta) = (2\rho a^2 M^2/\beta)\big(1 - (2/\pi) \times \tan^{-1}\{[c\xi/\beta l(1-\eta)] - 1\}^{1/2}\big)$

(c) over area C, $p(\xi, \eta) = (2\rho a^2 M^2/\beta)\big(1 - (2/\pi) \times \tan^{-1}\{[c\xi/\beta l(1-\eta)] - 1\}^{1/2} - (2/\pi)\tan^{-1}\{[c\xi/\beta l(1+\eta)] - 1\}^{1/2}\big)$

while the pressures in regions aft of C are small, being alternatively positive and negative for increasing ξ with decreasing magnitude. Therefore, for $0 \le \xi \le (\beta l/c)$, Eq. (11) becomes

$$b(\xi)/c^2 l = (2\rho a^2 M^2/\beta)\left(\int_0^1 G^2(\eta)d\eta - (2/\pi) \times \int_{1-(c\xi/\beta l)}^1 G^2(\eta)\tan^{-1}\{[c\xi/\beta l(1-\eta)] - 1\}^{1/2} d\eta\right) \qquad (12)$$

Without evaluating Eq. (12), we note the following points.

(a) $b(0)/c^2 l = (2\rho a^2\pi^2/\beta)\int_0^1 G^2(\eta)d\eta = (2\rho a^2 M^2/\beta)\,(0.249)$

(b) $b'(0)/c^2 l = -(2\rho a^2 M^2/\beta)\cdot[G^2(1)/2]\cdot(c/\beta l) = (2\rho a^2 M^2/\beta)[-0.500(c/\beta l)]$

(c) $b(\beta l/c)/c^2 l = (2\rho a^2 M^2/\beta)\cdot(1/\pi) \times \int_0^1 \{H(\eta)d\eta/[\eta(1-\eta)]^{1/2}\} = (2\rho a^2 M^2/\beta)(0.067)$

where $H(\eta) = \int_0^\eta G^2(\eta)d\eta$

It is seen that from the loading in area C

(d) $b(2\beta l/c)/c^2 l = 0$

As stated above, for $\xi \geq (2\beta l/c)$, $b(\xi)$ decreases between positive and negative values.

The approximation is now introduced that $b(\xi)$ may be represented by the equation

$$b(\xi)/c^2l = 0.249\ (2\rho a^2M^2/\beta)\ e^{-2.01(\xi c/\beta l)} \qquad (13)$$

for all ξ. This formula gives the exact values for $b(0)$ and $b'(0)$, together with $b[\beta(l/c)]/c^2l = (2\rho a^2M^2/\beta) \times (0.031)$ and $b[2(\beta l/c)]/c^2l = (2\rho a^2M^2/\beta)\ (0.004)$. Hence, the error in assuming the simple formula of Eq. (13) is small.

(4) Divergence for $M \sim 1$

The condition for divergence is given from the equilibrium condition that the total energy ($S.E. + P.E.$) must be a minimum with respect to the deflection function $W(\xi)$. This has to be considered for the two regions of $M \sim 1$ and $M > 1$ separately, since the theoretical pressure loading becomes infinite in the former case, although the force distribution remains finite.

Now, for $M \sim 1$—i.e., $\beta \sim 0$—Eq. (13) shows that $b(\xi)$ is large near $\xi = 0$ but is very small for $\xi > 0$, hence, Eq. (10) for the potential energy may be written

$$P.E. = (WW')_{\xi=0} \left\{\int_0^1 b(\xi)d\xi\right\}_{\beta\to 0} \qquad (14)$$

The minimization of the energy equation is

$$\delta(S.E. + P.E.) = 0 \qquad (15)$$

where the strain energy is given by Eq. (9) and the potential energy in this case, by Eq. (14). It should be remembered that in the application of this technique to the potential energy the loading is regarded to be invariant, so that in Eq. (14) above

$$\delta(P.E.) = (W'\delta W)_{\xi=0}\ K \qquad (16)$$

where

$$K = \left\{\int_0^1 b(\xi)d\xi\right\}_{\beta\to 0} = 2\rho a^2(0.249/2.01)cl^2 \qquad (17)$$

Hence, from Eqs. (9), (15), and (16), using the calculus of variations

$$a_0W^{IV} + (a_1 - a_3)W'' + a_2W = 0 \qquad (18)$$

where the constant $a_n's$ are defined by Eq. (9); together with the boundary conditions

$$[a_0W'' + (1/2)a_1W]_{\xi=0} = [a_0W'' + (1/2)a_1W]_{\xi=1} = 0,$$
$$\{Dl/c[a_0W''' + (1/2)a_1W' - a_3W'] + KW'\}_{\xi=0} =$$
$$[a_0W''' + (1/2)a_1W' - a_3W']_{\xi=1} = 0 \qquad (19)$$

Introducing the variable

$$\xi_1 = \xi c/l \qquad (20)$$

Eqs. (18) and (19) become

$$W^{IV} - 6.02W'' + 12.36W = 0 \qquad (21)$$

where W is now regarded as a function of ξ_1, and the dashes denote differentiation with respect to this quantity. And

$$[W'' + 0.265W]_{\xi_1=0} = [W'' + 0.265W]_{\xi_1=c/l} = 0,$$
$$[W''' - 6.285W' + K_1W']_{\xi_1=0} =$$
$$[W''' - 6.285W']_{\xi_1=c/l} = 0 \qquad (22)$$

where

$$K_1 = K/0.249D(c/l) = \rho a^2l^3/1.005D \qquad (23)$$

The solution of Eq. (21) is

$$W(\xi_1) = e^{-1.805\xi_1}\ (A_1 \cos 0.502\xi_1 + A_2 \sin 0.502\xi_1) +$$
$$e^{1.805\xi_1}(A_3 \cos 0.502\xi_1 + A_4 \sin 0.502\xi_1) \qquad (24)$$

where the A_n's are arbitrary constants. Since the only loadings in this case are shear forces on the leading edge we expect a decreasing function, so the approximate solution of Eq. (24) for any (c/l) could be obtained by putting $A_3 = A_4 = 0$ and satisfying only the boundary conditions on the leading edge. Substituting in the first equations of Eq. (22) the compatibility requirements, gives

$$K_1 = 10.8 \text{ and } A_2 = 1.8A_1 \qquad (25)$$

Finally, equating Eqs. (23) and (25),

$$D/\rho a^2l^3 = 0.0921$$

Therefore, the condition of stability at Mach 1 is

$$(E/\rho a^2)(t/l)^3 > 1.05 \qquad (26)$$

assuming that $\nu = 0.3$.

The formulas presented above are essentially those for a wing of zero aspect ratio—i.e., (c/l) infinite—but the effects of finite (c/l) are small, for example, for comparison with Eq. (25),

(a) $(c/l) = 1/2 \quad K_1 = 13.5$
(b) $(c/l) = 1 \quad K_1 = 11.7$

Therefore, for low aspect ratio wings $[(c/l) > 1]$, the error is small and conservative for the design criteria of Eq. (26) for transonic speeds.

In reference 6, the divergence of rectangular plate wings is investigated using exact linearized slender wing theory for the aerodynamic forces, and so should be comparable to the results obtained in this paper for $M \sim 1$. The method is essentially the same in both presentations, but, in reference 6, the spanwise distortion function is taken as η^2 compared with the more complicated form $G(\eta) = (1/26)[45\eta^2 - 20\eta^3 + \eta^6]$ used in this paper. A further difference is that the aerodynamic expressions used in this paper do not tend to the exact slender wing theory. According to this exact theory, in addition to the finite shearing force on the leading edge of the wing a pressure distribution exists over the wing depending on the rate of change of incidence in the chordwise direction. This loading aft of the leading edge is neglected in this paper by the initial loading assumptions but is retained in reference 6. The stability criterion obtained in reference 6 is

$$(E/\rho a^2)(t/l^3) > 0.54 \qquad (27)$$

Comparing this equation with Eq. (26), we see that

there is a considerable difference between those two approaches. This difference can arise either from the different structural assumptions or the aerodynamic simplifications. From a purely structural point of view, the assumption of $G(\eta) = \eta^2$ implies a much greater degree of tip constraint than $G(\eta) = (1/26)[45\eta^2 - 20\eta^3 + \eta^6]$ so that a reduction in $E/\rho a^2(t/l)^3$ is expected, but initially one would not expect a large reduction of Eq. (26). However, the author has repeated his analysis, assuming $G(\eta) = \eta^2$, and the equivalent expression to Eq. (26) is

$$(E/\rho a^2)(t/l)^3 > 0.50$$

This now agrees with Eq. (27). Therefore, it seems that the spanwise mode of distortion is most important in the development of this type of divergent instability. However, in view of the subsequent analysis presented in Section (6), using experimentally determined structural characteristics, is seems that the assumption that $G(\eta) = (1/26)[45\eta^2 - 20\eta^3 + \eta^6]$ gives reliable results, relative to the aerodynamic assumptions.

(5) Divergence for $M > 1$

The equations for establishing the conditions of divergence are developed, as in the preceding section, from the energy condition

$$\delta(S.E. + P.E.) = 0 \tag{28}$$

where the $S.E.$ is given by Eq. (9) and the potential energy by Eqs. (10) and (11). Using the calculus of variations, Eq. (28) becomes

$$a_0W^{IV} + (a_1 - a_3)W''' + a_2W + b(\xi)W' = 0 \tag{29}$$

with the boundary conditions

$$\left.\begin{aligned} &[a_0W'' + (1/2)a_1W]_{\xi=0,\,1} = 0 \\ &\{a_0W''' + [(a_1/2) - a_3]W'\}_{\xi=0,\,1} = 0 \end{aligned}\right\} \tag{30}$$

where the a_n's are given by Eq. (9). Substituting the numerical values of the a_n's with the new variable

$$\xi_1 = (c/l)\xi$$

Eq. (29) reduces to

$$W^{IV} - 6.02W'' + 12.36W = -\bar{K}e^{-(2.01/\beta)\xi_1}W' \tag{31}$$

using Eq. (13) for $b(\xi)$. The dashes now denote differentiation with respect to ξ_1 and

$$\bar{K} = (2\rho a^2M^2/\beta)[12(1 - \nu^2)/E(t/l)^3]$$

Similarly, the boundary conditions of Eq. (30) become

$$\left.\begin{aligned} &[W'' + 0.265W]_{\xi_1=0,\,c/l} = 0 \\ &[W''' - 6.285W']_{\xi_1=0,\,c/l} = 0 \end{aligned}\right\} \tag{32}$$

It can be shown that Eqs. (31) and (32) are identical with Eqs. (21) and (22) in the limiting case of $\beta \to 0$, either by solving Eq. (31) by iteration methods, obtaining a series solution for $W(\xi)$, and substituting in the boundary Eqs. (32), or by applying a Laplace transformation technique and reducing Eq. (31) to an integral equation. This latter method is applied in Section (5.2).

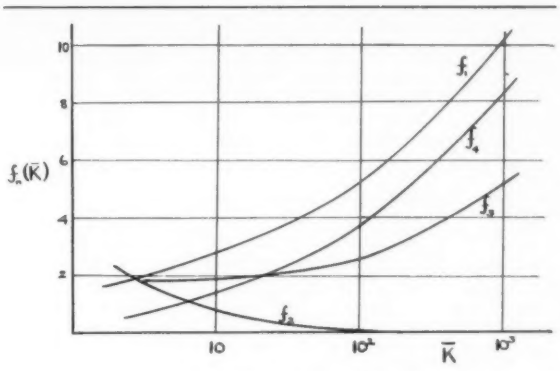

FIG. 3. Functions $f_n(\bar{K})$.

No general analytic solution is obtained by the author for Eq. (31). Therefore, the equation is investigated in two stages. In the first, the solution is investigated for very large β, replacing the term $e^{-(2.01/\beta)\xi_1}$ by unity and reducing the differential equation to one with constant coefficients. This should present the asymptotic criterion at large Mach Numbers The second stage is the investigation of Eq. (31) for low supersonic Mach Numbers of the order $\beta \sim 2$.

(5.1) Asymptotic Solution for Large M

For large Mach Number, Eq. (31) reduces to

$$W^{IV} - 6.02W'' + \bar{K}W' + 12.36W = 0 \tag{33}$$

where $\bar{K}$ is independent of ξ_1. Aerodynamically, the replacement of $e^{-(2.01/\beta)\xi_1}$ by unity means that the loading on the whole wing is represented by the two-dimensional region, assuming the wing tips have no effect. Now, for $\bar{K} > 2$, the solution of Eq. (33) may be written

$$W(\xi_1) = A_1e^{-f_1(\bar{K})\xi_1} + A_2e^{-f_2(\bar{K})\xi_1} + e^{f_3(\bar{K})\xi_1}\,[A_3\cos f_4(\bar{K})\xi_1 + A_4\sin f_4(\bar{K})\xi_1] \tag{34}$$

where the functions $f_n(\bar{K})$ have been calculated and are presented graphically in Fig. 3.

It is shown in the Appendix that there is no value of $\bar{K}$ which is related to $W(\xi)$ by Eq. (34) which gives a nonzero solution for A_n in the boundary Eqs. (32). Therefore, divergence *does not occur* at high Mach Numbers.

(5.2) Solution for Moderate M

Eq. (31) is

$$W^{IV} - 6.02W'' + 12.36W = -\bar{K}e^{-(2.01\xi_1/\beta)}\,W' \tag{35}$$

Now, this can be replaced by an integral equation by regarding the right-hand side to be a known function of ξ_1; hence, the complementary solution of the differential equation—i.e., the left-hand side—is given by Eq. (24) while the particular solution is given by the application of the Laplace transformation together with the reciprocal theorem. Therefore, Eq. (35) may be written

$$W(\xi_1) = e^{1.805\xi_1}(A_1 \cos 0.502\xi_1 + A_2 \sin 0.502\xi_1) + e^{-1.805\xi_1}(A_3 \cos 0.502\xi_1 + A_4 \sin 0.502\xi_1) - (\bar{K}/6.36)\int_0^{\xi_1} \{1.805 \sin 0.502(\xi_1 - u) \cosh 1.805(\xi_1 - u) - 0.502 \cos 0.502(\xi_1 - u) \times \sinh 1.805(\xi_1 - u)\} e^{-(2.01/\beta)u} W'(u)du \quad (36)$$

It can be verified that Eq. (36) is a "solution" of Eq. (35) by direct substitution. This formula also establishes that Eqs. (31) and (32) are compatible with Eqs. (21) and (22) in the limiting case of $\beta \to 0$.

Differentiation of Eq. (36) gives

$$W'(\xi_1) = e^{1.805\xi_1}\{A_1(1.805 \cos 0.502\xi_1 - 0.502 \sin 0.502\xi_1) + A_2(1.805 \sin 0.502\xi_1 + 0.502 \cos 0.502\xi_1)\} + e^{-1.805\xi_1}\{A_3(-1.805 \cos 0.502\xi_1 - 0.502 \sin 0.502\xi_1) + A_4(-1.805 \sin 0.502\xi_1 + 0.502 \cos 0.502\xi_1)\} - (\bar{K}/1.812)\int_0^{\xi_1} [\sin 0.502(\xi_1 - u) \sinh 1.805(\xi_1 - u)]e^{-(2.01/\beta)u} W'(u)du \quad (37)$$

Now the integral in Eq. (36) does not affect the values of W, W', W'', and W''' at $\xi_1 = 0$, hence, A_3 and A_4 can be eliminated from Eq. (37) by the boundary conditions of $\xi_1 = 0$. Therefore, Eq. (37) reduces to

$$W'(\xi_1) = A_1\{e^{1.805\xi_1}(1.805 \cos 0.502\xi_1 - 0.502 \sin 0.502\xi_1) + e^{-1.805\xi_1}(0.547 \cos 0.502\xi_1 - 4.758 \sin 0.502\xi_1)\} + A_2\{e^{1.805\xi_1}(1.805 \sin 0.502\xi_1 + 0.502 \cos 0.502\xi_1) + e^{-1.805\xi_1}(0.801 \cos 0.502\xi_1 - 0.553 \sin 0.502\xi_1)\} - (\bar{K}/1.812)\int_0^{\xi_1} [\sin 0.502(\xi_1 - u) \sin 1.805(\xi_1 - u)] e^{-(2.01/\beta)u} W'(u)du \quad (38)$$

Eq. (38) is now in a convenient form for step by step computation from $\xi_1 = 0$ to any value of ξ_1. The procedure, therefore, is to assume values of $\bar{K}$ and β, and compute $W(\xi_1)$ in terms of A_1 and A_2. Since the values of W, W'', and W''' follow directly from the step by step process, the boundary conditions can be set up at $\xi_1 = c/l$ in the form

$$\gamma_1 A_1 + \gamma_2 A_2 = 0$$
$$\gamma_3 A_1 + \gamma_4 A_2 = 0$$

where γ_n are numerical constants depending on the initial assumptions of β and $\bar{K}$. Hence, if we plot the determinental function

$$\Gamma = \begin{vmatrix} \gamma_1 & \gamma_2 \\ \gamma_3 & \gamma_4 \end{vmatrix} \quad (39)$$

against $\bar{K}$ for constant β, the divergence condition is obtained when $\Gamma = 0$.

This process has been performed for $c/l = 1$ and 2, and the graphs of $\Gamma(\bar{K})$ are shown in Figs. 4 and 5.

(5.3) Divergence Conditions

From the graph of $\Gamma(\bar{K})$ for $c/l = 1$ in Fig. 4, divergence does not take place for $\beta = 1.5$ and $\beta = 2$, but there are two values of $\bar{K}$, such that $\Gamma(\bar{K}) = 0$ for $\beta = 1$, and, presumably, there are two similar values for $\beta = 0.5$, assuming that this curve is similar to the others. For $c/l = 2$, no values of $\bar{K}$ for divergence appear for $\beta = 1.5$ and $\beta = 2$, but divergence appears for $\beta = 1$.

From these graphs and Section (4), the stability curve for rectangular plates at supersonic speeds can be deduced for $c/l = 1,2$, and are shown in Fig. 6. Curves for $(c/l) > 2$ were not computed but these should be similar to those shown, since even if $(c/l) \to \infty$, divergence does not take place as $\beta \to \infty$, as shown in the derivation of the asymptotic solution in the Appendix.

The interesting point of these graphs concerns the stability in the limiting case of zero plate thickness for nonzero β—i.e., whether the stability curves cross or meet the β-axis, or whether there is a further reversal in the curves, so avoiding the β-axis. Unfortunately, this would imply very high values of $\bar{K}$ which would make any computation on a desk machine formidable on the basis of the processes described in Section (5.2). However, returning to the asymptotic solution of Section (5.1), divergence is not possible—even, apparently, for zero thickness—for large β in which the loading is "two-dimensional" over the whole wing area. Physically, one would not expect any violent changes in the stability curves for $M > 2$, say, for the $c/l = 2$ wing, since the variation in the *distribution* of the loadings would be small for increasing speeds for constant distortion. On the basis of this argument, the curves should not be extended or modified. For design considerations, the transonic conditions are the deciding factors, and, since a wing has to pass $M = 1$ to reach a supersonic Mach Number, the design criteria [Eq. (27)] could be applied for all wings at $M = 1$, being independent of the final design or operating speeds.

The modes of divergence of the plate $c/l = 1$ are compared in Fig. 7 for $\beta = 0$ and $\beta = 1$. This indicates clearly that if one approached the divergence problem by assuming a mode of divergence to be independent of Mach Number, then large errors in any stiffness criterion would be expected.

(6) Method of Influence Coefficients

In view of the nature of the theoretical stability curves deduced in the preceding Sections, it was decided to investigate the stability of a specific plate from the semiexperimental approach of measuring the structural characteristics by means of stiffness influence coefficients, and using these with theoretical aerodynamic coefficients to calculate the divergence conditions.

A dural plate of 10 gauge (0.127 in. thickness) with chord of 20 in. and semispan l of 10 in.—i.e., $c/l =$

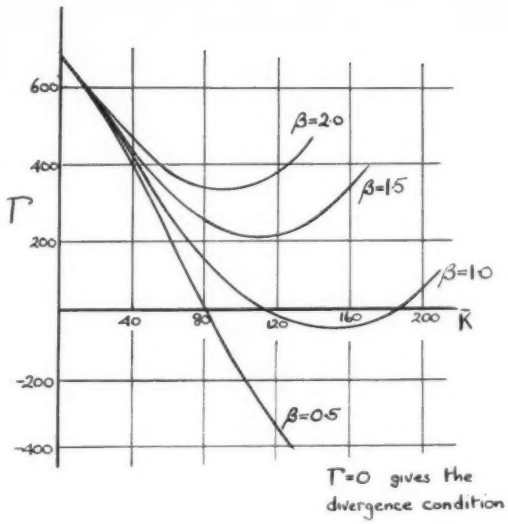

FIG. 4. Graph of $\Gamma(\beta, \bar{K})$ for $c/l = 1$.

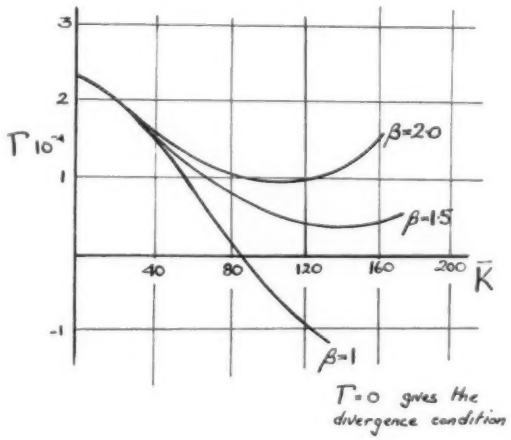

FIG. 5. Graph of $\Gamma(\beta, \bar{K})$ for $c/l = 2$.

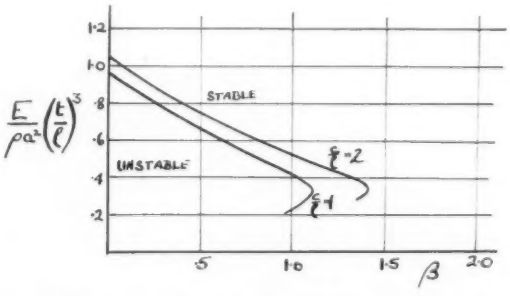

FIG. 6. Divergence of rectangular plate wings.

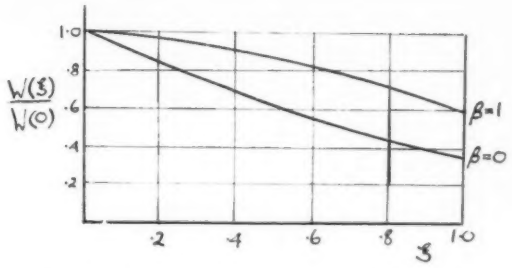

FIG. 7. Chordwise divergence modes for $c/l = 1$.

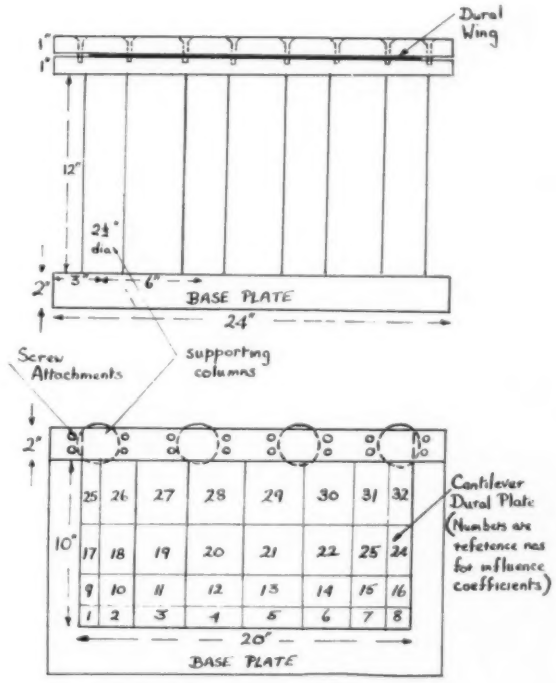

FIG. 8. Supporting frame for dural wing.

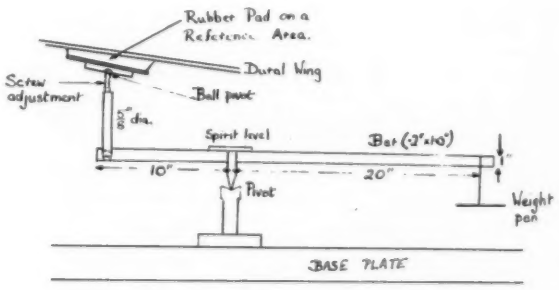

FIG. 9. Diagram of loading system.

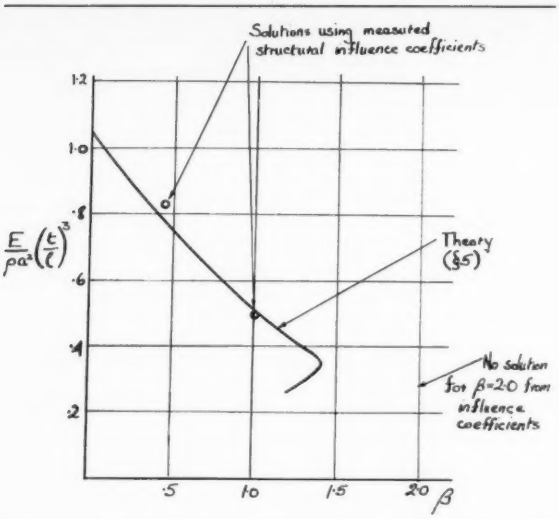

FIG. 10. Comparison of methods for divergence for $c/l = 2$.

2—is rigidly fixed along one of its longer sides to the supporting frame as shown in Fig. 8. The plate is subdivided into the 32 areas shown; the smaller areas are arranged at the plate edges since the conditions in these neighborhoods are fundamental in the estimation of any deflection modes.

Uniform loadings were applied to each of the 32 areas by means of the simple beam system shown in Fig. 9. The procedure for loading involved the leveling of the cross beam, indicated by the spirit level shown, for each increment of weight on the pan, by means of the screw adjustment. The deflections of the plate were measured on the four chordwise lines along the center of the areas—i.e., distances 2 in., $5^1/_2$ in., 8 in., and $9^1/_2$ in. from the wing root—by sweeping a single dial gauge held by a magnetic holder to the wing root supports. The deflections were kept small for reasonably linear deflection curves to be obtained.

The incidence distributions on the plate were then obtained from the deflection curves by graphical differentiation and were normalized for a coherent system. These final results were then presented in the matrix notation,

$$(\alpha_i) = \{\delta_{ij}\}(l_j) \tag{40}$$

where (α_i) = column matrix of incidences on area i $(i = 1, \ldots, 32)$
(l_i) = column matrix of total loads distributed over area j $(j = 1, \ldots, 32)$
$\{\delta_{ij}\}$ = flexibility matrix of order (32×32)

The assumption for the aerodynamic loading is the same as that in the previous analysis [presented in Section (3)]—that is,

$$l_j = p_{jj}\alpha_j A_j \tag{41}$$

where the coefficient p_{jj} is given by reference to Fig. 2, either as $p_{jj} = 2M^2\rho a^2/\beta$ if area j is in "two-dimensional" region (region A) or

$$p_{jj} = (2\rho a^2 M^2/\beta)\left(1 - (2/\pi) \times \tan^{-1}\left\{[c\xi_j/\beta l(1 - \eta_j)] - 1\right\}^{1/2}\right)$$

if area j is in the tip region (region B) or

$$p_{jj} = (2\rho a^2 M^2/\beta)\left(1 - (2/\pi) \times \tan^{-1}\left\{[c\xi_i/\beta l(1 - \eta_j)] - 1\right\}^{1/2} - (2/\pi)\tan^{-1}\left\{[c\xi_j/\beta l(1 + \eta_j)] - 1\right\}^{1/2}\right)$$

if area j is in the reflected region (region C); A_j = surface area of area j, and α_j is the local incidence. The coordinates (ξ_j, η_j) are taken to be those at the center of area j. If an area j lies partly in two regions (say, A and B), then the weighted average of the combined parts is taken in the usual fashion. Hence, Eq. (41) is written

$$(l_j) = \rho a^2\{P_{ij}\}(\alpha_i) \tag{42}$$

where $P_{ij} = 0$ if $i \neq j$
$P_{ij} = (1/\rho a^2)p_{jj}A_j$ if $i = j$

Hence, combining Eqs. (40) and (42) in the divergence condition,

$$(\alpha_i) = \rho a^2\{\delta_{ij}\}\{P_{ij}\}(\alpha_i) \tag{43}$$

It is now assumed that for any similar plate with $c/l = 2$, the flexibility matrix is inversely proportional to Young's modulus E and directly proportional to the ratio $(t/l)^3$. Therefore, a general flexible matrix is written

$$\{\bar{\delta}_{ij}\} = (10^7/E)[(0.127/10)^3/(t/l)^3]\{\delta_{ij}\} \tag{44}$$

Finally, from Eqs. (43) and (44)

$$(\alpha_i) = \rho a^2(10^7/E)[(0.0127)^3/(t/l)^3]\{\delta_{ij}\}\{P_{ij}\}(\alpha_i) = [\rho a^2/E(t/l)^3]\{B_{ij}\}(\alpha_i) \tag{45}$$

where $\{B_{ij}\} = 10^7(0.0127)^3\{\delta_{ij}\}\{P_{ij}\}$.

Eq. (45) is the usual type obtained in the matrix approach to the divergence problem and is solved by the method of iteration in which interest is only focused on the dominant latent root. This procedure has been carried out for $\beta = 0.45$, 1, and 2. The first two cases give real positive dominant latent roots which imply that divergence would take place. However, in the third case, a complex dominant root was iterated out,[3] implying that the divergence condition, if it exists, depends on one of the other latent roots. But if this is the case, it indicates that the *nature* of the divergence changes drastically between $\beta = 1$ and $\beta = 2$. Therefore, for a complete investigation, in general, more of the latent roots should be obtained, presumably by iteration.

However, the author did not consider that it was justifiable to spend further time in this computation since the results obtained tied up with the theoretical analysis of Sections (1)–(5) in which the final picture is given more clearly.

The results are given in Fig. 10, which indicates the close relationship between the two approaches. It is expected that the agreement should be better for the larger value of β since the exponential formula as-

sumed for the loading in the theoretical curve represents conditions over the wing more accurately as β increases.

(7) Rayleigh-Ritz Method (Series Solution)

In Sections (2)–(5), the divergence of a flat plate of constant thickness is investigated by simple numerical computation of the equilibrium differential equations relating the distorted structure to the supersonic loadings. These results were then compared in Section (6) to those obtained by using measured influence coefficients, and the comparison is highly satisfactory.

However, it is uncommon practice to have wings of constant thickness, and so the effect of thickness distribution should eventually be investigated. It is possible to extend the differential equation technique to these problems but it would take a considerable time in the computation. Therefore, it seems reasonable to seek a more approximate method which can be evaluated more quickly and which can incorporate thickness effects without too much complication. In this Section, the standard Rayleigh-Ritz method is applied to the problem of constant thickness, and it is shown to give good results. The extension to particular problems of varying thickness will not be considered in this report.

For the problem of the plate of constant thickness, the fundamental equations are formulated in exactly the same way as Section (2), assuming the spanwise mode of distortion, etc., arriving at Eqs. (9)–(11) and (13). These are again, for the sake of completeness in this section,

$$S.E. = (1/2)D(l/c)\int_0^1 \{a_0W''^2 + a_1WW'' + a_2W^2 + a_3W'^2\}d\xi \quad (46)$$

where $a_0 = 0.249$, $a_1 = 0.132(c/l)^2$, $a_2 = 3.077(c/l)^4$, $a_3 = 1.631(c/l)^2$

and

$$P.E. = \int_0^1 WW'b(\xi)d\xi \quad (47)$$

where $b(\xi)/c^2l = 0.249(2\rho a^2M^2/\beta)e^{-2.01(\xi c/\beta l)}$

Now, it is assumed that

$$W(\xi) = b_0 + b_1\xi + b_2\xi^2 + b_3\xi^3 \quad (48)$$

The procedure is to substitute Eq. (48) into Eq. (46) and (47), minimize the total energy in the usual way and to obtain a set of simultaneous equations for b_0, b_1, b_2, and b_3. The compatibility of these equations gives the divergence speed.

This method has been applied to the wing for $c/l = 2$ and the result is presented in Fig. 11. It is seen that, in this case, the comparison of the two methods is very good.

(8) Concluding Remarks

It has been established that the critical conditions for the divergence of rectangular plate airfoils occur in the transonic range in which the mode of divergence

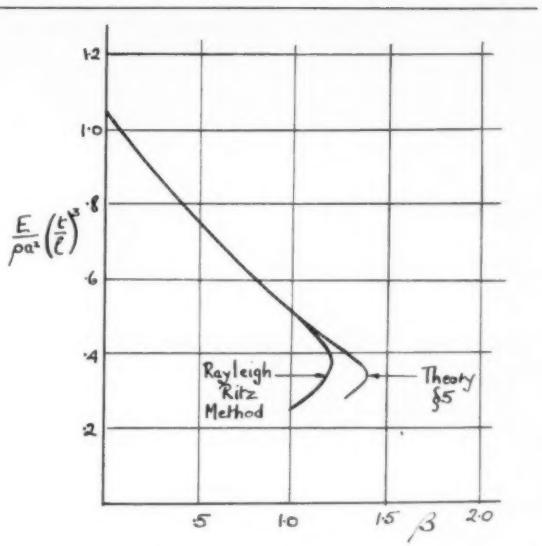

Fig. 11. Comparison of methods for divergence for $c/l = 2$.

is the rolling up of the leading edge. Hence, for design considerations, the stability of these plates is independent of Mach Number once it has been calculated for $M = 1$. This conclusion is based mainly on a theoretical investigation which constrains the wing distortion in a single spanwise mode. However, any restrictions which this assumption may have imposed do not appear to be serious since the use of experimentally determined influence coefficients give essentially the same results.

The physical explanation for these types of stability curves with variation of Mach Number has been given in fact by Biot[1] in terms of the anticlastic behavior of plates. At Mach 1, only shear forces are theoretically possible on the leading edge, and so if divergence takes place, it can only be in a mode in which the leading edge rolls up. As the Mach number increases, the effective aerodynamic center moves aft of the leading edge, and so the mode of divergence is now a combination of the tendencies of the leading edge to roll up under the aerodynamic forces and of the leading edge to roll down under the anticlastic effects. These latter effects, which are small for $M = 1$, apparently increase with Mach number until, as the calculations show, they predominate and preclude the possibility of divergence.

It is emphasized that the above discussion is limited to small deflections of the plate from its position of equilibrium. It appears, therefore, that for a further understanding of this problem recourse must be made to large deflection theories, especially at high Mach Numbers where some form of divergence is intuitively expected, although it is not predicted in this paper.

Appendix—Solution for Large M

Eq. (35) is given by

$$W(\xi_1) = A_1e^{-f_1\xi_1} + A_2e^{-f_2\xi_1} + e^{f_2\xi_1}(A_3\cos f_4\xi_1 + A_4\sin f_4\xi_1) \quad (A\text{-}1)$$

where f_n is a function of $\bar{K}$.

Now

$$W'(\xi_1) = -f_1A_1e^{-f_1\xi_1} - f_2A_2e^{-f_2\xi_1} + e^{f_3\xi_1}(A_3\cos[f_4\xi_1 + \alpha] + A_4\sin[f_4\xi_1 + \alpha]) \times (f_3^2 + f_4^2)^{1/2} \quad \text{(A-2)}$$

where $\alpha = \cos^{-1}[f_3/(f_3^2 + f_4^2)^{1/2}]$

Hence, by repeated differentiation of (A-2),

$$W^n(\xi_1) = (-f_1)^nA_1e^{-f_1\xi_1} + (-f_2)^nA_2e^{-f_2\xi_1} + (f_3^2 + f_4^2)^{n/2}e^{f_3\xi_1}(A_3\cos[f_4\xi_1 + n\alpha] + A_4\sin[f_4\xi_1 + n\alpha]) \quad \text{(A-3)}$$

Substituting Eq. (A-3) into the boundary Eqs. (33), hence

$$(A_1f_1^2 + 0.265) + A_2(f_2^2 + 0.265) + A_3\{(f_3^2 + f_4^2)\cos 2\alpha + 0.265\} + A_4\{(f_3^2 + f_4^2)\sin 2\alpha\} = 0$$

$$A_1(-f_1^3 + 6.285f_1) + A_2(-f_2^3 + 6.285f_2) + A_3(f_3^2 + f_4^2)^{1/2}\{(f_3^2 + f_4^2)\cos 3\alpha - 6.285\cos\alpha\} + A_4(f_3^2 + f_4^2)^{1/2}\{(f_3^2 + f_4^2)\sin 3\alpha - 6.285\sin\alpha\} = 0$$

at $\xi_1 = 0$, and

$$A_1(f_1^2 + 0.265)e^{-f_1(c/l)} + A_2(f_2^2 + 0.265)e^{-f_2(c/l)} + A_3e^{f_3(c/l)}\{(f_3^2 + f_4^2)\cos[f_4(c/l) + 2\alpha] + 0.265\cos f_4(c/l)\} + A_4e^{f_3(c/l)}\{(f_3^2 + f_4^2) \times \sin[f_4(c/l) + 2\alpha] + 0.265\sin f_4(c/l)\} = 0$$

$$A_1(-f_1^3 + 6.285f_1)e^{-f_1(c/l)} + A_2(-f_2^3 + 6.285f_2)e^{-f_2(c/l)} + A_3(f_3^2 + f_4^2)^{1/2}e^{f_3(c/l)}\{(f_3^2 + f_4^2) \times \cos[f_4(c/l) + 3\alpha] - 6.285\cos[f_4(c/l) + \alpha]\} + A_4(f_3^2 + f_4^2)^{1/2}e^{f_3(c/l)}\{(f_3^2 + f_4^2)\sin[f_4(c/l) + 3\alpha] - 6.285\sin[f_4(c/l) + \alpha]\} = 0$$

at $\xi_1 = c/l$.

Neglecting the terms $e^{-f_1(c/l)}$ and $e^{-f_2(c/l)}$, as compared with $e^{f_3(c/l)}$, then the condition that there is a nonzero solution for A_n is that

$$G_1(\bar{K})G_2(\bar{K}) = 0 \quad \text{(A-4)}$$

where

$$G_1(\bar{K}) = (f_1^2 + 0.265)(f_2^3 - 6.285f_2) - (f_2^2 + 0.265)(f_1^3 - 6.285f_1) = -f_1^2f_2^2(f_1 - f_2) - 6.285f_1f_2(f_1 - f_2) - 0.265(f_1^3 - f_2^3) + 1.665(f_1 - f_2)$$

and

$$G_2(\bar{K}) = \{(f_3^2 + f_4^2)\cos[f_4(c/l) + 2\alpha] + 0.265\cos f_4(c/l)\}\{(f_3^2 + f_4^2)\sin[f_4(c/l) + 3\alpha] - 6.285\sin[f_4(c/l) + \alpha]\} - \{[f_3^2 + f_4^2]\sin[f_4(c/l) + 2\alpha] + 0.265\sin f_4(c/l)\}\{(f_3^2 + f_4^2)\cos[f_4(c/l) + 3\alpha] - 6.285\cos[f_4(c/l) + \alpha]\} = (f_3^2 + f_4^2)\sin\alpha + 0.265(f_3^2 + f_4^2)\sin 3\alpha + 6.285(f_3^2 + f_4^2)\sin\alpha - 1.665\sin\alpha$$

Now $G_2(\bar{K}) > 0$ for all $\bar{K}$ and is independent of c/l, and $G_1(\bar{K}) < 0$ for all $\bar{K}$ when $f_1 \neq f_2$. If $f_1 = f_2$, then Eq. (A-1) is not the solution to the differential equation. Hence, in general, Eq. (A-4) cannot be satisfied, and the divergence condition cannot be found.

It is interesting to note that we should have expected from the trends indicated in Section (4) and by Eq. (26), that assuming a mode of divergence independent of Mach Number, $\bar{K} = O$ (32).

PART (II) SWEPT WINGS

(1) Introduction

In Part (I), a theory of the divergence of constant thickness rectangular plate wings of low aspect ratio is presented, based on the assumptions of the linear elastic theory and linearized aerodynamic theory. It is established that the critical conditions occurred at $M = 1$. The sweeping of the leading edge in an attempt to avoid instabilities of this type has been recognized for some time, and it is, therefore, desirable that the previous investigations should be continued to cover these cases.

The problem has been limited to the determination of the divergent characteristics of a constant aspect ratio wing (chord/semispan = 2) with constant thickness and varying sweep in supersonic motion. The Rayleigh-Ritz method has been adopted, the structural and aerodynamic characteristics being modifications of those considered in Part (I) to include the effect of the sweep. The stability curves are given in Fig. 16 and the general conclusions in Section (8).

(2) Theoretical Derivation

As in Part (I), the divergence of a plate airfoil in a supersonic stream is calculated from the equilibrium conditions in neutral stability at the critical divergence speed, considering the strain energy of the deformed plate and the potential energy of the applied aerodynamic forces.

The plate, of constant thickness, has parallel leading and trailing edges at sweep angle φ, and is rigidly fixed at its root, as indicated in Fig. 12.

Converting the Cartesian coordinates (x, y) to oblique coordinates (u, v), defined in Fig. 12, by the formulas,

$$u = x - y\tan\varphi, \quad x = u + v\sin\varphi, \quad v = y\sec\varphi, \text{ or } \quad y = v\cos\varphi \quad (1)$$

the strain energy $S.E.$ of the plate under a transverse displacement $w(x, y)$ is

$$S.E. = (1/2)D\cos\varphi \iint_{\text{plate}} \{\sec^4\varphi[w_{uu} - 2\sin\varphi\, w_{uv} + w_{vv}]^2 + 2(1 - \nu) \times \sec^2\varphi[w_{uv}^2 - w_{uu}w_{vv}]\}dudv \quad (2)$$

where $D = Et^3/12(1 - \nu^2)$ in the usual notation.

Nondimensional parameters (ξ, η) are defined by

$$u = c\xi, \quad v = l\sec\varphi\eta \quad (3)$$

so that the displacement function may be expressed as

$$w(x, y) = cf(\xi, \eta) \quad (4)$$

On substitution of Eqs. (3) and (4), Eq. (2) becomes

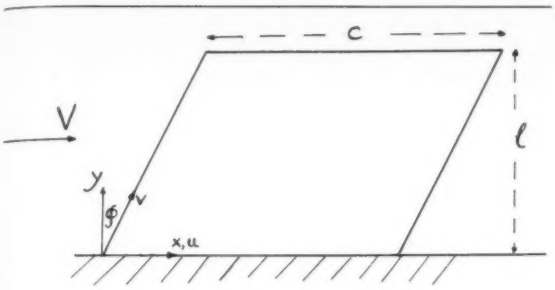

FIG. 12. Swept plate.

$$S.E. = (1/2)D(l/c)\int_0^1\int_0^1 \{\sec^4\varphi \times [f_{\xi\xi} - 2(c/l)(\sin\varphi/\sec\varphi)f_{\xi\eta} + (c/l\sec\varphi)^2 f_{\eta\eta}]^2 + 2(1-\nu)(c/l)^2[f_{\xi\eta}{}^2 - f_{\xi\xi}f_{\eta\eta}]\}d\xi d\eta \quad (5)$$

where the subscripts denote partial differentiation.

It is now assumed that

$$f(\xi, \eta) = W(\xi)G(\eta) \quad (6)$$

where $G(\eta)$ is the mode of deformation of a uniform beam under a parabolic loading distribution—that is,

$$G(\eta) = (1/26)[45\eta^2 - 20\eta^3 + \eta^6] \quad (7)$$

This assumption is discussed in detail in Part (I) and is here extended to the case of a swept plate.

Finally, substituting Eq. (6) in Eq. (5),

$$S.E. = (1/2)D(c/l)^3\int_0^1 \{a_0W''' + a_1W''W' + a_2W''W + a_3W'^2 + a_4W'W + a_5W^2\}d\xi \quad (8)$$

where

$$a_0 = (l/c)^4\sec^4\varphi\int_0^1 G^2d\eta = (l/c)^4\sec^4\varphi\ 0.249$$

$$a_1 = -4(l/c)^3\sec^3\varphi\sin\varphi\int_0^1 GG'd\eta = -2(l/c)^3 \times \sec^2\varphi\tan\varphi$$

$$a_2 = (l/c)^2[2\sec^2\varphi - 2(1-\nu)]\int_0^1 GG''d\eta = (l/c)^2 \times (2\sec^2\varphi - 1.4)\ 0.220$$

$$a_3 = (l/c)^2[4\sin^2\varphi\sec^2\varphi + 2(1-\nu)]\int_0^1 G'^2d\eta = (l/c)^2(4\tan^2\varphi + 1.4)\ 1.165$$

$$a_4 = -4(l/c)\tan\varphi\int_0^1 G'G''d\eta = -4(l/c)\tan\varphi\ 0.959$$

$$a_5 = \int_0^1 G''^2d\eta = 3.077$$

the dashes denote differentiation, and ν is taken equal to 0.30.

The potential energy $P.E.$ of the applied aerodynamic forces $P(x, y)$ is

$$P.E. = -\iint_{\text{plate}} P(x, y)w(x, y)dxdy \quad (9)$$

It is assumed for the sake of simplicity that the pressure loading at any point (x, y) depends only on the local angle of incidence at that point, so that Eq. (9) may be written

$$P.E. = \iint_{\text{plate}} [p(x, y)w_x]wdxdy \quad (10)$$

where the function $p(x, y)$ will be deduced from the linearized supersonic flow theory of thin symmetrical wings—that is, $p(x, y)$ will depend only on the point (x, y) relative to the geometry of the plate and the Mach Number, and is independent of $w(x, y)$.

Transforming Eq. (10) to the nondimensional coordinates (ξ, η), defined in Eq. (3),

$$P.E. = c^2l\int_0^1\int_0^1 p(\xi, \eta)f_\xi f\,d\xi d\eta = \int_0^1 W'Wb(\xi)d\xi \quad (11)$$

where $$b(\xi) = c^2l\int_0^1 G^2(\eta)p(\xi, \eta)d\eta$$

and $f(\xi, \eta)$, $W(\xi)$, $G(\eta)$ are defined in Eqs. (4), (6), and (7).

(3) Conditions at $M = 1$; i.e., $\beta = (M^2 - 1)^{1/2} = 0$

If the linearized theory of flow at supersonic speeds is extended to problems at $M = 1$ the loading $l(x\ y)$ on a rigid swept plate at incidence α can be shown to be[4]

$$l(x, y) = (2\rho a^2\alpha/\tan\varphi)\cdot[x/(x^2 - y^2\tan^2\varphi)^{1/2}] \text{ over region (1),}$$
$$= 0 \text{ elsewhere}$$

where region (1) is shown in Fig. 13.

Therefore, by definition, we take

$$p(x, y) \equiv p(\xi, \eta) = (2\rho a^2/\tan\varphi) \times [x/(x^2 - y^2\tan^2\varphi)^{1/2}]$$
$$= (2\rho a^2/\tan\varphi) \times \left([(c\xi/l) + \eta\tan\varphi]/\{(c\xi/l) \times [c(\xi/l) + 2\eta\tan\varphi]\}^{1/2}\right)$$

Hence, by Eq. (11)

$$b(\xi)/c^2l = [2\rho a^2/\tan\varphi(c\xi/l)^{1/2}]\int_{\eta=0}^{\eta=1-(c\xi/l)\tan\varphi} \{[c(\xi/l) + \eta\tan\varphi]/[(c\xi/l) + 2\eta\tan\varphi]\}^{1/2}G^2(\eta)d\eta$$
$$= [2\rho a^2/\tan\varphi(c\xi/l)^{1/2}]I(\xi) \quad \text{for } (c\xi/l\tan\varphi) < 1$$
$$= 0 \quad \text{for } (c\xi/l\tan\varphi) > 1 \quad (12)$$

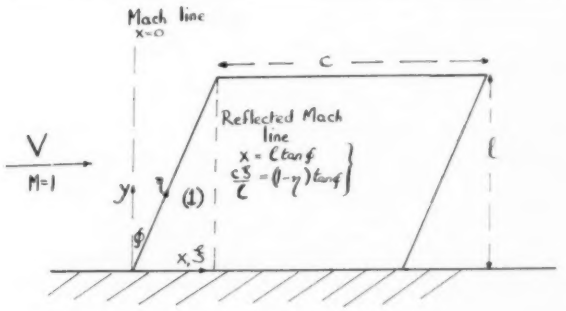

FIG. 13. Flight conditions at Mach 1.

Although the integral $I(\xi)$ is calculable theoretically, we shall approximate for convenience by writing

$$\left.\begin{aligned} b(\xi)/c^2l &= \rho a^2(2l/c\xi\tan\varphi)^{1/2}[A - B(c\xi/l) + C(c\xi/l)^2] \quad \text{for } (c\xi/l\tan\varphi) < 1 \\ &= 0 \quad \text{for } (c\xi/l\tan\varphi) > 1 \end{aligned}\right\} \quad (13)$$

where

$$A = (2/\tan\varphi)^{1/2}I(0) = \int_0^1 \eta^{1/2}G^2 d\eta = 0.222$$

$$B = -(l/c)(2/\tan\varphi)^{1/2}I'(0) = (1/\tan\varphi)\left[1 - (3/4)\int_0^1 (G^2/\eta^{1/2})d\eta\right] = 0.788/\tan\varphi$$

$$C = \left\{[B(c\xi/l) - A]/(c\xi/l)^2\right\}_{(c\xi/l)=\tan\varphi} = 0.566/\tan^2\varphi$$

This approximation is obtained by equating $b(0)$, $b'(0)$ and $b(l\tan\varphi/c)$ between Eqs. (12) and (13).

(4) Conditions at $\beta = \tan\varphi$

When $\beta = \tan\varphi$, the Mach line from the wing apex lies along the wing leading edge, as shown in Fig. 14.

In this case,[5]

$$p(x, y) = p(\xi, \eta) = [2\rho a^2M^2/(\pi/2)\tan\varphi] \times [x/(x^2 - y^2\tan^2\varphi)^{1/2}] = [2\rho a^2M^2/(\pi/2)\tan\varphi] \times \left([(c\xi/l) + \eta\tan\varphi] \times \left\{(c\xi/l)[(c\xi/l) + 2\eta\tan\varphi]\right\}^{1/2}\right) \text{ over region (1)}$$

and

$$p(x, y) = p(\xi, \eta) = [2\rho a^2M^2/(\pi/2)] \times [(s - y)/2\tan\varphi(x + y\tan\varphi)]^{1/2} = [2\rho a^2M^2/(\pi/2)] \times \left\{(1 - \eta)/2\tan\varphi[(c\xi/l) + 2\eta\tan\varphi]\right\}^{1/2} \text{ over region (2)}$$

It will be assumed that the loading in region (3) is zero.

Therefore,

$$b(\xi)/c^2l = [2\rho a^2M^2/(\pi/2)(c\xi/l)^{1/2}] \times \int_{\eta=0}^{\eta=1-(c\xi/2l\tan\varphi)} \left\{[(c\xi/l) + \eta\tan\varphi] \div [(c\xi/l) + 2\eta\tan\varphi]^{1/2}\right\} G^2(\eta)d\eta/\tan\varphi + \int_{\eta=1-(c\xi/2l\tan\varphi)}^{\eta=1} \left\{(1 - \eta) \div 2\tan\varphi[(c\xi/l) + 2\eta\tan\varphi]\right\}^{1/2}G^2(\eta)d\eta$$

$$= [2\rho a^2M^2/(\pi/2)]\, I_1(\xi) \quad \text{for } 0 \le (c\xi/l) \le 2\tan\varphi$$

$$= 0 \quad \text{for } (c\xi/l) > 2\tan\varphi$$

This formula is again approximated in a similar manner as before to

$$\left.\begin{aligned} b(\xi)/c^2l &= [\rho a^2M^2/(\pi/2)][(2/\tan\varphi)(l/c\xi)]^{1/2} \times [A_1 - B_1(c\xi/l) + C_1(c\xi/l)^2] \\ &\quad \text{for } 0 \le (c\xi/l) \le 2\tan\varphi \\ &= 0 \quad \text{for } (c\xi/l) > 2\tan\phi \end{aligned}\right\} \quad (14)$$

where

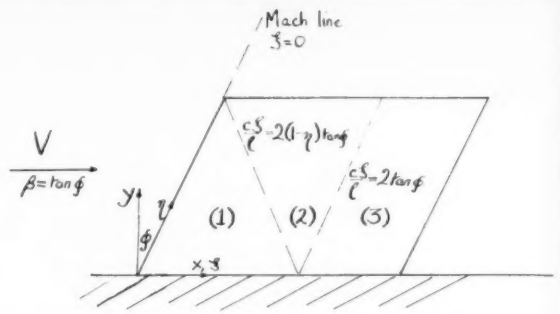

FIG. 14. Flight conditions at $\beta = \tan\varphi$.

$$A_1 = \int_0^1 \eta^{1/2}\, G^2(\eta)d\eta = 0.222$$

$$B_1 = (1/\tan\varphi)\left\{(1/2) - (3/4)\int_0^1 [G^2(\eta)/\eta^{1/2}]d\eta\right\} = 0.288/\tan\varphi$$

$$\left\{A_1 - B_1\, 2\tan\varphi + C_1\, 4\tan^2\varphi\right\} = \int_0^1 [(1 - \eta)/(1 + \eta)]^{1/2}G^2(\eta)d\eta = 0.76$$

so that $C_1 = 0.108/\tan^2\varphi$

(5) Conditions for $0 \le \beta \le \tan\varphi$

For the intermediate values of β between the two limiting conditions of 0 and $\tan\phi$, $b(\xi)$ is interpolated between the formulas (13) and (14). It is assumed that

$$\left.\begin{aligned} b(\xi)/c^2l &= \left(2\rho a^2M^2/E'(\beta/\tan\varphi)\left\{2\tan\varphi \times (c\xi/l)\right\}^{1/2}\right)[A_2 - B_2(c\xi/l) + C_2(\xi c/l)^2] \\ &\quad \text{for } 0 \le (c\xi/l) \le \beta + \tan\varphi \\ &= 0 \quad \text{for } (c\xi/l) > \beta + \tan\varphi \end{aligned}\right\} \quad (15)$$

where

$$E(\mu) = \text{elliptic integral} \int_0^{\pi/2} (1 - [1 - \mu^2]\sin^2\varphi)^{1/2}d\varphi$$

$$A_2 = 0.222$$

$$B_2 = [1/(\beta + \tan\varphi)] - (0.212/\tan\varphi)$$

$$C_2 = [1/(\beta + \tan\varphi)^2]\{0.076\,(\beta/\tan\varphi) + B_2\,(\beta + \tan\varphi) - A_2\}$$

(6) Conditions for $\beta > \tan\varphi$

The regions of pressure loading for speeds at which $\beta > \tan\varphi$ are shown in Fig. 15. By reference to Fig. 15;

(a) in the two-dimensional region (1)

$$p_1(\xi, \eta) = 2M^2\rho a^2/(\beta^2 - \tan^2\varphi)^{1/2}$$

(b) in the tip region (2)

$$p_2(\xi, \eta) = \left\{2M^2\rho a^2/(\beta^2 - \tan^2\varphi)^{1/2}\right\} \times \left(1 - (2/\pi)\tan^{-1}\left\{[c(\xi/l) - \tan\varphi - \beta(1 - \eta)] \div [(\beta + \tan\varphi)(1 - \eta)]\right\}^{1/2}\right)$$

(c) in the root region (3)

$$p_3(\xi, \eta) = \left\{2M^2\rho a^2/(\beta^2 - \tan^2\varphi)^{1/2}\right\}\left[1 - (2/\pi)\tan^{-1}\left(\tan^2\varphi\left\{[(c\xi/l) + \eta\sin\varphi]^2 - \beta^2\eta^2\right\} \div (\beta^2 - \tan^2\varphi)[(c\xi/l) + \eta\sin\varphi]^2\right)^{1/2}\right]$$

Therefore, for $c\xi/l \le (\beta^2 - \tan^2\varphi)/2\beta$,

$$b(\xi)/c^2l = \int_{\eta=c\xi/l(\beta-\tan\varphi)}^{\eta=1-[c\xi/l(\beta+\tan\varphi)]} p_1G^2d\eta + \int_{\eta=1-[c\xi/l(\beta+\tan\varphi)]}^{\eta=1} p_2G^2d\eta + \int_{\eta=0}^{\eta=c\xi/l(\beta-\tan\varphi)} p_3G^2d\eta \tag{16}$$

Eq. (16) will be approximated to in the same manner as Part (I) for the case of $\tan\varphi = 0$, by noting

$$b(0)/c^2l = [2M^2\rho a^2/(\beta^2 - \tan^2\varphi)^{1/2}] \int_0^1 G^2d\eta = 2M^2\rho a^2(0.249)/(\beta^2 - \tan^2\varphi)^{1/2}$$

and

$$b'(0)/c^2l = [2M^2\rho a^2/(\beta^2 - \tan^2\varphi)^{1/2}] \times \{-(1/2)[c/l(\beta + \tan\varphi)]\}$$

and then assuming

$$b(\xi)/c^2l = 0.249[2M^2\rho a^2/(\beta^2 - \tan^2\varphi)^{1/2}] \times e^{-[\xi c2.01/l(\beta+\tan\varphi)]} \tag{17}$$

valid for all $\beta > \tan\varphi$. This formula will be most inaccurate in the region of $\beta = \tan\varphi$ since it does not tend to formula (14), but is useful where the two dimensional region extends for a substantial area over the wing surface.

(7) Divergence Conditions

The present investigation is restricted to the case $c/l = 2$, with varying angles of sweep of $\phi = 10°$, $22\frac{1}{2}°$ and $45°$, and the method used is that of the Rayleigh-Ritz.

It is assumed that

$$W(\xi) = b_0 + b_1\xi + b_2\xi^2 + b_3\xi^3 \tag{18}$$

where the coefficients b_n are arbitrary constants. These are determined from the minimization considerations that

$$\delta(S.E. + P.E.) = 0$$

at the critical divergence condition. Hence,

$$\delta(S.E.) + \int_0^2 W'(\delta W)b(\xi)d\xi = 0 \tag{19}$$

where $S.E.$ is given by Eq. (8) and $b(\xi)$ by the appropriate Eq. of Eqs. (13), (14), (15), or (17), depending on the chosen Mach Number. On substitution of Eq. (18) into Eq. (19), a set of simultaneous equations for b_0, b_1, b_2, and b_3 is set up in the usual way, and the divergence condition is deduced from the compatibility relationship between these equations.

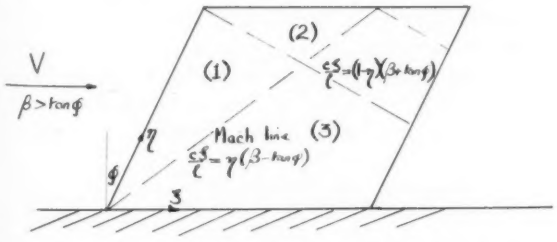

Fig. 15. Flight conditions for $\beta > \tan\varphi$.

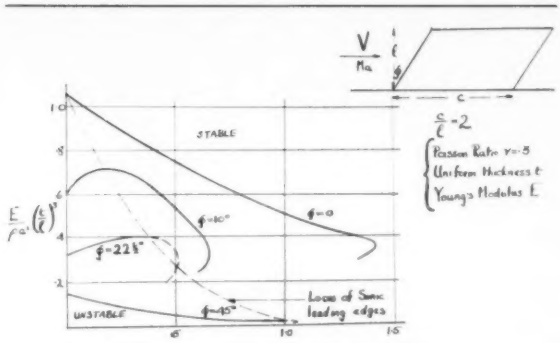

Fig. 16. Divergence of swept plates.

The process has been computed for the cases stated above, and the results are shown in Fig. 16. The result for $\varphi = 0$ has been taken from Part (I). The dotted portions are the parts of curves which are lacking in confidence, for example, in the case of $\varphi = 22\frac{1}{2}°$ the point for $\beta = 0.414$ was determined, based on formula (14), but no divergence was found for $\beta = 0.6$, using formula (17). Since formula (17) is not accurate in the range of β slightly greater than 0.414, it was decided to guess the stability curve here. In the case of $\varphi = 45°$, the derived graph was obtained essentially from the small difference between large quantities, so this can only be regarded as qualitative, but it is hoped that the essential characteristics are presented.

(8) Discussion

The main effect of sweep, as would be expected, is highly beneficial even for moderate angles of order of 10°. The fundamental point which emerges, again as would be expected, is that when the leading edge is subsonic—i.e., a theoretical infinite pressure loading along this edge—divergence is possible for all angles of sweep, but as soon as the leading edge becomes supersonic—i.e., a theoretical finite pressure loading on this edge—the possibility of divergence quickly disappears with increasing speed. According to the graphs, the critical condition is when the leading edge is sonic for $\varphi < 30°$, but for $\varphi > 30°$ the case of $M = 1$ assumes the role of the design criterion. However, in these latter cases, the wing will probably have to be designed on the basis of other aeroelastic behavior—e.g., flutter—or even from a strength point of view.

Although the calculations have been made only for the case when the leading and trailing edges are parallel, modifications to the shape of the trailing edge should not seriously affect the nature of the results, and, therefore, it is hoped that the above remarks apply equally well to the more practical cropped delta wing of low aspect ratio.

References

[1] Biot, M. A., *Divergence of Supersonic Wings Including Chordwise Bending*, Journal of the Aeronautical Sciences, Vol. 23, No. 3, pp. 237–251, 271, March, 1956.

(*Continued on page 517*)

Numerical Solution of the Boundary-Layer Equations Without Similarity Assumptions

R. F. KRAMER AND H. M. LIEBERSTEIN*

Space Technology Laboratories, Inc.

SUMMARY

The Crocco transformation combined with a Mangler transformation is used to carry the boundary-layer problem for axially symmetric blunt bodies into a form suitable for direct numerical computation without introduction of similarity assumptions. Conditions which in the original problem appear at infinity now are brought to a finite straight line, and the body is transformed to a parallel line. Data can be generated on the stagnation line (perpendicular to the body) to serve as initial values, and since the equations are a parabolic system of two second-order equations, the boundary-value problem is analogous to the slab problem for the heat equation. An implicit difference equation is used to reduce stability difficulties. Special techniques in forming the difference equation result in a linear system of algebraic equations to be solved on any given line of integration, and these solutions are computed from recursion relations generated by back substitution. For bluntnosed bodies with approach flow Mach Numbers greater than 8 (approximately), large temperature gradients occur across a thin boundary layer of dissociated gas, and it is necessary to use real-gas effects, approximated here by certain fits to the gas tables. A case is computed, however, for a lower Mach Number approach flow using perfect-gas theory to provide a standard against which similarity solutions may be tested.

SYMBOLS

ρ = density
μ = viscosity
P = pressure
h = static enthalpy
H = total enthalpy $= h + 1/2u^2$
H' = normalized total enthalpy $= (H - H_0)/(H_1 - H_0)$
τ = frictional shearing stress $= \mu \partial u/\partial y$
T = transform of stress $= \tau(2s)^{1/2}/r\rho_1\mu_1 u_1^2$
P_r = Prandtl Number
R = maximum radius of body
r = radius of body (later r/R replaced by r)
z = axial distance from nose (later z/R replaced by z)
x = arc length from nose in meridional plane (later x/R replaced by x)
y = distance perpendicular to wall
u = velocity in x-direction (later u_1/a_s replaced by u_1)
u' = normalized velocity in x-direction $= u/u_1$
v = velocity in y-direction
θ = angle of body measured from axis
a_s = velocity of sound at stagnation
δ = "thickness" of boundary layer, fictitious value of y at which u equals the inviscid tangential velocity
γ, n = parameters describing the state laws
N, m = parameters describing the viscosity distribution
a_1, a_2 = parameters describing body shape
s = Mangler transformed x; i.e., $s = \int_0^x r^2\rho_1\mu_1 u_1 dx$
Δ_s = increment in s
Δx_e = minimum allowed increment in x
I = number of grid points in u' direction, $\Delta u' = 1/I$
i = index of points on a row
$( )_0$ = values at the body wall
$( )_1$ = values at the "edge" of the boundary layer
$( )_s$ = values at stagnation

Received August 11, 1958. Revised and received December 4, 1958.

* Now at Mathematics Research Center, U.S. Army, Madison, Wisconsin.

(1) INTRODUCTION

IT IS POPULAR in works on boundary layers to introduce similarity assumptions, assumptions about the form of the solution which reduce a difficult nonlinear partial differential system to one or more nonlinear ordinary differential equations, and these mathematical assumptions imply physical simplifications.[1] Even with a similarity assumption, it is often necessary to resort to numerical methods, and it is not clear that the ordinary differential equations that arise in this manner are a better numerical framework than the original partial differential system. As will be shown, if the Crocco transformation, combined with a Mangler transformation in the axially symmetric case, is introduced, the boundary-layer equations take a form which for a blunt body is quite suitable for direct numerical computation. All conditions at infinity are brought to a finite straight line, and the body is transformed to another parallel line. Values can then be generated on the stagnation line—which, in Crocco form, is perpendicular to the body—to serve as initial values, and, since the system of two second-order equations is of parabolic type, the resulting boundary value problem is analogous to the classical slab problem for the heat equation. Extensive experience has been accumulated on the numerical solution of the slab type problem for the heat equation,[2] and the work of this paper is simply a reasonable adaptation of this experience. In particular, it was shown by J. Crank and P. Nicolson[3] that for the heat equation an implicit difference scheme overcomes very restrictive conditions on the time step necessitated for the explicit scheme by stability considerations. Although this result has not been extended to our nonlinear equations, the implicit difference scheme was adopted here to reduce stability difficulties. Other authors may still prefer integral approaches, but the accumulation of experience with finite difference techniques in problems very similar to this one seems to make the approach of this paper the more natural choice.

Unfortunately, the important mathematical questions of existence and uniqueness do not seem to be completely resolved—singularities occur on the data

lines, but these questions are left to other workers. For that matter, rigorous derivation of the boundary-layer equations must be left to others.[4]

For blunt-nosed bodies in hypersonic flow, the boundary layer is thin in the stagnation region, and excellent pressure data on the edge of the boundary layer is provided from the inviscid theory.[5] Due to close agreement of the inviscid pressure data in reference 5 with the modified Newtonian theory of L. Lees (for rounded bodies in hypersonic flow), pressures are used at the edge of the boundary layer from his empirical theory. A quadratic body shape is allowed for in the code.

For very high Mach Number approach flows (say, $M > 8$), the fluid immediately behind the shock is extremely hot and the gas dissociates. It is still possible to obtain good accuracy in the stagnation region for the inviscid portion of the flow by treating the fluid as a perfect gas with an effective γ (reference 5) because temperature, pressure, and density gradients in that region are very small. However, at the edge of the boundary layer, the gas is hot while the body is cold, so that across the thin boundary layer large temperature gradients occur. Thus, some real gas effects must be included for high Mach Number approach flows if the results are to be physically realistic.

A dual purpose is intended; to provide a new framework for practical solutions of boundary-layer problems and to provide a standard against which solutions arising from similarity assumptions can be tested. The authors are indebted to M. Sweeney for many discussions of a fundamental nature.

(2) Crocco-Mangler Transformation— The Boundary Value Problem

The following equations govern axially symmetric compressible flow in the boundary layer about a body of revolution:

$$\left.\begin{aligned} &(\partial/\partial x)\,(r\rho u) + (\partial/\partial y)\,(r\rho v) = 0 \\ &\rho u(\partial u/\partial x) + \rho v(\partial u/\partial y) = \\ &\qquad -(dp/dx) + (\partial/\partial y)\,[\mu(\partial u/\partial y)] \\ &\rho u(\partial H/\partial x) + \rho v(\partial H/\partial y) = \\ &\qquad (\partial/\partial y)\,((\mu/P_r)\,\{(\partial H/\partial y) + \\ &\qquad (P_r - 1)\,[\partial(1/2u^2)/\partial y]\}) \end{aligned}\right\} \quad (2.1)$$

Boundary conditions are

$$\begin{aligned} &\text{at } y = 0: \quad u = v = 0, \quad H = H_0 = h_0, \\ &\text{at } y = \delta: \quad u = u_1, \quad v = 0, \quad H = H_1 \end{aligned}$$

It is assumed that H_0 and H_1 are constants. Also,

$$\begin{aligned} r &= r(x) \\ \rho &= \rho(h) \\ \mu &= \mu(h) \\ P_r &= \text{a constant} \end{aligned}$$

and

$$dp/dx = -\rho_1 u_1 (du_1/dx), \text{ a function of } x \text{ alone}$$

The following state laws in terms of parameters n and γ are used:

$$\left.\begin{aligned} &\text{(a)} \quad (\rho_1/\rho) = (h/h_1)^n \\ &\text{(b)} \quad (h_1/H_1) = (p_1/p_s)^{(\gamma-1)/\gamma} \\ &\text{(c)} \quad (\rho_1/\rho_s) = (p_1/p_s)^{1/\gamma} \end{aligned}\right\} \quad (2.2)$$

and the viscosity is described by

$$\mu_1/\mu_s = (h_1/H_1)^m, \quad \rho\mu/\rho_1\mu_1 = (h/h_1)^{-N} \quad (2.3)$$

Here a perfect gas is obtained by putting $n = 1$, and a constant viscosity law, for example, can be had by putting $m = 0$, $N = n$. The state laws (2.2) and viscosity distribution (2.3) were supplied by F. Hartwig who also supplied the values of parameters μ, γ, N, m, and H_0/H_1, used to compute our numerical examples.

The quantity v is now eliminated from Eqs. (2.1), and the Crocco transformation,

$$\begin{aligned} &x = \xi, \quad \xi = x, \\ &y = y(\xi, u), \quad u = u(x, y), \quad \tau = \mu(\partial u/\partial y) \end{aligned}$$

yields

$$\left.\begin{aligned} &u(\partial/\partial\xi)\,(r\rho\mu/\tau) - r(dp/dx)\,(\partial/\partial u)\,(\mu/\tau) + \\ &\qquad r(\partial^2\tau/\partial u^2) = 0 \\ &P_r(\rho u\mu/\tau)\,(\partial H/\partial\xi) + P_r\,\rho_1 u_1 (du_1/dx) \times \\ &\qquad (\mu/\tau)\,(\partial H/\partial u) + (P_r - 1)\,(\partial\tau/\partial u) \times \\ &\qquad [(\partial H/\partial u) - u] - \tau[(\partial^2 H/\partial u^2) + \\ &\qquad (P_r - 1)] = 0 \end{aligned}\right\} \quad (2.4)$$

At $x = 0$, the transformation is defined by insisting that all functions and the highest order derivatives appearing in Eqs. (2.4) be continuous in the sense that they take on the value of their limits (finite or infinite) on the stagnation line.

Applying then a Mangler's transformation,

$$\begin{aligned} &u' = u/u_1, \quad s = \int_0^x r^2\,\rho_1\mu_1 u_1 dx \\ &T = \tau(2s)^{1/2}/r\rho_1\mu_1 u_1^2, \quad H' = (H - H_0)/(H_1 - H_0) \end{aligned}$$

and replacing u_1/a_s, x/R, r/R, z/R with u_1, x, r, and z, respectively, we obtain finally the differential equations to be used in this paper. They are

$$\left.\begin{aligned} &A_1(\partial^2 T/\partial u'^2) + B_1(\partial T/\partial s) + C_1(\partial H'/\partial s) + \\ &\qquad D_1(\partial T/\partial u') + E_1(\partial H'/\partial u') + F_1 = 0 \\ &A_2(\partial^2 H'/\partial u'^2) + B_2(\partial T/\partial s) + C_2(\partial H'/\partial s) + \\ &\qquad D_2(\partial T/\partial u') + E_2(\partial H'/\partial u') + F_2 + \\ &\qquad G_2(\partial T/\partial u')\,(\partial H'/\partial u') = 0 \end{aligned}\right\} \quad (2.5)$$

where

$$A_1 = 1, \quad B_1 = -2su'(h/h_1)^{-N}/T^2$$

$$C_1 = -(2Nsu'/T)\,[1 - (H_0/H_1)] \times (p_1/p_s)^{(1-\gamma)/\gamma}(h/h_1)^{-N-1}$$

$$D_1 = (2s/u_1T^2)\,(du_1/ds)\,(h/h_1)^{-N}\,[u'^2 - (h/h_1)^n]$$

$$E_1 = (2s/u_1T)\,(du_1/ds)\,(h/h_1)^{-N-1}\,(p_1/p_s)^{(1-\gamma)/\gamma} \times [1 - (H_0/H_1)]\,[Nu'^2 + (n - N)\,(h/h_1)^n]$$

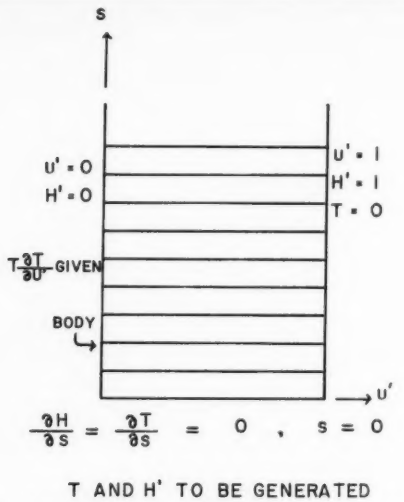

FIG. 1. Boundary value problem in the Crocco-Mangler variables.

$$F_1 = (u'/T)(h/h_1)^{-N}\,[1 - 4(s/u_1)\,(du_1/ds)] - 4(su'/u_1T)\,(du_1/ds)\,(h/h_1)^{-N-1} \times [(p_1/p_s)^{(1-\gamma)/\gamma} - 1]\,[Nu'^2 + (n - N)\,(h/h_1)^n] - [2Nsu'(\gamma - 1)/\gamma T]\,[u'^2 - (h/h_1)] \times (p_1/p_s)^{-1}\,(h/h_1)^{-N-1}\,(\partial/\partial s)\,(p_1/p_s)$$

$$A_2 = T^2, \quad B_2 = 0, \quad C_2 = -2P_r u' s (h/h_1)^{-N}$$

$$D_2 = (P_r - 1)u_1^2 u' T/(H_1 - H_0)$$

$$E_2 = (2P_r s/u_1)\,(du_1/ds)\,(h/h_1)^{-N}\,[u'^2 - (h/h_1)^n]$$

$$F_2 = u_1^2(P_r - 1)T^2/(H_1 - H_0)$$

$$G_2 = -(P_r - 1)T$$

The boundary conditions now become

$$\left.\begin{aligned} &\text{at } u' = 0\text{:}\quad T(\partial T/\partial u') = -2(s/u_1) \times [(p_1/p_s)^{(1-\gamma)/\gamma}(H_0/H_1)]^{n-N}(du_1/ds), \\ &\qquad\qquad H' = 0 \\ &\text{at } u' = 1\text{:}\quad T = 0, \quad H' = 1 \end{aligned}\right\} \tag{2.6}$$

The quantity u_1 is generated from the Bernoulli law which is valid at the edge of the boundary layer—i.e.,

$$u_1 = \{[2/(\gamma - 1)]\,[1 - (p_1/p_s)^{(\gamma-1)/\gamma}]\}^{1/2}$$

and the static enthalpy is given by

$$h/h_1 = (\rho_1/\rho_s)^{(1-\gamma)/\gamma}\,\{[1 - (H_0/H_1)]H' + (H_0/H_1)\} - [(\rho_1/\rho_s)^{(1-\gamma)/\gamma} - 1]\,u'^2$$

The modified Newtonian pressure distribution

$$p_1/p_s = \sin^2\theta \tag{2.7}$$

is assumed at the edge of the boundary layer, and the body of revolution is taken to be a quadratic

$$r^2 = a_2 z^2 + a_1 \tag{2.8}$$

It can be shown that system (2.5) is of parabolic type and that the characteristics are the lines s = constant. Hence, we would expect to be given initial data on the characteristic $s = 0$ as well as along the lines $u' = 0$ and $u' = 1$, as displayed in Eq. (2.6). But note that in Eqs. (2.5) as $s \to 0$, the coefficients of $\partial H'/\partial s$ and $\partial T/\partial s$ go to 0. Hence, at $s = 0$, Eqs. (2.5) become ordinary differential equations with two-point boundary conditions.

In the next section, we will derive this ordinary differential problem and show how it can be solved to yield initial data on $s = 0$. In passing, let us mention that the obvious singularity on the line $u' = 1$ causes no numerical difficulty since $u' = 1$ is not an initial line, and no differential equation coefficient is evaluated there (Fig. 1).

(3) Generation of Data at the Stagnation Line

Consider Eqs. (2.5) and boundary conditions (2.6) to be defined for $s < 0$, although they were derived in Section (2) only for $s \geq 0$. Further, consider a region R_ϵ for which $0 < u' < 1$, $-\epsilon < s < \infty$, $\epsilon > 0$, and define a solution of Eq. (2.5) to be regular in R_ϵ if all derivatives appearing in Eq. (2.5) are continuous on the interior of that R_ϵ. Then, *we assume that there exists one and only one solution of Eq. (2.5), satisfying conditions (2.6), which is regular in some* R_ϵ, and we seek that solution. This "unique continuation" assumption seems to be essential in the generation of data H', T on the stagnation line, and it also yields immediately the data $\partial H'/\partial s$, $\partial T/\partial s$ on that line. Thus, both Eqs. (2.5) and boundary conditions (2.6) are invariant if s is replaced by $-s$. Therefore, $H'(u', s) = H'(u', -s)$ and $T(u', s) = T(u', -s)$. But, according to the above assumption, $\partial H'/\partial s$ and $\partial T/\partial s$ are continuous at $s = 0$, and it follows that $\partial H'/\partial s = \partial T/\partial s = 0$ at $s = 0$. Consistent with the accuracy of the finite difference approximations (4.1)–(4.3) used in the rest of the scheme, we put H' and T on the first data line equal to the values generated for the initial data line.

It is interesting to note that the Crocco similarity solutions were obtained assuming that $\partial H'/\partial x = \partial p/\partial x = 0$ identically throughout.[1]

We adopt the convention that $f(x) \to 0$ like x^n if $\lim_{x\to 0} x^{-n} f(x) = a$, and $f(x) \to \infty$ like $1/x^n$ if $\lim_{x\to 0} x^n f(x) = a$, $0 < |a| < \infty$. Then the following limits, as $x \to 0$, are deduced:

$$\left.\begin{aligned} &(h/h_1) \to [1 - (H_0/H_1)]H' + (H_0/H_1), \quad (h_0/H_1) \to 1, \quad (p_1/p_s) \to 1 \\ &s \to 0 \text{ like } x^4, \quad u_1 \to 0 \text{ like } x \\ &s(d/ds)\,(p_1/p_s) \to 0 \text{ like } x^2, \quad (du_1/ds) \to \infty \text{ like } (1/x^3) \\ &(s/u_1)\,(du_1/ds) \to (1/4), \quad (d/ds)\,(p_1/p_s) \to \infty \text{ like } (1/x^2), \\ &(d/dx)\,(p_1/p_s) \to 0 \text{ like } x, \quad (du_1/dx) \to [-(1/\gamma)\,(d^2/dx^2)\,(p_1/p_s)]^{1/2}, \\ &[(2s)^{1/2}/ru_1] \to [32/\gamma a_1^2]^{-(1/4)} \end{aligned}\right\} \tag{3.1}$$

By virtue of the definition of our transformations on the stagnation line, we now substitute these limits in Eqs. (2.5) and obtain

$$\left.\begin{aligned}
(d^2T/du'^2) + \{(1/2T^2)\,(h/h_1)^{-N} \times \\
[u'^2 - (h/h_1)^n]\}\,(dT/du') + \\
\{(1/2T)\,(h/h_1)^{-N-1}\,[1 - (H_0/H_1)] \times \\
[Nu'^2 + (n - N)\,(h/h_1)^n]\}\,(dH'/du') = 0 \\
T^2(d^2H'/du'^2) + \{(P_r/2)\,(h/h_1)^{-N} \times \\
[u'^2 - (h/h_1)^n]\}\,(dH'/du') - (P_r - 1) \times \\
T(dT/du')\,(dH'/du') = 0
\end{aligned}\right\} \quad (3.2)$$

Adopting the notation

$$H^* = [1 - (H_0/H_1)]\,H' + (H_0/H_1)$$

$$A(u', H^*) = H^{*-N}[u'^2 - H^{*n}]$$

and noting that

$$A'(u', H^*) = -H^{*-N-1}\,[Nu'^2 + (n - N)H^{*n}] \times (dH^*/du') + 2u'H^{*-N}$$

Eqs. (3.2) become

$$\left.\begin{aligned}
(d^2T/du'^2) + (1/2T^2)A(u', H^*)\,(dT/du') - \\
(1/2T)A'(u', H^*) + (1/T)u'H^{*-N} = 0 \\
T^2(d^2H^*/du'^2) + (P_r/2)A(u', H^*)(dH^*/du') - \\
(P_r - 1)T(dT/du')(dH^*/du') = 0
\end{aligned}\right\} \quad (3.3)$$

with the boundary conditions

$$H^*(0) = H_0/H_1$$

$$T(dT/du')\,(0) = -(1/2)\,(H_0/H_1)^{n-N}$$

$$H^*(1) = 1, \quad T(1) = 0$$

Now making the definitions

$$Q = dH^*/du', \quad P = [A(u', H^*)/2] - T(dT/du')$$

Eqs. (3.3) reduce to the following system:

$$\left.\begin{aligned}
(d/du')\,(PT^2) &= u'H^{*-N}\,T^2 + \\
&\quad 3P\{[A(u, H^*)/2] - P\}, \\
dH^*/du' &= Q, \\
dT^2/du' &= 2\{[A(u', H^*)/2] - P\}, \\
(d/du')\,(QT^2) &= Q\{[A(u', H^*)/2] - P\} - \\
&\quad P_r \cdot P \cdot Q
\end{aligned}\right\} \quad (3.4)$$

with boundary conditions

$$H^*(0) = H_0/H_1, \quad PT^2(0) = 0,$$

$$H^*(1) = 1, \quad T^2(1) = 0$$

This ordinary differential system is solved by an iterative scheme in which an initial guess is made for $T^2(0)$ and $Q(0)$, and this guess is corrected in proportion to the errors in $H^*(1)$ and $T^2(1)$. Solutions are formed by the Runge-Kutta-Gill method. We thus generate data H', T for the stagnation line.

(4) Partial Difference Equations

Having obtained data H' and T at a finite number of points on the initial line $s = 0$, we wish to generate data on successive lines s = constant at values of u' where data points appear on the initial line. Denoting mesh sizes in the u'- and s-directions by $\Delta u'$ and Δs, and choosing a set of three points on each of two successive lines,

$$\begin{array}{ccc} d & e & f \\ x & x & x \\ \\ x & x & x \\ a & b & c \end{array}$$

we make the following finite difference approximations to the derivatives that appear in Eqs. (2.5):

$$\partial H'/\partial s = [(H_e' - H_b')/\Delta s], \quad \partial H'/\partial u' = (1/4\Delta u')\,(H_a' - H_c' + H_d' - H_f') \quad (4.1)$$

$$\partial^2 H'/\partial u'^2 = [1/2(\Delta u')^2] \times (H_a' - 2H_b' + H_c' + H_d' - 2H_e' + H_f') \quad (4.2)$$

$$(\partial H'/\partial u')\,(\partial T/\partial u) = [1/8(\Delta u')^2]\,[(H_a' - H_c') \times (T_d - T_f) + (H_d' - H_f')\,(T_a - T_c)] \quad (4.3)$$

Such approximations lead to implicit numerical schemes since more than one unknown quantity (those with subscripts d, e, and f) now appear in the difference analog to the differential Eqs. (2.5). The technique is to write the difference equation for each set of three points on a new data line and, since the end points of the line are given, to obtain a system of n equations in n unknowns to be solved on the new line. This system of equations can be solved in a simple way if the system of n equations obtained for each row is linear. Thus, the difference approximations (4.1) and (4.2) are standard for an implicit scheme, but Eq. (4.3) is especially chosen so that unknown quantities appear linearly. Admittedly, this difference scheme is complicated by comparison with an explicit formula (involving one unknown only in every difference approximation); but implicit schemes have been very successful in work on the heat equation. For that equation, they avoid very restrictive conditions on the time step (analogous to s-step here) necessitated by stability considerations in explicit schemes.[3] Although no stability analysis has been attempted here, computations have been carried out here to three significant digits without revealing any trace of instability. It hardly needs to be emphasized that stability is the basic consideration in numerical solution of boundary-layer problems, but we do wish to emphasize that a severe restriction on the step size Δs could be a very limiting condition because of the relation of the Mangler variable s to arc length x.

In passing from Eq. (2.5) to the difference equation by way of Eqs. (4.1)–(4.3), coefficients of Eq. (2.5) are evaluated at the point b. Letting i be an index of points on a given row (s = constant) such that $i = 0$ at $u' = 0$ and $i = I$ at $u' = 1$, the set of $2(I - 1)$ linear equations in the $2(I - 1)$ unknowns H_i, T_i to be solved on that row takes the following form:

TABLE 1(a)
Selection of Values of $H' = H'(u', x)$ for Case 1 (Perfect Gas)

.901	.000	.053	.111	.175	.246	.325	.414	.517	.636	.782	1.000
.798	.000	.056	.116	.182	.254	.334	.424	.525	.643	.786	1.000
.702	.000	.058	.120	.187	.261	.341	.431	.531	.648	.789	1.000
.601	.000	.060	.123	.192	.266	.347	.436	.536	.652	.791	1.000
.500	.000	.061	.126	.195	.270	.351	.440	.540	.655	.793	1.000
.398	.000	.062	.128	.198	.273	.354	.444	.543	.657	.794	1.000
.299	.000	.063	.129	.199	.275	.357	.446	.545	.659	.795	1.000
.198	.000	.063	.130	.201	.276	.358	.448	.547	.660	.795	1.000
.102	.000	.064	.130	.201	.277	.359	.449	.548	.660	.796	1.000
0	.000	.064	.131	.202	.278	.359	.449	.548	.661	.796	1.000
x / u'	0	.1	.2	.3	.4	.5	.6	.7	.8	.9	1.0

TABLE 1(b)
Selection of Values of $T = T(u', x)$ for Case 1 (Perfect Gas)

.901	.971	.909	.841	.767	.688	.603	.512	.413	.303	.175	.000
.798	.917	.863	.803	.738	.666	.589	.504	.410	.303	.176	.000
.702	.882	.833	.778	.718	.652	.579	.498	.407	.302	.176	.000
.601	.855	.809	.759	.703	.641	.572	.494	.405	.302	.176	.000
.500	.834	.792	.745	.692	.633	.566	.491	.404	.302	.177	.000
.398	.820	.780	.734	.684	.627	.562	.488	.403	.301	.177	.000
.299	.810	.771	.727	.678	.622	.559	.486	.402	.301	.177	.000
.198	.803	.765	.722	.674	.619	.557	.485	.401	.301	.177	.000
.102	.799	.762	.720	.672	.618	.556	.484	.401	.301	.177	.000
0	.798	.761	.719	.671	.617	.556	.484	.401	.301	.177	.000
x / u'	0	.1	.2	.3	.4	.5	.6	.7	.8	.9	1.0

TABLE 2(a)
Selection of Values of $H' = H'(u', x)$ for Case 2 (Hot Gas)

.900	.000	.053	.113	.178	.251	.334	.426	.532	.654	.799	1.000
.799	.000	.057	.119	.187	.262	.345	.437	.541	.661	.802	1.000
.699	.000	.060	.125	.194	.270	.354	.446	.547	.666	.805	1.000
.599	.000	.062	.129	.200	.277	.361	.452	.554	.670	.806	1.000
.502	.000	.064	.132	.204	.282	.366	.457	.558	.672	.807	1.000
.398	.000	.066	.135	.208	.286	.370	.461	.561	.675	.808	1.000
.298	.000	.067	.137	.210	.289	.373	.464	.564	.676	.809	1.000
.199	.000	.067	.138	.212	.291	.375	.465	.565	.677	.809	1.000
.099	.000	.068	.139	.213	.292	.376	.467	.566	.678	.809	1.000
.000	.000	.068	.139	.213	.292	.376	.467	.566	.678	.809	1.000
x / u'	0	.1	.2	.3	.4	.5	.6	.7	.8	.9	1.0

TABLE 2(b)
Selection of Values of $T = T(u', x)$ for Case 2 (Hot Gas)

.900	.900	.845	.783	.716	.642	.564	.480	.389	.287	.167	.000
.799	.838	.793	.741	.683	.620	.550	.473	.386	.287	.168	.000
.699	.796	.757	.712	.661	.604	.540	.467	.384	.287	.169	.000
.599	.767	.732	.692	.645	.592	.532	.463	.383	.288	.170	.000
.502	.746	.715	.677	.634	.584	.527	.460	.382	.288	.170	.000
.398	.731	.701	.666	.626	.578	.523	.458	.381	.288	.171	.000
.298	.720	.692	.659	.620	.574	.520	.456	.380	.288	.171	.000
.199	.714	.687	.654	.616	.571	.518	.455	.380	.288	.171	.000
.099	.710	.683	.652	.614	.570	.517	.454	.379	.288	.171	.000
.000	.709	.682	.651	.613	.569	.517	.454	.379	.287	.170	.000
x / u'	0	.1	.2	.3	.4	.5	.6	.7	.8	.9	1.0

$$\left.\begin{aligned} A_{1i}H'_{i+1} + B_{1i}H_i' + C_{1i}H'_{i-1} + D_{1i}T_{i+1} + \\ E_{1i}T_i + F_{1i}T_{i-1} = G_{1i} \\ A_{2i}H'_{i+1} + B_{2i}H_i' + C_{2i}H'_{i-1} + \\ D_{2i}T_{i+1} + E_{2i}T_i + F_{2i}T_{i-1} = G_{2i}, \\ i = 1, 2, \ldots, \quad I - 1 \end{aligned}\right\} \quad (4.4)$$

Here

$$H_0' = 0, \quad T_0 = T_1 + (\Delta u' 2s/u_1 T_0^{(j-1)_1}) \times [(p_1/p_s)^{(1-\gamma)/\gamma}\ (H_0/H_1)]^{n-N}\ (du_1/ds), \quad H_I = 1, \quad T_I = 0$$

Exact equations for the coefficients in Eq. (4.4) can be derived from Eqs. (2.5), (4.1)–(4.3), and they will not be quoted here. It should be emphasized that these coefficients are to be evaluated at the point i on the previous or known row.

(5) Solution of the Difference Equations

Certain recursions allow one to solve the system (4.4) for the unknown values of H_i', T_i on a new row making use, of course, of boundary relations at $u' = 0$ and $u' = 1$. This will be accomplished in two scannings of the row proceeding in opposite directions. These formulas are well adapted for machine computation—e.g., one row of 40 points takes 5 sec. on an IBM-704 computer. One notes, incidentally, that the coefficient matrix of Eq. (4.4) can be partitioned into four tridiagonal matrices of equal order, and thus has, as expected, a certain similarity to the single tridiagonal matrix associated with the heat equation.

It is clear that there exist relations of the form

$$\left.\begin{aligned} H'_{i-1} &= L^{(1)}{}_{i-1} + L^{(2)}{}_{i-1}H_i' + L^{(3)}{}_{i-1}T_i \\ T_{i-1} &= K^{(1)}{}_{i-1} + K^{(2)}{}_{i-1}H_i' + K^{(3)}{}_{i-1}T_i \end{aligned}\right\} \quad (5.1)$$

In order to determine coefficients, we substitute the expressions (5.1) in Eqs. (4.4) and collect like terms. Then, we have

$$\left.\begin{aligned} B_{1i}{}^*H_i + E_{1i}{}^*T_i &= G_{1i}{}^* - A_{1i}H_{i+1} - D_{1i}T_{i+1} \\ B_{2i}{}^*H_i + E_{2i}{}^*T_i &= G_{2i}{}^* - A_{2i}H_{i+1} - D_{2i}T_{i+1} \end{aligned}\right\} \quad (5.2)$$

where

$$\left.\begin{aligned} B_{1i}{}^* &= B_{1i} + F_{1i}K_{i-1}{}^{(2)} + C_{1i}L_{i-1}{}^{(2)} \\ E_{1i}{}^* &= E_{1i} + F_{1i}K_{i-1}{}^{(3)} + C_{1i}L_{i-1}{}^{(3)} \\ B_{2i}{}^* &= B_{2i} + F_{2i}K_{i-1}{}^{(2)} + C_{2i}L_{i-1}{}^{(2)} \\ E_{2i}{}^* &= E_{2i} + F_{2i}K_{i-1}{}^{(3)} + C_{2i}L_{i-1}{}^{(3)} \\ G_{1i}{}^* &= G_{1i} - F_{1i}K_{i-1}{}^{(1)} - C_{1i}L_{i-1}{}^{(1)} \\ G_{2i}{}^* &= G_{2i} - F_{2i}K_{i-1}{}^{(1)} - C_{2i}L_{i-1}{}^{(1)} \end{aligned}\right\} \quad (5.3)$$

Solving for H_i' and T_i, we have

$$\left.\begin{aligned} H_i' &= L_i{}^{(1)} + L_i{}^{(2)}H'_{i+1} + L_i{}^{(3)}T_{i+1} \\ T_i &= K_i{}^{(1)} + K_i{}^{(2)}H'_{i+1} + K_i{}^{(3)}T_{i+1} \end{aligned}\right\} \quad (5.4)$$

where

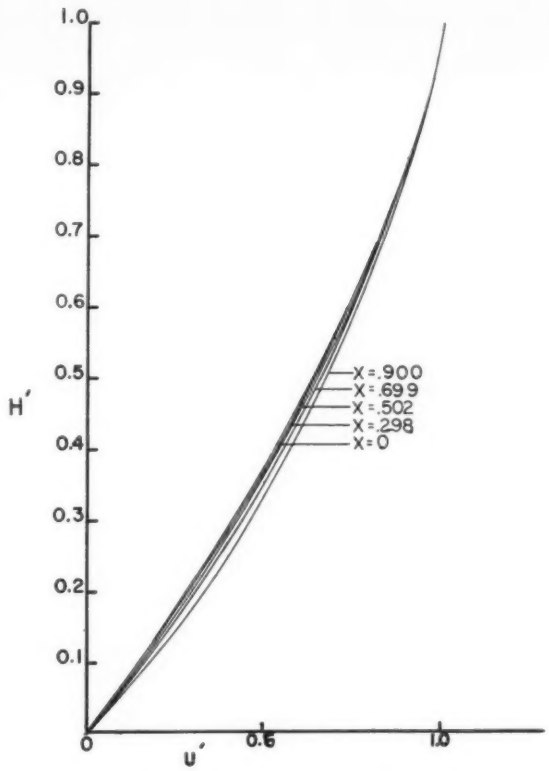

FIG. 1(a). H' vs. u' for selected values of x, case 1 (perfect gas).

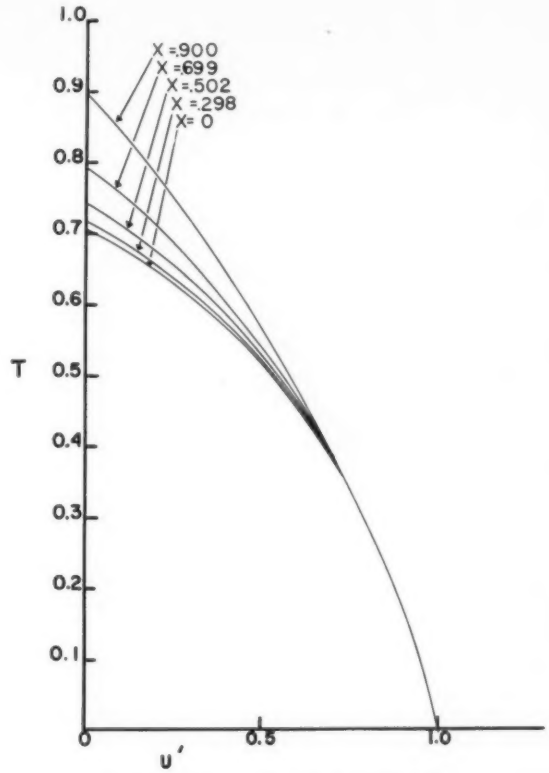

FIG. 1(b). T vs. u' for selected values of x, case 1 (perfect gas).

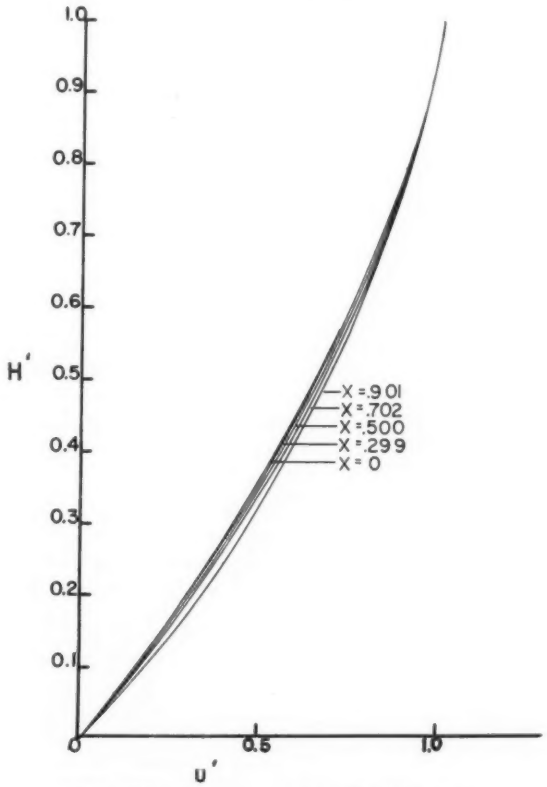

FIG. 2(a). H' vs. u' for selected values of x, case 2 (hot gas).

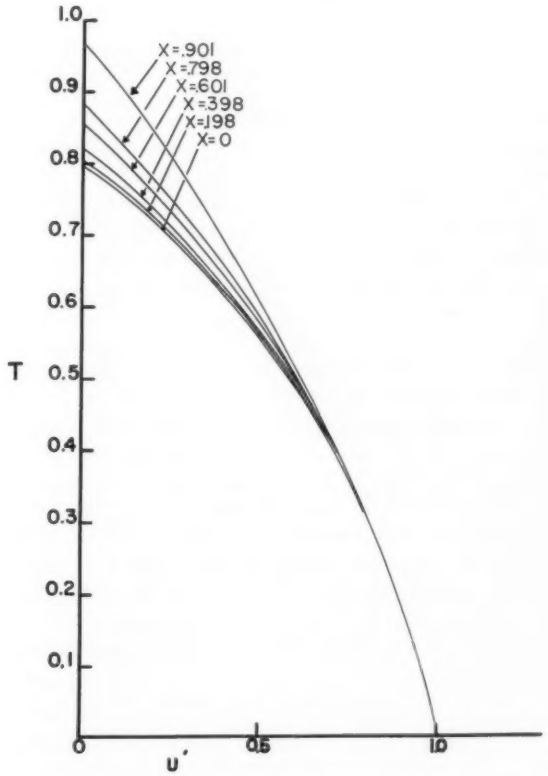

FIG. 2(b). T vs. u' for selected values of x, case 2 (hot gas).

$$
\left.
\begin{aligned}
L_i^{(1)} &= (E_{2i}{}^*G_{1i}{}^* - E_{1i}{}^*G_{2i}{}^*) \div (E_{2i}{}^*B_{1i}{}^* - E_{1i}B_{2i}{}^*) \\
L_i^{(2)} &= (E_{1i}{}^*A_{2i} - E_{2i}{}^*A_{1i}) \div (E_{2i}{}^*B_{1i}{}^* - E_{1i}{}^*B_{2i}{}^*) \\
L_i^{(3)} &= (E_{1i}{}^*D_{2i} - E_{2i}{}^*D_{1i}) \div (E_{2i}{}^*B_{1i}{}^* - E_{1i}{}^*B_{2i}{}^*) \\
K_i^{(1)} &= (B_{2i}{}^*G_{1i}{}^* - B_{1i}{}^*G_{2i}{}^*) \div (B_{2i}{}^*E_{1i}{}^* - B_{1i}{}^*E_{2i}{}^*) \\
K_i^{(2)} &= (B_{1i}{}^*A_{2i} - B_{2i}{}^*A_{1i}) \div (B_{2i}{}^*E_{1i}{}^* - B_{1i}{}^*E_{2i}{}^*) \\
K_i^{(3)} &= (B_{1i}{}^*D_{2i} - B_{2i}{}^*D_{1i}) \div (B_{2i}{}^*E_{1i}{}^* - B_{1i}{}^*E_{2i})
\end{aligned}
\right\} \quad (5.5)
$$

But from the boundary conditions at the body we know that

$$
\left.
\begin{aligned}
K_0^{(1)} &= 2\Delta u'(s/u_1T_0) \times [(p_1/p_s)^{(1-\gamma)/\gamma}\,(H_0/H_i)]^{n-N}\,(du_1/ds) \\
K_0^{(3)} &= 1, \\
K_0^{(2)} &= L_0^{(1)} = L_0^{(2)} = L_0^{(3)} = 0
\end{aligned}
\right\} \quad (5.6)
$$

Thus, scanning first from the body to the edge of the boundary layer and starting with initial values (5.6), we use the recursions (5.3) and (5.5) to find $K_i^{(1)}$, $K_i^{(2)}$, $K_i^{(3)}$, $L_i^{(1)}$, $L_i^{(2)}$, and $L_i^{(3)}$ for $i = 1, \ldots, I-1$. Then, returning in the reverse direction, we use recursions (5.4) to obtain H_i' and T_i for $i = I-1, \ldots, 0$ using $H_I' = 1$, $T_I = 0$ as initial values.

(6) Inversion of the Crocco Transformation—Variable Mesh

One is interested in examining solutions in terms of the physical coordinate x on the body. Further, one must know θ at each new point on the edge of the boundary layer in order to get p_1 since one of the boundary conditions at $u' = 0$ is given in terms of p_1. Given the body shape (2.8) and the pressure distribution (2.7), from the definition of s,

$$ds/dx = r^2 p_1 \mu_1 u_1$$

formulas can be written for dx/ds and $d\theta/ds$. These are integrated numerically along the boundary $u' = 0$ (simultaneously with the partial integration on the interior) by the Runga-Kutta-Gill procedure.

As stated earlier, s tends to zero like x^4, so that, if the same mesh size Δs is used throughout, one will reach a point where many lines of integration will be required to make even a small advance in arc length x. Thus, the calculation is started with a certain small Δs, but, whenever one line of integration corresponds to a change in x which is less than Δx_c, an input parameter, then Δs is doubled. In this way, Δs controls only truncation errors near the stagnation line, while Δx_c is the critical overall mesh parameter.

(7) Numerical Examples

Physical consequences and comparison to similarity solutions will not be discussed here. In fact, it is to be hoped that other authors whose training and interests uniquely equip them for the task will undertake that phase of the work. We give two numerical examples for a hemisphere: case 1, for a perfect or cold gas; and case 2, for a dissociated or hot gas.

The choice of H_0/H_1, an input parameter here, depends both on approach flow conditions and on materials used in construction of the body. In order to be able to compute H_1 as a part of the mathematical program, one would require a routine for solving the boundary-layer problem and heat conduction problem for the body simultaneously. Incidentally, no theoretical difficulty would be introduced by treating H_1 as a function of arc length x, but the differential equations would be slightly altered.

In the two cases cited above for which data is given here, the same value of H_0/H_1 is used, so that a comparison of real- and perfect-gas results can be seen. The parameters are, as follows:

case 1: (perfect gas) $m = 0.76$, $\gamma = 1.4$, $P_r = 0.71$, $N = 0.24$, $H_0/H_1 = 0.25$, $n = 1$, $I = 40$

case 2: (hot gas) $m = 0.41$, $\gamma = 1.17$, $P_r = 0.71$, $N = 0.35$, $H_0/H_1 = 0.25$, $n = 0.76$, $I = 40$

Calculations have been carried out to three significant digits. Tables of a selection of data are given for H' and T for case 1 in Tables 1(a) and 1(b); for case 2 in Tables 2(a) and 2(b). Plots of H' vs. u' and T vs. u' for selected values of x for cases 1 and 2 are given in Figs. 1(a) and 1(b) and Figs. 2(a) and 2(b), respectively.

References

[1] Pai, S. I., *Viscous Flow Theory*, Vol. 1, pp. 201–205; D. Van Nostrand, Inc., Princeton, N.J., 1956.

[2] Ehrlich, L., *A Numerical Method of Solving a Heat Problem with Moving Boundary*, J. Assoc. Comp. Mach.

[3] Crank, J., and Nicolson, P., *A Practical Method for Numerical Evaluation of Solutions of Partial Differential Equations of the Heat Conduction Type*, Proc. Cambridge Phil. Soc., Vol. 45, pp. 50–67, Cambridge, 1947.

[4] Friedrichs, K. O., *Asymptotic Phenomena in Mathematical Physics*, Bull. Am. Math. Soc., Vol. 61, No. 6, pp. 489–490.

[5] Garabedian, P. R., and Lieberstein, H. M., *On the Numerical Calculation of Detached Bow Shock Waves in Hypersonic Flow*, Journal of the Aeronautical Sciences, Vol. 25, No. 2, pp. 109–118, February, 1958.

[6] Schlichting, H., *Boundary Layer Theory;* McGraw-Hill Book Co., Inc., London, 1955.

A Cool Mercury Plasma Tunnel

HANS U. ECKERT*

Convair, San Diego, A Division of General Dynamics Corporation

SUMMARY

Radio-frequency excitation of supersonic flow is discussed as a possible means to study effects of ionization at moderate temperatures. The heat of recombination counteracts liquefaction of the flow during expansion and permits the use of a vaporized liquid as testing medium. The flow can therefore be generated without pumps by an evaporation-condensation cycle. Mercury is selected as the most suitable medium. A small tunnel built upon these considerations is described.

INTRODUCTION

IN ORDER TO PERMIT the study of ionization effects in continuous flows while avoiding the high temperatures required for thermal ionization, applicability of glow discharges to supersonic flows has been investigated since September, 1956, at the Convair Scientific Research Laboratory. It is well known that in discharges of this type only the electron component of the gas acquires energy comparable to the gas ionization potential, while the main body remains far below this level.[1] If heating of duct walls by electron diffusion becomes excessive, a magnetic field parallel to the duct and strong enough to make radii of electron orbits small compared to their mean free path should provide efficient shielding.[2]

For production of breakdown and ionization in the gas it appears advantageous to employ a high-frequency electromagnetic field, since then the discharge can be made "electrodeless"—i.e., electrodes need not be in contact with the flow and do not cause obstruction or contamination.[3] If a high-frequency discharge is maintained in the supersonic portion of a Laval nozzle, the heat conveyed to the flow by recombination and other loss processes will raise static and total temperatures and counteract the cooling by expansion.† While larger area and total-pressure ratios will be required to produce a certain Mach Number, in this way one does not have to heat the gas to high temperature in the stagnation chamber to prevent liquefaction and therefore avoids the problem of cooling the throat. It is, in fact, not necessary to use a permanent gas. One can vaporize a liquid at a suitable pressure and superheat the vapor to that temperature at which recondensation in the nozzle is avoided before the discharge takes over. The low-pressure zone into which the flow discharges can then simply be provided by recondensation of the vapor on a cold surface. The advantage of such a two-phase drive system for low-density tunnels over conventional pumping has been pointed out and first verified in a water-vapor tunnel by Chuan.[6]

For the present case the testing fluid should preferably be a pure monatomic substance to avoid unnecessary complications of the discharge processes. It should also be easy to ionize without being corrosive. Further, with respect to the two-phase operation it should display the relevant portion of the vapor-pressure curve, say 10^{-3} to 10^{3} mm. Hg, in a convenient temperature range. The best compromise between these requirements seems to be mercury, as is indicated by its extensive use for electrical discharges as well as for diffusion pumps. Some properties of Hg-vapor that are of gasdynamic interest have been compiled in reference 7.

The above considerations have led to design and construction of a small tunnel plus electronic equipment which is briefly described in the following. Fig. 1 shows a schematic drawing of the tunnel and explains the main features. The entire system is blown out of pyrex glass except for the nozzle, which is made of vycor to withstand higher temperatures. The biconical nozzle has a throat diameter of 4 mm. The exit diameter is 50 mm. and the length of the supersonic portion 130 mm. The nozzle and the other parts are connected by ground joints and are interchangeable. A small vacuum pump keeps the residual air pressure at the micron level. The mercury at the bottom of the boiler is heated to temperatures between 200 and 250°C., corresponding to vapor pressures (and approximately stagnation pressures) between 15 and 75 mm. Hg. A resistance coil embedded in a glass spiral that stretches from top to bottom of the boiler allows superheating of the vapor to about 450°C. To reduce heat losses the walls are also heated electrically and carry heavy asbestos insulation.

The spherical condenser vessel downstream of the nozzle is cooled by water flowing from a perforated ring over the sphere into a funnel. This allows the maintainance of a vapor pressure inside the vessel of about 10 micron Hg. The available pressure ratio is therefore of the order of 5,000. Ground joints on top and at rear end of the condenser permit insertion of probes or windows for flow observation. The mercury condensed on the walls flows by gravity through the return duct back into the boiler. Mass flow at $p_0 = 50$ mm. Hg and $T_0 = 450$°C. is about 0.35 grams/sec. At these stagnation conditions the flow can expand to a Mach Number of only 1.55 before reaching the saturation line, and energy addition is required to avoid lique-

Received September 2, 1958.

* Staff Scientist, Convair Scientific Research Laboratory.

The author wishes to thank J. B. Roes for designing the special electronic equipment and assistance at the tests and to C. Hodapp for his skillful glass work.

† This has also been suggested recently by Chuan.[4] Experiments by Smith and Early[5] to employ a direct current arc for this purpose were not successful.

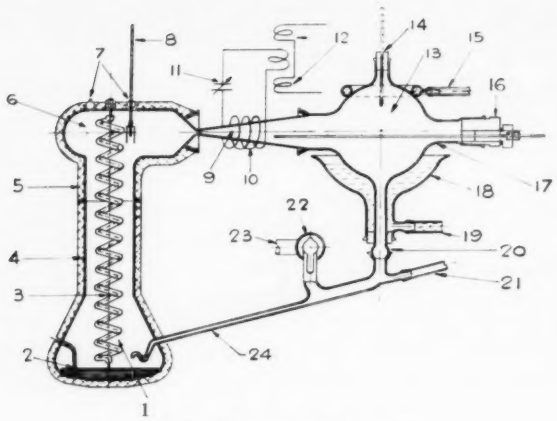

FIG. 1. Mercury vapor tunnel.

(1)	Boiler vessel with mercury pool	(12)	Radio frequency generator tank cycle coil
(2)	Thermocouple for pool temperature	(13)	Flow condensation chamber
(3)	Superheater coil	(14)	Thermometer
(4)	Resistance wires	(15)	Cooling water inlet
(5)	Asbestos insulation	(16)	Conical joint with probe holder
(6)	Settling chamber	(17)	Probe or model sting
(7)	Ball joints for probing stagnation conditions	(18)	Funnel
(8)	Shielded thermometer	(19)	Water outlet
(9)	Laval nozzle with ball joints	(20)	Ball joint
(10)	Excitation coil	(21)	Connection to vacuum gage
(11)	Variable high voltage condenser	(22)	Stop cock
		(23)	Connection to vacuum pump
		(24)	Return duct with liquid trap

faction at higher Mach Numbers. This can be done by electrostatic or electromagnetic action of the high-frequency field. In the latter type of excitation, which has been given preference, the supersonic portion of the nozzle is surrounded by a coil of from two to six windings which, together with the oscillator coupling coil and a variable condenser, forms a circuit as indicated in Fig. 1. This circuit is tuned for optimum load adaptation.

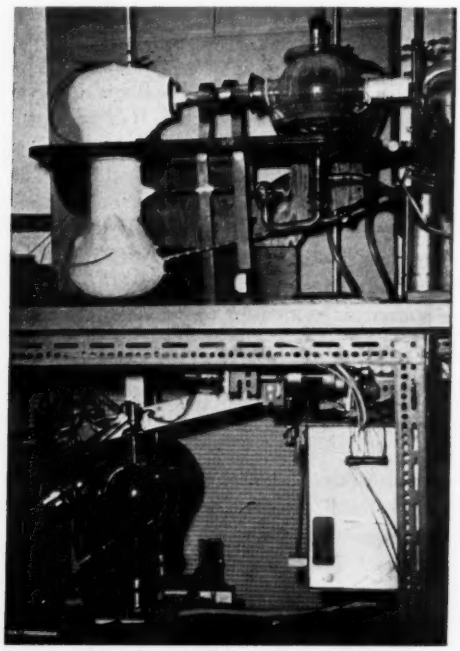

FIG. 2. Arrangement of tunnel and radio frequency generator.

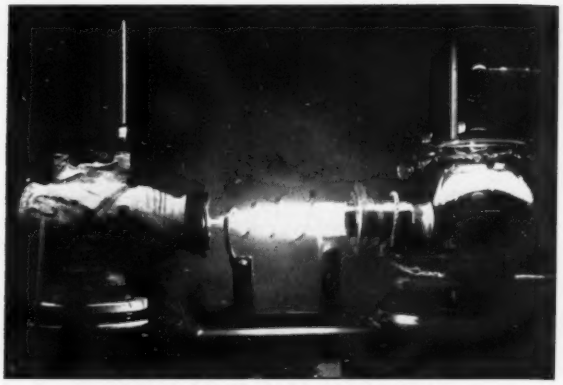

FIG. 3. Flow in high excitation state. Radio frequency power ≈ 1 kilowatt.

Fig. 2 shows a view of the tunnel and part of the oscillator which is separated from the power supply and control unit. The self-excited oscillator works at a fixed frequency of about 29 megacycles and employs two Eimac T2000 tubes in push-pull circuitry which are capable of an output of 10 kw. This equipment is described in detail in reference 8.

Visual observation of the discharge indicates qualitatively the same phenomena that have been reported from tests with static gas volumes.[9] This appears obvious if one considers that a discharge of this kind is controlled by electron and ion diffusion[10] and that the gas velocity is only a fraction of their diffusion velocity.

Breakdown is initiated by the electrostatic field between the coil ends. If the oscillator output is increased to an extent where the induced voltage can sustain the discharge, ring currents are generated in the gas. They can be easily recognized by the large increase in brightness which starts at the downstream end of the nozzle and with increasing oscillator power gradually moves upstream until the entire divergent portion is filled. This condition has been photographed and is shown in Fig. 3. Oscillator output is here of the order of 1 kw. and the flow is probably choked. That supersonic flow exists at lower outputs has been demonstrated with small glass models inserted into the stream. Fig. 4 shows the flow around a cone-cylinder of 6 mm. base diameter. Assuming $\gamma = 1.67$, a Mach Number of 3.1 has been determined

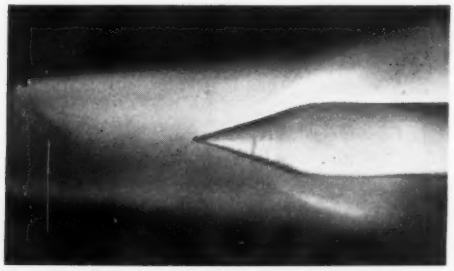

FIG. 4. Flow in low excitation state around cone-cylinder model. Mach Number ≈ 3.

from cone and shock angles[11] for this case. The Mach Number appears to be limited by flow separation.

Future work will reveal what ionization rates in the flow can be generated by high-frequency fields. Aside from this, it appears that combination of the two-phase driving system with radio frequency heating has advantages for hypersonic and low-density tunnels.

References

[1] Alfven, H., *Cosmical Electrodynamics*, Chapt. III, "Electric Discharges in Gases," p. 46; Oxford Clarendon Press, 1953.

[2] Bickerton, R. J., and von Engel, A., *The Positive Column in a Longitudinal Magnetic Field*, Proc. Phys. Soc. (London) Sect. B, Vol. 69, pp. 468–481, 1956.

[3] Meek, T. M., and Craggs, T. D., *Electrical Breakdown of Gases*, Chapt. 9, "High Frequency Breakdown," Oxford Clarendon Press, 1953.

[4] Chuan, R. L., *Plasma Heating of Hypersonic Gas Flow*, Univ. So. Calif. Eng. Ctr. Rept. 56-202(AF)SRTN57-762, December, 1957.

[5] Smith, H. L., and Early, H. C., *Investigation of Heating of Air Stream in a Wind Tunnel by Means of an Electrical Discharge*, Res. Inst. Univ. of Michigan, Ann Arbor, Final Report Project 2154-3-F, October, 1954.

[6] Chuan, R. L., *A Heat Cycle Low Reynolds Number Transonic Tunnel*, Readers' Forum, Journal of the Aeronautical Sciences, Vol. 20, No. 1, pp. 59, 60, January, 1953. See also, Chuan, R. L., and Krishnamurti, K., *Principle and Application of the Two-Phase Wind Tunnel System*, Univ. So. Calif. Eng. Ctr., Spec. Interim Rept. USCEC 42-201, December, 1955.

[7] Eckert, H. U., *On the Choice of Mercury Vapor as Testing Medium for a Plasma Tunnel and some of its Aerodynamic Properties*, Convair Scient. Res. Lab. Res. Note No. 12, November, 1957.

[8] Roes, J. B., *Design of an R. F. Generator for the Excitation of an Ion Tunnel*, Convair Scient. Res. Lab. Res. Memo., April, 1958.

[9] Birkhoff, G., *Messung der elektrischen Vorgaenge innerhalb einer Hochfrequenz-ringentladung*, ZAP, Vol. 10, pp. 204–206, May, 1958.

[10] Brown, S. C., *Breakdown in Gases; Alternating and High Frequency Fields*, Encyclopedia of Physics, Vol XXII, pp. 531–575, Springer, Berlin, 1956.

[11] Linnell, R. D., and Bailey, J. Z., *Similarity-Rule Estimation Methods for Cones and Parabolic Noses*, Journal of the Aeronautical Sciences, Readers Forum, Vol. 23, No. 8, pp. 796, 797, August, 1956.

Aerodynamics of Wings and Bodies at Transonic Speeds

(*Continued from page 486*)

[55] Michel, R., Marchaud, F., and Le Gallo, J., *Etude des Ecoulements Transsoniques Autour des Profils Lenticulaires, à Incidence Nulle*, ONERA Pub. No. 65, 1953.

[56] Nocilla, Silvio, *Campi di Moto Transonici Attorno a Profili Alari: Applicazioni*, Accademia Delle Scienze De Torino, Atti, Vol. 90, pp. 311–331, 1955–56.

[57] Tomotika, S., and Tamada, K., *Studies on Two-Dimensional Transonic Flows of Compressible Fluid, Part III*, Quart. Appl. Math., Vol. IX, No. 2, pp. 129–147, July, 1951.

[58] Michel, R., Marchaud, F., and Le Gallo, J., *Influence d'un Point d'Inflexion à l'Arrière d'un Profil en Ecoulement Transsonique*, La Recherche Aéronautique, No. 40, pp. 15–19, Juillet-Aout, 1954.

[59] Milne, William Edmund, *Numerical Calculus*, p. 135; Princeton Univ. Press, 1949.

[60] Schlichting, Hermann, *Problems and Results of Investigations on Cascade Flow*, Journal of the Aeronautical Sciences, Vol. 21, No. 3, pp. 163–178, March, 1954.

[61] Schlichting, Hermann, *Some Problems of Cascade Flow*, pp. 175–187, Proc. Conf. on High-Speed Aeronautics, Polytechnic Institute of Brooklyn, Brooklyn, N.Y., January 20–22, 1955.

[62] Feindt, Ernst-Günther, and Schlichting, Hermann, *Berechnung der reibungslosen Strömung für ein vorgegebenes ebenes Schaufelgitter bei hohen Unterschallgeschwindigkeiten*, ZAMP, Vol. IXb, Fasc. 5/6 Sonderband, pp. 274–284, 1958.

[63] Whitham, G. B., *The Flow Pattern of a Supersonic Projectile*, Com. Pure Appl. Math., Vol. V, No. 3, pp. 301–348, August, 1952.

[64] Berndt, Sune B., *Theoretical Aspects of the Calibration of Transonic Test Sections*, ZAMP, Vol. IXb, Fasc. 5/6 Sonderband, pp. 105–124, 1958.

[65] Taylor, Robert A., and McDevitt, John B., *Pressure Distributions at Transonic Speeds for Parabolic-Arc Bodies of Revolution Having Fineness Ratios of 10, 12, and 14*, NACA TN 4234, 1958.

[66] Oswatitsch, K., *Die Berechnung wirbelfreier achsensymmetrischer Überschallfelder*, Österreichisches Ingenieur-Archiv, Band X, Heft 4, pp. 359–382, 1956.

[67] Oswatitsch, K., and Keune, F., *The Flow Around Bodies of Revolution at Mach Number 1*, pp. 113–131, Proc. Conf. on High-Speed Aeronautics, Polytechnic Institute of Brooklyn, Brooklyn, N.Y., January, 20–22, 1955.

Divergence of Plate Airfoils of Low Aspect Ratio at Supersonic Speeds

(*Continued from page 507*)

[2] Timoshenko, S., *Theory of Plates and Shells*, pp. 49–51; McGraw-Hill Book Co., New York, 1940.

[3] Duncan, W. J., Frazer, R. A., and Collar, A. R., *Elementary Matrices*, pp. 134–141; Cambridge University Press, Cambridge, England, 1938.

[4] Robinson, A., *Rotary Derivatives of a Delta Wing at Supersonic Speeds*, J.R.Ae.S., Vol. 52, pp. 735–752, November, 1948.

[5] Evvard, J. C., *Use of Source Distributions for Evaluating Theoretical Aerodynamics of Thin Wings at Supersonic Speeds*, NACA TR 951, 1950.

[6] Hedgepeth, J. M., and Waner, Paul G., *Analysis of Static Aeroelastic Behavior of Low Aspect Ratio Rectangular Wings*, NACA TN 3958, 1957.

Analysis of a Simplified Model of Solid Propellant Resonant Burning†

W. NACHBAR* AND L. GREEN, JR.**

Lockheed Aircraft Corporation and Aerojet-General Corporation

SUMMARY

A model which has been proposed to describe resonant burning of solid propellants assumes burning under conditions where the burning rate is determined by the rate of heat transfer from gas at flame temperature across a thin boundary film to the propellant surface. An idealized, film-type, heat-transfer mechanism is used. It is shown that if a certain "critical" frequency is present in the frequency spectrum of gas phase oscillations in the combustion chamber, this will cause oscillations in the heat input to the propellant surface which then couple with the decomposition mechanism to cause a change in the mean burning rate. The effect is what has been termed resonant or unstable burning of the propellant. Results which are obtained in the present paper permit calculation of this critical frequency as a function of the propellant parameters and the steady-state burning conditions. The analysis makes possible predictions of the relative effect of these parameters on the probability of encountering resonant burning, and these predictions appear at present to be in accord with experience.

SYMBOLS

Primary

- B = frequency factor for surface decomposition reaction (cm./sec.)
- c = heat capacity of solid propellant (cal./g °K.)
- E = activation energy for surface decomposition reaction (cal./mole)
- $f(x)$ = x-dependence of temperature variation (°K.)
- F = film coefficient factor (cal./cm. sec.^{2} °K.)
- k' = mean value of the total thermal conductivity of gas in the film of thickness, δ (cal./cm. sec. °K.)
- k = thermal conductivity of solid propellant (cal./cm. sec. °K.)
- l = length parameter characteristic of parallel gas flow (cm.)
- L_s = heat of phase change for surface decomposition reaction (cal./g)
- q = heat flux per unit area normal to propellant surface (cal./cm.^{2} sec.)
- r = linear burning (or regression) rate of propellant (cm. ÷ sec.)
- $\bar{r}$ = mean value of oscillating burning rate over one cycle (cm./sec.)
- R = universal gas constant = 1.986 (cal./mole °K.)
- T = temperature (°K.)
- t = time (sec.)
- v_1 = velocity of parallel gas flow (main stream (cm.)/sec.)
- x = space coordinate, positive into the propellant (cm).
- α = thermal diffusivity of solid propellant $\equiv k/\rho_p c$ (cm.^{2} ÷ sec.)
- δ = effective thickness of hypothetical film $\cong \rho_p r l/\rho_1 v_1$ (cm.)
- κ = heat transmission parameter = $k'\rho_1 v_1/l$ (cal.-gm./°K.-sec.^{2}-cm.^{4})
- ρ_p = mass density of solid propellant (g/cm.^{3})
- ρ_1 = mass density of gas in main stream (g/cm.^{3})
- τ = intrinsic time delay for surface decomposition reaction (sec.)
- τ_n^* = critical values of time delay, $n = 0, 1, 2 \ldots$ [see Eq. (20a)] (sec.)
- ω = circular frequency of oscillation of film coefficient factor (sec.$^{-1}$)
- ω^* = critical value of circular frequency (sec.$^{-1}$)

Secondary

- A = see Eq. (8a) (cm.$^{-2}$)
- C = see Eq. (8b) (cm.$^{-1}$)
- D = see Eq. (8c) (°K. cm.$^{-1}$)
- K_1, K_2, K_3 = see Eqs. (15a), (15b), and (15c)
- M = see Eq. (A-18)
- N_1, N_2, N_3, N_4 = see Eqs. (A-19), (A-20), (A-21), and (A-22)
- Q = see Eq. (23)
- z = dimensionless frequency parameter; see Eq. (17a)
- z_m^* = lower bound on z^*; see Eq. (22a)
- z_M^* = upper bound on z^*; see Eq. (22b)
- ϵ = a number much less than one
- θ^* = time lag angle; see Eq. (20b)
- λ_1, λ_2 = complex-valued roots of secular equations; see Eqs. (11) and (12)
- Ψ = dimensionless frequency parameter $\equiv 4\omega\alpha \div r_0^2$
- Ψ_M^*, Ψ_m^* = upper and lower bounds on Ψ^* corresponding to z_M^* and z_m^*
- Ψ_{m1}^* = approximation to Ψ_m^*; see Eq. (25a)
- Ψ_{HF}^* = high-frequency regime approximation to Ψ^*; see Eq. (26)

Subscripts and Superscripts

- $(\ )_f$ = refers to flame conditions
- $(\ )_s$ = refers to conditions at propellant surface, $x = 0$
- $(\ )_0$ = refers to steady-state operation
- $(\ )_i$ = refers to initial (pre-ignition) conditions
- $(\ )_n$ = integer index for critical time delay, $n = 0, 1, 2, 3 \ldots$
- $(\ )^*$ = refers to derived critical values

Received August 4, 1958. Revised and received December 29, 1958.

† This research was supported in part by the United States Air Force through the Air Force Office of Scientific Research of the Air Research and Development Command under Contract AF 18(603)-146.

* Head, Applied Mechanics, Missile and Space Division, Lockheed Aircraft Corporation.

** Formerly, Head, Applied Mechanics, Corporate Research Division, Aerojet-General Corporation. Now with Aeronutronic Systems, Inc.

INTRODUCTION

IN ORDER TO ATTACK the problem of the nonsteady burning behavior of a solid propellant which is subjected to a fluctuating, parallel gas stream, a thermal model of burning behavior was proposed by one of the authors.[1] In this model, the complex situation involving chemical-reaction, thermal, and mass diffusion in the gas phase was replaced by a simplified boundary condition assuming convective heat transfer to the propellant surface from a parallel flow of gas at flame temperature, as shown schematically in Fig. 1. It was assumed that the hypothetical film thickness, δ, govern-

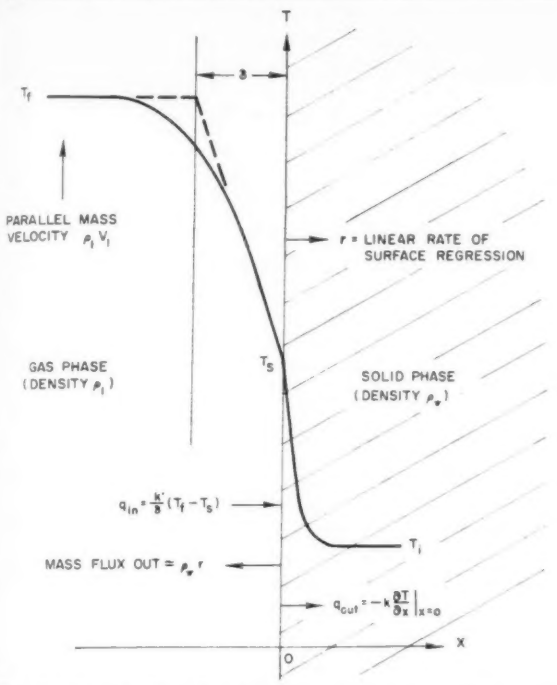

FIG. 1. Hypothetical situation and temperature profile at surface of burning solid propellant.

ing the heat-transfer rate was an inverse function of the parallel mass velocity of the stream and was a direct function of the "injection" mass velocity normal to the burning surface—viz.,

$$\delta \cong l(\rho_s r/\rho_1 v_1) \tag{1}$$

The length parameter "l" is identified with the distance downstream from the main stream stagnation point; thus, in the limit $l \to 0$, δ approaches the hydraulic diameter of the perforation of the propellant grain. It was also assumed that decomposition of the solid phase of the gaseous state requires an endothermic heat of phase change, L_s. The boundary condition at the propellent surface then took the form

$$\frac{F}{r}(T_f - T_s) = \rho_s r L_s - k\left.\frac{\partial T}{\partial x}\right|_s \tag{2}$$

where the "film-coefficient factor" F, defined as

$$F \equiv k'r/\delta \cong k'\rho_1 v_1/\rho_s l$$

provides a measure of the degree to which the heat-transfer coefficient k'/δ is influenced by the parallel gas flow. Thus the value of F will depend upon the history of the boundary layer upstream from the station in question.

Heat conduction in the solid phase was represented by the equation

$$\partial T/\partial t = \alpha(\partial^2 T/\partial x^2) + r(\partial T/\partial x) \tag{3}$$

which neglects any heat generation within a solid slab moving in the $-x$ direction at the linear burning rate $|r|$. The burning surface is fixed at the coordinate $x = 0$. The boundary conditions governing the solid-phase conduction problem were Eq. (2) above, where $T_s = T(0, t)$, and

$$T(\infty, t) = T_i \tag{4}$$

It was assumed that the nonsteady variations in temperatures and burning rate could be represented as small perturbations from steady-state conditions. These perturbations were assumed to be caused by small-amplitude oscillations of circular frequency, ω, in the parallel flow conditions, which oscillations then affected the magnitude of the film coefficient factor, F. Using the complex representation for harmonically oscillating small perturbations (i.e., "take the real part of . . . "), and introducing the small, positive number ϵ, $\epsilon \ll 1$, to measure perturbation amplitude, the non-steady-state representation of F was assumed to be of the form

$$F = F_0 + \Delta F(t)$$

where
$$\Delta F(t) = \epsilon F_1 e^{i\omega t} \tag{5a}$$

The nonsteady temperatures were then represented by

$$T = T_0 + \Delta T \equiv T_0(x) + \epsilon f(x)e^{i\omega t} \tag{5b}$$

$$T_s = T_{s0} + \Delta T_s \equiv T_{s0} + \epsilon f(0)e^{i\omega t} \tag{5c}$$

The propellant burning rate r at any time t was assumed to depend only upon the propellant surface temperature, T_s, at a previous time, $t - \tau$. For the time-dependent surface temperature as given by Eq. (5c), the instantaneous burning rate was then given, to the first order in ϵ, by

$$r = r_0 + \Delta r \equiv r_0(T_{s0}) + \epsilon f(0)\left.\frac{dr}{dT_s}\right|_{T_{s0}} e^{i\omega(t-\tau)} \tag{5d}$$

The time delay, τ, was assumed to be required for transition of the propellant matter from an ordered solid state at a temperature $(T_s - \theta)$, where θ is a small temperature difference, through a semiordered "surface" region at mean temperature, T_s, to a disordered gaseous state at temperature $(T_s + \theta)$. It was suggested that, in the case of composite propellants, τ may also include the time required for diffusion and mixing of the fuel and oxidizer components in the semiordered surface region, since T_s in this case represents an average between the fuel and oxidizer surface temperatures. (These temperatures may differ appreciably.)

Finally, it was assumed that the steady-state propellant burning rate could be expressed as an Arrhenius function of the steady-state surface temperature—i.e.,†

$$r_0 = B \exp(-E/RT_{s0}) \tag{5e}$$

and that the same functional form held for the perturbed burning rate under the perturbed surface temperature, Eq. (5c). The instantaneous burning rate from Eq. (5d) thus became

$$r = r_0(T_{s0}) + \epsilon f(0)\,(Er_0/RT_{s0}^2)e^{i\omega(t-\tau)} \tag{5f}$$

† See comment on this relation on p. 524.

Substitution of Eqs. (5) into Eqs. (2) and (3), collection of terms of zero order in ϵ, and application of the boundary conditions of Eqs. (4) determined the steady-state relation between the surface temperature, the propellant properties, and the parallel flow conditions, as follows:

$$\frac{\rho_p c B^2}{F_0}\left[\frac{(L/cT_f) + (T_{s0}/T_f) - (T_i/T_f)}{1 - (T_{s0}/T_f)}\right] = \exp\frac{2(E/RT_f)}{(T_{s0}/T_f)} \quad (6)$$

Assuming a reasonable range of propellant and gas-flow parameters, the previous paper[1] presented graphs of steady-state propellant temperatures, burning rates, and temperature gradients which covered the range of experimental values reported for these quantities.

By collecting the first-order terms in ϵ resulting from the substitutions mentioned above, the complex-valued function, $f(x)$, which represents the space variation of the temperature perturbation in the solid phase, was shown to be the solution of the differential equation‡

$$f'' + (r_0/\alpha)f' - (i\omega/\alpha)f = Af(0)e^{-(r_0 x/\alpha)} \quad (7a)$$

with boundary conditions, at $x = 0$,

$$f' - Cf + D = 0 \quad (7b)$$

and, at $x \to \infty$,

$$f \to 0 \quad (7c)$$

The complex-valued parameter groups A, C, and D were defined as

$$A \equiv (r_0/\alpha)^2\,[E(T_{s0} - T_i)/RT_{s0}^2]\,e^{-i\omega\tau} \quad (8a)$$

$$C \equiv (r_0 E/RT_{s0}^2)\left\{[(T_{s0} - T_i)/\alpha] + (2\rho_p L_s/k)\right\}e^{-i\omega\tau} + (F_0/kr_0) \quad (8b)$$

$$D \equiv (F_1/kr_0)\,(T_f - T_{s0}) \quad (8c)$$

ω, the circular frequency of the oscillations of the film coefficient factor, is real.

Solutions of the nonsteady problem were presented for the limiting cases of low-frequency and high-frequency oscillations. In the low-frequency case, it was shown that deviations from the steady burning behavior would be small. In the high-frequency case, on the other hand, the occurrence of "resonance" conditions under which high-amplitude fluctuations in surface temperature could effect significant deviations in mean burning rate was indicated. Examination of a graphical representation of the double-eigenvalue problem characterizing a high-frequency resonance condition indicated that the occurrence of such a condition is favored by (1) a low thermal conductivity in the solid phase, (2) a large heat of phase change, (3) a high flame temperature, and (4) a low activation energy and high-frequency factor in the burning-rate versus surface-temperature relationship. Owing to the difficulty of interpreting the graphical presentation, however, these conclusions were regarded as tentative, requiring confirmation by a better developed analysis which is given in the present paper.

‡ Primed quantities are derivatives with respect to x.

Critical Frequency and Time Lags

It is convenient to replace the perturbation frequency, ω, by the dimensionless quantity, Ψ, defined as

$$\Psi \equiv 4\omega\alpha/r_0^2 \quad (9)$$

The particular solution of Eq. (7a), which obeys the boundary condition Eq. (7c), is found to be of the form

$$f(x) = a\exp(-r_0 x/\alpha) + b_2\exp(r_0\lambda_2 x/2\alpha) \quad (10)$$

where a and b_2 are undetermined and complex-valued coefficients, and λ_2 is one root of the secular equation belonging to the left-hand side of Eq. (7a)—viz.,

$$\lambda_2^2 + 2\lambda_2 - i\Psi = 0 \quad (11)$$

Explicitly, λ_2 is given by

$$\lambda_2 \equiv -1 - (1/\sqrt{2})\,[(1+\Psi^2)^{1/2} + 1]^{1/2} - i(1/\sqrt{2})\,[(1+\Psi^2)^{1/2} - 1]^{1/2} \quad (12)$$

The coefficients a and b_2 are determined by substituting Eq. (10) into Eqs. (7a) and (7b). Using these expressions for a and b_2 in Eq. (10), we are then able to determine $f(x)$ and, subsequently, $T(x, t)$ and $T_s(t)$ by using Eqs. (5b) and (5c). The algebraic manipulations will not be detailed here, as only the expression for the perturbations of surface temperature is of interest. This expression is ultimately determined to be

$$\Delta T_s = -\left[\frac{i\alpha\Psi(T_f - T_{s0})}{kr_0^2}\right]\times\left\{\frac{\Delta F}{(4A\alpha^2/r_0^2) - i(\alpha C/r_0)\Psi + (\lambda_2/2)\,[(4A\alpha^2/r_0^2) + i\Psi]}\right\} \quad (13)$$

The amplitude of ΔT_s depends in part upon the amplitude of ΔF and upon the magnitudes of the terms contained inside the first bracket on the right of Eq. (13). All of these quantities are bounded, however, and their combined magnitude is small if ϵ is chosen sufficiently small. Clearly, however, $|\Delta T_s|$ will become indefinitely large, regardless of ϵ, if the denominator within the second bracket should vanish. That is, if ω and τ assume values ω^* and τ^* so that the complex equation

$$(4A\alpha^2/r_0^2) - i(\alpha C/r_0)\Psi + (\lambda_2/2)\,[(4A\alpha^2/r_0^2) + i\Psi] = 0 \quad (14)$$

is satisfied, then ΔT_s will become infinite. Of course, the infinity is a consequence of linearization; the true amplitude $|\Delta T_s|$ cannot be determined from the linearized problem if ω and τ are equal to ω^* and τ^*.

Linearization of the Arrhenius function, as performed in Eq. (5f), depends upon both $|\Delta T_s/T_{s0}|$ and $(E/RT_{s0}) \times (|\Delta T_s/T_{s0}|)$ being small compared to one. This linearized expression would predict that the mean burning rate $\bar{r}$, which is defined to be the time-averaged burning rate over one cycle for surface temperature oscillating harmonically about T_{s0} with amplitude $|\Delta T_s|$, is equal to r_0. However, even if $|\Delta T_s/T_{s0}|$ were small, the nonlinearity of the exponential Arrhenius function would predict a change in $\bar{r}$ provided that

$(E/RT_{s0})(|\Delta T_s|/T_{s0})$ were not small. As mentioned in reference 1, this change would generally be an increase in $\bar{r}$; however, for certain operating conditions discussed later, it could be a decrease of $\bar{r}$.

The values τ^* and ω^* (or, equally, Ψ^*), which satisfy Eq. (14), will be called critical values for the propellant time lag, τ, and for the oscillation frequency, ω, respectively. It will be shown below that for given operating conditions there can be at most one nonzero value of ω^*, but that for any such value of ω^* there is an infinite set of values $\tau_n{}^*$, $n = 0, 1, 2, 3, \ldots$. We find that ω^* and $\tau_n{}^*$ depend upon propellant parameters and steady-state burning conditions. If $\omega = \omega^*$ and if, simultaneously, $\tau = \tau_n{}^*$ for any n, there will generally be an increase in the mean burning rate, $\bar{r}$, for this model (as is observed above) and a consequent increase in chamber pressure from its steady-state value. This is the condition observed experimentally in so-called "resonant burning" of actual solid propellant rocket motors, and thus the critical values for the model can also be identified as resonant burning or resonance values. However, the term "resonant frequency" cannot be applied here in the usual sense because, in this model, there is no "resonance condition," unless both ω and τ assume critical values.

In the present paper, ω^* and τ^* are shown to be exactly determinable from one root of a certain fourth degree polynomial. A closed-form, approximate expression for Ψ^* is then derived, which is valid if $(\Psi^*)^2$ is large; along with this derivation there is developed an expression to bound the error in the approximation. We are also able to determine $\tau_n{}^*$ approximately. By examining the effect on ω^* and $\tau_n{}^*$ of changing propellant properties and steady-state burning conditions, the influence of these changes on probability of resonant behavior can be assessed.

Exact Calculation of Critical Values

For convenience in the algebra, we introduce the dimensionless groups K_1, K_2, and K_3, which are defined to be

$$K_1 \equiv (2E/RT_{s0}) \left\{ [(T_{s0} - T_i)/T_{s0}] + (2L_s/cT_{s0}) \right\} \quad (15a)$$

$$K_2 \equiv 1 + 2(F_0/\rho_p c r_0{}^2) \quad (15b)$$

$$K_3 \equiv (2E/RT_{s0})\ [(T_{s0} - T_i)/T_{s0}] \quad (15c)$$

Substituting these expressions into Eq. (14) and collecting terms, we get the equation

$$(4K_3 + 2K_3\lambda_2 - iK_1\Psi)e^{-i\omega\tau} = i\Psi[K_2 - 1 - \lambda_2] \quad (16)$$

A necessary condition for the satisfaction of Eq. (16) is that the absolute value of each side be equal. This condition eliminates τ and reduces Eq. (16) to a real-valued equation in Ψ only. If we now replace Ψ by a new frequency parameter, z, defined as

$$z \equiv (1/\sqrt{2})\ [\sqrt{1 + \Psi^2} + 1]^{1/2} \quad (17a)$$

so that

$$\Psi \equiv 2z\sqrt{z^2 - 1} \quad (17b)$$

then, taking the absolute value of Eq. (16), the following polynomial equation of fourth degree in z is derived:†

$$z^4 + (K_2 + 1)z^3 - (1/2)\ (K_1{}^2 - K_2{}^2 - 2K_2 + 1)z^2 - (1/2)\ (K_1{}^2 - K_2{}^2 + 1 + 2K_1K_3)\ z - K_1K_3 - K_3{}^2 = 0 \quad (18a)$$

It is shown below that a resonance condition can occur only if there exists a real root z^* of Eq. (18a) which exceeds a certain lower bound greater than one; this bound corresponds to a positive lower bound on ω^* [see Eq. (21)]. It is important to know, therefore, what relationship must hold between the parameters K_1, K_2, and K_3 in order to ensure the existence or nonexistence of this root of Eq. (18a). This question is answered in a simple way by the following Theorem A, the proof of which is given in the Appendix.

Theorem A: The necessary and sufficient condition on K_1, K_2, and K_3, that there exists one and only one real, critical value Ψ^* (or, equally, ω^*) which is greater than zero, is

$$K_1 + K_3 > 1 + K_2 \quad (19)$$

If this inequality is violated, resonance is not possible, and the only real, non-negative root of Eq. (16) is $\omega = 0$.

Being thus able to determine ω^* for all cases, the values of τ^* which are necessary to satisfy Eq. (16) are then determined to be

$$\tau_n{}^* = (\theta^* + 2n\pi)/\omega^*, \quad n = 0, 1, 2 \ldots \quad (20a)$$

where θ^* is given by

$$\theta^* = \pi - \tan^{-1} \left\{ \sqrt{\frac{z^* - 1}{z^* + 1}} \times \frac{K_3(2z^* + K_2 + 1) + K_1z^*(z^* + 1)}{K_3(K_2 + 1) + K_1z^*(z^* + K_2)} \right\} \quad (20b)$$

The principal value of the inverse tangent is understood in Eq. (20b). If $1 \leq z^* < \infty$, then

$$\pi \geqq \theta^* \geqq (3\pi/4) \quad (20c)$$

with corresponding limits.

An interesting result is obtained immediately from Eqs. (20) for the case $n = 0$. We find that if the propellant time lag τ is less than the calculated time lag $\tau_0{}^*$, then no resonance is possible even if ω should equal ω^*. Stated another way, if ω^* is calculated to be so small that

$$\omega^* < (3\pi/4\tau) \quad (21)$$

then no resonant burning is possible. For example, if τ were estimated as being no greater than 1 millisec., then two conclusions could be drawn: (a) there is no possibility of resonance if ω^* is made less than 2,360 rad./sec. or 375 cycles/sec.; and (b) oscillations of frequency less than 375 cycles/sec. in the parallel flow can never excite resonance.

† See the Appendix for details.

Approximate Calculation of Critical Values

The foregoing conclusions indicate that resonance is not possible if Ψ^* or ω^* is too small, and therefore an approximate solution to Eq. (18a), which will be valid if Ψ^* is not small compared to one, will probably be useful. Such an approximation can be derived by first writing Eq. (18a) in the following equivalent form:

$$[z + (1/2)K_2]^2 = (1/2)K_1^2 - (1/4)K_2^2 + (1/2) + K_3\{(K_1/z) + [K_3/z(z+1)]\} \quad (18b)$$

Assuming that Eq. (19) holds, a lower bound for z^*, denoted by the symbol $z_m{}^*$, can be determined by allowing z on the right-hand side of Eq. (20b) to become infinite. The term in braces in Eq. (18b) then vanishes, and we obtain the expression $z_m{}^*$:

$$z_m{}^* \equiv (1/2)\,[2 + 2K_1^2 - K_2^2]^{1/2} - (1/2)K_2 \quad (22a)$$

An upper bound on z^*, to be denoted by the symbol $z_M{}^*$, is obtained by replacing z on the right-hand side of Eq. (18b) by $z_m{}^*$; viz.,

$$z_M{}^* \equiv (1/2)\,\{2 + 2K_1^2 - K_2^2 + (4K_1K_3/z_m{}^*) + [4K_3^2/z_m{}^*(z_m{}^*+1)]\}^{1/2} - (1/2)K_2 \quad (22b)$$

Now z^* is bounded from above and from below by Eqs. (22a) and (22b)

$$z_m{}^* \leqq z^* \leqq z_M{}^* \quad (22c)$$

and either bound can be used to approximate z^* provided that the error, as estimated by the following formula, is sufficiently small—viz.,

$$\frac{z_M{}^* - z_m{}^*}{z_m{}^*} \cong \frac{K_3\{K_1 + [K_3/(z_m{}^*+1)]\}}{\sqrt{2}(z_m{}^*)^2\,[1 + (1-Q^2)\,K_1^2]^{1/2}} \quad (22d)$$

where Q is defined as

$$Q \equiv K_2/\sqrt{2}\,K_1 \quad (23)$$

Eq. (22d) is derived in the Appendix. If the bound on the error as calculated from Eq. (22d) is small enough, then $z_m{}^*$ is a good approximation to z^*, and $\Psi_m{}^*$, which is found by using Eq. (17a), can be used to approximate Ψ^*. To obtain a $\psi_m{}^*$ which is greater than zero, however, it is necessary that $z_m{}^* > 1$. To ensure satisfaction of this condition, the necessary and sufficient condition is found from Eq. (22a) to be

$$K_1 > 1 + K_2 \quad (I)$$

Since we always have $K_3 > 0$, Condition I is more stringent than the inequality of Eq. (19). As a consequence of Condition I and since we always have $K_2 > 1$, the following inequalities hold:

$$K_1 > 2 \quad \text{and} \quad Q < (1/\sqrt{2})\,[1 - (1/K_1)] < 1/\sqrt{2}$$

Provided that Condition I holds and that the bound on the error found from Eq. (22d) is sufficiently small, $\Psi_m{}^*$ will be a good approximation for any Ψ^* greater than zero. However, a simpler approximation for Ψ^* is obtained if it is further assumed that

$$(\Psi^*)^2 \gg 1 \quad (24a)$$

Upon expansion of the radical in Eq. (17a), the relation between z^* and Ψ^* can be approximated, neglecting $(1/2)\,(\Psi^*)^{-2}$ with respect to one, as follows:

$$z^* \cong \sqrt{(\Psi^* + 1)/2} \quad (24b)$$

Let $\Psi_{m1}{}^*$ be defined through Eq. (24b) as

$$\Psi_{m1}{}^* \equiv 2(z_m{}^*)^2 - 1 \quad (25a)$$

or explicitly,

$$\Psi_{m1}{}^* \equiv K_1^2 - 2QK_1[1 + (1-Q^2)K_1^2]^{1/2} \quad (25b)$$

The identity $$(\Psi_m{}^*)^2 = (\Psi_{m1}{}^*)^2 - 1 \quad (25c)$$

follows from Eq. (25a) and shows immediately that the assumption of Eq. (24a) will be valid if the condition

$$(\Psi_{m1}{}^*)^2 \gg 2 \quad (II)$$

is imposed. Under Condition II, Eq. (25c) can be expanded, and since terms of order $(1/2)\,(\Psi_{m1}{}^*)^{-2}$ are neglected compared to one, we conclude that $\Psi_{m1}{}^*$ can then be used as an approximation to Ψ_m:

$$\Psi_{m1}{}^* \cong \Psi_m{}^* \quad (25d)$$

It is useful to have an expression for directly estimating the error made in approximating Ψ^* by $\Psi_{m1}{}^*$ under Condition II. It is shown in the Appendix that, neglecting terms which are small of order $(1/2)\,(\Psi_{m1}{}^*)^{-2}$, the error is bounded as follows:

$$\left|\frac{\Psi^* - \Psi_{m1}{}^*}{\Psi_{m1}{}^*}\right| < \frac{2\sqrt{2}\,K_3\,\{K_1 + [K_3/(z_m{}^*+1)]\}}{\Psi_{m1}{}^*[1 + (1-Q^2)K_1^2]^{1/2}} \quad (25e)$$

In most cases of interest, Conditions I and II are expected to hold, in which event $\Psi_{m1}{}^*$ can be held to approximate Ψ^*. The error in this approximation can be estimated by using Eq. (25e). If Condition II is not satisfied, then $\Psi_m{}^*$ can be used as an approximation, and the error incurred can be estimated from Eq. (22d). If neither Conditions I nor II hold, or if the estimated magnitude of the error in either approximation is too large, then Ψ^* can be determined exactly by finding the positive root of either of Eqs. (18a) or (18b). This is most easily carried out by iterating Eq. (18b) to find z. The first two iterates in this process are $z_m{}^*$ in Eq. (22a) and $z_M{}^*$ in Eq. (22b); the next iterate is found by replacing z^* on the right-hand side of Eq. (18b) by $z_M{}^*$.

If an approximation to Ψ^* is used, then $\tau_n{}^*$ can be determined approximately by substituting $z_m{}^*$, Eq. (22a), for z^* in Eqs. (20a), (20b), and (20c).

The low- and high-frequency regimes, for which solutions of Eq. (14) were presented previously,[1] correspond to imposing the assumptions of $\Psi \ll 1$ and $\Psi \gg 2$, respectively. The present analysis shows that, because of the nonexistence of a resonance condition for critical frequencies which obey the inequality of Eq. (21), consideration of the low-frequency regime is unnecessary. Where the earlier analysis was able to show the nonexistence of resonance in the low-fre-

quency regime (estimated as below approximately 10 cps), a lower limit is precisely indicated by Eq. (21) as a function of τ.

Using the high-frequency approximation $\Psi^* \gg 2$, we are able to derive an approximate analytical form $\Psi_{HF}{}^*$ for Ψ^* which is slightly simplified over $\Psi_{m1}{}^*$, Eq. (25a); this is

$$\Psi_{HF}{}^* \equiv K_1{}^2[1 - 2Q\sqrt{1 - Q^2}] \tag{26}$$

However, $\Psi_{m1}{}^*$ will be a better approximation to Ψ^* than will $\Psi_{HF}{}^*$ as Ψ^* becomes small, since we require only that $(\Psi_{m1}{}^*)^2 \gg 2$, and therefore the derivation of Eq. (26) will not be presented.

Influence of Propellant Parameters and Operating Conditions on Stability of Burning

To promote the stability of burning of a solid propellant in the presence of a fluctuating, parallel gas flow in the event that $\omega^* > 3\pi/4\tau$, the physical parameters and the operating conditions must be changed so as to reduce the calculated value of ω^*. Even if ω^* is not reduced below the limit given by Eq. (21), reduction of ω^* will still "spread out the thicket" of critical values of $\tau_n{}^*$; for Eq. (20a) shows that, with decreased ω^*, there is a greater interval between successive values of $\tau_n{}^*$ with less likelihood that τ will coincide with one of these values. Thus, since resonance depends upon the simultaneous coincidence of ω with ω^* and τ with some $\tau_n{}^*$, reduction of ω^* improves the overall probability of sustaining stable burning without encountering resonance.

The independent physical parameters which determine operating conditions in this model are nine in number—viz., κ, ρ_π, c, L_s, B, E, T_i, T_f, k. The parameter κ, defined as

$$\kappa \equiv k'\rho_1 v_1/l \tag{27a}$$

embodies the total influence of the gaseous combustion zone and the parallel gas flow on ω^*. In terms of previously defined parameters

$$\kappa/c\rho_\pi{}^2 r_0{}^2 \equiv F_0\alpha/kr_0{}^2 \equiv (1/2)\ (K_2 - 1) \tag{27b}$$

Two additional parameters, T_{s0} and r_0, are not independent but are given, when the nine parameters listed above are fixed, by the steady-state solution through Eqs. (5e) and (6); the latter equation can be written in new notation as

$$1 + (\kappa/c\rho_\pi{}^2 r_0{}^2) = \{[(L_s/c) + (T_f - T_i)] \div (T_f - T_{s0})\} \tag{28}$$

To investigate the effect on stability of changing only one of the independent parameters while holding the others fixed, the partial derivatives of ω^* are sought. We will assume that Ψ^* is given adequately by $\Psi_{m1}{}^*$ using Eq. (25a) under Conditions I and II as described above. For performing the differentiation with respect to one of the nine parameters, it is found convenient to write ω^* in the form

$$\omega^* = (\kappa/2\rho_\pi k)\ [\Psi_{m1}{}^*/(K_2 - 1)] \tag{29}$$

Table 1

u	$(u/\omega^*)\ (\partial\omega^*/\partial u)$	u	$(u/\omega^*)\ (\partial\omega^*/\partial u)$
κ	0.6045	B	0.7908
ρ_π	−0.2083	E	−1.7973
c	−0.4074	T_i	−0.2515
L_s	0.8041	T_f	1.2590
		k	−1.0000

Let u stand for any one of the nine parameters. Then the partial derivatives of ω^* are calculated by carrying out the operation indicated in the formula

$$\begin{aligned}(u/\omega^*)\ (\partial\omega^*/\partial u) = {} & (2\rho_\pi k/\kappa)\ (\partial/\partial y)\ (\kappa/2\rho_\pi k) + \\ & \{[(K_2 - 1)/\Psi_{m1}{}^*]\ (\partial/\partial K_1)\ [\Psi_{m1}{}^*/(K_2 - 1)]\} \times \\ & \{u(\partial K_1/\partial u) + [T_{s0}(\partial K_1/\partial T_{s0})]\ [(u/T_{s0}) \times \\ & (\partial T_{s0}/\partial u)]\} + \{[(K_2 - 1)/\Psi_{m1}{}^*]\ (\partial/\partial K_2) \times \\ & [\Psi_{m1}{}^*/(K_2 - 1)]\}\{u(\partial K_2/\partial u) + \\ & [r_0(\partial K_2/\partial r_0)]\ [(u/r_0)\ (\partial r_0/\partial u)]\}\end{aligned} \tag{30}$$

The partial derivatives of r_0 and T_{s0} are evaluated by means of Eqs. (5e) and (28). Explicit forms of Eq. (30) for each of the nine independent parameters are given in the Appendix.

As an example, we will take the data previously used in reference 1: $\kappa = 0.17$, $\rho_\pi = 1.7$, $c = 0.294$, $L_s = 100$, $B = 100$, $E = 11{,}920$, $T_i = 300$, $T_f = 3{,}000$, and $k = 5 \times 10^{-4}$ (c.g.s. dimensions given in Symbols). From these data were calculated the steady-state values $r_0 = 0.56$ and $T_{s0} = 1{,}150$. For these values, we now calculate $K_1 = 13.88$, $K_2 = 2.29$, $K_3 = 7.68$, and $E/RT_{s0} = 5.21$. Consequently, it is found by using the formulas derived above that $\Psi_{m1}{}^* = 148$; $\omega^* = 1.16 \times 10^4$ rad./sec. = 1,846 cps; and $\tau_n{}^* = 2.13 \times 10^{-4}$, 7.54×10^{-4} (modulo 5.41×10^{-4}). In comparing the results on critical frequency and time-lag with results found in reference 1, the values determined here, using the same numerical example, are $\omega^*\tau_0{}^* = 0.79\pi$, $\omega^*\tau_1{}^* = 2.79\pi$ and $\omega^*\tau_2{}^* = 4.79\pi$. Previously, the same values for $\omega^*\tau_1{}^*$ and $\omega^*\tau_2{}^*$ were found using a graphical method; $\omega^*\tau_0{}^*$ was roughly estimated.

For these parameter values, Conditions I and II of the preceding section are seen to be satisfied, but using Eq. (25e), it is found that the error bound $|(\Psi^* - \Psi_{m1}{}^*)/\Psi_{m1}{}^*|$ equals 0.16. For purposes of establishing the algebraic sign and the order of magnitude of the derivatives of ω^*, this magnitude of error in the approximation is not intolerable, in view of the uncertainty in establishing values for the parameters, particularly for κ, B, and E. The exact value of Ψ is found for this example from Eq. (18b) to be 167; the value of $\Psi_M{}^*$, corresponding to $z_M{}^*$ from Eq. (22b), is found to be 168.5, a much closer approximation but using a more complicated formula.

The calculated values of the derivatives of ω^* are given in Table 1. The algebraic sign of these partial derivatives indicate whether the effect of changing the value of the parameter from the given steady-state will be stabilizing or destabilizing. Thus, stability is seen to be improved in this case by increasing ρ_π, c, T_i, E, k and by decreasing κ, L_s, T_f, B. The numerical magnitudes of these derivatives indicate the relative change in ω^* due to a unit change in the parameter. The most

sensitive parameters are seen to be, in order of sensitivity: E, T_f, k, B, L_s, κ, T_i, c, and ρ_s. The effects of the individual variables, however, may not always be experimentally separable, as discussed below; see, for example, the discussion regarding T_i.

Interpretation of Results

Effect of Propellant Parameters

Frequency Factor and Activation Energy—Increasing B always increases the tendency to resonate, as seen by Eq. (A-27) of the Appendix, since all factors on the right are positive (see Appendix). Increasing B, with all other factors held constant, will increase r_0 and decrease T_{s0}, as seen by examining Figs. 3 and 4 of reference 1. This supports the experimental observation[2] that high-burning-rate propellants tend more to unstable burning than do low-burning-rate propellants, other factors (such as calorific content) being constant.

In the selected example, the effect of E was the most marked of all the parameters. Decreasing the activation energy has the greatest destabilizing effect of all possible variations of the parameters. It must be recalled that in the present usage, E is a purely empirical constant determined by fitting Eq. (5e) to experimental data on burning rate versus steady surface temperature. Also, the relative accuracy of the various methods employed for estimation (if not also definition) of surface temperature is a subject of debate. It has been suggested[1] that this activation energy may be related to the difficulty in ignition. Composite propellants employing ammonium nitrate or potassium perchlorate are difficult to ignite, presumably showing high activation energies; instances of resonant burning of these propellants have not been reported. If the above surmise is correct, the activation energy E may depend upon initial temperature, decreasing as T_i is increased. In this case, instability at high values of T_i can be expected.[1] Such behavior is frequently observed experimentally.

Flame Temperature—Increasing the flame temperature, T_f, increased ω^* in the example given and thus promoted instability. Since flame temperature is a measure of the energy content (heat of reaction) of the propellant, this would tend to support the observation that high-energy propellants are, in general, more prone to unstable combustion than are low-energy propellants.

Physical Properties—The propellant density, thermal conductivity, and specific heat affect ω^* individually, not only in combination as $\alpha = k/\rho_s c$. In fact, stability of burning is always promoted by increasing the propellant thermal conductivity, k, and, in this case, by increasing the density, ρ_s, and the specific heat capacity, c. The effect of changing α is thus seen to be indeterminate. A large heat of phase change, L_s, is in this case seen as tending to promote resonance. Different conditions of steady-state operation might change this conclusion, however.

General Observations—Since all partial derivatives $(u/\omega^*)\ (\partial\omega^*/\partial u)$ are of order unity, we expect that the most marked effect on stability can be expected from those parameters which can markedly change. Fig. 4 of reference 1 shows that B and E can vary markedly without altering r_0. It would appear then that these factors, determining as they do the surface decomposition reaction Eq. (5c), would also be determining in the calculation of stability.

Taking the partial derivatives of Eq. (5c) and assuming that r_0 is held constant, we get

$$dT_{s0}/T_{s0} = (dE/E) - (RT_{s0}/E)\ (dB/B) \qquad (31)$$

To improve stability we must always have $dB/B < 0$. On the other hand, it can be generally shown that $dE/E > 0$ for improvement of stability. Therefore, to improve stability, the propellant composition and structure should be designed with low B and high E, or using Eq. (31) with substitution of the inequalities $(dB/B) < 0$ and $(dE/E) > 0$

$$dT_{s0}/T_{s0} > 0 \qquad (32)$$

Then the steady-state surface temperature, T_{s0}, should be made as large as possible to promote stable burning.

Further examination of the influence of steady surface temperature upon resonant burning is of interest, since Price and Sofferis[3] state that, under some conditions, gas-phase oscillations can effect a *decrease* in mean burning rate. It should be noted that the burning rate versus surface temperature relation assumed in Eq. (5e) is S-shaped with zero slope at $T_s = 0$ or $T_s = \infty$, and with an inflection point at $T_s = E/2R$. For $T_s < E/2R$, the curvature of Eq. (5e) is concave upward, for $T_s > E/2R$ it is concave downward. In the case discussed in reference 1 and further examined above, $T_{s0} < E/2R$ and oscillations in T_s about this mean value would effect an increased mean burning rate, as integrated over a complete cycle. However, the authors of this paper have pointed out that if a different set of parameters (such as might characterize a slow-burning but easily "activated" propellant of high flame temperature) were selected, oscillations in T_s could effect a decrease in mean burning rate (see reference 4).

Effect of Operating or Design Conditions

Initial Propellant Temperature—Varying initial temperature only and keeping the other parameters (including B and E) fixed, we conclude that low initial temperatures tend toward producing resonance. For the selected example, however, the effect of reducing T_i was not great. Also, as mentioned above, increasing T_i may have the effect of decreasing E, a much more sensitive factor in determining stability conditions. It has been conjectured[1] that this dual influence of T_i may explain the experimental observation that resonant burning is generally encountered more frequently in motor tests performed at extreme temperatures (either very hot or very cold) than in ambient-temperature firings.

Heat Transmission Parameter—Our results show that resonance is made more probable if the heat transmis-

sion parameter, κ, is increased. Since κ is proportional to the density ρ, the streamwise velocity gradient v_1/l in the parallel flow, and to the mean thermal conductivity k' in the film, resonance is more likely in regions of high density (high pressure), high streamwise velocity gradient in the parallel flow, and where the thermal conductivity of the film is high. The first two factors indicate that unstable burning is likely to occur in the velocity *nodes* of an oscillating flow or in the vicinity of the stagnation point for steady flow. This conclusion agrees with experimental results of Price and Sofferis,[3] as has been noted by the present authors.[4] Table 1 shows that the relative effect on stability of varying κ is also large. If significant changes can be made in the effective mean conductivity, k', across the film, then this conductivity should be reduced to promote stable burning.

Pressure—Judging from its influence upon the gas properties entering into the heat transmission parameter, the effect of raising the chamber pressure might be to increase the chance of resonant burning. However, the propellant transition time lag defined by Eq. (5d) would be decreased by increased pressure if the transition zone were compressible.[1] The resonance condition is more sensitive to small variations in this time lag than to variations in the heat-transfer parameter.

Effect of Transition Time Lag

In the discussion leading to Eq. (21), it was shown that if τ is so small that $\tau < (3\pi/4\omega^*)$ then no resonance is possible. We do not know anything at present about the size of τ other than the selection of arbitrary values in reference 1. If τ is so small for actual propellants that it always satisfies Eq. (21) for practical conditions, then the resonance condition predicted by this model can never exist. Thus, it was suggested that stable operation might be assured at pressures high enough to yield sufficiently low values of τ. The graphical examination also indicated that a resonance condition is not possible when τ is very large, but this result is not confirmed by the present analysis.

Conclusions and Recommendations

Although the methods employed in the present analysis differ markedly from the methods previously used to determine the existence of the double-eigenvalue problem,[1] the tentative conclusions reached earlier have been confirmed. The results obtained on the magnitude of the partial derivatives of ω^* indicate that the most serious difficulties with resonance are to be expected generally in propellants with low activation energies, high frequency factors, and high flame temperatures. The occurrence of a resonance condition is also found generally to be favored by a low thermal conductivity in the solid phase. In addition, based on calculations of a particular numerical example, it appears that a condition of resonance is likely to be favored by a large heat of phase change, a low density and a low heat capacity in the solid, and (except for its possible effect upon activation energy) a low initial temperature. It is further concluded from the numerical results, through the involvement of terms in κ, that a condition of resonance is likely to be favored where there is a high density and high streamwise velocity gradient in the parallel gas flow.

The conclusions based upon numerical calculations are strictly valid only for small changes from the steady-state values which were chosen for the given numerical example. Because of the quadratic dependence of ω^* on the parameters, it is possible that, for some other conditions of steady-state operations, some of these conclusions could be reversed. This possibility is also apparent from examination of the form of the partial derivatives in the Appendix. This type of mathematical behavior might allow an alternative (aside from the one advanced earlier) to the experimental observation that certain propellants exhibit unstable burning when the initial temperature is varied greatly in either direction from a normal value.

The degree of agreement between the predicted model behavior and observed behavior of actual propellant charges is encouraging, and it is recommended that controlled experiments be undertaken to provide a precise evaluation of the various propellant parameters which enter into the analysis. One type of experiment should be a careful investigation of the *steady* burning properties of propellants, employing refined methods for definition and measurement of surface temperature and, hence, for determination of values for B and E as defined by Eq. (5e). The other type of experiment which appears highly desirable is measurement of the transition time lag, τ, which characterizes the *nonsteady* burning properties of the propellant.

Appendix—Additional Notes on Mathematical Development

Derivation of Eqs. (18a) and (18b)

Using the definition of z in Eq. (17a), λ_2 is written from Eq. (12) as

$$-\lambda_2 = 1 + z + i\sqrt{z^2 - 1} \qquad \text{(A-1)}$$

Taking the absolute value of both sides of Eq. (16) and substituting Eq. (A-1) leads to the following polynomial equation of sixth degree in z:

$$z(z-1)\{2K_3^2 + 2(z+1)K_1K_3 + z(z+1)K_1^2 - z(z+1) \times [2z^2 + 2K_2^2 z + K_2^2 - 1]\} = 0 \qquad \text{(A-2)}$$

Eq. (21) and the discussion surrounding it show that the values $\omega^* = 0$ or, correspondingly, $z^* = 1$ cannot result in a resonant condition and thus can have no physical significance. According to the bound of Eq. (21), therefore, we are interested only in those real roots z^* of Eq. (A-2) which are definitely larger than one. Consequently, since the two factors appearing outside the braces in Eq. (A-2) are both positive for $z > 1$, they can be cancelled, thus reducing this equation to

a fourth degree polynomial in z. By algebraic manipulation, the terms within the braces can be cast into the form of Eq. (18b) or into the canonical polynomial form of Eq. (18a).

Proof of Theorem A

Let us write Eq. (18b) in the form

$$W(z) = 0$$

where

$$W(z) \equiv [z + (1/2)K_2]^2 - (1/2)K_1^2 - (1/2) + (1/4)K_2^2 - K_3\{(K_1/z) + [K_3/z(z+1)]\} \quad \text{(A-3)}$$

W increases monotonically from $-\infty$ to $+\infty$ as z goes from 0 to $+\infty$. Therefore, there is one and only one real root of Eq. (18b) in the interval $0 < z < \infty$. We are interested in whether or not this root lies in the interval $1 < z < \infty$; this is possible if and only if

$$W(1) < 0 \quad \text{(A-4)}$$

But

$$W(1) = (1/2)(1 + K_2)^2 - (1/2)(K_1 + K_3)^2 \quad \text{(A-5)}$$

Since K_1, K_2, and K_3 are positive by definition, Eqs. (A-4) and (A-5) then become Eq. (19) and Theorem A is proved.

Bounds on the Errors in Approximate Formulas

For the purpose of this development only, let us define δ, a, b, and c as follows:

$$\delta \equiv (z_M^* - z_m^*)/z_m^* \quad \text{(A-6)}$$

$$a \equiv (1/2)[1 + (1 - Q^2)K_1^2] \quad \text{(A-7)}$$

$$b \equiv (1/2)K_2 \quad \text{(A-8)}$$

$$c \equiv (K_3/z_m^*)\{K_1 + [K_3/(z_m^* + 1)]\} \quad \text{(A-9)}$$

Thus, Eqs. (22a) and (22b) can be written as

$$z_m^* \equiv \sqrt{a} - b \quad \text{(A-10)}$$

$$z_M^* \equiv \sqrt{a}\sqrt{1 + (c/a)} - b \quad \text{(A-11)}$$

Assuming that $\delta \ll 1$ (A-12)

it then follows that c/a is small, and that z_M^* can be written approximately as

$$z_M^* \cong z_m^* + (c/2\sqrt{a}) \quad \text{(A-13)}$$

From this equation, then,

$$\delta = c/2z_m^*\sqrt{a} \quad \text{(A-14)}$$

and so, by substituting the foregoing definition, Eq. (22d) is established.

To determine the error in the approximation of Ψ^* by Ψ_{m1}^* under Condition II, we use the inequality

$$|\Psi^* - \Psi_{m1}^*| < |\Psi_M^* - \Psi_m^*| + |\Psi_m^* - \Psi_{M1}^*|$$

Neglecting terms of order $(1/2)(\Psi_{m1}^*)^{-2}$ with respect to one, the bound can be written

$$\left|\frac{\Psi^* - \Psi_{m1}^*}{\Psi_{m1}^*}\right| < \left|\frac{\Psi_M^* - \Psi_m^*}{\Psi_m^*}\right| \quad \text{(A-15)}$$

Now, if $\Delta\Psi^*$ and Δz^* are small differences, it follows from Eq. (24b) that

$$\Delta\Psi^*/\Psi^* = 2(\Delta z^*/z^*)\cdot[(\Psi^* + 1)/\Psi^*] \quad \text{(A-16)}$$

If the differences are small, we can use Eq. (A-14) to write Eq. (A-16) approximately as

$$\left|\frac{\Psi_M^* - \Psi_m^*}{\Psi_m^*}\right| \cong 2 \cdot \frac{c}{2z_m^*\sqrt{a}} \cdot \frac{\Psi_{m1}^* + 1}{\Psi_{m1}^*} \quad \text{(A-17)}$$

Substituting Eq. (A-7) and (A-9) into Eq. (A-17) and using Eq. (A-17) in Eq. (A-15) leads to Eq. (25e).

Partial Derivatives of ω^*

Performing the differentiations indicated by Eq. (30) and using the following definitions for auxiliary symbols—viz.,

$$M \equiv [T_{s0}/(T_f - T_{s0})][(K_2 + 1)/2] + (K_2 - 1)(E/RT_{s0}) \quad \text{(A-18)}$$

$$N_1 \equiv (2K_1/\Psi_{m1}^*) \times \{1 - [QK_1/\sqrt{1 + (1 - Q^2)K_1^2}]\} \quad \text{(A-19)}$$

$$N_2 \equiv 1 + [\sqrt{2}(K_2 - 1)/\Psi_{m1}^*] \times \{[1 + (1 - 2Q^2)K_1^2]/\sqrt{1 + (1 - Q^2)K_1^2}\} \quad \text{(A-20)}$$

$$N_3 \equiv (N_1/M)[2K_1 - (2E/RT_{s0})] \quad \text{(A-21)}$$

$$N_4 \equiv (2N_2/M)(E/RT_{s0}) \quad \text{(A-22)}$$

we then can derive the following formulas:

$$(\kappa/\omega^*)(\partial\omega^*/\partial\kappa) = 1 - N_2 + (N_4 - N_3) \times [(K_2 - 1)/2] \quad \text{(A-23)}$$

$$(\rho_x/\omega^*)(\partial\omega^*/\partial\rho_x) = -1 + 2N_2 - (N_4 - N_3)(K_2 - 1) \quad \text{(A-24)}$$

$$(c/\omega^*)(\partial\omega^*/\partial c) = -N_1(4L_sE/cR\,T_{s0}^2) - (N_4 - N_3)[(T_{s0} - T_i)/(T_f - T_{s0})] + N_2 \quad \text{(A-25)}$$

$$(L_s/\omega^*)(\partial\omega^*/\partial L_s) = N_1(4L_sE/cR\,T_{s0}^2) - (N_4 - N_3)[L_s/c(T_f - T_{s0})] \quad \text{(A-26)}$$

$$(B/\omega^*)(\partial\omega^*/\partial B) = N_3(K_2 - 1) + N_4(RT_{s0}/E)[T_{s0}/(T_f - T_{s0})][(K_2 + 1)/2] \quad \text{(A-27)}$$

$$(E/\omega^*)(\partial\omega^*/\partial E) = N_1K_1 - N_3(E/RT_{s0}) \times (K_2 - 1) - N_4[T_{s0}/(T_f - T_{s0})][(K_2 + 1)/2] \quad \text{(A-28)}$$

$$(T_i/\omega^*)(\partial\omega^*/\partial T_i) = -N_1(2E/RT_{s0})(T_i/T_{s0}) + (N_4 - N_3)[T_i/(T_f - T_{s0})] \quad \text{(A-29)}$$

$$(T_f/\omega^*)(\partial\omega^*/\partial T_f) = (N_4 - N_3) \times [T_f/(T_f - T_{s0})][(K_2 - 1)/2] \quad \text{(A-30)}$$

$$(k/\omega^*)(\partial\omega^*/\partial k) = -1 \quad \text{(A-31)}$$

References

[1] Green, L., Jr., *Some Properties of a Simplified Model of Solid-Propellant Burning*, Jet Propulsion, Vol. 28, No. 6, pp. 386–392, June, 1958.

[2] Green, L., Jr., *Some Effects of Oxidizer Concentration and Particle Size on Resonance Burning of Composite Solid Propellants*, Jet Propulsion, Vol. 28, No. 3, pp. 159–164, March, 1958.

[3] Price, E. W., and Sofferis, J. W., *Combustion Instability in Solid Propellant Rocket Motors*, Jet Propulsion, Vol. 28, No. 3, pp. 190–192, March, 1958.

[4] Green, L., Jr., and Nachbar, W., *A Comment on Combustion Instability in Solid Propellant Rocket Motors*, Jet Propulsion, Vol. 28, No. 11, p. 769, November, 1958.

Readers' Forum

BRIEF REPORTS of investigations in the aerospace sciences and discussions of papers published in the JOURNAL are presented in this special department. Entries must be restricted to a maximum of 1,300 words or the equivalent of one JOURNAL page including formulas and illustrations. Publication is completed as soon as possible after receipt of the material. The Editorial Committee does not hold itself responsible for the opinions expressed by the correspondents.

Contents

A Study of the Adiabatic Exponent of the "Hydrodynamical Gas" by Statistical Thermodynamics. SYŌGO MATSUNAGA 527

On "Transformation of the Compressible Turbulent Boundary Layer". . . . . MICHIRU YASUHARA 528

Inviscid Hypersonic Flow Around Spheres and Circular Cylinders. . . . . E. DALE MARTIN 529

Approximate Bending Moment Diagrams for Flight Maneuvers. . . . . P. W. SHARMAN 530

Heat Transfer for Laminar Flow in an Annulus With Porous Walls. . . . . ROBERT M. INMAN 532

Preliminary Results of Measurement of Effects of Diffusion of Helium Into the Laminar Boundary Layer of a Supersonic Flow of Air in a Tube at Mach 5. . . . . S. WILLIAM GOUSE, JR., GEORGE A. BROWN, AND JOSEPH KAYE 533

On the Application of the Ursell-Ward Theorem to Wings With Edge Forces. . . . . JOSEPH H. CLARKE 535

A Note on Magnetohydrodynamic-Hypersonic Flow Past a Blunt Body. . . . . WILLIAM B. BUSH 536

The Effect of Vehicle Deceleration on a Melting Surface. . . . . D. M. TELLEP 537

Summary of Laminar Heat Transfer Between Parallel Plates With Unsymmetrical Wall Temperatures. . . . . R. D. CESS AND E. C. SHAFFER 538

An Investigation of a Low-Drag Auxiliary Body Utilizing Favorable Interference. . . . . ANTHONY MARTELLUCCI 538

Application of Generalized Gauss-Laguerre Quadrature to Boundary-Layer Problems. . . . . WILLIAM SQUIRE 540

Errata—"Coupled Free Vibrations of a Swept Wing". . . . . A. E. ENGELBRECHT AND W. P. RODDEN 541

The Law of the Wake in Compressible Turbulent Boundary Layers. . . . . PAUL A. LIBBY AND MARIAN VISICH, JR. 541

Vorticity Effect on the Stagnation-Point Flow of a Viscous Incompressible Fluid. . . . . NICHOLAS ROTT AND MICHAEL LENARD 542

Vorticity Interaction at an Axisymmetric Stagnation Point in a Viscous Incompressible Fluid. . . . NELSON H. KEMP 543

A Study of the Adiabatic Exponent of the "Hydrodynamical Gas" by Statistical Thermodynamics

Syōgo Matsunaga
Tire Design Department, Bridge Stone Tire Company Ltd., Kurume, Fukuoka, Japan

March 2, 1959

THE HYDRODYNAMICAL model tests are very useful for the study of two-dimensional high-speed gas flows. The adiabatic exponent of the imaginary "hydrodynamical gas" is obtained by the hydrodynamical-analogy relations,[1] and the thermodynamical explanations cannot be seen.

In this paper, the author wishes to study the adiabatic exponent $\gamma = C_p/C_v$ of the "hydrodynamical gas" by means of two-dimensional statistical thermodynamics.

Let γ = exponent of the adiabatic change
C_p = specific heat of gas at constant pressure
C_v = specific heat of gas at constant volume

By statistical thermodynamics, the energy per molecule of permanent perfect gas with no energy due to the internal degrees of freedom (rotational and vibrational energies) can be written, as follows[2]

$$E = (3/2)kT$$

where E = total energy summing up the three-dimensional energy components
$k = 1.380 \times 10^{-16}$ erg/deg. = Boltzmann's constant
T = absolute temperature

For the two-dimensional "hydrodynamical gas," the author wishes to use the following energy summing up two-dimensional energy components:

$$E = (3/2)kT \times (2/3) = kT$$

Contributors Please Note

Readers' Forum items must be confined to the equivalent of one page in the *Journal*. Contributions that exceed this limit will be returned to the authors for condensation and rewrite. To avoid inconvenience and delay, please adhere to the following specifications:

(1) Five, double-spaced, typewritten, manuscript pages ($8\frac{1}{2}$ by 11 in.), including wide margins, formulas, and headings, equal one printed page.

(2) For every illustration, deduct at least one-half or as much as one manuscript page, depending on the size of the illustration.

By the following relation[3]

$$PV = kT$$

where P = pressure
V = molecular volume

the next relation[4] of

$$C_v = (\partial E/\partial T)_V = k$$

and, further, the following relation[5]

$$C_p = [\partial(E + PV)/\partial T]_P = (\partial E/\partial T)_P + k = 2k$$

are obtained for the two-dimensional "hydrodynamical gas." Then the adiabatic exponent of the "hydrodynamical gas" is

$$\gamma = C_p/C_v = 2.0$$

which is the value obtained by the hydrodynamical-analogy method.

In conclusion, the "hydrodynamical gas" can be understood as a two-dimensional monatomic-molecule gas by statistical thermodynamics, but the "hydrodynamical gas" is an imaginary gas because the movement of molecules cannot be restricted to two-dimensional directions. Thus, the concept of a two-dimensional monatomic-molecule gas can be understood only in connection with the two-dimensional shallow water flow analogy.

References

[1] Ostwatitsch, Klaus, *Gasdynamik*, p. 442; Springer Verlag, Vienna, 1952.
[2] Fowler, R. H., and Guggenheim, E. A., *Statistical Thermodynamics*, p. 80; Cambridge at the University Press, Cambridge, 1939.
[3] Ibid., p. 72 [Eq. (301.8)].
[4] Ibid., p. 80 [Eq. (309.2)].
[5] Ibid., p. 80 [Eq. (309.4)].

On "Transformation of the Compressible Turbulent Boundary Layer"

Michiru Yasuhara
Assistant Professor, Department of Aeronautical Engineering, Nagoya University, Nagoya, Japan

February 26, 1959

In a recent paper,[1] A. Mager showed that the transformation of the compressible turbulent boundary-layer equations to their incompressible equivalent can be made under assumptions that the Prandtl Number equals unity and the flow is adiabatic, and also under the postulation that the apparent turbulent shear associated with an elemental mass remains invariant in the transformation, etc. He also showed that the flat-plate skin-friction law and the pressure ratio of shock-separated boundary layer in compressible turbulent flow calculated by this method approximate the experimental data with good accuracy.

If the turbulent mechanism in the transformed plane plays the same role as that in the incompressible one, then also the mean

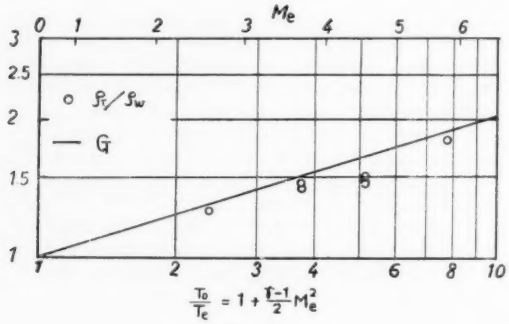

Fig. 1.

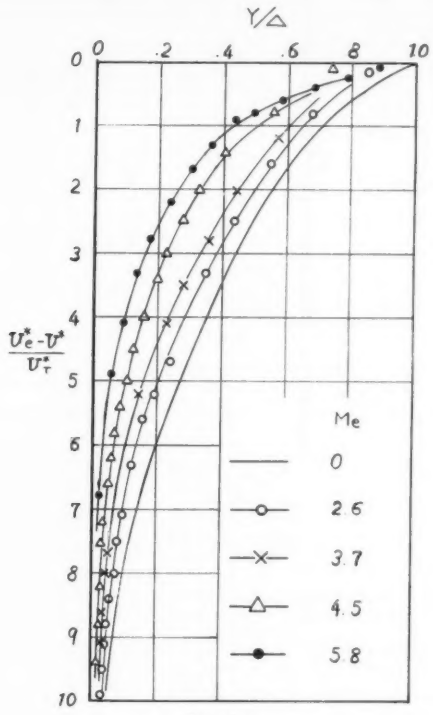

Fig. 2.

quantities expressed in the transformed plane must follow the incompressible turbulent wall law and the velocity-defects law for the equilibrium flow. To check this, first, the coordinates used to express the wall law in the imaginary plane are transformed back into the physical one, as follows:

$$U^*/U_\tau^* = U/\sqrt{\tau_w/\rho_w}\cdot G^{1/2} \tag{1}$$

$$\eta^* = U_\tau^* Y/\nu_0 = (\sqrt{\tau_w/\rho_w}/\nu_w)\left[\int_0^y (\rho/\rho_w)dy\right]\cdot G^{1/2} \tag{2}$$

where the same notations as in reference 1 are used, and

$$G \equiv \mu_w/\mu_0 \tag{3}$$

On the other hand, Professor Coles[2] recently derived the streamline hypothesis from the wall law. This states that U/U_τ keeps constant on the mean streamline in the turbulent boundary layer near the wall. He extended the above concept to compressible flow by introducing the friction density to be determined from the experimental data, so as to make the deduced wall law the best fit with the incompressible one. The coordinates used to express the wall law are given, as follows:

$$U/U_\tau = (U/\sqrt{\tau_w/\rho_w})\cdot(\rho_\tau/\rho_w)^{1/2} \tag{4}$$

$$\eta = (\rho_\tau U_\tau/\rho_w\mu_w)\left(\int_0^y \rho dy\right) = (\sqrt{\tau_w/\rho_w}/\nu_w)\left[\int_0^y (\rho/\rho_w)dy\right]\cdot(\rho_\tau/\rho_w)^{1/2} \tag{5}$$

ρ_τ/ρ_w as the function of free-stream Mach Number, obtained from experimental data in insulated cases, are plotted in Fig. 1. By comparing Eq. (1) and Eq. (2) with Eq. (4) and Eq. (5) formally, it is easily known that, if G equals to ρ_τ/ρ_w, these coincide completely. In Fig. 1, also G is shown against the free-stream Mach Number by applying the same $\mu - T$ and $\mu - \rho$ relation as Mager's. The coincidence is fairly good. This seems to give proof that Mager's postulation is correct for the present problem (Fig. 1).

In the outer layer where the pressure gradients affect the flow

pattern, the velocity-defects law is derived for the equilibrium flow, for example, for the flat-plate turbulent boundary layer. The coordinates used to express the velocity-defects law in the imaginary plane are transformed back into physical one, as follows:

$$(U_e^* - U^*)/U_\tau^* = (U_e - U)/\sqrt{\tau_w/\rho_w}\cdot G^{1/2} \qquad (6)$$

$$Y/\Delta = \eta^*(y)/\eta^*(\delta) = \int_0^y \rho dy \Big/ \int_0^\delta \rho dy \qquad (7)$$

Relations between $(U_e^* - U^*)/U_\tau^*$ and Y/Δ are plotted in Fig. 2 for several Mach Numbers obtained from the experimental data measured by Coles[3] and Korkegi[4] for insulated cases. The curves show unexpected appreciable effects of Mach Number in contrast to the case of the wall law (Fig. 2).

It may be difficult to explain such discrepancies satisfactorily, except to say that some assumptions are made in the calculation. But in view of transforming procedure of equations of mean flow, it seems to be an explanation for such discrepancies that the transformed turbulent shear is affected by compressibility, though this explicit term is cancelled out when integrated over the boundary layer. If the variation of velocity profile has, practically, only a little effect on the momentum integral equation in high-speed flow, it may be expected also that these discrepancies have only little effects on the skin friction or the wall pressure.

But these discussions are not decisive, and further investigations are expected to give more reasonable explanations.

References

[1] Mager, A., *Transformation of the Compressible Turbulent Boundary Layer*, Journal of the Aeronautical Sciences, Vol. 25, No. 5, pp. 305–311, May, 1958.

[2] Coles, D., *50 Jahre Grenzschichtforschung, The Law of the Wall in Turbulent Shear Flow*, F. Vieweg und Sohn, Braunschweig, pp. 153–163, 1955.

[3] Coles, D., *Measurements of Turbulent Friction on a Smooth Flat Plate in Supersonic Flow*, Journal of the Aeronautical Sciences, Vol. 21, No. 7, pp. 433–447, July, 1954.

[4] Korkegi, R. H., *Transition Studies and Skin-Friction Measurements on an Insulated Flat Plate at a Mach Number of 5.8*, Journal of the Aeronautical Sciences, Vol. 23, No. 2, pp. 97–107, 192, February, 1956.

Inviscid Hypersonic Flow Around Spheres and Circular Cylinders†

E. Dale Martin*

Aeronautical Research Engineer, NASA, Ames Research Center, Moffett Field, Calif.

February 26, 1959

Symbols

δ	= shock detachment distance
K	= $1/R$ where R is the body radius
k	= ratio of free-stream density to density behind normal shock
α	= $(1 - k)/k$
u, v	= velocity components parallel and perpendicular, respectively, to the body surface
U	= free-stream velocity
u^*, v^*	= u/U, v/U, respectively
j	= 0 for the circular cylinder
	= 1 for the sphere
ϕ	= body angle measured from the stagnation streamline
y	= distance from the body surface
β	= $K\alpha/(1 + K\delta)$
Ω	= $(1 + Ky)/K$
ω^*	= ω/KU, where ω = vorticity (curl of velocity)
ψ^*	= $K^{j+1}\psi/\rho_\infty U$, where ψ = the stream function
C_p	= $(P - P_\infty)/(1/2)\rho_\infty U^2$
M	= local Mach Number

† The research performed at Rensselaer Polytechnic Institute in connection with reference 1, on which this note is based, was supported in part by the USAF under Contract No. AF 18(600)-1591, monitored by the Air Force Office of Scientific Research of ARDC.

* Formerly, National Science Foundation Fellow, Rensselaer Polytechnic Institute, Troy, N.Y.

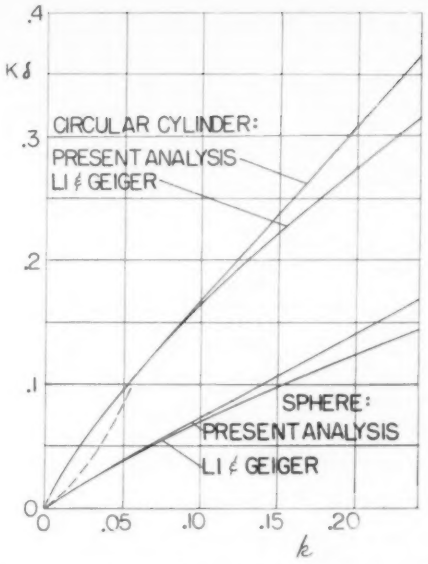

FIG. 1. Detachment distance vs. shock density ratio.

Subscripts

∞ = value in the free steam
B = value on the body (at $y = 0$)

AN APPROXIMATE METHOD for calculating the flow about spheres and circular cylinders in steady inviscid hypersonic flow has been presented in reference 1. An analysis which yields identical results for the sphere was given by Lighthill,[2] and that for the circular cylinder was also given by G. B. Whitham.[3] However, Lighthill and Whitham gave very few numerical or graphical results. It is the purpose of this note to summarize the final equations for the flow properties from reference 1 and to present some graphical results.

In addition to the customary assumptions and approximations of inviscid flow problems, the following two approximations are made: the detached bow shock wave is nearly concentric with the body, and the density in the region between the body and the shock wave is nearly constant. These approximations are discussed in reference 1 and are shown to be valid for sufficiently high free-stream Mach Numbers.

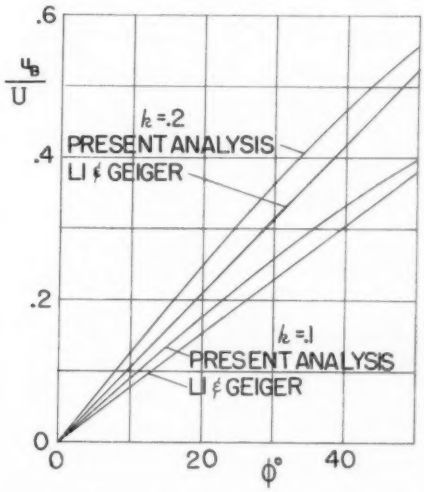

FIG. 2. Surface velocity distribution on a sphere.

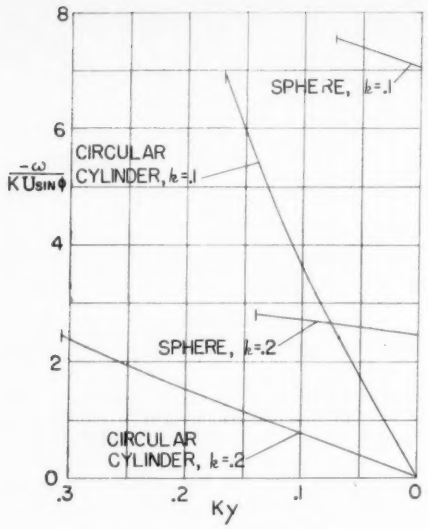

FIG. 3. Vorticity distribution.

Axisymmetric shock detachment distance is the value of δ for which, at a given k,

$$F_1 = 2\zeta^5(\alpha^2 - 5\alpha) - 5\zeta^2(\alpha^2 - 2\alpha - 3) + 3\alpha^2 = 0 \quad (1)$$

where $\zeta = 1 + K\delta$, while cylindrical shock detachment distance is the root of

$$F_0 = [I_1(\beta/K)/K_1(\beta/K)] - \{[(\alpha + 2)I_1(\alpha) - \alpha I_0(\alpha)]/[\alpha K_0(\alpha) + (\alpha + 2)K_1(\alpha)]\} = 0 \quad (2)$$

where I_0, I_1, K_0, and K_1 are "modified Bessel Functions." These two equations are easily solved for given values of k by substituting values of $K\delta$ and plotting F vs. $K\delta$ to find where $F = 0$. The solutions to these equations are plotted in Fig. 1. The velocity components are

$$u^* = \sin\phi\, G_j' \quad (3)$$

$$v^* = (j + 1)\cos\phi\, G_j \quad (4)$$

where

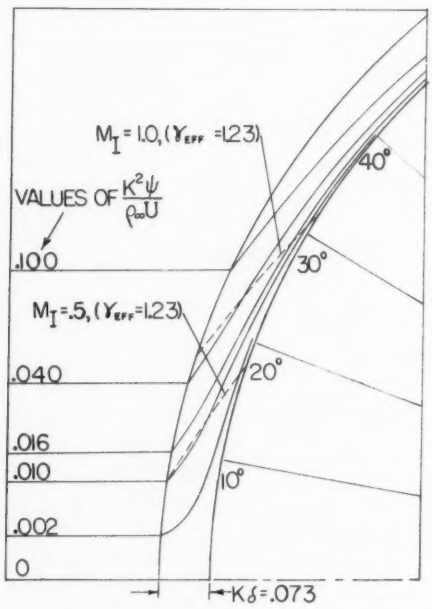

FIG. 4. The flow pattern about a sphere at $k = 0.10$.

$$G_1 = (k/30)\,[3(\beta z)^2 - 5(\alpha^2 - 2\alpha - 3) + 2\alpha^4(\alpha - 5)\,(1/\beta z)^3] \quad (5)$$

$$G_1' = (k/30)\,[12(\beta z)^2 - 10(\alpha^2 - 2\alpha - 3) - 2\alpha^4(\alpha - 5)\,(1/\beta z)^3] \quad (6)$$

$$G_0 = (1/\beta z)k\alpha^2[C_1 I_1(\beta z) + C_2 K_1(\beta z)] \quad (7)$$

$$G_0' + G_0 = k\alpha^2[C_1 I_0(\beta z) - C_2 K_0(\beta z)] \quad (8)$$

and where

$$\left.\begin{aligned} C_1\alpha &= \alpha K_0(\alpha) + (\alpha + 2)K_1(\alpha) \\ C_2\alpha &= \alpha I_0(\alpha) - (\alpha + 2)I_1(\alpha) \end{aligned}\right\} \quad (9)$$

$$\omega_j^* = -\sin\phi[k\alpha/(1 + K\delta)]\,(\beta z)\,(G_j/k)^{1-j} \quad (10)$$

$$\psi_j^* = (1/k)\,(\sin\phi)^{j+1}\,(1 + Ky)^{j+1}\,G_j \quad (11)$$

Pressure coefficient at any point may be found from

$$C_p = 2 - k\{1 - \sin^2\phi\,(\beta z)^2\,[G_j(y)/G_j(\delta)]^{2/(j+1)} + (1/k)^2\,[u^{*2} + v^{*2}]\} \quad (12)$$

On the body, the pressure coefficient is simply

$$C_{pB} = 2 - k - (1/k)u_B^{*2} \quad (13)$$

Define $$M_I = \sqrt{(\rho_\infty/k)\,(u^2 + v^2)/\gamma P} \quad (14)$$

—i.e., the local Mach Number based on nearly constant density. Then, lines of constant M_I may be plotted from the following equation by substituting values of y into the right side and solving for ϕ:

$$\sin^2\phi = [g_5 - g_1 g_2]/[g_1(g_4 - g_2) - g_3] \quad (15)$$

where $g_1 = (1/k)\,[(2/\gamma M_I^2) + 1]$, $g_2 = [(j + 1)G_j]^2$, $g_3 = k(\beta z)^2\,[G_j(y)/G_j(\delta)]^{2/(j+1)}$, $g_4 = [G_j']^2$, $g_5 = 2/(\gamma_\infty M_\infty^2) + 2 - k$

and where γ is an "effective γ," found from equilibrium gas charts, as suggested in reference 1. It should be noted that, on Fig. 4, the $M_I = 1$ line is not a good approximation to the sonic line, since it is out of the region of applicability of the method.

REFERENCES

1 Martin, E. Dale, *Inviscid Hypersonic Flow Around Spheres and Circular Cylinders*, Rensselaer Polytechnic Institute, TR AE5807, April, 1958.

2 Lighthill, M. J., *Dynamics of a Dissociating Gas, Part I, Equilibrium Flow*, J. Fluid Mech., Vol. 2, Pt. 1, pp. 1–32, January, 1957.

3 Whitham, G. B., *A Note on the Standoff Distance of the Shock in High Speed Flow Past a Circular Cylinder*, Communications on Pure and Applied Mathematics, New York University, New York, November, 1957.

4 Li, Ting-Yi, and Geiger, Richard E., *Stagnation Point of a Blunt Body in Hypersonic Flow*, Journal of the Aeronautical Sciences, Vol. 24, No. 1, pp. 25–32, January, 1957.

Approximate Bending Moment Diagrams for Flight Maneuvers

P. W. Sharman
G. W. Division, Bristol Aircraft, Ltd., Bristol, England

February 20, 1959

IN SPLITTING the lift and weight distributions along a body into a number of discrete loads, substantial errors in bending moment diagrams may be produced by using too few elements. However, in the early project stage, a rapid answer is usually required which dictates a small number of elements. A better approximation than a small number of discrete loads may be obtained by using a few uniformly distributed loads, three or four usually being sufficient. This method is considerably quicker and, thus, more cases may be studied in a given time. A knowledge of the bending moment in the worst flight case enables the body skin thickness or effective thickness to be fixed, and, hence, body structure weight may be estimated, and also the lightest type of structure may be selected.[1]

The lengths along which the distributed loads act are usually

determined from the layout, and the magnitudes of the distributed loads may be adjusted to give the correct *CP* and *CG*. Assuming that four uniformly distributed loads are sufficient, then referring to Fig. 1, the *CP* and *CG* positions are:

$$x_L = l_1[(K_1/2) + K_2 + K_3 + K_4] + l_2[(K_2/2) + K_3 + K_4] + l_3[(K_3/2) + K_4] + l_4(K_4/2)$$

$$x_w = l_1[(R_1/2) + R_2 + R_3 + R_4] + l_2[(R_2/2) + R_3 + R_4] + l_3[(R_3/2) + R_4] + l_4(R_4/2)$$

If more elements are required, these equations may be written for n elements:

$$x_L = \sum_1^n \left\{ l_j \left[(K_j/2) + \sum_{j+1}^n K_j \right] \right\}$$

and, similarly, for x_w. K_j is the ratio of the lift on the element j to the total lift L (zero control force), R_j is the ratio of the weight of element j to the total weight W, note

$$\sum_1^n K_j = \sum_1^n R_j = 1$$

Steady-State Maneuver

The control force F (positive lifting) for a maneuver of ng normal acceleration may be found from a static balance—i.e.,

$$F/nW = (x_w - x_L)/(x_F - x_L)$$

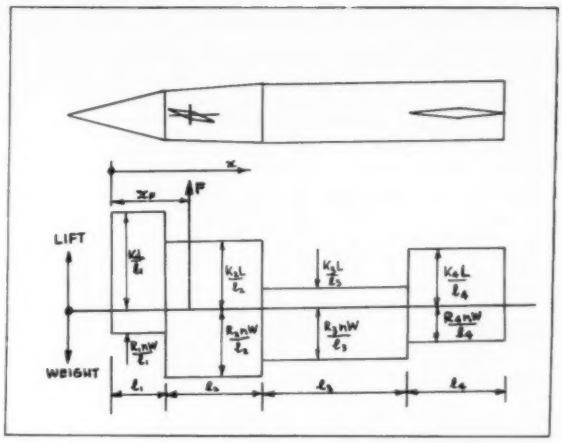

FIG. 1. Idealized distributions of lift and weight.

and, hence, the total lift required is

$$L/nW = 1 - (F/nW) = (x_F - x_w)/(x_F - x_L)$$

Using Macaulay's notation[2]—i.e., items in square brackets are zero when algebraically less than zero—the nondimensional bending moment along the body is:

$$M(x)/nWl = -(F/nW)\,[(x/l) - (x_F/l)] + (l/2l_1)\,(R_1 - K_1L/nW)\,\{[x/l]^2 - [(x/l) - (l_1/l)]^2\} + (l/2l_2)\,(R_2 - K_2L/nW)\,\{[(x/l) - (l_1/l)]^2 - [(x/l) - (l_1/l) - (l_2/l)]^2\} + (l/2l_3)\,(R_3 - K_3L/nW) \times \{[(x/l) - (l_1/l) - (l_2/l)]^2 - [(x/l) - (l_1/l) - (l_2/l) - (l_3/l)]^2\} + (l/2l_4)\,(R_4 - K_4L/nW)\,[(x/l) - (l_1/l) - (l_2/l) - (l_3/l)]^2$$

for n elements:

$$M(x)/nWl = (1/2)\sum_1^n \left\{ (l/l_j)\,(R_j - K_jL/hW) \left(\left[(x/l) - \sum_1^{j-1} (l_j/l) \right]^2 - \left[(x/l) - \sum_1^{j} (l_j/l) \right]^2 \right) \right\} - (F/nW)\,[x/l - x_F/l]$$

where l is some characteristic length.

To find the position and value of the maximum bending moment in any section, these equations may be differentiated, etc., provided the notation is retained.

Transient Maneuvers

For transient maneuvers involving pitching (or yawing) accelerations only, with no aerodynamic loads other than the control force F producing the maneuver, the nondimensional bending moment due to angular acceleration q is:

$$M(x)g/Wl^2\dot{q} = -i'[(x/l) - (xF/l)] + (Rl/2l_1)\,[i' - (xw/l)]\,\{[x/l]^2 - [(x/l) - (l_1/l)]^2\} + (R_2l/2l_2)\,[i' - (xw/l)] \times \{[(x/l) - (l_1/l)]^2 - [(x/l) - (l_1/l) - (l_2/l)]^2\} + (R_3l/2l_3)\,[i' - (xw/l)]\,\{[(x/l) - (l_1/l) - (l_2/l)]^2 - [(x/l) - (l_1/l) - (l_2/l) - (l_3/l)]^2\} + (R_4l/2l_4)\,[i' - (xw/l)]\,[(x/l) - (l_1/l) - (l_2/l) - (l_3/l)]^2 + (R_1l/2l_1) \times \{1/3[x/l]^3 - (1/3)[(x/l) - (l_1/l)]^3 - (l_1/l)\,[(x/l) - (l_1/l)]^2\} + (R_2l/2l_2)\,\{(1/3)[(x/l) - (l_1/l)]^3 - (1/3)\,[(x/l) - (l_2/l)]^3 - (l_1/l)\,[(x/l) - (l_1/l)]^2 - [(l_1/l) + (l_2/l)]\,[(x/l) - (l_1/l) - (l_2/l)]^2\} + (R_3l/2l_3)\,\{(1/3)[(x/l) - (l_1/l) - (l_2/l)]^3 - (1/3)\,[(x/l) - (l_1/l) - (l_2/l) - (l_3/l)]^3 + [(l_1/l) + (l_2/l)]\,[(x/l) - (l_1/l) - (l_2/l)]^2 - [(l_1/l) + (l_2/l) + (l_3/l)]\,[(x/l) - (l_1/l) - (l_2/l) - (l_3/l)]^2\} + (R_4l/2l_4)\,\{(1/3)[(x/l) - (l_1/l) - (l_2/l) - (l_3/l)]^3 + [(l_1/l) + (l_2/l) + (l_3/l)]\,[(x/l) - (l_1/l) - (l_2/l) - (l_3/l)]^2\}$$

where $i' = i + [(x_F/l) - (xw/l)]$, and i is the nondimensional longitudinal moment of inertia given by:

$$i = Ig/Wl^2 = R_1[(xw/l) - (l_1/2l)]^2 + R_2[(xw/l) - (l_1/l) - (l_2/2l)]^2 + R_3[(xw/l) - (l_1/l) - (l_2/l) - (l_3/2l)]^2 + R_4[(xw/l) - (l_1/l) - (l_2/l) - (l_3/l) - (l_4/2l)]^2 + (1/12)\,\{R_1(l_1/l)^2 + R_2(l_2/l)^2 + R_3(l_3/l)^2 + R_4(l_4/l)^2\}$$

for n elements:

$$M(x)g/Wl^2\dot{q} = (1/2)[i' - (x_w/l)]\sum_1^n \left\{ R_j(l/l_j) \left(\left[(x/l) - \sum_1^{j-1} (l_j/l) \right]^2 - \left[(x/l) - \sum_1^{j} (l_j/l) \right]^2 \right) \right\} + (1/2)\sum_1^n \left\{ R_j(l/l_j)(1/3) \left[(x/l) - \sum_1^{j-1} (l_j/l) \right]^3 - (1/3) \left[(x/l) - \sum_1^{j} (l_j/l) \right]^3 + \left[\sum_1^{j-1} (l_j/l) \right] \left[(x/l) - \sum_1^{j-1} (l_j/l) \right]^2 - \left[\sum_1^{j} (l_j/l) \right] \left[(x/l) - \sum_1^{j} (l_j/l) \right]^2 \right\} - i'[(x/l) - (x_F/l)]$$

$$i = \sum_1^n \left\{ R_j \left[(xw/l) - \sum_1^{j-1} (l_j/l) - (l_j/2l) \right] \right\} + (1/12)\sum_1^n \{R_j(l_j/l)^2\}$$

The control force F is given by

$$F = (Wl\dot{q}/g)i'$$

(Note that I is in slug units.)

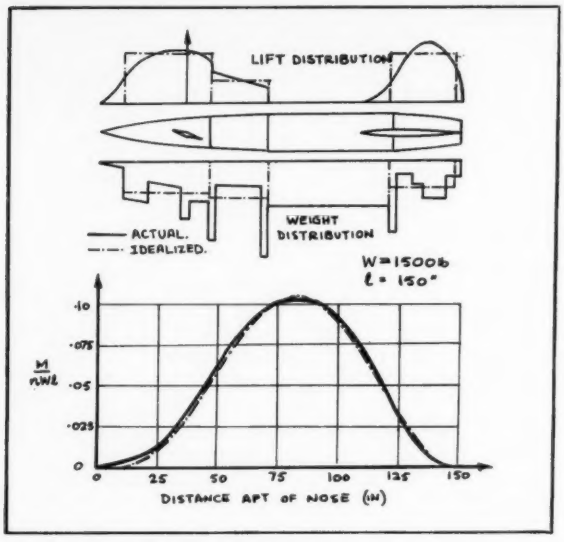

FIG. 2. Comparison of idealized solution ($n = 4$) with standard method.

In some cases, a uniform weight distribution along an effective length will suffice for bending moment calculations in maneuvers. Substituting $wl^2/12g$ for I gives:

$$6M(x)g/Wl^2\dot{q} = \{1/2[2(x_F/l) - 1] - (3/2)\} \times \{[x/l]^2 - [x/l]^3\} - \{1/[2(x_F/l) - 1]\}\,[(x/l) - (x_F/l)]$$

The method is applied to a hypothetical missile with a given weight and lift distribution and compared with an 18-element discrete load solution in Fig. 2.

REFERENCES

[1] Gerard, G., *Comparative Efficiency in Bending of Structural Elements of Various Design and Solidity*, New York University, College of Engineering, 1952.

[2] Macaulay, W. H., *Note on the Deflection of Beams*, Messenger of Mathematics (now Quart. J. Math.), Vol. 48, pp. 129, 130, Cambridge, England, January, 1919.

Heat Transfer for Laminar Flow in an Annulus With Porous Walls

Robert M. Inman

Assistant in Engineering, Department of Engineering, University of California, Los Angeles, Calif.

March 2, 1959

SYMBOLS

a	=	radius of the outer pipe of the annulus
b	=	radius of the inner pipe of the annulus
Pe	=	Peclet Number (PrR)
Pr	=	Prandtl Number ($\mu C_p/\kappa$)
q	=	heat-transfer rate per unit area
R	=	Reynolds Number for the cross flow (av_a/ν)
v_a, v_b	=	cross-flow velocities at the outer and inner walls of the annulus, respectively
ζ	=	a dimensionless distance parameter equal to $(\lambda - \sigma)/(1 - \sigma)$
θ	=	dimensionless temperature parameter equal to $(T - T_b) \div (T_a - T_b)$
λ	=	dimensionless distance parameter equal to (r/a), $\sigma \leq \lambda \leq 1$
σ	=	radius ratio of the annulus, (b/a)

Subscripts

a	refers to outer pipe of the annulus
b	refers to inner pipe of the annulus

THE PROBLEM of fluid flowing two-dimensionally between bounding walls with one or both of the walls porous is of considerable practical interest. Interest has recently been directed toward the problem of laminar flow in an annulus with porous walls.[1]

However, little effort has been expended in determining the effects of injection and/or suction at the walls of porous channels and pipes on the temperature distribution and heat transfer. Up to the present, there has been presented the solution to the problem of heat transfer in laminar pipe flow with uniform coolant injection.[2] The purpose of this work is to determine the effects of the variation of cross-flow velocity on the temperature distribution and heat transfer for flow in an annulus with porous walls. In this investigation, a solution of the energy equation in cylindrical coordinates is obtained in which the radial velocity component was obtained from reference 1.

The assumptions made in the present study are: (a) the fluid is incompressible, and viscous dissipation and axial heat conduction is negligible; (b) the fluid injection rate at one wall is equal to the fluid withdrawal rate at the other wall; (c) the wall temperatures are constant; and (d) no diffusion takes place.

By introducing a curvilinear coordinate system with the origin at the center of the cross section of the inner concentric pipe, where x is taken in the direction of the flow and r in the radial direction, and, by assuming that the terms due to the pressure gradient and the dissipation can be neglected, the energy equation for axial symmetry reduces to the following:

$$\rho C_P[u(\partial T/\partial x) + v(\partial T/\partial r)] = \kappa[(\partial^2 T/\partial r^2) + (1/r)\,(\partial T/\partial r) + (\partial^2 T/\partial x^2)] \quad (1)$$

Because of the condition that the withdrawal rate at one wall be equal to the injection rate at the other wall, and the assumption of constant wall temperatures, the fluid temperature T does not depend on x. Hence, Eq. (1) can be reduced to the form

$$\rho C_P v(\partial T/\partial r) = \kappa[(\partial^2 T/\partial r^2) + (1/r)\,(\partial T/\partial r)] \quad (2)$$

In reference 1, it was shown that the axial velocity component u does not depend on x; and the solution to the cross-flow velocity was given as

$$v = v_a/\lambda \quad (3)$$

Defining a dimensionless temperature variable θ by

$$\theta = (T - T_b)/(T_a - T_b) \quad (4)$$

Eq. (2) can be simplified to the nondimensional form

$$(d^2\theta/d\lambda^2) + (1 - Pe)\,(1/\lambda)\,(d\theta/d\lambda) = 0 \quad (5)$$

where $Pe = PrR$ and $R = (av_a)/\nu$, $Pr = (\mu C_P)/\kappa$. The boundary conditions are:

$$\theta = 1 \quad \lambda = 1 \quad (r = a) \quad (6)$$

$$\theta = 0 \quad \lambda = \sigma \quad (r = b) \quad (7)$$

The solution to Eq. (5), subject to the boundary conditions given in Eqs. (6) and (7), is

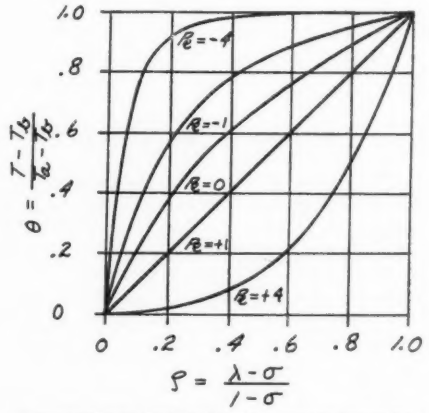

FIG. 1. Temperature distribution in a porous annulus ($\sigma = 0.2$) [$Pe > 0$, suction at outer wall; $Pe < 0$, injection at outer wall].

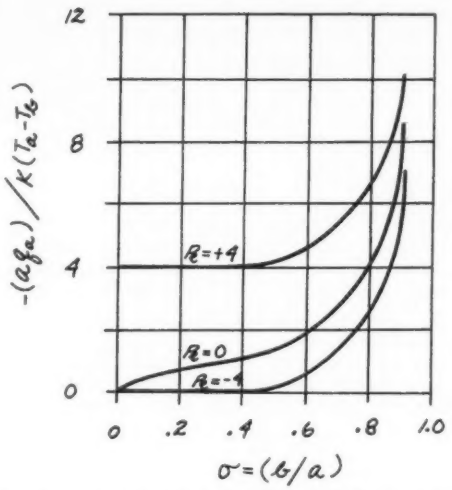

FIG. 2. Heat-transfer rate at the outer wall of porous annuli.

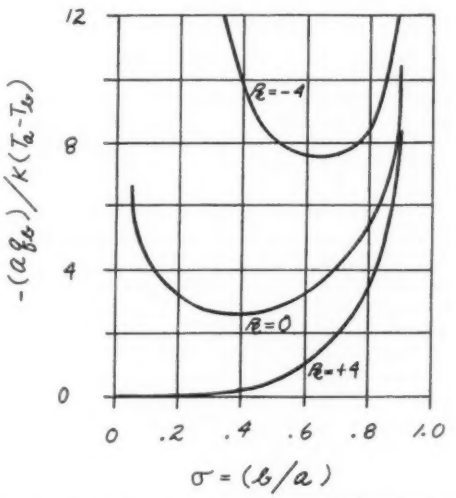

FIG. 3. Heat-transfer rate at the inner wall of porous annuli.

$$\theta = (\lambda^{Pe} - \sigma^{Pe})/(1 - \sigma^{Pe}) \tag{8}$$

Introduction of the variable $\zeta = (\lambda - \sigma)/(1 - \sigma)$ into Eq. (8) yields

$$\theta = \{[\sigma + (1 - \sigma)\zeta]^{Pe} - \sigma^{Pe}\}/(1 - \sigma^{Pe}) \tag{9}$$

For the special case of impermeable walls ($v_a = v_b = 0$), the temperature distribution can be readily determined by solution of Eq. (5) with the restriction $Pe = 0$. Using Eqs. (6) and (7), we obtain

$$\theta = 1 - (\ln \lambda/\ln \sigma) \tag{10}$$

or in terms of the variable ζ,

$$\theta = 1 - \{\ln [\sigma + (1 - \sigma)\zeta]/\ln \sigma\} \tag{11}$$

The heat-transfer rate per unit area at the outer wall of the annulus is given by

$$q_a = -\kappa(\partial T/\partial r)_{r=a} = -\kappa[(T_a - T_b)/a(1 - \sigma)] \times (\partial\theta/\partial\zeta)_{\zeta=1} \tag{12}$$

and that at the inner wall by

$$q_b = -\kappa(\partial T/\partial r)_{r=b} = -\kappa[(T_a - T_b)/a(1 - \sigma)](\partial\theta/\partial\zeta)_{\zeta=0} \tag{13}$$

For an annulus with porous walls, Eqs. (12) and (13) become, respectively,

$$q_a = -(\kappa/a)(T_a - T_b)[Pe/(1 - \sigma^{Pe})] \tag{14}$$

$$q_b = -(\kappa/a)(T_a - T_b)[Pe(\sigma^{Pe-1})/(1 - \sigma^{Pe})] \tag{15}$$

while for an annulus with impermeable walls, there results

$$q_a = (\kappa/a)(T_a - T_b)/\ln \sigma \tag{16}$$

$$q_b = (\kappa/a)(T_a - T_b)/(\sigma \ln \sigma) \tag{17}$$

In Fig. 1, the temperature difference ratio for various injection and suction rates is shown for the case of the radius ratio $\sigma = 0.2$. The effect of a cross-flow velocity is markedly evident, with injection at the outer wall "blowing" the temperature profile toward the porous inner wall, and suction at the outer wall pulling the profile toward that wall.

The heat-transfer rates at the outer and inner walls, arranged in nondimensional forms, are plotted against the radius ratio for several Peclet Numbers, in Figs. 2 and 3. For predesignated wall temperatures, the heat-transfer rates can be readily determined for any radius ratio if the outer radius a and fluid thermal conductivity κ are known.

REFERENCES

[1] Berman, Abraham, *Laminar Flow in an Annulus with Porous Walls*, J. Appl. Phys., Vol. 29, No. 1, pp. 71–75, January, 1958.

[2] Yuan, S. W., and Finkelstein, A. B., *Heat Transfer in Laminar Pipe Flow with Uniform Coolant Injection*, Jet Propulsion, Vol. 28, No. 3, pp. 178–181, March, 1958.

Preliminary Results of Measurement of Effects of Diffusion of Helium Into the Laminar Boundary Layer of a Supersonic Flow of Air in a Tube at Mach 5

S. William Gouse, Jr.,* George A. Brown,* and Joseph Kaye**
Department of Mechanical Engineering,
Massachusetts Institute of Technology, Cambridge, Mass.
March 3, 1959

DURING the past 3 years, an analytical and experimental program has been under way in the Mechanical Engineering Department of Massachusetts Institute of Technology, to investigate the effects of injection of helium, nitrogen, argon, and other gases, under carefully controlled conditions, into the laminar boundary layer of a supersonic flow of air at Mach 5 on the pressure, temperature, and recovery-factor distributions along the injection region. This program has been supported by the Office of Naval Research and the Air Force Office of Scientific Research.† Some of the experimental results are presented below.[1]

An inexpensive, continuously operating, axially symmetric wind tunnel has been designed, constructed, and operated. This tunnel comprises the following: an air supply system which can deliver air at a dew point of −90°F., at pressures up to 100 psig, and temperatures up to 200°F.; a flowmeter; an upstream stagnation tank; a supersonic nozzle (throat diameter 0.262 in., exit diameter 1.416 in.); a test section of variable length (0 to 81 dia.); a downstream stagnation tank; a three-stage ejector to provide the necessary low back pressure; a foreign-gas supply system; and all necessary instrumentation.

The adiabatic wall temperatures and other temperatures were measured with 109 copper-constantan thermocouples which were distributed along the tunnel length. All temperatures except ambient were measured and recorded by a Brown Flight Recorder. The static wall pressures were measured at stations distributed along the tunnel length. Pressures at most stations were measured either by means of a micromanometer or by a vacuum reference manometer system.

* Assistant Professor of Mechanical Engineering.
** Professor of Mechanical Engineering.
† Reproduction of this material is permitted for any purpose of the United States Government.

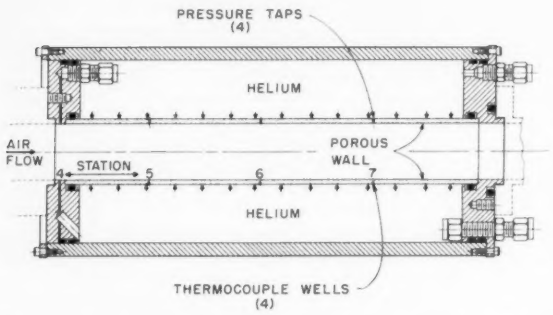

FIG. 1. Assembly drawing of porous test section for uniform helium injection.

	RUN	Re_D	w_g lbm/hr	w_{He} lbm/hr	$-Re_{DI}$
○	GB-20-He-1	87,200	57.2	0.016	0.889
○	GB-20-He-2	87,900	57.0	0.187	10.5
△	GB-23-He-1	122,300	82.8	0.010	0.539
△	GB-23-He-2	122,900	82.7	0.189	10.2
□	GB-25-He-1	58,800	36.7	0.014	0.819
□	GB-25-He-2	61,400	37.4	0.167	10.0
○	GB-26-He-1	86,500	57.3	0.182	10.0
○	GB-26-He-2	85,300	56.6	0.012	0.681
◇	GB-32-He-1	83,600	55.6	0.093	5.07
◑	GB-32 He-2	86,200	55.8	0.264	14.9

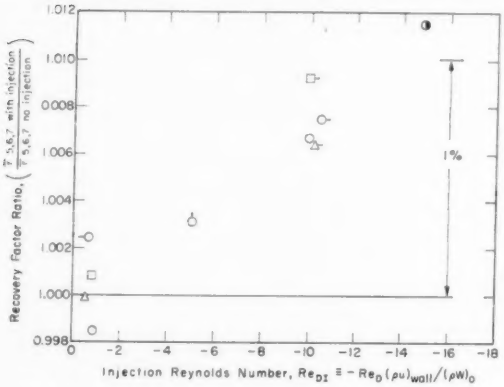

FIG. 2. Effect on recovery factor of injection of helium into laminar boundary layer for supersonic flow of air in tube at Mach 5.

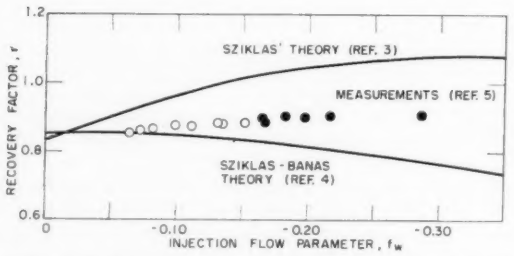

FIG. 3. Effect on recovery factor of injection of helium into laminar boundary layer on cone.

For the experimental results presented here, the length of the overall test section was 41 dia., comprising a porous test section, approximately 7.2 dia., whose leading edge was approximately 1.8 dia. from the nozzle exit plane, and four nylon sections of 8 dia. each. Fig. 1 is an assembly drawing of the porous test section.

A total of 15 runs are reported herein, 5 without injection and 10 with helium injection. The overall behavior of the apparatus with and without injection was excellent in terms of the design specifications. The supersonic nozzle, a critical component in the system, designed to give a uniform, shock-free flow at Mach 5, at a diameter Reynolds Number, Re_D, of 70,000, yielded a calculated Mach Number of 4.7 at a diameter Reynolds Number of 88,000. This calculated performance is well within the probable design and machining errors.

Five series of injection runs were made. Each series started with a zero injection run in order to establish a base with which to compare the effects of helium injection. Series 23 was made at a diameter Reynolds Number of 123,000, Series 25 at 57,000, and the remaining series at 88,000

Within a given series of runs, the control of independent variables during operation of the tunnel was excellent. For example, in the 23 series of runs reported herein, the upstream stagnation temperature, the upstream stagnation pressure, and the back pressure were held constant for many hours to within 0.2 per cent, 0.5 per cent, and 0.3 per cent, respectively. For a given series of runs, the average value of recovery factors at stations 5, 6, and 7, along the porous wall section, shown in Fig. 1, was determined for each run. The ratio of this average recovery factor with helium injection to the corresponding average recovery factor without injection is plotted versus the injection Reynolds Number, in Fig. 2.

In each run with injection, helium was injected at a temperature equal to or slightly less than the adiabatic wall temperature of the porous wall section without injection.

From the results shown in Fig. 2, we conclude that the presence of a diffusion field of helium in a laminar boundary layer of supersonic flow of air had no effect, within 1 per cent, on the average recovery factor over the injection region as long as the basic flow pattern is not disturbed—i.e., as long as apparent separation or transition from laminar to turbulent flow does not occur. These experiments agree well with the predictions of Radbill and Kaye,[6] and may also be compared with the predictions of Baron,[2] and of Sziklas.[3]

The experimental results shown in Fig. 2 may also be compared with the experiments of two other investigations,[4, 5] shown in Figs. 3 and 4, provided one bears in mind that two major differences exist. First, the flow in Figs. 3 and 4 corresponds to flow over a cone rather than flow inside a tube. Second, these other

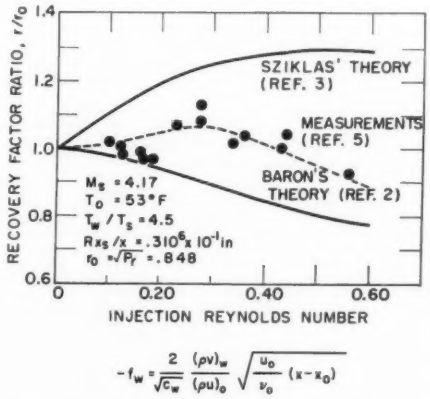

FIG. 4. Effect on recovery factor of injection of helium into laminar boundary layer on cone.

experimenters attempted to obtain an injection rate inversely proportional to the square root of the distance from the leading edge of the cone, whereas, in our apparatus, the injection rate was maintained uniform over the porous wall section. Nevertheless, the results of these different investigations agree qualitatively—i.e., the injection of helium leads to a slight increase in the recovery factor. In general, we conclude that the experimental results for helium injection, which are shown in Figs. 3 and 4, agree quantitatively with our results—namely, that the injection of helium into a laminar boundary layer produces only a slight increase in the recovery factor for adiabatic flow.

References

[1] Gouse, S. W., Jr., *Experimental Investigation of the Effects of a Diffusion Field on a Laminar Boundary Layer in Supersonic Flow*, Sc.D. thesis, Massachusetts Institute of Technology, Department of Mechanical Engineering, Cambridge, Mass., November, 1957.

[2] Baron, J. R., *The Binary-Mixture Boundary Layer Associated with Mass Transfer Cooling at High Speeds*, Massachusetts Institute of Technology, Naval Supersonic Lab. Tech. Rep. No. 160, May, 1956.

[3] Sziklas, E. A., *An Analysis of the Compressible Laminar Boundary Layer with Foreign-Gas Injection*, United Aircraft Corp., Res. Dept., May, 1956.

[4] Sziklas, E. A., and Banas, E. M., *Mass Transfer Cooling in Compressible Laminar Flow*, United Aircraft Corp., July, 1957. Presented at Symposium on Mass-Transfer Cooling for Hypersonic Flight at Santa Monica, Calif.

[5] Leadon, B. M., Scott, C. J., and Anderson, G. E., *Transpiration Cooling of a 20° Porous Cone at M5*, University of Minnesota, Minneapolis, Minn., July, 1957.

[6] Radbill, J. R., and Kaye, J., *Analysis of Effects of Diffusion of a Foreign Gas Into the Laminar Boundary Layer of a Supersonic Flow of Air in a Tube*, to be published in Readers' Forum, Journal of the Aero/Space Sciences, Vol. 26, No. 9, September, 1959.

On the Application of the Ursell-Ward Theorem to Wings With Edge Forces*

Joseph H. Clarke

Associate Professor, Division of Engineering, Brown University, Providence, R.I.

March 3, 1959

IT IS INTENDED HERE to show explicitly how the familiar Ursell-Ward Reverse-Flow Theorem[1, 2] must sometimes be modified to account for edge forces on wings, to consider several applications, and to correct certain mistakes in the literature. Consideration of only isolated wings with planar reference surfaces is sufficient since the required adaptation for more general quasi-cylinders is slight.

It is well known that two types of square-root singularities in the linearized perturbation velocity components can arise over all elements of the wing edges in subsonic flow and over any subsonic edges in supersonic flow. In the case of lifting wings with no thickness, these result in lineally distributed suction forces directed outward from the plan form in its plane on leading edges and trailing edges not satisfying the Kutta Condition. In the case of symmetric nonlifting wings, the forces are directed inward along edges which exhibit parabolic bluntness. The singular parts of the edge flows, which alone contribute to the edge forces, are two-dimensional, subsonic, and mutually distinguished by only a single parameter K, the strength of the singularity,[2] for both types and for both flow directions.

Adopting notation substantially that of reference 2, let $\boldsymbol{U} = U\boldsymbol{i}$ be the remote stream velocity in the direction of the cartesian coordinate x with corresponding unit vector $\boldsymbol{i}$; let ρ_0 be the stream density and M be the stream Mach Number; let p be the pressure, $\boldsymbol{V}$ be the perturbation velocity, and $\rho_0\boldsymbol{W}$ be the closely related perturbation mass flow;[2] let the drag D be the component of force in the flow direction. The drag may be evaluated from the momentum theorem by choosing for the control surface both sides of the wing reference surface Σ plus a vanishing tubular surface S_E which encloses the singular edges. There results

$$D = -(U/|U|)\int_{\Sigma} p\boldsymbol{n}\cdot\boldsymbol{i}\,dS - (\rho_0/|U|)\int_{S_E}[\boldsymbol{U}\cdot\boldsymbol{V}\boldsymbol{W}\cdot\boldsymbol{n} - (1/2)\boldsymbol{V}\cdot\boldsymbol{W}\boldsymbol{U}\cdot\boldsymbol{n}]dS \quad (1)$$

the outward unit normals being to the wing surface and to S_E, respectively. With proper choice of the tube shape, the second term in the edge force integral does not contribute to the result.

Consider a subsonic or supersonic forward flow $U_F > 0$ identified by the subscript F and also a reverse flow $U_R = -U_F < 0$ identified by the subscript R which satisfy, respectively, the boundary conditions $\boldsymbol{V}_F\cdot\boldsymbol{N} = -\boldsymbol{U}_F\cdot\boldsymbol{n}_F$ and $\boldsymbol{V}_R\cdot\boldsymbol{N} = -\boldsymbol{U}_R\cdot\boldsymbol{n}_R$ on the common reference surface Σ, where $\boldsymbol{N}$ is the outward normal to Σ, and where $\boldsymbol{n}_F$ and $\boldsymbol{n}_R$ are the respective normals to the wing surfaces. Utilization of a volume-surface integral identity, the governing equations, the pressure relation $(p - p_0)/\rho_0 = -\boldsymbol{U}\cdot\boldsymbol{V}$, and the boundary conditions at infinity, over the wing wakes and on Σ, yields[1, 2] the following modified statement of the Ursell-Ward Theorem:

$$0 = \int_{\Sigma}(p_F\boldsymbol{n}_R\cdot\boldsymbol{i} + p_R\boldsymbol{n}_F\cdot\boldsymbol{i})dS - (\rho_0/|U|)\int_{S_E}[\boldsymbol{U}_F\cdot\boldsymbol{V}_F\boldsymbol{W}_R\cdot\boldsymbol{n} - (1/2)\boldsymbol{V}_F\cdot\boldsymbol{W}_R\boldsymbol{U}_F\cdot\boldsymbol{n} - \boldsymbol{U}_R\cdot\boldsymbol{V}_R\boldsymbol{W}_F\cdot\boldsymbol{n} + (1/2)\boldsymbol{V}_R\cdot\boldsymbol{W}_F\boldsymbol{U}_R\cdot\boldsymbol{n}]dS \quad (2)$$

For the integrals over S_E in Eq. (2) to make a contribution in the limit, it is necessary that both forward and reverse flows contribute square-root singularities over the same edge elements. For wings which are not parabolically blunted and which satisfy the Kutta Condition in both flow directions, such is not the case, and the integrals over S_E vanish. This is the only case considered by Ursell and Ward. Any results concerning the drag obtained from the reduced theorem will not include the contribution of any edge forces thereto.

However, consider the case of the same symmetric, blunt-edged, nonlifting wing in forward and reverse flow. The subsonic singular edge flow $\boldsymbol{V}_E$ at each point along the blunt edge merely undergoes a change in sign under flow reversal.[2] Substitution of the relations

$$\boldsymbol{n}_F = \boldsymbol{n}_R \quad \text{and} \quad \boldsymbol{V}_{EF} = -\boldsymbol{V}_{ER} \quad (3)$$

into Eq. (2) and comparison with Eq. (1) then gives at once

$$D_F = D_R \quad (4)$$

for the complete drag, and

$$D_{EF} = -D_{ER} \quad (5)$$

for the edge drag, as is clear physically. The subscript E refers throughout to the singular edge. Eq. (4) confirms the result obtained in reference 3 by physical reasoning. The derivation of Eq. (4) given in references 4 and 5 is not correct.

Consider next a forward flow over a lifting wing (with no thickness) which exhibits singular edge flows along elements of the leading edge and which fulfills the Kutta Condition on subsonic trailing edge elements. Suppose that the same plan form in reverse flow has a geometry which results in the same distribution of lift; this is the case of flow reversal for a given distribution of horseshoe vortices. The hypothetical reverse flow evidently satisfies a Kutta Condition on the reverse leading edge and is singular on the reverse trailing edge. Then, on Σ

$$p_F = p_R, \text{ and } \boldsymbol{V}_{EF} = -\boldsymbol{V}_{ER} \quad (6)$$

along the forward subsonic leading edge elements.[2] Eqs. (6), (2), and (1) again yield the result[3] (4) and the result (5) for the present case. It is interesting that the edge forces cancel when the drag in the combined flow field[3] is constructed from Eq. (4).

In reference 3, it is shown on the basis of physical arguments that if a lift distribution produces a prescribed total lift over a given plan form with minimum drag, then the sum of its down-

* This research was supported by the USAF under Contract No. AF 49(638)-444 monitored by the AF Office of Scientific Research of the Air Research and Development Command.

wash in forward flow and reverse flow is constant over the plan form. The result is confirmed in reference 6, using the calculus of variations, but distributions giving leading-edge singularities are excluded from the space of admissible functions in order to use the reduced Ursell-Ward Theorem. In reference 7, it is inferred from an improper application of the theorem that the downwash criterion is invalid when edge forces are present; the latter conclusion forms the basis of deductions on the nature of optimum lift distributions in reference 8. In order to show that the downwash criterion holds when distributions giving edge singularities are admitted, the integrations over Σ in Eqs. (1) and (2) are first rewritten in terms of arbitrary lift distributions l, and the integrals over S_E are evaluated[2] explicitly (heretofore unnecessary). Eqs. (1) and (2), respectively, become

$$D = -(1/|U|)\int_{\Sigma'} lwdS - (U/|U|)\int_{C_E} g(\sigma)K^2(\sigma)d\sigma \quad (7)$$

and

$$(1/|U|)\int_{\Sigma'}(l_F w_R - l_R w_F)dS + 2\int_{C_E} g(\sigma)K_F(\sigma)K_R(\sigma)d\sigma = 0 \quad (8)$$

where Σ' is one side of the reference surface, $w = \boldsymbol{V}\cdot\boldsymbol{k}$, σ is the arc length along the singular edges C_E with local sweep χ, and $g(\sigma) = \pi\rho_0 \cos\chi/\sqrt{1 - M^2\cos^2\chi}$. For minimum drag in forward flow, with given lift L, the lift distribution l is necessarily such that

$$\delta(D_F + \lambda L) = 0 = -(1/|U|)\times \int_{\Sigma'} l\delta w_F dS - (1/|U|)\int_{\Sigma'} w_F \delta l dS + \lambda\int_{\Sigma'}\delta l dS - 2\int_{C_E} g(\sigma)K_F(\sigma)\delta K_F(\sigma)d\sigma \quad (9)$$

from Eq. (7), where λ is a constant Lagrange multiplier. To re-express the first integral, take the variation of Eq. (8) due to a variation in the forward flow and then choose $l_R = l_F \equiv l$, so that $K_R = -K_F$:

$$(1/|U|)\int_{\Sigma'}(l\delta w_F - w_R\delta l)dS + 2\int_{C_E} g(\sigma)K_F(\sigma)\delta K_F(\sigma)d\sigma = 0 \quad (10)$$

Eqs. (9) and (10) give

$$\delta(D_F + \lambda L) = 0 = \int_{\Sigma'}(\lambda - w_F/|U| - w_R/|U|)\delta l dS \quad (11)$$

or $w_F + w_R = |U|\lambda$ on Σ', which is the downwash criterion. Evidently, this is the integral Euler equation for the extremal l.

References

[1] Ursell, F., and Ward, G. N., *On Some General Theorems in the Linearized Theory of Compressible Flow*, Quart. J. Mech. & Appl. Math., Vol. 3, Part 3, pp. 326–348, September, 1950.

[2] Ward, G. N., *Linearized Theory of Steady High-Speed Flow;* Cambridge University Press, Cambridge, England, 1955.

[3] Jones, R. T., *The Minimum Drag of Thin Wings in Frictionless Flow*, Journal of the Aeronautical Sciences, Vol. 18, No. 2, pp. 75–81, February, 1951.

[4] Heaslet, M. A., and Spreiter, J. R., *Reciprocity Relations in Aerodynamics*, NACA Rep. 1119, 1953.

[5] Sears, W. R., ed., *High Speed Aerodynamics and Jet Propulsion*, Vol. 6, pp. 319, 323; Princeton University Press, Princeton, N.J., 1954.

[6] Sedney, R., *On Jones's Criterion for Thin Wings of Minimum Drag*, Readers' Forum, Journal of the Aeronautical Sciences, Vol. 21, No. 9, pp. 639–640, September, 1954.

[7] Yoshihara, H., and Strand, T., *On Jones' Criterion for Optimum Lifting Wings*, Readers' Forum, Journal of the Aero/Space Sciences, Vol. 25, No. 9, p. 600, September, 1958.

[8] Yoshihara, H., Kainer, J., and Strand, T., *On Optimum Thin Lifting Surfaces at Supersonic Speeds*, Journal of the Aero/Space Sciences, Vol. 25, No. 8, pp. 473–479, 496, August, 1958.

A Note on Magnetohydrodynamic-Hypersonic Flow Past a Blunt Body

William B. Bush

Physical Research Laboratory, Space Technology Laboratories, Inc., Los Angeles, Calif.

March 11, 1959

When reference 1 was written, it was not made completely clear what the significance of the parameter Q_{cr} was. However, a closer investigation of the results has solved this problem. Its significance can best be brought out by considering what happens to the value of the parameter $Q^* = (\sigma B_0^2 r_b \div \rho_\infty U)$ where B_0 is the strength of the magnetic field at the stagnation point on the body.

From this definition of Q^*, it follows that

$$Q^* = [4M^2(R_b)Q]/R_b^3 = 4M^2(1/1 + \Delta)\cdot(1 + \Delta)^3 Q \quad (1)$$

and for the magnetic Reynolds Number approaching zero, the dipole magnetic field yields

$$Q^* \cong 4(1 + \Delta)^5\cdot Q \quad (2)$$

From Fig. 3 of reference 1 it can be seen that as Q approaches Q_{cr}, Δ, the stand-off distance, approaches infinity, and, thus, Q^* must also approach infinity. In other words, to produce Q_{cr} and its attendant results, the strength of the magnetic field produced at the body must approach infinity.

Another point from reference 1 that merits clarification is the effect of the magnetic field on the velocity gradient at the body. In order to compute the heat transfer near the stagnation point, the quantity du_e/dx (using the usual boundary-layer notation) must be known. This quantity is related to the quantities V_s, Δ, and R_b by the expression

$$du_e/dx = (U/r_b)\,[V_s/(1 + \Delta)] = (U/r_b)\,(V_s R_b) \quad (3)$$

Thus, for the same size vehicle traveling at the same velocity:

$$(du_e/dx)/(du_e/dx)_{NM} = (V_s R_b)/(V_s R_b)_{NM} \quad (4)$$

Meyer[2] points out in his paper that the heat-transfer coefficient, h_t, is related to du_e/dx (given the symbol A in his paper) by the expression

$$h_t/(h_t)_{NM} \cong [(du_e/dx)/(du_e/dx)_{NM}]^{1/2} = [(V_s R_b)/(V_s R_b)_{NM}]^{1/2} \quad (5)$$

Fig. 1 shows this last quantity as function of Q^*. The points for this figure were computed from the numerical results found in reference 1 for $\epsilon = 1/11$, but subsequent calculations for values of ϵ of 0.115 and 0.140 showed that $[(V_s R_b)/(V_s R_b)_{NM}]^{1/2}$ vs. Q^* is almost independent of ϵ for these values of ϵ.

Finally, an order of magnitude for the reduction in heat transfer by magnetohydrodynamic means can be found by computing a typical value of the parameter Q^*. For the case where $\sigma = 3 \times 10^2$ mho/m., $B_0 = 1$ weber/(m.)^2 = 10,000 guass, $r_b = 1$ m., $\rho_\infty = 10^{-3}$ kg./(m.)^3, $U = 5 \times 10^3$ m./sec., so that $Q^* = 60$, the heat transfer is reduced to about a third of what it would be

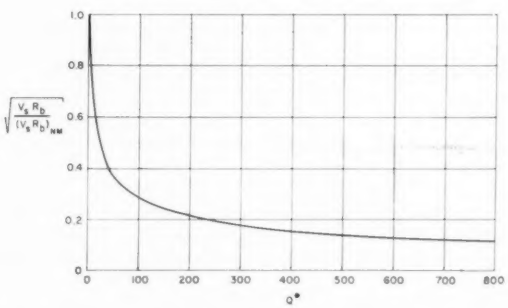

Fig. 1. Heat-transfer parameter vs. magnetic parameter.

if there were no magnetic field applied. It should be noted that values of Q^* of up to 80 have been obtained in the laboratory.[3]

REFERENCES

[1] Bush, W. B., *Magnetohydrodynamic-Hypersonic Flow Past a Blunt Body*, Journal of the Aero/Space Sciences, Vol. 25, No. 11, pp. 685–690, 728, November, 1958.

[2] Meyer, R. C., *On Reducing Aerodynamic Heat-Transfer Rates by Magnetohydrodynamic Techniques*, Journal of the Aero/Space Sciences, Vol. 25, No. 9, pp. 561–566, 572, September, 1958.

[3] Ziemer, R. W., *Experimental Magneto-aerodynamics*, presented at the American Rocket Society 13th Annual Meeting, Paper 707–58, November 17–21, 1958.

The Effect of Vehicle Deceleration on a Melting Surface

D. M. Tellep

Head, Thermal Research, Lockheed Missiles and Space Division, Sunnyvale, Calif.

March 4, 1959

THE DECELERATIONS experienced by hypersonic vehicles entering the atmosphere create body forces on boundary-layer fluid elements. For gaseous boundary layers, these body forces are negligible in comparison with inertia forces. However, when ablation is used as a heat absorption method, body forces acting on the dense, viscous, molten layer can be of comparable magnitude to shear and inertia forces and warrant consideration. This note contains an analysis of the effect of the body forces on a melting surface.

The flow model selected to investigate the effect of body forces on a melting surface is a flat plate, aligned with the stream (see Fig. 1). In the frame of reference fixed with respect to the plate, the equations of motion are[1]

$$\text{Momentum} \quad \rho[(\partial u/\partial t) + u(\partial u/\partial x) + v(\partial u/\partial y) = \rho a + (\partial/\partial y)[\mu(\partial u/\partial y)] \quad (1)$$

$$\text{Energy} \quad \rho c_p[(\partial T/\partial t) + u(\partial T/\partial x) + v(\partial T/\partial y)] = (\partial/\partial y)[k(\partial T/\partial y)] + \mu(\partial u/\partial y)^2 \quad (2)$$

$$\text{Continuity} \quad (\partial u/\partial x) + (\partial v/\partial y) = 0 \quad (3)$$

The a term in the momentum equation represents the acceleration of the plate. Formally, it is analogous to the conventional body force term arising from the x-component of the acceleration due to gravity. In the present case, however, the "gravity field" is due to the deceleration of the plate. This gravity field can be quite large.

It is assumed that the deceleration of the plate is constant and that the motion is quasi-steady. The dissipation term in the energy equation is also neglected. The density, thermal conductivity, and specific heat of the molten material are taken as constant. The viscosity is allowed to vary with temperature. With these assumptions, Eqs. (1) and (2) reduce to a set of ordinary differential equations through the following transforms:

$$\text{Let} \quad \eta = y(3/4\nu_*)^{1/2}(2g)^{1/4}x^{-1/4} \quad (4)$$

where ν_* is the kinematic viscosity evaluated at an arbitrary reference temperature, T_*, and g is the acceleration due to gravity. Now, introduce the stream function

$$\Psi = (4\nu_*/3)^{1/2}(2g)^{1/4}x^{3/4}f(\eta) \quad (5)$$

$$\text{where} \quad u = \partial\Psi/\partial y \quad \text{and} \quad v = -(\partial\Psi/\partial x) \quad (6)$$

$$\text{Also, let} \quad \theta = (T - T_0)/T_* \quad (7)$$

where T_0 is the bulk temperature.

Eqs. 1 and 2 now take the form

$$\text{Momentum} \quad [(\mu/\mu_*)f'']' + ff'' + (2/3)[(a/g) - f'^2] = 0 \quad (8)$$

$$\text{Energy} \quad (1/Pr_*)\theta'' + f\theta' = 0 \quad (9)$$

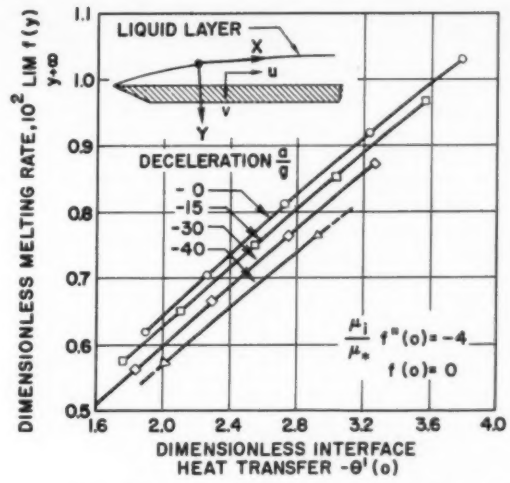

FIG. 1. Variation of melting rate with interface heat transfer for various decelerations.

Five boundary conditions are required on the transformed equations. Conditions on shear, temperature, and mass transfer at the interface are specified, as follows:

$$\partial u(0)/\partial y = -(\tau_i/\mu_i), \qquad T(0) = T_i, \qquad v(0) = 0 \quad (10)$$

By specifying $v = 0$ at the interface, the solutions are restricted to the case where the film does not vaporize, although it is possible to include finite values of $v(0)$ with no additional complexity.

The two remaining boundary conditions apply for glassy materials, as suggested by Sutton.[2]

$$\lim_{y\to\infty} u(y) = 0, \qquad \lim_{y\to\infty} T(y) = T_0 \quad (11)$$

Pyrex glass was chosen as a material for an example, and the property values in reference 2 were used. Solutions to Eqs. (8) and (9), subject to boundary conditions given by Eqs. (10) and (11), were obtained by forward integration on a Univac Scientific 1103-AF computer. Typical results are shown in Figs. 1 and 2.

Fig. 2 shows the variation of interface temperature with interface heat rate and deceleration. It is seen that deceleration can increase the interface temperature by 300°F. to 400°F. Although the results are not shown, solutions for $\mu_i/\mu_* f''(0) = -1$ showed increases of several hundred degrees in T_i at decelerations of only $7g$. Thus, the deceleration required to cause a given change in the interface temperature is a sensitive function of the interface shear.

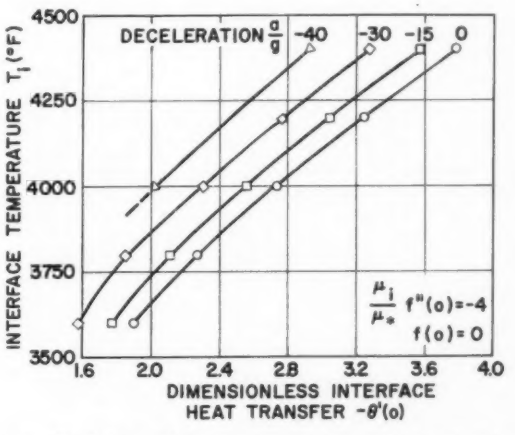

FIG. 2. Variation of interface temperature with interface heat rate for various decelerations.

Fig. 1 shows the variation of the nondimensional melting rate with interface heat transfer and deceleration. The results show that deceleration tends to decrease the melting rate. For a constant value of $\theta'(0)$, the maximum reduction in the melting rate is about 15 per cent. However, because the interface temperature increases due to deceleration, the heat rate at the interface does not remain constant but decreases. Hence, reductions in the melting rate larger than 15 per cent are possible. A more detailed report on this study may be found in reference 3.

REFERENCES

[1] Moore, F. K., *Unsteady Laminar Boundary Layer Flow*, NACA TN 2471, September, 1951.

[2] Sutton, G. W., *The Hydrodynamics and Heat Conduction of a Melting Surface*, Journal of the Aeronautical Sciences, Vol. 25, No. 1, pp. 29–32, 36, January, 1958.

[3] Lockheed Missiles and Space Division, *Fluid Mechanics: Viscous Flows*, Vol. 1, General Research in Flight Sciences, LMSD-48381, Sunnyvale, Calif., January, 1959.

Summary of Laminar Heat Transfer Between Parallel Plates With Unsymmetrical Wall Temperatures

R. D. Cess and E. C. Shaffer
Heat Transfer Section, Mechanics Department, Westinghouse Research Laboratories, Pittsburgh, Pa.

March 6, 1959

CONSIDER LAMINAR FLOW between parallel flat plates with unsymmetrically prescribed wall temperatures, as shown in Fig. 1. For $x < 0$ the flow is isothermal at temperature t_0, whereas for $x > 0$ the temperature is prescribed as $t_1(x)$ on the upper wall ($y = a$) and as $t_2(x)$ on the lower wall ($y = -a$). As shown by Yih and Cermack,[1] the temperature within the fluid for $x > 0$ is expressed in terms of Stieltjes integrals as

$$t - t_0 = \int_0^x \{[(1+\eta)/2] - \theta(x-\xi, \eta)\}\,[dt_1(\xi)/d\xi]d\xi + \int_0^x \{[(1-\eta)/2] - \theta(x-\xi, -\eta)]\,[dt_2(\xi)/d\xi]d\xi \quad (1)$$

where $\eta = y/a$.

The function $\theta(x, \eta)$ is given by a series of even and odd eigenfunctions as

$$\theta(x,\eta) = 1/2 \sum_{n=0}^{\infty} \{A_n Y_n(\eta) \exp[-(8/3)(\lambda_n^2/Pe)(x/a)] + B_n Z_n(\eta) \exp[-(8/3)(\beta_n^2/Pe)(x/a)]\} \quad (2)$$

where Pe is the Peclet Number defined as $Pe = 4u_m a/\alpha$, for which α is the therimal diffusivity and u_m the mean velocity. Since $Y_n(\eta)$ and $Z_n(\eta)$ are even and odd functions, respectively, then

$$Y_n(\eta) = Y_n(-\eta); \qquad Z_n(\eta) = -Z_n(-\eta)$$

The heat flux at either wall of the parallel plate system may be determined through application of the Fourier-Biot law to Eq. (1). In the expressions that result, the derivatives $Y_n'(1)$ and $Z_n'(1)$ are required in addition to the eigenvalues and series coefficients. Prins, Mulder, and Schenk[2] have presented values for the even quantities λ_n, A_n, and Y_n' (1), whereas the odd

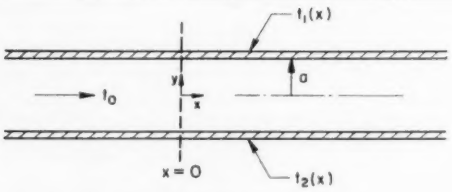

FIG. 1. Coordinate system.

TABLE 1
Even Eigenvalues and Constants

n	λ_n	A_n	$Y_n'(1)$
0	1.681595	1.20083	−1.42916
1	5.669857	−0.29916	3.80707
2	9.66824	0.1609	−5.9202

TABLE 2
Odd Eigenvalues and Constants

n	β_n	B_n	$Z_n'(1)$
0	3.672291	1.84537	−0.71446
1	7.668809	−1.62178	0.63450
2	11.66791	1.5100	−0.5920

eigenvalues β_n and series coefficient B_n have been considered by Yih and Cermack,[1] and by Schenk and Beckers.[3] These quantities have been recalculated by the present authors, and the results, as well as the odd eigenfunction derivatives $Z_n'(1)$, are given in Tables 1 and 2.

For higher values of n, the asymptotic expressions

$$\lambda_n = 4n + (5/3)$$
$$A_n = (-1)^n \{[3^{2/3}2^{13/6}\Gamma(2/3)]/\pi^{3/2}\}\,\lambda_n^{-(7/6)} = (-1)^n\, 2.2711\,\lambda_n^{-(7/6)}$$
$$Y_n'(1) = (-1)^{n+1}\{(2^{1/6}\pi^{1/2})/[3^{5/6}\Gamma(4/3)]\}\,\lambda_n^{5/6} = (-1)^{n+1}\, 0.89195\lambda_n^{5/6}$$

as determined by Sellars, Tribus, and Klein,[4] may be employed. In a similar manner, it may readily be shown that the asymptotic expressions for the odd quantities are:

$$\beta_n = 4n + (11/3)$$
$$B_n = (-1)^n \{[3^{2/3}\,2^{13/6}\Gamma(2/3)]/\pi^{3/2}\}\,\beta_n^{-(1/6)} = (-1)^n\, 2.2711\beta_n^{-(1/6)}$$
$$Z_n'(1) = (-1)^{n+1}\{(2^{1/6}\pi^{1/2})/[3^{5/6}\Gamma(4/3)]\}\beta_n^{-(1/6)} = (-1)^{n+1}\, 0.89195\beta_n^{-(1/6)}$$

REFERENCES

[1] Yih, C. S., and Cermack, J. E., *Laminar Heat Convection in Pipes and Ducts*, Civil Engineering Department. Colorado Agricultural and Mechanical College, Fort Collins, Colo., September, 1951. ONR Contract No. N90nr-82401, NR 063–071/1-19-49.

[2] Prins, J. A., Mulder, J., and Schenk, J., *Heat Transfer in Laminary Flow Between Parallel Plates*, Applied Scientific Research, Section A, Vol. 2, pp. 431–438, 1949–51.

[3] Schenk, J., and Beckers, H. L., *Heat Transfer in Laminar Flow Between Parallel Plates*, Applied Scientific Research, Section A, Vol. 4, pp. 405–413, 1953–54.

[4] Sellars, J. R., Tribus, M., and Klein, J. S., *Heat Transfer to Laminar Flow in a Round Tube or Flat Conduit— The Graetz Problem Extended*, Trans. ASME, Vol. 78, pp. 441–448, 1956.

An Investigation of a Low-Drag Auxiliary Body Utilizing Favorable Interference*

Anthony Martellucci
Research Assistant, Aerodynamics Laboratory, Polytechnic Institute of Brooklyn, Freeport, N.Y.

March 6, 1959

INTERFERENCE PRINCIPLES utilizing linearized flow techniques have been employed for the optimum replacement of bodies to the underside of a configuration so that, for a given lift of the system, the drag changes in such a manner that the L/D increases.[1] The present investigation considers the placement of a body of large volume to the underside of a wing or fuselage,

* This research was supported by the USAF through the Air Force Office of Scientific Research, Air Research and Development Command, under Contract AF 49(638)-217, Project No. 9781, under the supervision of Prof. Antonio Ferri.

flying at a Mach Number of 3.09, such that for a constant lift of the system, the additional wave drag will theoretically be zero. Since the body ducts air internally, it could be used as a ramjet engine to be used during the acceleration phase of flight, then cut out at design speed and carried along with only a small penalty in drag.

Design Criteria

The body shape is generated by following the streamlines obtained by intersecting the flow about a cone, at an angle of yaw, with a cylinder whose longitudinal axis is aligned with the free-stream flow. The outer wetted surface of the body is the circumference of the cylinder while the internal surface is a stream surface of the conical flow field. The forebody was designed from the conical flow about a cone of semiapex angle of 15° placed at an angle of attack of 2° relative to the free stream, flying at a free-stream Mach Number of 3.09. The intersecting surface was assumed to be a circular cylinder of radius, r, with its longitudinal axis parallel to the free stream. The cone semiapex angle ϑ_c, the angle of yaw of the cone ϵ, the radius of the cylinder r, and the distance from the axis of the cone to the axis of the cylinder h, influence the internal shape of the forebody or scoop. The selection of a 15° cone semiapex angle, 2° angle of attack, and a value of h/r of 1.200 gave an aerodynamic body of suitable volume for a given length.

The velocity components are known for the entire conical flow field;[2] thus, the problem that remained was to find the streamlines of the flow. First, the streamlines in the meridian plane due to the velocity components v_r and v_n were determined, then the trace of the stream surface in the plane normal to the meridian plane containing w was found. The starting points of the streamlines are defined by the intersection of the conical shock with the cylinder in the various meridian planes. By the method of isoclines the forebody, up to the region of interference of the shock reflected off the wing, was designed. A typical cross section of the resultant body is shown in Fig. 1. To obtain a solution in the region of interference of the wing on the body, the assumption was made that one could superimpose an equivalent conical flow field above the wing, such that the wing would be a plane of symmetry. This assumption is permissible in linear problems and can be used here in this nonlinear problem. The velocity vector immediately behind the reflected shock is of almost constant magnitude and direction; therefore, the flow downstream of the shock can be considered as a quasi-two-dimensional flow. The linearized characteristic method readily lends itself applicable here, as is borne out in references 3 and 4.

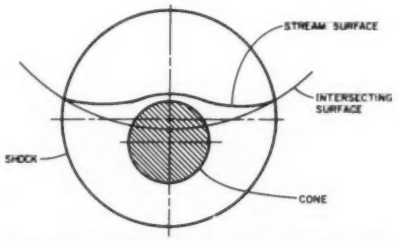

Fig. 1. Stream surface formed in a conical flow field with yaw.

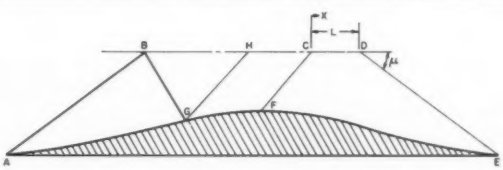

Fig. 2. Defining the body length in the centerline meridian plane.

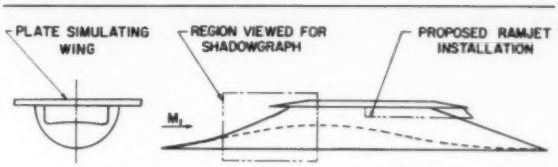

Fig. 3. Illustration of the design configuration.

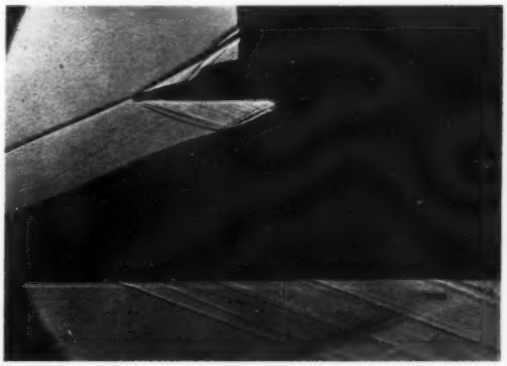

Fig. 4. Shadowgraph of the flow field entering the inlet.

To start closing the body, the curvature of the wall surface from point G to the minimum section F (Fig. 2) was specified arbitrarily but in a manner such that the ensuing expansion was not too severe, and the minimum section sufficient to permit supersonic flow to be established. To continue closing the body, merely specifying the curvature of the body along FE arbitrarily will not suffice (Fig. 2). One must impose the condition that the velocity variation along CD is defined so that there is no discontinuity at C. At D, the velocity should be such that not only the pressure is equal to atmospheric but also that the acceleration is zero. With these conditions satisfied, the body from the reflected shock to the aft end was completely designed for the assumed quasi-two-dimensional flow. It was found that by simply considering the two-dimensional velocity components, the body closed for all practical engineering purposes. Actually, from the analysis, at the trailing edge the thickness of the body became negative. The distance l that this occurred at was 97.8 per cent of L so that for a given physical model it is negligible. Therefore, the three-dimensional portion of the velocity components need not be considered as the improvement that would be obtained by considering them is within the accuracy of the preceding analysis. The body shape resulting from the preceding analysis is shown in Fig. 3. For a detailed design analysis, the reader is referred to the author's original report.[5]

The investigation of the low-drag model was conducted in the 10 in. × 10 in. supersonic blowdown wind tunnel of the Polytechnic Institute of Brooklyn Aerodynamics Laboratory in Freeport, N.Y. Tests were conducted in the $M = 3.09$ tunnel at a stagnation pressure of 200 psia with a corresponding test section Reynolds Number per ft. of 3.37×10^7. A shadowgraph of the inlet portion of the model is shown in Fig. 4. The pressure drag of the model was determined from a numerical integration of the surface static pressures obtained by experiment.

To illustrate the drag qualities of the design configuration, it will be compared to various bodies of revolution to substantiate that there is an order of magnitude difference in the drag. For this comparison, interference effects have not been considered. The bodies considered have different maximum cross-sectional areas, hence, the drag coefficients based on this reference area cannot be compared, but values of D/q will be considered. Comparison of the design configuration to bodies of equal volume and length indicates that the drag is one order of magnitude less than that of a cone, parabolic arc body, or a Haack-Adams body. Thus, the body could be used as an efficient storage system for

TABLE 1*

Body	A_{max}	Pressure drag D_p/q	Base drag D_b/q	Total drag D_t/q	Wetted area	Skin-friction, drag C_f
Low drag	2.120	0.020	0	0.020	69.10	0.0024
4° cone	2.697	0.050	0.270	0.320	40.24	0.0018
Parabolic arc (reference 6)	1.685	0.185	0	0.185	42.29	
Haack-Adams (reference 7)	1.940	0.0263	0.194	0.220	34.10	
TR1271 (reference 7)	1.940	0.0221	0.194	0.216	34.10	

* Volume = 12,400, length = 13.190.

long-range vehicles. A design feature of the body permits it to be mounted directly to a wing which will, when attached, add local rigidity to the wing.

Since the forebody is similar to a scoop type inlet, a system of this type could also be used for an auxiliary ramjet engine or as a by-pass for a ramjet engine. In the first case, the engine would be used during acceleration, then cut out at design speed and carried along with only a small penalty in drag. In the second case, a normal shock inlet with variable spillage could be placed internally somewhat behind the section of minimum area (Fig. 3). Table 1 illustrates the drag comparison.

REFERENCES

[1] Reyn, John W., and Clarke, Joseph H., *An Assessment of Body Lift Contributions, and of Linearized Theory for Some Particular Wing-Body Configurations*, PIBAL Report No. 305, June, 1956.

[2] Staff of the Computing Section, Center of Analysis (under the direction of Zdenek Kopal), *Tables of Supersonic Flow Around Cones*, Technical Reports Nos. 1 and 3, Massachusetts Institute of Technology, Cambridge, Mass., 1947.

[3] Sears, W. R., *General Theory of High Speed Aerodynamics, Vol. VI*, pp. 666ff, pp. 700ff, pp. 721ff; Princeton University Press, Princeton, N.J., 1954.

[4] Ferri, Antonio, *The Linearized Characteristics Method and its Application to Practical Nonlinear Supersonic Flow Problems*, NACA TN 2515, 1951.

[5] Martellucci, A., *A Theoretical and Experimental Investigation at a Mach Number of 3.09 of a Low-Drag Auxiliary Body Utilizing Favorable Interference*, PIBAL Report No. 432, December, 1957.

[6] Jones, R. T., and Margolis, K., *Flow Over a Slender Body of Revolution at Supersonic Velocities*, NACA TN 1081, 1956.

[7] Harder, Keith C., and Rennemann, Conrad, Jr., *On Boattail Bodies of Revolution Having Minimum Wave Drag*, NACA TN 1271, 1956.

Application of Generalized Gauss-Laguerre Quadrature to Boundary-Layer Problems

William Squire
Bell Aircraft Corporation, Buffalo, N.Y.

March 13, 1959

A CHARACTERISTIC FEATURE of boundary-layer problems is that a nonlinear system of differential equations is subject to conditions as zero and ∞. In order to integrate the differential equations numerically, it is necessary to assume values for enough additional derivatives at zero to make the system determinate and verify that the assumed values are satisfactory by integrating out to a large value of the independent variable to see if the conditions at infinity are satisfied. Because of the nonlinearity and infinite range, conventional methods of correcting the estimated initial conditions are not applicable and a lengthy trial-and-error process is involved, especially when there are several initial conditions to be adjusted.

The object of this note is to show the applicability of the generalized Gauss-Laguerre quadrature formulas[1] to this type of problem. These quadrature formulas state:

$$\int_0^\infty x^p e^{-x} g(x)dx = \sum_{j=1}^{j=n} H_j g(a_j) \tag{1}$$

The values of a_j are the roots of the nth generalized Laguerre polynomial or order p and degree n, defined as:

$$L_n^p(x) = x^{-p}e^x(d^n/dx^n)e^{-x}x^{p+n} \tag{2}$$

and the weights H_j are given by

$$H_j = n!\,\Gamma(n+p+1)/\{a_j[L_n^{p\prime}(x)]^2\} \tag{3}$$

This quadrature formula is exact when $g(x)$ is a polynomial of degree $2n-1$ or less.

Boundary-layer problems will usually involve the formula for $p = -(2/3)$. It is easily shown that:

$$\left.\begin{aligned} L_1^{-2/3}(x) &= 1/3 - x \\ a_1 = 1/3, \quad H_1 &= \Gamma(1/3) = 2.6790 \end{aligned}\right\} \tag{4}$$

and

$$\left.\begin{aligned} L_2^{-2/3}(x) &= 4/9 - 8/3x + x^2 \\ a_1 = 0.17864 \quad H_1 &= 2.4996 \\ a_2 = 2.4880 \quad H_2 &= 0.17948, \text{ etc.} \end{aligned}\right\} \tag{5}$$

The proposed method is best explained by considering a simple example. We will take the well-known Blasius equation for a flat plate:

$$\left.\begin{aligned} f''' + ff'' &= 0 \\ f(0) = f'(0) &= 0 \\ f'(\infty) &= 1 \end{aligned}\right\} \tag{6}$$

For numerical integration, we must have a value for $f''(0)$ which will be designated by α. This is actually the parameter of interest physically since it determines the drag coefficient. A formal integration of Eq. (6) gives

$$f''(\eta) = \alpha e^{-\int_0^\eta f d\eta} \tag{7}$$

Integrating Eq. (7) from zero to ∞ and using the boundary conditions on Eq. (6) gives

$$\alpha^{-1} \int_0^\infty d\eta\, e^{-\int_0^\eta f d\eta} \tag{8}$$

This type of formal integration of the boundary-layer equations combined with an asymptotic evaluation of the integrals has been used extensively by Meksyn.[2]

The present method is to transform the integral to the form of Eq. (1) by introducing the new variable:

$$Y = \int_0^\eta f d\eta \tag{9}$$

This gives

$$\alpha^{-1} = \int_0^\infty (e^{-Y}/Y')dY = \int_0^\infty Y^{-2/3}e^{-Y}(Y^{2/3}/Y')dY \tag{10}$$

where

$$Y' = dY/d\eta = f \tag{11}$$

The reason for introducing the $Y^{-2/3} \cdot Y^{2/3}$ is that from the leading term of the power-series expansion around the origin

$$f = Y' = (\alpha/2)\eta^2 + \ldots \tag{12}$$

we see that

$$Y = (\alpha/6)\eta^3 + \ldots \tag{13}$$

so that

$$Y' = (9\alpha/2)^{1/3}\, Y^{2/3} + \ldots \tag{14}$$

Therefore, the limit as $Y \to 0$ of $Y^{2/3}/Y'$ is finite and it is a suitable $g(Y)$ for the Gauss-Laguerre quadrature formula. Since this power dependence is due to the initial conditions rather than the differential equation, it will be applicable to many other boundary-layer problems.

We can obtain a reasonably good estimate of α by simply using Eq. (14). Since our $g(Y)$ is then a constant, it is only necessary to use the first-degree formula and obtain:

$$\alpha^{-1} = 2.679(2/9\alpha)^{1/3} \tag{15a}$$

or

$$\alpha = 0.480 \tag{15b}$$

This differs from the "exact" value $\alpha = 0.4696$ by 2 per cent. This procedure is equivalent to the first approximation in Meksyn's method.

Still better estimates can be obtained by using higher-degree quadrature formulas and numerically integrating the differential equation

$$\left.\begin{aligned} &Y^{IV} + Y'Y''' = 0 \\ &Y(0) = Y'(0) = Y''(0) = 0 \\ &Y'''(0) = \alpha \end{aligned}\right\} \quad (16)$$

to find the values of Y' for $Y = a_j$ and obtaining an improved value of α by the quadrature formula. Usually boundary-layer equations do not involve the independent variable, so it as possible to change to Y as the independent variable and $Y'=f$ as the dependent variable. Eq. (16) would become

$$f^2[(d^3f/dY^3) + (d^2f/dY^2)] + f(df/dY) \times [4(d^2f/dY^2) + (df/dY)] + (df/dY)^3 = 0 \quad (17)$$

This has a singularity at $Y = 0$, and the solution must be started by using Eq. (14).

REFERENCES

[1] Kopal, Z., *Numerical Analysis*, p. 385; John Wiley and Sons, New York, 1955.

[2] Meksyn, D., *Integration of the Boundary Layer Equations*, Proc. Roy. Soc., Series A237, p. 543, 1956.

Errata—"Coupled Free Vibrations of a Swept Wing"

A. E. Engelbrecht and W. P. Rodden

Supervisor and Research Specialist, Respectively, Vibration, Flutter and Acoustics Group, North American Aviation, Inc., Los Angeles, Calif.*

March 20, 1959

IN THE PREVIOUS TREATMENT of the coupled free vibrations of a swept wing,[1] it was assumed that the structural behavior could be represented by an elastic axis which, in turn, could be approximated by a series of straight and curved bar sections. It has been noted that the differential equation for the angle of twist, Eq. (18), contains an incorrect sign and should read:

$$\phi = +(1/R)\,(dz/ds) + (d\beta/ds) \quad (18a)$$

The correct sign is given by Lové[2] [Ch. XXI, Eq. (16)]. The different sign requires a reconsideration of the differential-equation system, which yields the following solution:

$$\left.\begin{aligned} z_{n-1} = z_n - z_n'\,R\sin\theta + \beta_n R(1-\cos\theta) + (V_nR/2) \times \\ [A(\sin\theta - \theta\cos\theta) + B(3\sin\theta - \theta\cos\theta - 2\theta)] + \\ (M_n/2)\,[A\,\theta\sin\theta + B\,(\theta\sin\theta + 2\cos\theta - 2)] + \\ (T_n/2)\,(A+B)\,(\theta\cos\theta - \sin\theta) \end{aligned}\right\} \quad (31a)$$

$$\left.\begin{aligned} z_{n-1}' = z_n'\cos\theta - \beta_n\sin\theta - (V_n/2)\,[A\,\theta\sin\theta + \\ B(\theta\sin\theta + 2\cos\theta - 2)] - (M_n/2R)\,[A\,(\theta\cos\theta + \\ \sin\theta) + B(\theta\cos\theta - \sin\theta)] + \\ (T_n/2R)\,(A+B)\,\theta\sin\theta \end{aligned}\right\} \quad (32a)$$

$$\left.\begin{aligned} \beta_{n-1} = z_n'\sin\theta + \beta_n\cos\theta + (V_n/2)\,(A+B) \times \\ (\theta\cos\theta - \sin\theta) - (M_n/2R)\,(A+B)\,\theta\sin\theta + \\ (T_n/2R)\,[A(\sin\theta - \theta\cos\theta) - B(\sin\theta + \theta\cos\theta)] \end{aligned}\right\} \quad (33a)$$

The above relations have been checked thoroughly by elastic-energy techniques. The practical significance of the preceding difficulty can be estimated by a series expansion of both solutions. The earlier and present solutions for z_{n-1} and z_{n-1}' agree with an error of order θ^2. The solutions for β_{n-1} also agree with an error of order θ^2, except for a discrepancy in the signs of the coefficients of A and z_n'. In order to make the previous solution agree with the present solution (to order θ^2), the signs of the coefficients of A and z_n' in Eq. (33) should be reversed. Obviously, the limiting values of both solutions as $\theta \to 0$, $R \to \infty$ are the same, and the straight bar section matrix of Eq. (39) is correct.

* Now, Engineering Specialist, Dynamics Branch, Norair Division, Northrop Corporation, Hawthorne, Calif.

REFERENCES

[1] Engelbrecht, A. E., *Coupled Free Vibrations of a Swept Wing*, Journal of the Aeronautical Sciences, Vol. 18, No. 5, pp. 329–338, May, 1951.

[2] Love, A. E. H., *A Treatise on the Mathematical Theory of Elasticity*; Dover Publications, New York, 1927.

The Law of the Wake in Compressible Turbulent Boundary Layers

Paul A. Libby and Marian Visich, Jr.

Professor and Assistant Professor of Aeronautical Engineering, Respectively, Aerodynamics Laboratory, Polytechnic Institute of Brooklyn, Freeport, N.Y.

March 16, 1959

IT IS GENERALLY accepted that the well-known law of the wall in incompressible turbulent boundary layers can be extended to adiabatic compressible flows. This was shown, for example, by Coles[1] and, more recently, by Fenter and Stalmach.[2] It is the purpose of this note to point out that a similar extension of the law of the wake, proposed by Coles[3] for incompressible turbulent boundary layers, has been used to correlate some experimentally determined profiles corresponding to the mixing of two streams in the presence of a wall. Details of the investigation are presented in reference 4.

By considering a large number of incompressible turbulent profiles under conditions of constant and of streamwise variable pressure, Coles showed that the entire velocity profile could be represented by a superposition of the usual law of the wall and of the wake. The contribution of the latter is measured by a function $\Pi(x)$; for the flat-plate case $\Pi \backsimeq 0.55$. Despite the present difficulties associated with the theoretical determination of $\Pi(x)$ for general flows, the Coles correlation is considered significant.

The theoretical basis for an extension of Coles' correlation to the compressible case lies in the demonstration by Mager[5] that the partial differential equations describing the mean motion of an adiabatic compressible turbulent boundary layer with a turbulent Prandtl Number of unity can be transformed to an incompressible form. This suggests that the generalization of Coles' profiles to the compressible case would be

$$u/v^* = A\ln\xi + B + AW(\bar{\eta})\,\Pi(X) \quad (1)$$

where the usual notation applies to u, $v^* \equiv \sqrt{\tau_w/\rho_w}$, ν_w, A, and B; where $\xi = v^*\int_0^y(\rho/\rho_w)dy/\nu_w$, $\bar{\eta} = \int_0^y(\rho/\rho_w)dy \Big/ \int_0^\delta(\rho/\rho_w)\,dy$, $X \equiv \int_0^x \sqrt{\rho_e/\rho_w}\,(\mu_e/\mu_w)dx$ and where W is the wake function tabulated in reference 3. Note that $\Pi = 0$ gives a law of the wall for compressible flow. If a measured velocity profile in terms of $u = u(\xi)$ is to be correlated by Eq. (1), values of v^*, δ, and Π must be selected at each value of x.

A schlieren photograph of the flow investigated is presented in Fig. 1; a two-dimensional supersonic flow with a Mach Number of 3.95 interacts with a subsonic secondary flow issuing from a slot. After the usual expansion and recompression of the supersonic stream, there is established a turbulent boundary layer with a large "wake" contribution. This boundary layer was surveyed by a total-head rake at several streamwise stations and

FIG. 1. Schlieren picture of flow field at origin of mixing.

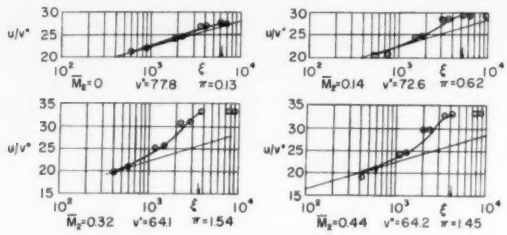

FIG. 2. Correlation of velocity profiles.

several values of the mean Mach Number of the secondary flow denoted by $\bar{M}_2$.

In Fig. 2 there is shown the correlation afforded by Eq. (1) at one streamwise station and several values of $\bar{M}_2$. The relatively large values of Π will be noted. The results at other stations indicate, as might be anticipated on physical grounds, that Π decreases and v^* increases in the downstream direction. The difficulties associated with the theoretical analysis of incompressible boundary layers with significant wake contributions apply to the generalization to compressible flows discussed here. From this point of view, the correlations represented by Fig. 2 must be, at the present time, accepted pragmatically.

REFERENCES

[1] Coles, D., *Measurements in the Boundary Layer on a Smooth Flat Plate in Supersonic Flow. Part I—The Problem of the Turbulent Boundary Layer*, Report No. 20-69, Jet Propulsion Laboratory, Pasadena, Calif., June 1, 1953.

[2] Fenter, F. W., and Stalmach, C. J., Jr., *The Measurement of Turbulent-Boundary-Layer Shear Stress by Means of Surface Impact-Pressure Probes*, Readers' Forum, Journal of the Aero/Space Sciences, Vol. 25, No. 12, pp. 793–794, December, 1958.

[3] Coles, D., *The Law of the Wake in the Turbulent Boundary Layer*, J. Fluid Mech., Vol. 1, Part 2, pp. 191–226, July, 1956.

[4] Visich, Marian, Jr., and Libby, Paul A., *Experimental Investigation of a Mach Number 3.95 Stream in the Presence of a Wall* (Report submitted to NASA in fulfillment of the requirements of Contract NAw-6480, December, 1958.)

[5] Mager, A., *Transformation of the Compressible Turbulent Boundary Layer*, Journal of the Aeronautical Sciences, Vol. 25, No. 5, May, pp. 305–311, 1958.

Vorticity Effect on the Stagnation-Point Flow of a Viscous Incompressible Fluid*

Nicholas Rott and Michael Lenard
Professor of Aeronautical Engineering, and Research Assistant, Respectively, Cornell University, Ithaca, N.Y.

March 20, 1959

A COMMONLY ACCEPTED improvement in boundary-layer theory is obtained by considering the inviscid flow past a body which is augmented by the displacement thickness of the viscous layer. Actually, the improvement is only obvious in the case of large wakes. The "improvement" for the leading edge of a flat plate (and for sharp corners) has turned out to be a formidable problem, due to the singular character of the corner flow.

This difficulty does not occur in the case of the boundary layer beginning at an ordinary stagnation point. However, it can be shown that curvature corrections to the ordinary boundary-layer theory are of the same order as the corrections due to the displacement effects caused by the thickness of the laminar boundary layer. Also of the same order is the slip effect treated in the approximation proposed by Lin and Schaaf.[1]

The present note is concerned with still a further effect which can influence the stagnation-point boundary-layer calculations to the same order—namely, the effect of vorticity in the oncoming stream. An important distinction exists between the two-dimensional and the axisymmetric cases, corresponding to the distinction between the "incompressible rotational" inviscid flow cases behind a cylindrical shock[2] and a spherical shock.[3] In two dimensions, the vorticity ω is proportional to the stream function ψ, while in three dimensions ω varies with the distance r from the axis. The leading term in plane flow is $\psi \sim xy$ and $\omega \sim xy$, which has a "stronger" zero at the stagnation point than the axisymmetric $\omega \sim r$. It can be shown that the effect of vorticity is negligible compared to the effects mentioned above in plane flow, but not so in the axisymmetric case. This effect is the subject of the present note.

Consider the (Stokes) stream function

$$\psi = (A/2R)r^2[2Rz + r^2 - 2(2 - c)z^2] \tag{1}$$

The flow is an exact solution of the Navier-Stokes equations, although naturally the no-slip condition is not fulfilled along the "body" $\psi = 0$, which has a radius of curvature R at $r = z = 0$. The part of the solution involving c is rotational:

$$\omega = 2cAr/R \tag{2}$$

Indeed, for $c = 5/2$, Eq. (1) is identical with Lighthill's solution behind a spherical shock for the special case of the density ratio $K = 6$ across the shock; Lighthill's general solution is a superposition of Eq. (1) with $c = 5/2$ and an irrotational flow past a sphere. Locally, however, it is possible to fit the flow represented by Eq. (1) to Lighthill's general solution. One has to identify $R\psi_{zz}/\psi_z$ for $z = 0$ with the corresponding expression of Lighthill's, giving the relation

$$c = (K - 1)/2[1 - (x^5 - 1)(K - 6)/5] \tag{3}$$

where $xR = R_s$ defines the shock radius. For many purposes, it is sufficient to put $x = 1$ in Eq. (3).

If there is a boundary layer over the body of radius of curvature R, the "outside" flow represented by Eq. (1) has to be modified as follows: the constant A is influenced by the displacement effect over the whole body. The determination of this change is the most difficult part of the problem, as it is not a "local" effect at the stagnation point. Also, one replaces z by $z - \delta^*$, and R by $R + \delta^*$.

For the boundary-layer solution, put

$$\psi = r^2\sqrt{\nu A}\{f_0(\zeta) + Re^{-(1/2)}f_1(\zeta)\} \tag{4}$$

where

$$\zeta = z\sqrt{A/\nu}, \quad Re = AR^2/\nu \tag{5}$$

f_0 is the usual stagnation-point boundary-layer solution. f_1 represents the correction under consideration. A detailed investigation of the many effects mentioned so far is the subject of a forthcoming report by the present authors. Here only the vorticity effect (which, apparently, was not treated before in this case) is singled out for discussion. It is found that for $c \neq 0$ an *additional* term in f_1 is needed (f_{1v}, say) if the "outside" flow has the vortical part

$$\Delta\psi = cAr^2(z - \delta^*)^2/R \tag{6}$$

which has to be joined by f_{1v}, and this term fulfills the homogeneous, "perturbed," stagnation flow boundary-layer equation—namely,

$$\Lambda(f_{1v}) \equiv 2f_0''f_{1v} - 2f_0'f_{1v}' + 2f_0f_{1v}'' + f_{1v}''' = 0 \tag{7}$$

A known solution of Eq. (7) is f_0', which was used by Lin and Schaaf for the treatment of the slip effect. For the vorticity effect, according to Eq. (6), a solution is needed which behaves as ζ^2 at infinity. Eq. (7) does admit such a solution. To determine it, put

$$f_{1v} = c[2\zeta f_0 - \zeta^2 f_0' + 2h_1] \tag{8}$$

The first two terms in Eq. (8), given explicitly by the known function f_0, have the proper behavior at $\zeta = \infty$, as a comparison with Eq. (6) will show. The function h_1 then fulfills the inhomogeneous equation

$$\Lambda(h_1) = 2\zeta f_0''' \tag{9}$$

* This research has been supported in part by the Office of Scientific Research of the USAF under contract No. 18(600)-1523.

with the boundary conditions $h_1(0) = h_1'(0) = h_1'(\infty) = 0$. This function was determined by numerical integration at the Cornell Computing Center. In particular, $h_1''(0) = 0.649$ was found; the shear caused by the vorticity effect is proportional to this value. The magnitude of this shear term is, using Eq. (4) and Eq. (3) (approximated by putting $x = 1$):

$$\Delta\tau_w = 0.649(K - 1)\mu Ar/R \tag{10}$$

This term is positive and is found to be surprisingly large as compared to the other effects of the same order mentioned before.

The authors were informed after submitting this note that the same effect was discussed by N. H. Kemp, whose note follows below. The difference in the two treatments is that while here a perturbation (f_{1_ν}) was calculated to the stagnation-point flow, Kemp solves the nonlinear equation for f_0 with properly modified boundary conditions. The slope of the shear curve (at zero vorticity) as calculated by Kemp agrees perfectly with the value deduced from Eq. (10).

An investigation which implicitly contains the results of the present note was made by Oguchi.[4] He solves the equation for f_0 between the body and the shock, so that he obtains in one step both the shock stand-off distance and the flow in the viscous region. Properly interpreted, his solutions agree with the present results. However, Oguchi's results do not contain any curvature effects, which were found to be of the same order as the vorticity effect. The advantage of the present approach is that all four "low Reynolds Number effects" can be compared on an equal footing.

References

[1] Lin, T. C., and Schaaf, S. A., *Effect of Slip on Flow Near a Stagnation Point and in a Boundary Layer*, NACA TN 2568, 1951.

[2] Whitham, G. B., *A Note on the Stand-off Distance of the Shock in High Speed Flow Past a Circular Cylinder*, Comm. on Pure and Appl. Math., Vol. 10, No. 4, pp. 531–535, November, 1957.

[3] Lighthill, M. J., *Dynamics of a Dissociating Gas*, Part 1—Equilibrium Flow, J. Fluid Mech., No. 2, pp. 1–32, January, 1957.

[4] Oguchi, H., *Hypersonic Flow Near the Forward Stagnation Point of a Blunt Body of Revolution*, Journal of the Aero/Space Sciences, Vol. 25, No. 12, pp. 789–790, December, 1958; also, Aero. Res. Inst. Tokyo Rep. No. 337, 1958.

Vorticity Interaction at an Axisymmetric Stagnation Point in a Viscous Incompressible Fluid*

Nelson H. Kemp

Principal Research Scientist, Avco Research Laboratory, Everett, Mass.

March 23, 1959

Interest has recently arisen in the effect on boundary layers of vorticity in the external inviscid flow. This effect is especially important at hypersonic speeds, where the external flow may pass through a strong curved shock wave, and, therefore, contain vorticity comparable to that in the boundary layer.

A series of notes by Li and Glauert (see references in reference 1) have considered the flat plate with vorticity in the external stream. Recently, Stuart[1] has given an exact solution of the incompressible Navier-Stokes equations for a two-dimensional stagnation point with constant vorticity in the oncoming flow. The purpose of the present note is to give an exact solution of the incompressible Navier-Stokes equations at an axisymmetric stagnation point with vorticity in the oncoming flow which varies linearly with distance from the axis. This solution has application to the hypersonic axisymmetric blunt body problem, for

* This work was supported by the Ballistic Missile Division, Air Research and Development Command, USAF, under Contract AF 04(647)-278. Thanks are due to Patricia Jackson for performing the numerical calculations, and to Prof. R. F. Probstein for introducing me to the subject of vorticity interaction.

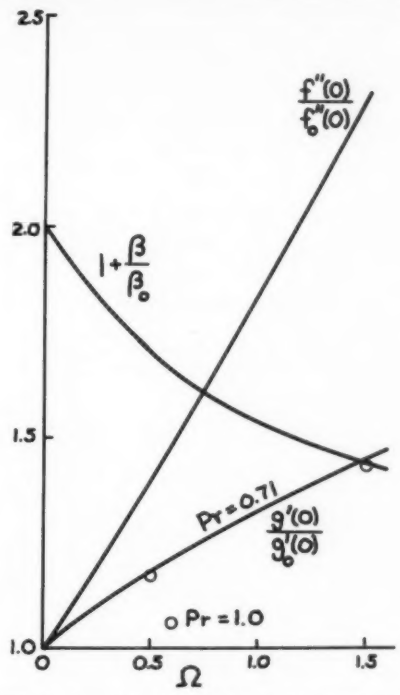

Fig. 1. Effect of vorticity interaction parameter Ω on wall shear stress and heat-transfer rate.

which Lighthill[2] has shown that the vorticity in the inviscid shock layer is very nearly of this form.

Consider a cylindrical coordinate system r, z with velocity components u, w, respectively. A solution to the inviscid equations of motion and continuity is

$$u = Ar + Brz, \qquad w = -2Az - Bz^2 \tag{1}$$

This represents flow in the half-plane $z > 0$ against the plane $z = 0$. The vorticity is $\omega = Br$, and the pressure is

$$p = -\rho(r^2A^2 + w^2)/2 \tag{2}$$

Notice that if z is replaced by $z - \delta$ everywhere, the result is still a solution, but now for flow against the plane $z = \delta$.

To find a solution of the Navier-Stokes equations which approaches this inviscid solution, we use the usual boundary-layer substitutions:

$$u = Arf'(\eta), \qquad w = -(2A\nu)^{1/2}f(\eta), \qquad \eta = z(2A/\nu)^{1/2} \tag{3}$$

The equation of motion in the r direction reduces to the familiar boundary-layer equation

$$f''' + ff'' + (1/2)(1 - f'^2) = 0 \tag{4}$$

where Eq. (2) has been used for the pressure gradient $\partial p/\partial r$. The boundary conditions at the body $\eta = 0$ are the no-slip conditions

$$f(0) = f'(0) = 0 \tag{5}$$

As $\eta \to \infty$, we require the velocities to approach those of Eqs. (1), except that we allow for the possibility that, as far as the inviscid flow is concerned, the body is displaced a distance $\delta = \beta(\nu/2A)^{1/2}$. This is in agreement with the result found in the classical case $\omega = 0$, in which $\beta = \beta_0 = 0.8045$. Under this condition, the outer boundary conditions are:

$$\eta \to \infty: \quad f' \to 1 + \Omega(\eta - \beta), \qquad f \to (\eta - \beta) + \Omega(\eta - \beta)^2/2 \tag{6}$$

Here Ω is defined by

$$\Omega = (\nu/2A)^{1/2}(B/A) = (\nu/2A)^{1/2}(Br/Ar) \tag{7}$$

and may be called the vorticity interaction parameter. It is of the order of the ratio of the vorticity in the external flow, Br, and the average vorticity in the boundary layer, $Ar/(\nu/2A)^{1/2}$, where $(\nu/2A)^{1/2}$ is proportional to the boundary-layer thickness. This parameter is the incompressible limit of the one introduced by Hayes and Probstein.[3]

The two outer boundary conditions (6) are really the same, since either one can be derived from the other by use of the limiting form of the differential equation (4). A numerically convenient form for this outer boundary condition is found by eliminating $(\eta - \beta)$ between f and f' to yield

$$\eta \to \infty: \quad f'^2 \to 1 + 2\Omega f \tag{8}$$

This form agrees with the one discussed in reference 3 for more general vorticity interaction problems.

Eq. (4) has been integrated using boundary conditions (5) and (8), for $\Omega = 0, 0.1, 0.5, 1.0, 1.5$. The shear stress at the wall $\eta = 0$ is given by

$$\tau_w = \mu r A (2A/\nu)^{1/2} f''(0) \tag{9}$$

The quantity $f''(0)/f_0''(0)$ is plotted against Ω in Fig. 1, where $f_0''(0) = 0.9277$, the value for $\Omega = 0$. Also plotted in Fig. 1 is the nondimensional distance β which the inviscid flow is displaced, in the form $1 + \beta/\beta_0$, $\beta_0 = 0.8045$. It can be seen that the effect of external vorticity is to increase the wall shear stress sharply while reducing the displacement effect of the boundary layer on the external flow.

The effect of vorticity on heat transfer can be found by solving the usual stagnation-point energy equation:

$$g'' + Prfg' = 0 \tag{10}$$

$$g(0) = 0; \qquad \eta \to \infty: \ g \to 1 \tag{11}$$

Here $g = (T - T_w)/(T_{st} - T_w)$, where T_{st} is the stagnation temperature of the free stream. Pr is the Prandtl Number. This equation has also been solved, with the f found above, for the same values of Ω. The heat-transfer rate at the wall is

$$q_w = k(2A/\nu)^{1/2}(T_{st} - T_w)g'(0) \tag{12}$$

The quantity $g'(0)/g_0'(0)$ is plotted in Fig. 1 for $Pr = 0.71$, where $g_0'(0) = 0.4371$, the value for $\Omega = 0$. Two points are also shown for $Pr = 1.0$, for which $g_0'(0) = 0.5389$, and indicate that the ratio is only affected slightly by Prandtl Number. These results show that heat transfer is much less sensitive to external vorticity than is shear stress, a not too surprising result in view of the fairly weak coupling that is known to occur between the momentum and energy Eqs. (4) and (10).

For purposes of computation in the range $0 \leq \Omega \leq 0.6$, the following expressions are good approximations to the curves of Fig. 1:

$$f''(0)/f_0''(0) = 1 + 0.78\Omega$$
$$g'(0)/g_0'(0) = 1 + 0.36\Omega$$

These may be compared with the compressible values 0.49 and 0.19, respectively, which are suggested in reference 3.

Essentially the same problem as that considered here was studied by Mark,[4] using Crocco variables and $Pr = 1$. However, he used an outer boundary condition corresponding to $f'' = \Omega$ at $f' = 1$, which does not agree with (6) or (8), and so obtained different numerical results. If his momentum equation is integrated using $f'' = \Omega$ at $f' \to \infty$, which does agree with (6), the results are in substantial agreement with those given here.

References

[1] Stuart, J. T., *The Viscous Flow Near a Stagnation Point When the External Flow Has Uniform Vorticity*, Readers' Forum, Journal of the Aero/Space Sciences, Vol. 26, No. 2, pp. 124–125, February, 1959.

[2] Lighthill, N. J., *Dynamics of a Dissociating Gas. Part I: Equilibrium Flow*, J. Fluid Mech., Vol. 2, Part 1, pp. 28–31, January, 1957.

[3] Hayes, W. D., and Probstein, R. F., *Hypersonic Flow Theory*, Sec. 9.6; Academic Press, New York, 1959.

[4] Mark, R. M., *Effect of Externally Generated Vorticity on Laminar Heat Transfer*, Readers' Forum, Journal of the Aeronautical Sciences, Vol. 24, No. 12, pp. 923, 924, December, 1957.

Experimental Study of the Flow Field About Swept and Delta Wings (*Cont. from page 494*)

(4) In the region outboard of the swept-off vortex, the velocity above the wing is parallel to the leading edge and approximately equal to the free-stream velocity. The pressure on the wing is constant.

(5) All the preceding results apply to turbulent flows; they are independent of Reynolds Number and apparently of Mach Number as long as the leading edge is appreciably behind the apex Mach cone.

References

[1] Legendre, R., *Écoulement au voisinage de la pointe avant d'une aile a forte flèche aux incidences moyennes*, Rech. Aero., No. 30, pp. 3–8, November–December, 1952, No. 31, pp. 3–6, January–February, 1952.

[2] Brown, C. E., and Michael, W. H., Jr., *On Slender Delta Wings with Leading Edge Separation*, NACA TN 3430, June, 1955.

[3] Edwards, R. H., *Leading-Edge Separation from Delta Wings*, Readers' Forum, Journal of the Aeronautical Sciences, Vol. 21, No. 2, pp. 134–135, February, 1954.

[4] Mangler, K. W., and Smith, J. H. B., *Flow Past Slender Delta Wings with Leading Edge Separation*, RAE Rep. Aero. 2593, May, 1957.

[5] Nikolski, A. A., *Investigation of Separated Vortex Flows*, presented at the 9th International Congress of Applied Mechanics, Brussels, 1956.

[6] Pappas, C. E., and Kunen, A. E., *An Investigation of the Aerodynamics of Sharp Leading-Edge Swept Wings at Low Speeds*, Journal of the Aeronautical Sciences, Vol. 21, No. 10, pp. 649–658, October, 1954.

[7] Emslie, K., Hosking, L., and Marshall, W. S. D., *Some Experiments on the Flow in the Boundary Layer of a 45° Swept-back Untapered Wing of Aspect Ratio 4*, Cranfield Rep. No. 69, February, 1953.

[8] Ornberg, T., *A Note on the Flow Around Delta Wings*, KTH—Aero. TN No. 38, 1954.

[9] Black, J., *Flow Studies of the Leading Edge Stall on a Swept-Back Wing at High Incidence*, J. RAeS., Vol. 60, No. 541, pp. 51–60, January, 1956.

[10] Drougge, G., *Pressure Measurements and Flow Investigation on Delta Wings at Supersonic Speed*, FFA Rep. No. 57, 1956.

[11] Kuethe, A. M., McKee, B. B., and Curry, W. H., *Measurements in the Boundary Layer of a Yawed Wing*, NACA TN 1946, September, 1949.

[12] Fink, P. T., *Wind Tunnel Tests on a Slender Delta Wing at High Incidence*, Z. Luftfahrt Wiss., Vol. 4, No. 7, pp. 247–249, July, 1956.

[13] Fink, P. T., and Taylor, J. T., *Some Low Speed Experiments with 20° Delta Wings*, Imperial College Rep., 1955.

[14] Hopkins, E. J., and Sorensen, N. E., *A Device for Vortex-Core Measurements*, Readers' Forum, Journal of the Aeronautical Sciences, Vol. 23, No. 4, pp. 396–398, April, 1956.

[15] Küchemann, D., *Types of Flow on Swept Wings with Special Reference to Free Boundaries and Vortex Sheets*, J. RAeS., Vol. 57, No. 515, pp. 683–699, November, 1953.

[16] Küchemann, D., *The Effects of Viscosity on the Type of Flow on Swept Wings*, Symp. on Boundary Layer Res., NPL, April 1, 1955, Teddington, England.

[17] Jaszlics, I., and Trilling, L., *An Experimental Study of the Flow Field About Swept Delta Wings with Sharp Leading Edges*, OSR-TN-58-6, October, 1957.

(12)

where
shown
at the
results
rticity
of the
omen-

6, the
rves of

49 and

e was
How-
ing to
and so
uation
th (6),
here.

External
o/Space

librium

Sec. 9.6;

ar Heat
Vol. 24,

Some
Swept-
No. 69,

XTH—

Swept-
pp. 51–

igation
6.
easure-
1946,

Ving at
7–249,

iments

ex-Core
autical

Special
., Vol.

of Flow
April 1,

of the
Edges,

REQUIREMENTS *for* CONTRIBUTIONS

to the publications of the

INSTITUTE *of the* AERONAUTICAL SCIENCES

The Institute of the Aeronautical Sciences invites both members and nonmembers from any country to submit papers for publication in the JOURNAL OF THE AERO/SPACE SCIENCES and AERO/SPACE ENGINEERING. The Institute, following the practice of other societies, does not pay for contributions.

The following directions for the preparation of papers, if followed by authors, will save correspondence, avoid the return of papers for changes, minimize the work of preparation for the printer, and save the expense due to the charges made for "author's corrections."

MANUSCRIPTS: The original typewritten copy of the paper is desired. **To expedite review, an additional copy of both the manuscript and figures should be submitted.** The manuscript must be double or triple spaced on one side of white paper sheets, consecutively numbered. There should be wide margins to allow for the marking of directions to the printer. Correcting, changing, or adding to papers after they are in type is costly. It is, therefore, imperative that papers submitted be in final form. Typographical errors may be corrected on proofs, but if authors wish to add material, they may do so at their own expense. In mailing, drawings may be rolled, but manuscripts should be sent flat. Send by first-class mail (register if you wish for your own protection) to the Editorial Office, Institute of the Aeronautical Sciences, 2 East 64th Street, New York 21, N.Y. All manuscripts will be examined by the Editorial Committee and by the Editor. Authors will be advised as promptly as possible whether the paper is acceptable for publication.

TITLES: The title of the paper should be brief. The name and initials of the author should be written as he prefers. The use of the full name of an author is advocated because of the frequent duplication of initials and surnames which sometimes makes it difficult to establish the identity of the author. This is particularly important for large annual indexing and abstracting services. All titles and degrees or honors are omitted. The name of the organization with which the author is associated should be placed after his name on a separate line. The date on which the paper is received will be inserted by the Editor. The author's title or position should be indicated in a footnote.

SUMMARIES OR ABSTRACTS: An abstract to be printed at the beginning should accompany each article. It should be adequate as an *index* and as a *summary*. It should contain a statement of major conclusions reached, since summaries in many cases constitute the only source of information used in compiling scientific reference indexes. Abstracts printed in other journals, especially foreign, in most cases consist of summaries from printed papers. The summary should explain as adequately as possible the major conclusions to a nonspecialist in the subject and should contain from 100 to 300 words, depending on the length of the paper.

SUBHEADINGS: Subheadings should be inserted by the author at frequent intervals. The work of editorial preparation will be simplified by the author's provision of many subheadings.

MATTER USUALLY DELETED: Photographs or illustrations of little technical interest and not showing advances in general practice. Too detailed tabular matter (general results of such tables may be included in the text). Lengthy descriptions of materials or processes or of preliminary experiments or theories that preceded final results; salient features only are of interest.

REFERENCES: References should be numbered consecutively and grouped together at the end of the manuscript, with only the corresponding number being mentioned in the text. The arrangement should be as follows. For books: [1]Durand, W. F., *Aerodynamic Theory*, 1st Ed., Vol. 1, p. 23; Julius Springer, Berlin, 1934. For magazines: [1]England, C. R., Crawford, A. B., and Mumford, W. W., *Some Results of a Study of Ultra-Short-Wave Transmission Phenomenon*, Proc. IRE, Vol. 20, No. 12, pp. 481–482, March, 1933. Please give author, title, edition, volume, number, page, publisher, and place and date of publication as indicated. Omission of one required fact causes much extra editorial work and possible inaccuracies.

ILLUSTRATIONS: Illustrations should accompany manuscripts, and each should always be referred to in the text by number. Drawings or graphs should not be larger than 12 × 16 inches, and must be made with jet black India ink on white paper or tracing cloth, the latter being preferred. *Do not use typewriter for lettering.* The smallest lettering on 8 × 10 inch figures should be no less than $^1/_4$ inch high. Cross-section paper (white with black lines) may be used, but it should not have more than 4 lines per inch. If finer ruled paper is used, the major division lines should be drawn in with black ink, omitting the finer divisions. In the case of finely ruled paper, only blue-lined paper can be accepted. *Tracing paper and blueprints* are not acceptable. Lettering and all markings must be large enough to be readable after reduction to single-column width ($3^5/_{16}$ in.). Mail rolled or flat; never fold. Drawings that cannot be reproduced (including pencil drawings) will be returned to the author for redrawing, thus delaying publication of the paper. Photographs should be distinct and show clear black and white contrasts. They must be on glossy white paper. Avoid round and oval photographs.

CAPTIONS AND LEGENDS: Legends or captions must accompany each drawing or photograph submitted. If written on the drawing or photograph, they should be placed below and well outside the part to be reproduced. Each table should have a caption such as Table 1, Table 2, Table 3, etc. Captions should be complete in themselves so as to make the data intelligible to the reader without reference to the text. A duplicate list of captions for figures should be included as the last page of the manuscript. Use "Fig. 1" (not Figure 1), "Figs. 3 and 4," etc., in both the text and the numbering of illustrations. In the text, "Eq. (1)" or "Eqs. (1) and (2)" is used, not "Equation (1)." In captions, legends, and in table headings, write all words in full; do not abbreviate, except for "Fig." and "Eq."

MATHEMATICAL WORK: Formulas may be typewritten or carefully written in pen and ink, the writing to be large enough so that it can be marked for the printer. Considerable space for marking should be allowed above and below all equations. All complicated equations should be repeated on separate sheets with plenty of space left for marking. The solidus should be used for simple fractions appearing within the text. Make all expressions clear to the typesetter. Greek letters used in formulas should be clearly designated by name in the margin of the manuscript. The difference between capital and lower-case letters should be clearly distinguished and care taken to avoid confusion between zero (0) and the letter (o), between the numeral (one), and the letter (ell) and the prime (′), between alpha and a, kappa and k, u and mu, v and nu, n and eta. All subscripts and exponents should be clearly distinguished. Avoid complicated exponents and subscripts. Dots and bars over letters or mathematical expressions should also be avoided. When it is necessary to repeat a complicated expression, it should be represented by some convenient symbol.

SYMBOLS AND ABBREVIATIONS: The symbols recommended in the American Standard Association "Letter Symbols for Aeronautical Sciences," ASA Y10.7—1954, should be used wherever practicable. All symbols should be clearly written and carefully checked. Standard abbreviations should be used, and it should be noted that most abbreviations are lower case, such as m.p.h., b.m.e.p., i.h.p., b.hp., hp., etc.

CORPORATE MEMBERS

OF THE

INSTITUTE OF THE AERONAUTICAL SCIENCES

AC SPARK PLUG DIVISION, GENERAL MOTORS CORPORATION

ACADEMY OF AERONAUTICS

ADAMS RITE MANUFACTURING COMPANY

AEROJET-GENERAL CORPORATION

AEROLAB DEVELOPMENT COMPANY

AERONCA MANUFACTURING CORPORATION

AERONUTRONIC SYSTEMS, INC.

AEROQUIP CORPORATION

AGAWAM AIRCRAFT PRODUCTS, INC.

ALLIED RESEARCH ASSOCIATES, INC.

ALLISON DIVISION, GENERAL MOTORS CORPORATION

ALUMINUM COMPANY OF AMERICA

AMERICAN AIRLINES, INC.

AMERICAN BOSCH ARMA CORPORATION

AMERICAN NON-GRAN BRONZE COMPANY

AMERICAN STEEL & WIRE DIVISION, UNITED STATES STEEL CORPORATION

AMOCO CHEMICALS CORPORATION

AMPHENOL-BORG ELECTRONICS CORPORATION

ANDERSON, GREENWOOD & CO.

ARDE ASSOCIATES

ASSOCIATED AVIATION UNDERWRITERS

AVCO RESEARCH LABORATORY

AVIEN, INC.

AVRO AIRCRAFT LIMITED

BAKER STEEL & TUBE COMPANY

BEECH AIRCRAFT CORPORATION

BELL AIRCRAFT CORPORATION

BENDIX AVIATION CORPORATION

BOEING AIRPLANE COMPANY

BOOZ, ALLEN & HAMILTON

THE BRISTOL AEROPLANE COMPANY (U.S.A.) INC.

BULOVA RESEARCH AND DEVELOPMENT LABORATORIES, INC.

CANADAIR, LTD.

THE CESSNA AIRCRAFT COMPANY

CHANCE VOUGHT AIRCRAFT, INCORPORATED

THE CHASE MANHATTAN BANK

CHICAGO AERIAL INDUSTRIES, INC.

THE CLEVELAND PNEUMATIC INDUSTRIES, INC.

CONSOLIDATED CONTROLS CORPORATION

CONTINENTAL MOTORS CORPORATION

CORNELL AERONAUTICAL LABORATORY, INC.

CURTISS-WRIGHT CORPORATION

DANIEL, MANN, JOHNSON, & MENDENHALL

THE DECKER CORPORATION

DEL MAR ENGINEERING LABORATORIES

DELCO-REMY DIVISION, GENERAL MOTORS CORPORATION

DOAK AIRCRAFT COMPANY ,INC.

DOUGLAS AIRCRAFT COMPANY, INC.

DZUS FASTENER COMPANY, INC.

EASTERN AIR LINES, INC.

EATON MANUFACTURING COMPANY

EDO CORPORATION

ELASTIC STOP NUT CORPORATION OF AMERICA

ELECTROL INCORPORATED

ENGINEERING SUPERVISION COMPANY

ESSO STANDARD OIL COMPANY

FAIRCHILD CAMERA AND INSTRUMENT CORPORATION

FAIRCHILD ENGINE AND AIRPLANE CORPORATION

THE FIRESTONE TIRE & RUBBER COMPANY

THE GARRETT CORPORATION

GENERAL DYNAMICS CORPORATION

GENERAL ELECTRIC COMPANY

GENERAL PRECISION EQUIPMENT CORPORATION

G. M. GIANNINI & CO., INC.

GIANNINI PLASMADYNE CORPORATION

THE B. F. GOODRICH COMPANY

GOODYEAR AIRCRAFT CORPORATION

GRUMMAN AIRCRAFT ENGINEERING CORPORATION

HYDRO-AIRE, INC.

INSURANCE COMPANY OF NORTH AMERICA COMPANIES

INTERNATIONAL BUSINESS MACHINES CORPORATION

THE INTERNATIONAL NICKEL COMPANY, INC.

ITT LABORATORIES, DIVISION OF INTERNATIONAL TELEPHONE AND TELEGRAPH CORPORATION

JANITROL AIRCRAFT DIVISION, SURFACE COMBUSTION CORPORATION

JOHNS-MANVILLE SALES CORPORATION

EARLE M. JORGENSEN CO.

WALTER KIDDE & COMPANY, INC.

KOLLSMAN INSTRUMENT CORPORATION

LAVELLE AIRCRAFT CORPORATION

LEAR, INCORPORATED

C. W. LEMMERMAN, INC.

LIBRASCOPE, INCORPORATED

THE LIQUIDOMETER CORPORATION

LOCKHEED AIRCRAFT CORPORATION

LOEWY-HYDROPRESS DIVISION OF BALDWIN-LIMA-HAMILTON CORPORATION

LONGINES-WITTNAUER WATCH COMPANY, INC.

THE MARQUARDT CORPORATION

THE MARTIN COMPANY

MARTIN STEEL PRODUCTS CORPORATION

McDONNELL AIRCRAFT CORPORATION

MELETRON CORPORATION

MID-CONTINENT MANUFACTURING, INC.

MINNEAPOLIS-HONEYWELL REGULATOR COMPANY

NATIONAL CREDIT OFFICE, INC.

NORTH AMERICAN AVIATION, INC.

NORTHROP CORPORATION

NUCLEAR DEVELOPMENT CORPORATION OF AMERICA

PAN AMERICAN WORLD AIRWAYS, INC.

THE RALPH M. PARSONS COMPANY

PESCO PRODUCTS DIVISION, BORG-WARNER CORPORATION

PHILLIPS PETROLEUM COMPANY

PIASECKI AIRCRAFT CORPORATION

RADIO CORPORATION OF AMERICA DEFENSE ELECTRONIC PRODUCTS

REPUBLIC AVIATION CORPORATION

ROHR AIRCRAFT CORPORATION

PAUL ROSENBERG ASSOCIATES

RYAN AERONAUTICAL COMPANY

SANDBERG-SERRELL CORPORATION

SHAFER BEARING DIVISION, CHAIN BELT COMPANY

SHELL OIL COMPANY

SIMMONDS AEROCESSORIES, INC.

SOCONY MOBIL OIL COMPANY, INC.

SOLAR AIRCRAFT COMPANY

SOUTHWEST PRODUCTS CO.

SPACE TECHNOLOGY LABORATORIES, INC.

R. DIXON SPEAS ASSOCIATES

SPERRY GYROSCOPE COMPANY DIVISION OF SPERRY RAND CORPORATION

STANDARD OIL COMPANY OF CALIFORNIA

STANDARD OIL COMPANY (INDIANA)

STANDARD-THOMSON CORPORATION CLIFFORD MANUFACTURING DIVISION

STANLEY AVIATION CORPORATION

THIOKOL CHEMICAL CORPORATION

THOMPSON RAMO WOOLDRIDGE INC.

TRANS WORLD AIRLINES, INC.

TURBO PRODUCTS, INC.

UNION CARBIDE CORPORATION

UNITED AIR LINES, INC.

UNITED AIRCRAFT CORPORATION

UNITED STATES AVIATION UNDERWRITERS, INC.

VARD, INC.

VERTOL AIRCRAFT CORPORATION

VITRO CORPORATION OF AMERICA

WESTERN GEAR CORPORATION

WESTINGHOUSE ELECTRIC CORPORATION

WESTON INSTRUMENTS DIVISION OF DAYSTROM, INC.

WYMAN-GORDON COMPANY

YOUNG RADIATOR COMPANY